# Transport properties in nanostructures

Alejandro González Inostroza

**Profesor:** Pedro Orellana Dinamarca

Universidad Técnica Federico Santa María

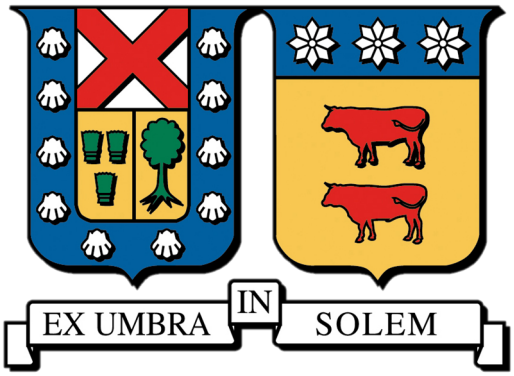

# Contents

# List of Figures

This work is dedicated to my wife Karen and my family, who have supported my studies and work.

# 1

# Introduction

## 1.1 Quantum Dots, Coulomb Blockade, Kondo and Dicke effect

A quantum dot (QD) is an artificially fabricated device in which a few electrons are confined in a small three-dimensional region whose dimensions are smaller than the coherence length of the electrons in the material (on the order of 100 nm). Because of their reduced size, QDs exhibiting interesting effects due to quantum confinement such as discrete energy levels and charging effect. For this reason, quantum dots are called "artificial atoms". There are many ways to construct a quantum dot. One of these methods is the formation of nanosized semiconductor particles through colloidal suspensions of semiconductor nanoparticles. Due to their tunable optical properties, based on their size, shape, and composition, this type of Quantum dots allows a variety of research and commercial applications including bioimaging, solar cells, LEDs, diode lasers, and transistors. Just this year's Nobel Prize in Chemistry recognizes the discovery and synthesis of nanometre-sized semiconductor crystals by Moungi G. Bawendi, Louis E. Brus, and Aleksey Yekimov. Another method is the epitaxial growth and/or nanoscale patterning, i.e. employing lithography-based technology. By means of these methods, different types of quantum dots can be manufactured, among them: lateral quantum dots, vertical semiconductor dots, and carbon nanotube quantum dots. For example, a lateral QD is defined by imposing metal "gate" electrodes on top of a semiconductor heterostructure (e.g. GaAs/AlGaAs) as shown in Fig. 1.1, so that the electrons are confined to move only in the x-y plane, at the interface between GaAs and AlGaAs, while a potential in the z-direction confines them. The quantum dot is embedded between two extended sections named source and drain. The side gates allow for control of the tunneling with the leads, which act as electron reservoirs and are tunnel-coupled to the quantum dot. The device can be driven out of equilibrium by applying a bias voltage $V_{SD}$ between the two leads. The bias voltage $V_{SD} = (\mu_D - \mu_S)/e$ defines a transport window, a span of dot energies for which electronic transport is in principle, possible. Whether the quantum dot is conducting depends on whether one of the discrete dot levels is within the transport window. Electronic transport is possible when one of the discrete dot levels of the QD is within the transport window. Thus, whenever there is no dot level within the transport window, no electron transport between the source and the drain reservoir is possible.

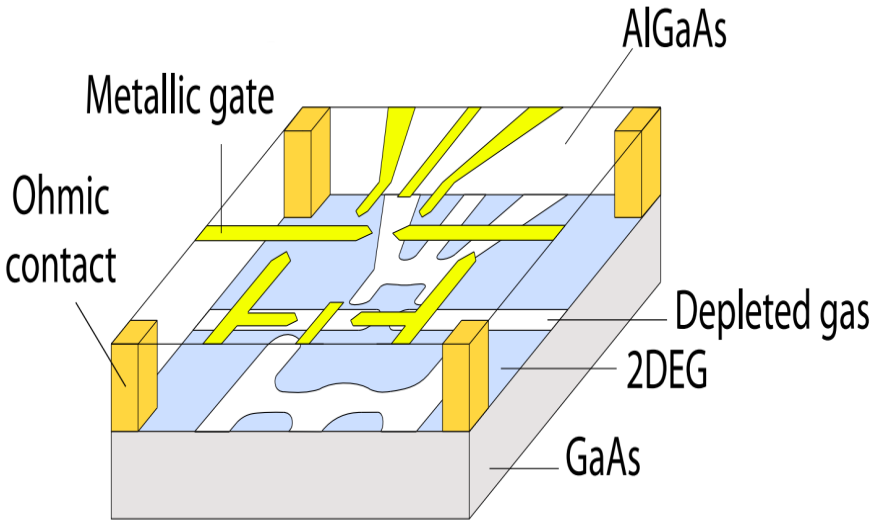


Figure 1.1: Schematic representation of the electrostatically defined quantum dots coupled in parallel(Kondo physics in side coupled quantum dots. 12-2010) [1].

QDs allow for the adjustment of several parameters, including the coupling strength, voltage bias, and impurity energy level. The coupling strength between the dot and the source (and drain) determines the probability of tunneling from one to another and is established by applying a potential to the gold-colored electrical contacts in (Fig. 1.1). This forms quantum point contacts (QP). A bias voltage can be set by connecting external leads to the 2DEG using ohmic contacts, as shown in Fig. 1.1, which enables conductance measurements of the QD itself. The plunger gate regulates the energy level, a gold electrical contact that uses an applied negative potential (of varying magnitude) to control the number of electrons in the QD. The number of electrons in the dot can be varied from 0 to the order of 50 and is fixed when the system is at a low enough temperature due to the Coulomb blockade. The Coulomb blockade describes a situation in which the highest occupied energy state of the quantum dot lies significantly below the Fermi energy of the system, while the next energy level corresponding to adding another electron to the dot lies significantly above the Fermi energy. Adding or removing an electron has an energy cost $U = 2e^2/C$ (charge effect). As shown in Fig.2.2, no electron transport between the source and the drain reservoir is possible whenever there is no dot level within the transport window. Then, the number of electrons on the QD is stable, and the system is Coulomb-blocked. On the contrary, when one of the energy levels of the quantum dot is aligned with the chemical potential of the leads, it is straightforward for an electron to tunnel in or out of the dot without any energy cost. Consequently, the linear conductance through the dot shows a succession of peaks associated with the Coulomb peaks, separated by regions of low conductance.

A false-colored SEM image of QD showing the 2DEG in blue, the gates responsible for establishing the QPCs to the dot in gold, and the gates that only confine the dot in light grey.

An interesting phenomenon that QDs allow us to study is the Kondo effect. The Kondo

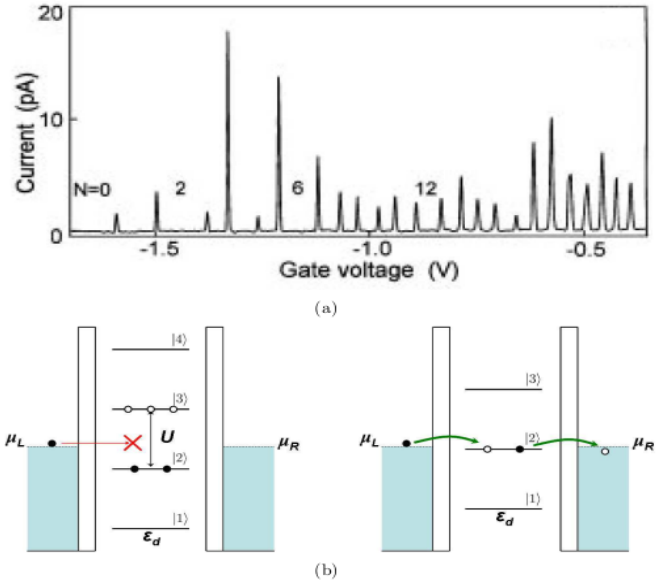


Figure 1.2: (a) Linear (zero-bias) conductance as a function of the gate voltage in the Coulomb blockade regime [2]. (b) Cartoon explaining single-particle tunneling processes through a dot with degenerate energy levels $\epsilon_d$ and a Coulomb repulsion between electrons U. Transport is possible only when the effective dot energy level is aligned with the chemical potential of the leads (right). This is responsible for the conductance peaks in (a). In the other regimes (left), the occupation number of the dot is fixed, and transport through the quantum dot is blocked.

effect is a quantum mechanical phenomenon that occurs in certain materials, particularly metals and alloys, at very low temperatures and is primarily associated with the behavior of magnetic impurities in a non-magnetic host material. For temperatures lower than the Debye temperature, the resistivity of a metal is essentially determined by electron-phonon scattering and decreases with T as $\rho(T) \sim T^5$. At even lower temperatures, it eventually saturates to a minimum resistivity, which was found to be related to the scattering by the defects of the crystal lattice. Copper and gold remain conductive, with a constant and finite resistance even at the lowest temperatures reachable (for instance, lead, niobium, and aluminum can suddenly lose all their resistance to electrical current and become superconducting). However, an experiment revealed a distinct behavior in 1934 (Fig. 2.3). In this year, at the Kamerlingh Onnes Laboratory in the Netherlands, W. J. de Haas, J. de Boer and G.J. van dën Berg discovered that the resistance curve of impure gold wires has a minimum at low temperatures [7]. This remained a mystery until 1964, when an experiment showed evidence of a relationship between this behavior and the presence of dilute magnetic impurities [8] motivated the Japanese theorist Jun Kondo to consider a model involving an alternative electron scattering process that includes a temporary exchange of spin state between the conduction electron and magnetic impurity [9]. Using perturbation theory to model the scattering from a magnetic impurity interacting with the spins of conducting electrons, he observed that the next-to-leading order terms involve logarithmic corrections responsible for increasing resistivity at low temperatures. As Kondo's theory describes, the metal's resistance increases logarithmically as temperature decreases. However, it also makes an unphysical prediction that the resistance will be

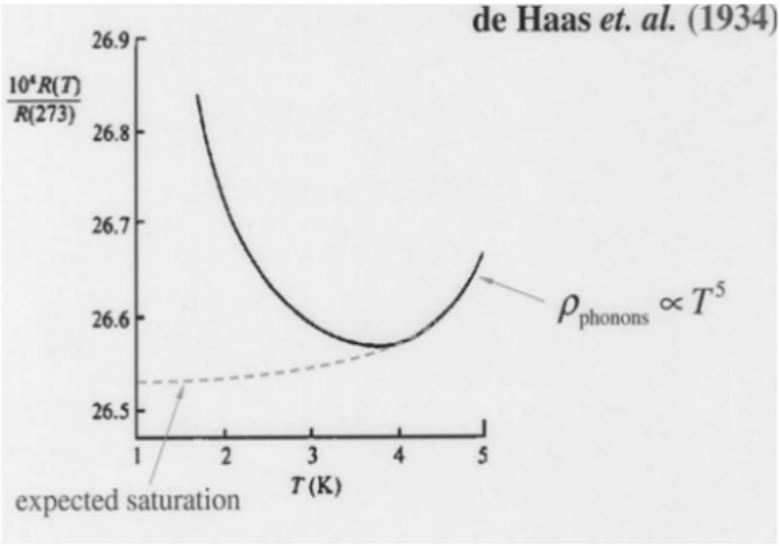


Figure 1.3: Results showing resistivity minimum from original 1934 experiement on gold [3].

infinite at lower temperatures. It turns out that Kondo's result is correct only above a specific temperature, which became known as the Kondo temperature, $T_K$.

These QDs are effective models of a single magnetic impurity in a bulk metal system while providing the ability to tune (in situ) the voltage bias, magnetic field, temperature, energy level of the impurity, and the coupling strength between the impurity and the source of the conduction electrons [10]. The mechanism for controlling the overall spin of the system is as follows: the electrons fill the energy bands below the Fermi level with pairs of spin-up and spin-down electrons. At low temperatures, an even number of electrons results in no net spin on the dot. On the other hand, an odd number of electrons results in the highest accessible energy level being occupied by only one electron, giving a net spin of $\pm 1/2$ (depending on the spin of that single electron). With a net spin and controllably connected to the 2DEG, the quantum dot effectively replicates a magnetic impurity caused by ions in a metal such as the classic dilute copper-cobalt alloy system. While the Kondo effect in bulk systems induces an additional scattering process that increases the resistivity, it strongly enhances the transport in quantum dots because the QD creates a 1D channel for the electrons to pass through and increases interaction between the spins of the electrons in the leads and dot creates a Kondo resonance which allows electrons to tunnel through. In other words, the Kondo effect produces the opposite behavior in a quantum dot to that of a bulk metal.

The first experiments showing evidence for the Kondo effect in quantum dots were realized about ten years ago. Fig. 1.4 shows the crossover from the Coulomb blockade regime to the Kondo regime measured by lowering the temperature. At high temperatures, we recover a succession of Coulomb peaks and valleys in which the conductance is blocked. When the temperature is lowered, the conductance is enhanced in one valley in the two. It can be interpreted by associating an odd number of electrons to these valleys, which implies that they carry a nonzero spin responsible for the enhanced conductance by the Kondo effect at low temperatures. The conductance eventually reaches the unitary

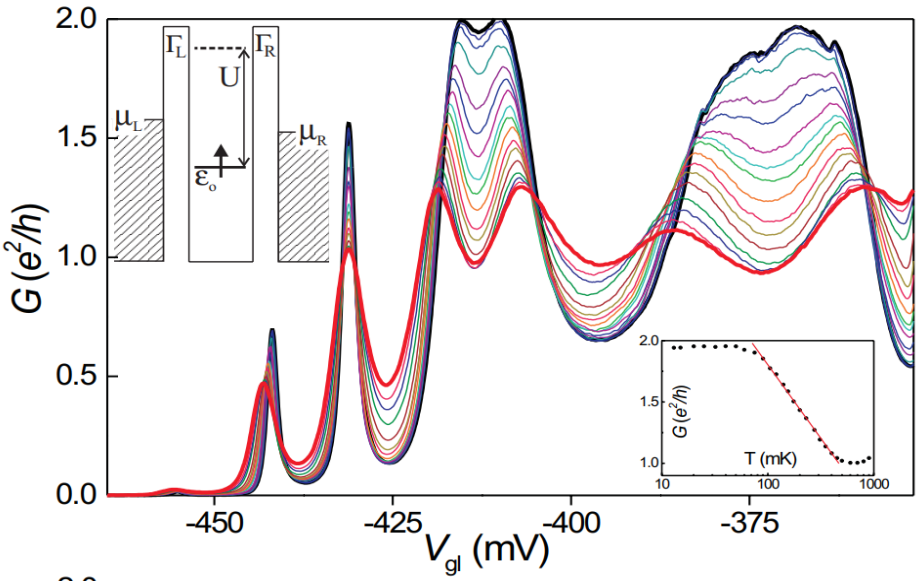


Figure 1.4: Linear conductance as a function of the gate voltage for different temperatures [4]. At high temperature ($T \gg T_K$, red curve), the conductance is blocked when the occupation number of the dot is fixed, while it shows peaks in the regions of degeneracy. At lower temperatures ($T \ll T_K$, black curve), the conductance is enhanced in the odd occupancy regions because of the emergence of the Kondo effect.

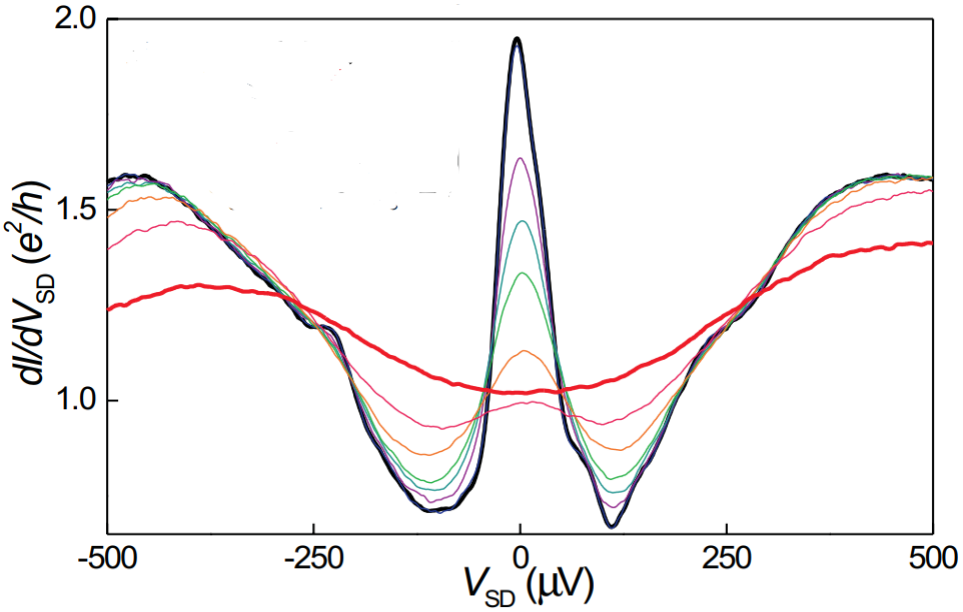


Figure 1.5: Differential conductance $dI/dV$ as a function of the bias voltage V [4]. The narrow peak at low bias is due to the Kondo effect, whereas the high-voltage peaks are related to single-particle transport.

quantum limit $2e^2/h$ at zero temperature. On the contrary, the regions of even occupancy, where no Kondo effect is possible, show a conductance that decreases with temperature because of the reinforcement of the Coulomb blockade.

Another characteristic of the Kondo effect in quantum dots can be found in the bias-voltage dependence of the differential conductance $dI/dV$, which shows a narrow peak at low bias voltage V 1.5. As noted previously, the height of the peak reaches the unitary limit of $2e2/h$ at zero bias and zero temperature. When either the temperature or the bias voltage is increased, the spin-flip scattering processes become incoherent, destroying the coherent Kondo effect, and the conductance decreases. The increase in differential conductance at very high voltage occurs when the chemical potential of one lead aligns with a dot level. In that case, the electrons can easily tunnel into or out of the dot through single-particle processes. From a theoretical point of view, the nonequilibrium transport for the Anderson model in the presence of a bias voltage has not been solved exactly so far.

Another interesting phenomenon originating in quantum optics and which has also been predicted in electronic transport in quantum systems is the Dicke effect. This effect, predicted by Dicke in 1954 (Fig. 1.6), in quantum optics means the presence of a strong and narrow spontaneous emission line in addition to much broader lines of a collection of atoms, which are separated by a distance smaller than the wavelength of the emitted light [11]. The narrow line (called a sub-rradiant) is associated with a state which is weakly coupled to the electromagnetic field and, therefore, is a long-lived state. On the contrary, the broad line (called a superradiant) is associated with a state that is strongly coupled to the electromagnetic field and, therefore, is a short-lived state. The Dicke effect in the mesoscopic system was first predicted in two-channel resonant tunneling [12], since then the analogies to the Dicke effect have been found in some other mesoscopic systems where the behavior of the spectral function resembles the transition from subradiant to superradiant mode (or vice versa) in the usual Dicke effect. In a coupled DQD system, the Dicke effect in the conductance can be controlled by the magnetic flux [13]. More recently, the Dicke effect has been predicted in a QD coupled to a two-sided QD structure in the Coulomb blockade regime and the Kondo regime [14, 15], in which the effective coupling between localized levels and a conduction channel gives rise to effectively fast super-tunneling and slow sub-tunneling modes. Since the local density of states (LDOS) can exhibit an almost $\delta$-like shape for appropriate parameters due to the Dicke effect, significant enhancement of thermal efficiency is expected. In nanostructures, where the central quantum dot (QD0) with two side-attached dots ($QD \pm 1$) are arranged in a crossed bar configuration, the sub- and superradiant contributions can be achieved either upon increasing the interdot coupling or tuning the quantum dot energy levels.

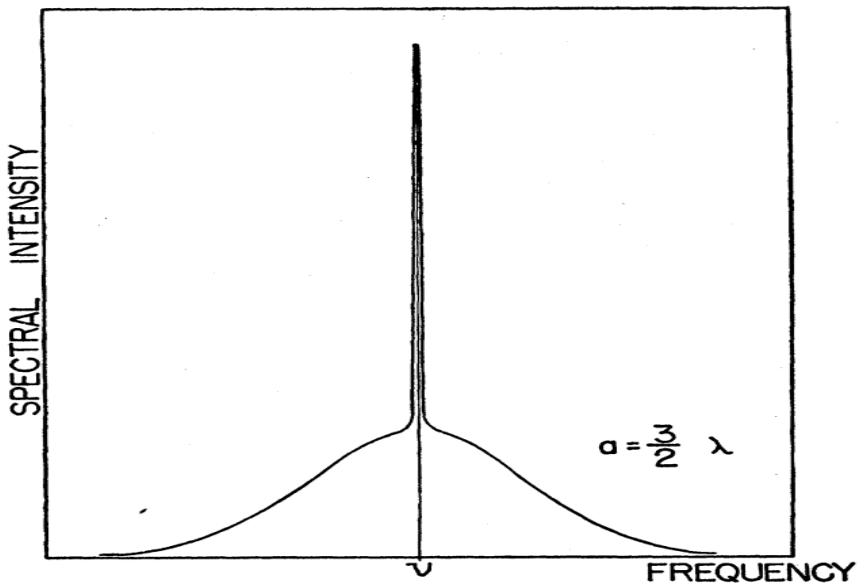


Figure 1.6: Line narrowing due to collisions of a Doppler–broadened spectral line in the original 1953 Dicke paper [5]. The radiating gas is modeled within a one–dimensional box of width a; $\lambda$ is the light wavelength.

## 1.2 Andreev Reflection and proximity effect

Superconductivity is a phenomenon that occurs when electrons pair up due to an effective attractive interaction and condense into a state that can carry dissipationless currents, also known as supercurrents. This state is characterized by a macroscopic phase. It was observed and understood for a long time that in hybrid structures where superconductors are put in contact with non-superconducting materials, for example, a normal metal, electronic pairs propagating from the superconductor 'leak' the non-superconducting material inducing pairing correlations, conferring it superconducting-like properties close to the interface, among which notably the ability to transmit supercurrent and a superconducting gap [16]. This "leak" is known as the proximity effect. The main mechanism responsible for the proximity effect is known as the Andreev reflection [17]. The Andreev tunneling occurs in the normal metal-insulator-superconductor (NIS) interface, in which an incident electron from the normal side is reflected as a hole(of opposite spin) and simultaneously by creating a Cooper pair in the superconductor. While electron excitation is a filled state at energy $\epsilon$ above Fermi energy $E_f$, hole excitation is an empty state at energy $\epsilon$ below $E_f$. This process is possible for $\epsilon < \Delta$, with $\Delta$ being the energy gap of the superconductor. Due to this feature, Andreev reflections provide a mechanism for current flow through the normal metal-superconductor interface. The proximity effect is also expected when the N conductor is reduced to a small QD with a discrete electronic spectrum. In that confined geometry, this process can create a pair of discrete Andreev energy levels in the superconducting gap. When a normal metal electrode is additionally coupled to the system, the discrete Andreev energy levels can broaden to form the so-called Andreev bound states (ABSs) with excitation energies within the superconducting energy gap. They are hybrids of quantum dot energy levels and many-body Bogoliubov

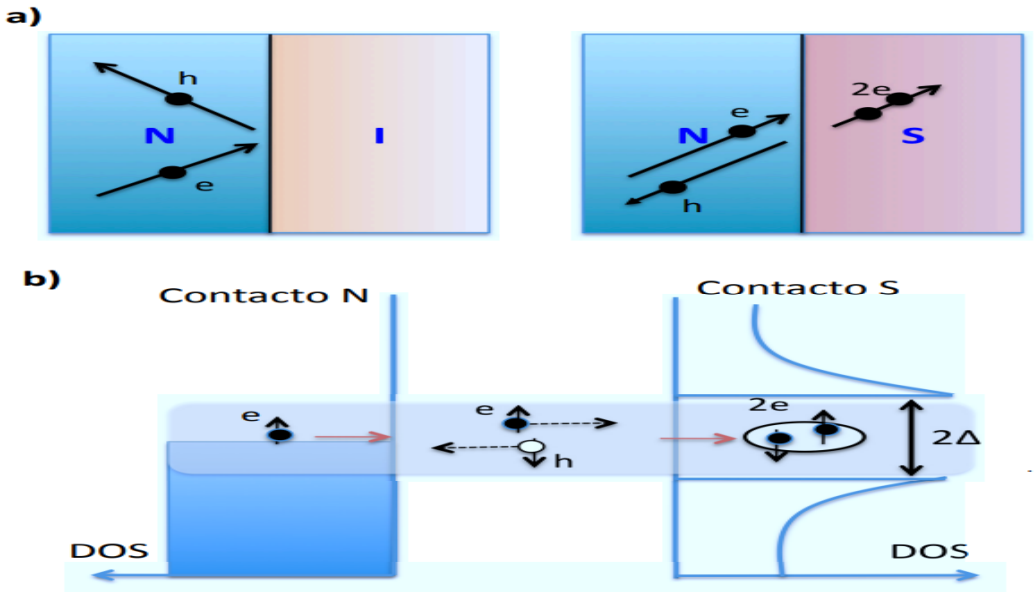


Figure 1.7: Density of states of the superconductor with a gap of $2\Delta$. An NIS interface with the normal state on the left and the superconductor to the right. An electron with energy $E < \Delta$ can be Andreev reflected as a hole, resulting in the injection of a Cooper pair into the superconductor. Outside the gap quasiparticle excitations are possible. [6]

quasiparticles. Cooper-pair tunneling can take place through it because the coherence length of Cooper pairs is significantly larger compared to the size of the QD. These ABSs dominate low-bias subgap electronic transport at low temperatures. Single-particle or quasiparticle tunneling becomes essential when the thermal energy is comparable to the superconducting energy gap or when the dot energy level lies outside the superconducting energy gap. Additionally, different Andreev processes are distinguished in a three-terminal device, such as a couple of two normal leads and one superconducting lead. In the direct Andreev reflection (DAR) two electrons enter the superconductor, and the backscattered hole is from the same lead, while in the crossed Andreev reflection (CAR), electrons stem from different normal leads. These nonlocal processes (CAR) are a potential source of entangled particles as they result from a singlet state of the Cooper pair. The processes competing with CAR are single electron transfers (ETs) between normal electrodes.

It is interesting to note that the superconducting proximity effect competes with the Coulomb blockade phenomenon, which follows from the electrostatic repulsion among the electrons of the QD. While superconductivity privileges the tunneling of electron pairs with opposite spin, thereby favoring QD states with even numbers of electrons and zero total spin (i.e. spin singlets), the local Coulomb repulsion enforces a one-by-one filling of the QD, thereby stabilizing not only even but also odd electron numbers.

# 2

# Dicke and Fano-Andreev reflections in a triple quantum-dot system.

Electron transport through multiple quantum dots systems exhibits exciting interference effects such as Fano [6,18–23] and Aharonov-Bohm [24–28]. The interference phenomenon, which resembles the well-known Dicke resonance in atomic physics, appears to be of particular importance [5]. It manifests itself by a narrow (subradiant) and a broad (superradiant) line shape, spontaneously emitted by closely linked atoms, separated by a distance smaller than the wavelength of the emitted light [11]. In the electronic case, the decay rates (level broadening) are produced by the couplings between localized levels and the conduction channel, and the proximity and effective couplings give rise to fast (super-tunneling) and slow (sub-tunneling) modes [29].

The presence of the Dicke effect has been predicted theoretically and experimentally in different nanoscopic systems [12–15,30–34]. On the other hand, the Fano effect is another quantum interference phenomenon that has been studied in quantum transport for some time. This effect is due to quantum interference from localized states and continuum states. It produces characteristic asymmetric Fano lineshape, characterized by the Fano factor $q$, which is a measure of the coupling strength between the continuum and the localized state.

Electronic transport through quantum dots (QDs), double quantum dots (DQDs), and triple quantum dots (TQDs) coupled to normal / ferro-ferromagnetic and superconductor leads has been studied recently [35–40]. The Cooper pairs [41] transport, along with interference effects among electrons and holes, give rise to novel and interesting phenomena [42, 43]. Within this context, several features of the Dicke effect have been considered in the presence of superconductor correlations. In particular, it has been found that the Dicke effect occurs in the Andreev conductance spectrum by modulating interdot coupling and side-dot levels [44,45]. A description of the relationship between the induced electron pairing and the Dicke effect has been studied [46] by focusing specifically on how electron pairing and correlation effects are affected by side-attached quantum dots, ranging from the interferometric to the molecular limits. However, a detailed description of the interplay between the Dicke effects and the charging effect induced by the Coulomb intra-dot correlations is still missing.

In this paper, we present an investigation of the influence of the Dicke and Fano effects on electronic transport through a coupled triple quantum dot system coupled to

normal and superconducting leads in a linear and nonlinear regime. In particular, we study the interplay between the proximity effect due to the superconducting lead and the conjunction of two phenomena: Dicke and Fano-Andreev reflections. We shall focus on the electronic properties of TQDs within the regime of low temperatures and sub-gap energies ($eV \ll \Delta$), where electronic transport is carried mainly by Andreev reflection (AR). We consider Coulomb correlations in all the quantum dots and study their influence on the electronic conductance. The interdot Coulomb interaction is assumed to be much smaller than the corresponding intradot interaction, and, in consequence, is omitted. Transport characteristics, such as the Andreev conductance and the electrical current of the system at the low-temperature limit, are derived using the nonequilibrium Green function method in the linear and nonlinear response regime. We use the Hubbard I approximation [47] to obtain the relevant Green functions from the equations of motion. Our results show that the Andreev reflection spectra, both in the presence and absence of Coulomb interaction, reveal Dicke and Fano-like resonances in analogy to their counterpart effects in atomic physics. As one of the main effects, we see that the charge shows abrupt changes due to the Dicke effect, which has not been shown in previous reports.

The paper is organized as follows. Section II introduces the model and describes the general background of the transport properties in the TQD system. Next, Sect. III presents the corresponding numerical results in the equilibrium and non-equilibrium regime for both non-interacting and interacting cases. Finally, Sect. IV closes with a summary and general conclusions.

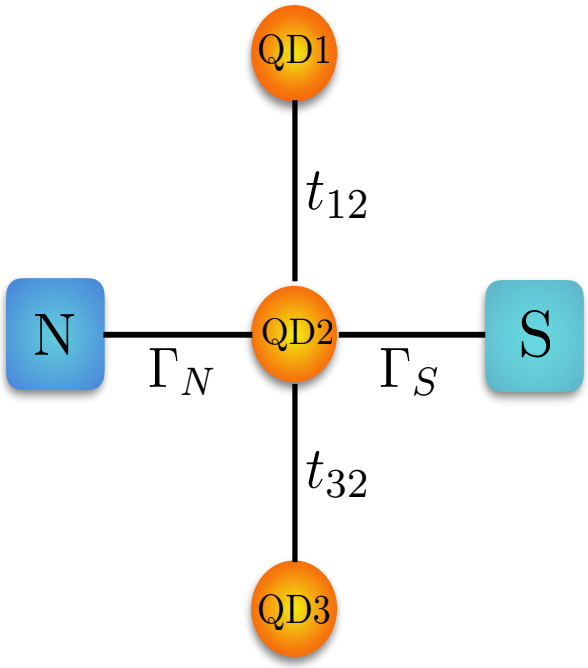


Figure 2.1: A sketch of triple-QD system coupled to normal metal and superconducting leads.

## 2.1 Model

The system under consideration consists of a single-level central quantum dot (QD2) attached to a normal metallic and one superconducting lead and two side quantum dots (QD1 and QD3), as shown schematically in Fig. 2.1. The following Hamiltonian models the system:

$$H = H_N + H_S + H_{TQD} + H_T. \tag{2.1}$$

The first term is the Hamiltonian for the normal electrode and it is given by:

$$H_N = \sum_k \sum_\sigma \epsilon_{kN\sigma} c^\dagger_{kN\sigma} c_{kN\sigma}, \tag{2.2}$$

where $c^\dagger_{kN\sigma}$ ($c_{kN\sigma}$) is the electron creation (annihilation) operator of an electron with spin $\sigma$ and energy $\epsilon_{kN\sigma}$ in the normal electrode.

The second term stands for the $BCS$ Hamiltonian [41] of the superconducting (right) lead and reads:

$$H_S = \sum_k \sum_\sigma \epsilon_{kS} c^\dagger_{kS\sigma} c_{kS\sigma} + \sum_k (\Delta^* c_{kS\downarrow} c_{-kS\uparrow} + \Delta c^\dagger_{-kS\uparrow} c^\dagger_{kS\downarrow}) \tag{2.3}$$

where $c^\dagger_{kS\sigma}$ ($c_{kS\sigma}$) is the electron creation (annihilation) operator of an electron with spin $\sigma$ and energy $\epsilon_{kS}$ in the superconducting electrode, and $\Delta$ denotes the superconducting energy gap.

The third term is the Hamiltonian of three coupled $QDs$, given by

$$H_{TQD} = \sum_{m,\sigma} \epsilon_{dm,\sigma} d^\dagger_{m,\sigma} d_{m,\sigma} + \sum_\sigma \sum_{j=1,3} \Big[ t_{j2} d^\dagger_{2\sigma} d_{j\sigma} + H.c \Big] + \sum_m U_m n_{m\sigma} n_{m\bar{\sigma}} \tag{2.4}$$

where $d^\dagger_{m\sigma}$ ($d_{m\sigma}$) is the electron creation (annihilation) operator of an electron with spin $\sigma$ and energy $\epsilon_{dm}$ in the $m$-th quantum dot with $m = 1, 2, 3$. We assume that each quantum dot has only a single-electron spin-degenerate level, with $\epsilon_{dm\uparrow} = \epsilon_{dm\downarrow}$; $U_m$ is the strength of the Coulomb interaction in the $m$-th quantum dot while $t_{j2}$ with $j = 1, 3$ stands for the interdot coupling parameter.

The last term in Eq.(1) describes tunneling of electrons between the leads $(N, S)$ and the central quantum dot $(QD2)$ :

$$H_T = \sum_{k\sigma} \sum_{\beta=N,S} (V_{k\beta\sigma} c^\dagger_{k\beta\sigma} d_{2\sigma} + H.c), \tag{2.5}$$

where $V_{k\beta\sigma} (\beta = N, S)$ is the tunneling matrix element between the central $QD2$ and the electrode $\beta$. In the wide-band limit approximation, the coupling constants with the leads can be introduced: $\Gamma_\beta = 2\pi \sum_k |V_{k\beta}|^2 \delta(\omega - \epsilon^\beta_k)$.

The retarded Green's function $\mathbf{G}^r_\sigma$ in the generalized $6 \times 6$ Nambu representation is obtained from the Dyson equation:

$$\mathbf{G}^r = \mathbf{g}^r + \mathbf{g}^r \mathbf{\Sigma}^r \mathbf{G}^r \tag{2.6}$$

where $\mathbf{g}^r$ denotes the retarded Green's function of the triple quantum dot isolated from the leads being written as:

$$\mathbf{g}^r = \begin{bmatrix} [\mathbf{g}_1^r]^{-1} & \mathbf{t} & \mathbf{0} \\ \mathbf{t}^* & [\mathbf{g}_2^r]^{-1} & \mathbf{t} \\ \mathbf{0} & \mathbf{t}^* & [\mathbf{g}_3^r]^{-1} \end{bmatrix}^{-1} \tag{2.7}$$

where $\mathbf{g}_m^r$ matrices are defined as:

$$\mathbf{g}_m^r = \begin{bmatrix} \dfrac{1-n_m}{\omega-\epsilon_{dm}} + \dfrac{n_m}{\omega-\epsilon_{dm}-U_m} & 0 \\ 0 & \dfrac{1-n_m}{\omega+\epsilon_{dm}} + \dfrac{n_m}{\omega+\epsilon_{dm}+U_m} \end{bmatrix}, \tag{2.8}$$

with $m = 1, 2, 3$. The interdot coupling matrix $\mathbf{t}$ is given by:

$$\mathbf{t} = \begin{bmatrix} -t & 0 \\ 0 & t \end{bmatrix}. \tag{2.9}$$

The retarded self-energy of the leads, in the wide-band approximation, acquires the following form:

$$\mathbf{\Sigma}^r = \begin{bmatrix} \mathbf{0} & \mathbf{0} & \mathbf{0} \\ \mathbf{0} & \mathbf{\Sigma}_N^r + \mathbf{\Sigma}_S^r & \mathbf{0} \\ \mathbf{0} & \mathbf{0} & \mathbf{0} \end{bmatrix} \tag{2.10}$$

where

$$\mathbf{\Sigma}_N^r = -\frac{i}{2}\Gamma_N \begin{bmatrix} 1 & 0 \\ 0 & 1 \end{bmatrix} \tag{2.11}$$

and

$$\mathbf{\Sigma}_S^r = -\frac{i}{2}\rho_s(\omega)\Gamma_S \begin{bmatrix} 1 & -\frac{\Delta}{\omega} \\ -\frac{\Delta}{\omega} & 1 \end{bmatrix} \tag{2.12}$$

where $\rho_s$ denotes the dimensionless modified BCS density of states in the superconductor given by:

$$\rho_s(\omega) = \frac{|\omega|\theta(|\omega|-\Delta)}{\sqrt{\omega^2-\Delta^2}} - i\frac{\omega\theta(\Delta-|\omega|)}{\sqrt{\Delta^2-\omega^2}}. \tag{2.13}$$

We have adopted the equation of motion method and the Hubbard-I decoupling scheme to find Green's functions. The general expression for the charge current through a barrier from the normal lead can be calculated in terms of non-equilibrium Green's function $G^{r,a}$. The charge current $I$ flowing in a biased system from left to right can be calculated from the following expression.

$$I = -e\left\langle \frac{dN}{dt} \right\rangle \tag{2.14}$$

with $N = \sum_{k\sigma} c_{k\sigma}^\dagger c_{k\sigma}$.

Using the equation of motion (EOM), we can obtain the following.

$$I = \frac{2e}{\hbar}\sum \int d\omega \left[\mathbf{G}_2^r(\omega)\mathbf{\Sigma}_N^<(\omega) + \mathbf{G}_2^<(\omega)\mathbf{\Sigma}_N^a(\omega) + H.c.\right]_{(11)} \tag{2.15}$$

where $\mathbf{G}^{\mathbf{r},<}(\omega)$ is the Fourier transform of retarded and lesser Green's function of the system, and $\mathbf{\Sigma}_N^{<,a}$ is the Fourier transform of lesser, advanced self-energy of the normal lead.

In order to obtain the lesser Green's function $G_\sigma^<(\omega)$, we use the Keldysh equation

$$\mathbf{G}^< = \mathbf{G}^\mathbf{r}(\omega)\mathbf{\Sigma}^<\mathbf{G}^\mathbf{a}(\omega) \tag{2.16}$$

where the lesser self-energy is given by

$$\mathbf{\Sigma}^<(\omega) = \mathbf{\Sigma}_N^< + \mathbf{\Sigma}_S^< = \begin{bmatrix} \mathbf{0} & \mathbf{0} & \mathbf{0} \\ \mathbf{0} & \mathbf{f}_N(\omega)\mathbf{\Gamma}_N + \mathbf{f}_S(\omega)\mathbf{\Gamma}_S & \mathbf{0} \\ \mathbf{0} & \mathbf{0} & \mathbf{0} \end{bmatrix} \tag{2.17}$$

while $\mathbf{f_i}$ is the Fermi matrix, given by

$$\mathbf{f}_i = \begin{bmatrix} f_i & 0 \\ 0 & \bar{f}_i \end{bmatrix}. \tag{2.18}$$

with the Fermi functions for electrons and holes defined as $f_i = f(\omega - V_i)$ and $\bar{f}_i = f(\omega + V_i)$, respectively. For $i = N$ and $f_i = \bar{f}_i = f(\omega)$ for $i = S$. Also,

$$\mathbf{\Gamma}_N = \begin{bmatrix} \Gamma_N & 0 \\ 0 & \Gamma_N \end{bmatrix} \tag{2.19}$$

and

$$\mathbf{\Gamma}_S = \bar{\rho}_s(\omega)\Gamma_S \begin{bmatrix} 1 & -\frac{\Delta}{\omega} \\ -\frac{\Delta}{\omega} & 1 \end{bmatrix} \tag{2.20}$$

denotes the coupling constants in the matrix form of the leads, while $\bar{\rho}_s$ denotes the density of states in the superconductor given by

$$\bar{\rho}_s(\omega) = \frac{|\omega|\theta(|\omega| - \Delta)}{\sqrt{\omega^2 - \Delta^2}} \tag{2.21}$$

Finally, by substituting the matrix elements previously calculated, the current in the subgap regime ($e|V| < \Delta$), i.e. the Andreev current in the limit of low temperature, can be written as

$$I_A = \frac{2e}{h}\int_{-e\,V}^{e\,V} d\omega\, T_A(\omega) \tag{2.22}$$

where $V$ is the bias voltage, and $T_A$ is the Andreev transmittance, given by:

$$T_A = \Gamma_N^2 |G_{2,12}^r(\omega)|^2. \tag{2.23}$$

It is important to note that the Coulomb correlations make $T_A$ dependent on the average occupations of the QDs. For the non-magnetic case, the averaged occupation number does not depend on the spin, which allows us to set for each QD: $\langle n_{i,\sigma}\rangle = \langle n_i\rangle$,

$i = 1, 2, 3$. These occupation numbers are obtained by solving the following system of equations:

$$\langle n_1 \rangle = -i \int \frac{d\omega}{2\pi} G^{<}_{1,11}[\omega, \langle n_1 \rangle, \langle n_2 \rangle, \langle n_3 \rangle], \tag{2.24a}$$

$$\langle n_2 \rangle = -i \int \frac{d\omega}{2\pi} G^{<}_{2,11}[\omega, \langle n_1 \rangle, \langle n_2 \rangle, \langle n_3 \rangle], \tag{2.24b}$$

$$\langle n_3 \rangle = -i \int \frac{d\omega}{2\pi} G^{<}_{3,11}[\omega, \langle n_1 \rangle, \langle n_2 \rangle, \langle n_3 \rangle]. \tag{2.24c}$$

As one may notice by inspecting Eqs. (2.24a), (2.24b) and (2.24c), they form a system of equations for $\langle n_1 \rangle$, $\langle n_2 \rangle$ and $\langle n_3 \rangle$ that must be solved in a self-consistent way.

The LDOS of the quantum dots come from matrix elements of the retarded Green's function matrix (electron components in Nambu space). The LDOS for the dots 1, 2, and 3 are, respectively:

$$\rho_1(\omega) = -\frac{1}{\pi} Im(G^{r}_{1,11}[\omega, \langle n_1 \rangle, \langle n_2 \rangle, \langle n_3 \rangle]), \tag{2.25a}$$

$$\rho_2(\omega) = -\frac{1}{\pi} Im(G^{r}_{2,11}[\omega, \langle n_1 \rangle, \langle n_2 \rangle, \langle n_3 \rangle]), \tag{2.25b}$$

$$\rho_3(\omega) = -\frac{1}{\pi} Im(G^{r}_{3,11}[\omega, \langle n_1 \rangle, \langle n_2 \rangle, \langle n_3 \rangle]). \tag{2.25c}$$

Then, the total DOS of the triple quantum dot is given by the addition of the LDOS of each QD:

$$\rho(\omega) = \rho_1(\omega) + \rho_2(\omega) + \rho_3(\omega) \tag{2.26}$$

## 2.2 Beyond Coulomb Blockade: Kondo correlations

From a physical point of view, the Coulomb repulsion U is responsible for the charging effect and, at lower temperatures, for the Kondo effect, i.e., the formation of the singlet resonant state between the spin localized on a QD and spins of itinerant electrons from the normal leads [48]. These effects manifest themselves spectroscopically by the appearance of the peaks around $E = \epsilon_0$ and $E = \epsilon_0 + U$ and the Kondo resonance (or Abrikosov-Suhl) in the density of states at the Fermi energy of normal lead [49, 50]. The width of the resonance is a characteristic scale, which is the Kondo temperature $T_K$. To estimate its value for a given set of parameters, we use the formula

$$k_B T = \sqrt{U\Gamma_N} exp\left[\frac{\pi}{2}\frac{\epsilon_0(\epsilon_0 + U)}{U\Gamma_N}\right] \tag{2.27}$$

In non-equilibrium transport via a quantum dot attached to two external electrodes, two such resonances appear at the positions corresponding to the chemical potentials in the biased system [51]. If the quantum dot is also coupled to the superconducting electrode, competition is observed [52] between the mentioned features and proximity-induced on-dot pairing. To analyze competition between currents beyond the Coulomb blockade

limit, we treat electron interactions using the EOM procedure [53]. This technique has previously been used to study interacting quantum dots in different settings [54].

The equation of motion approach [55], is probably one of the simplest methods, qualitatively capturing the physics of the non-equilibrium Kondo correlations at arbitrary $U$.

To capture Kondo physics we use the Dyson equation with the non-interacting Green function (Ec. (2.6) )and impose the self-energy matrix $\Sigma^{r,U}(E)$ in the following diagonal form.

$$\Sigma^{r,U} = \begin{bmatrix} \Sigma_N(E) & 0 \\ 0 & -[\Sigma_N(-E)]^* \end{bmatrix} \tag{2.28}$$

and Within EOM approach the self-energy $\Sigma_N(E)$( [54])

$$\Sigma_N = E - \epsilon_0 - \frac{[E-\epsilon_0-\Sigma_0]\,[E-\epsilon_0-\Sigma_0-U-\Sigma_3]+U\Sigma_1}{E-\epsilon_0-\Sigma_0-[\Sigma_3+U(1-\langle n_\downarrow\rangle)]} \tag{2.29}$$

where $\Sigma_0 = -i\frac{\Gamma_N}{2}$ and $\Sigma_{1,3}$ are given by

$$\Sigma_\nu = \sum_{\mathbf{k}} |V_{\mathbf{kN}}|^2 \left[\frac{1}{E-\xi_{\mathbf{k},N}} + \frac{1}{E-U-2\epsilon_0+\xi_{\mathbf{k},N}}\right] [f(\xi_{\mathbf{k},N})]^{(3-\nu)/2} \tag{2.30}$$

with $\xi_{\mathbf{k},N} = \epsilon_{\mathbf{k},N} - eV$

This approach [56] qualitatively captures the following important aspects of Coulomb interactions: 1) the charging effect and 2) the appearance of the Kondo resonance at $\epsilon = 0$ for low temperatures, smaller than $T_K$. Under non-equilibrium conditions the Kondo resonance shifts to $\mu_N$ and this behavior differs from the N-QD-N setup where there are two Kondo peaks at both chemical potentials $\mu_\beta$.

## 2.3 Results

We now discuss the transport properties within the Andreev regime. Within this regime, the range of Fermi energy and QD levels is restricted in the range of the superconductor gap, $\Delta$. We denote $r$ as the coupling ratio of the leads $\Gamma_S/\Gamma_N$ and assume that the levels of the quantum dots are spin-degenerate $\epsilon_{di,\sigma} = \epsilon_{di}$ (for $i = 1, 2, 3$). In addition, we have introduced the parameter $\eta$, which describes the separation of levels $\epsilon_{d1}$ and $\epsilon_{d3}$ from levels $\epsilon_{d2} = \epsilon_d$. We have assumed that the energy levels of the side dots (QD1 and QD3) are symmetrically placed in relation to the energy level of the middle dot (QD2), that is, $\epsilon_{d1} = \epsilon_d + \eta$ and $\epsilon_{d3} = \epsilon_d - \eta$. Furthermore, unless stated otherwise, we set the coupling between the two side dots and the central dot to be symmetric ( $t_{12} = t_{32} = t$ ) and consider two regimes: the interferometric regime (when $t$ is very small regarding $\Gamma$) and the molecular regime (when $t$ is very close to the value of $\Gamma$ ). In the linear response regime, the chemical potentials of the leads are set to zero, $\mu_N = \mu_S = 0$. On the other hand, in the non-linear regime, we set the chemical potential of the leads as $\mu_N = eV$ and $\mu_S = 0$, therefore, $\mu_N - \mu_S = eV$, where $V$ is the applied voltage. In addition, we assume in all our calculations that $k_B\tau = 0$, where $\tau$ is the temperature. Finally, we assume that the intradot Coulomb interaction is equal at all quantum dots, that is, $U_m = U$, for $m = 1, 2, 3$. In what follows, we rename $\Gamma_N = \Gamma$.

### 2.3.1 Noninteracting case

Let us first consider the limit where the Coulomb interaction is neglected, $U_i = 0$ for $i = 1, 2, 3$.

In Fig. 2.2 we show the differential conductance as a function of the bias voltage for different values of $r = \Gamma_S/\Gamma_N$, choosing a small $t$ (interferometric regime) and an even smaller value of $\eta$ to investigate Dicke resonances. We can observe that when $r$ does not exceed a certain critical value, the differential conductance exhibits one very narrow central peak and two broader and smaller side peaks symmetrically located at zero energy. However, for higher values of $r$, we observe that $dI/dV$ has six peaks in this energy interval. In other words, these peaks split as $r$ increases from a specific critical value (see inset in Fig. 2.2). Also, we note from Fig. 2.3 that the spacing of these peaks increases with the value of $r$ when $eV$ is very near zero, and conversely, they move closer when the range of $eV$ increases. To better understand Fig. 2.2, we will analyze the effect of $r$ and $\eta$ on the differential conductance. For that purpose, we will study the expression for $T_A$ given by Eq. (2.23), in the limit of $\Delta \to \infty$ with $\tilde{\omega} = \omega - \epsilon_d$, for which we obtain

$$T_A = \frac{r^2\Gamma^4(\tilde{\omega}^2 - \eta^2)^2}{S} \tag{2.31}$$

with

$$S = 4\Gamma^2\tilde{\omega}^2\left(\tilde{\omega}^2 - \eta^2 - 2t^2\right)^2 + \frac{\left(4\tilde{\omega}^2\left(\tilde{\omega}^2 - \eta^2 - 2t^2\right)^2 - \left(1 + r^2\right)\Gamma^2\left(\tilde{\omega}^2 - \eta^2\right)^2\right)^2}{4(\tilde{\omega}^2 - \eta^2)^2}$$

From Eq. (2.31) we can deduce that the roots of $T_A$ are $\tilde{\omega} = \pm\eta$. In the case of symmetric coupling with the leads ($\Gamma_S = \Gamma$), the Andreev transmittance is given by the expression:

$$T_A = \frac{\Gamma^4(\tilde{\omega}^2 - \eta^2)^4}{\Gamma^4\left[\tilde{\omega}^2 - \eta^2\right]^4 + 4\tilde{\omega}^4\left[\tilde{\omega}^2 - \eta^2 - 2t^2\right]^4} \tag{2.32}$$

Equation (2.32) shows that in the transmittance function resonant peaks appear at $\tilde{\omega} = \pm\sqrt{\eta^2 + 2t^2}$, $\tilde{\omega} = 0$, and two Fano antiresonances located at $\tilde{\omega} = \pm\eta$. The narrow central peak in the transmittance may be considered as one long-lived (subradiant) state, while the other two peaks correspond to short-lived (superradiant) states. Since the central peak is located at zero, the width of the central peak is defined by the value of $\eta$. For small values of $\eta$, the width of the central peak becomes much narrower. With $\eta$ increasing, the width of the central line also increases, while the two satellite peaks become broader with $\eta$. This effect resembles the Dicke effect in atomic physics, where a strong narrow emission line appears when the distance between atoms is smaller than the Fermi wavelength of the corresponding radiation. In the present case, the difference of energy between the levels, $\eta$, plays the role of the distance between atoms.

On the other hand, when we consider an asymmetric coupling to the leads, for instance, $r = 2$, the Andreev transmittance function is given by Eq. (2.33) :

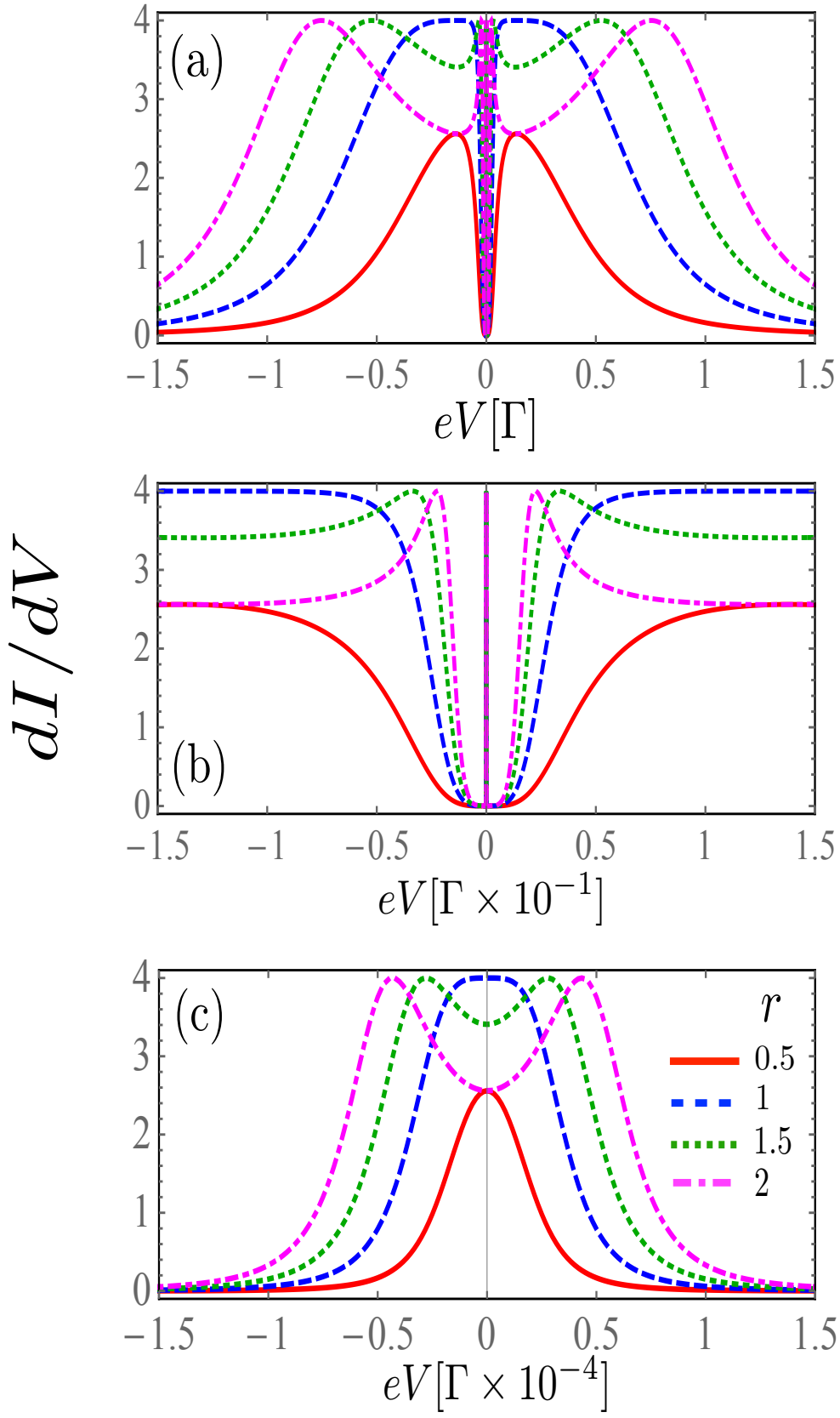


Figure 2.2: Differential conductance in the noninteracting case, calculated as a function of the bias voltage when $\epsilon_d = 0$ and indicated values of $r$: $r = 0.5(red)$, $r = 1.0(blue)$, $r = 1.5(green)$, $r = 2.0(magenta)$. Fixed parameters: $\eta = 0.001\Gamma$, $t = 0.1\Gamma$. b) Close-up of central peak presented in panel (a). c) Closeup of central peak presented in panel (b).

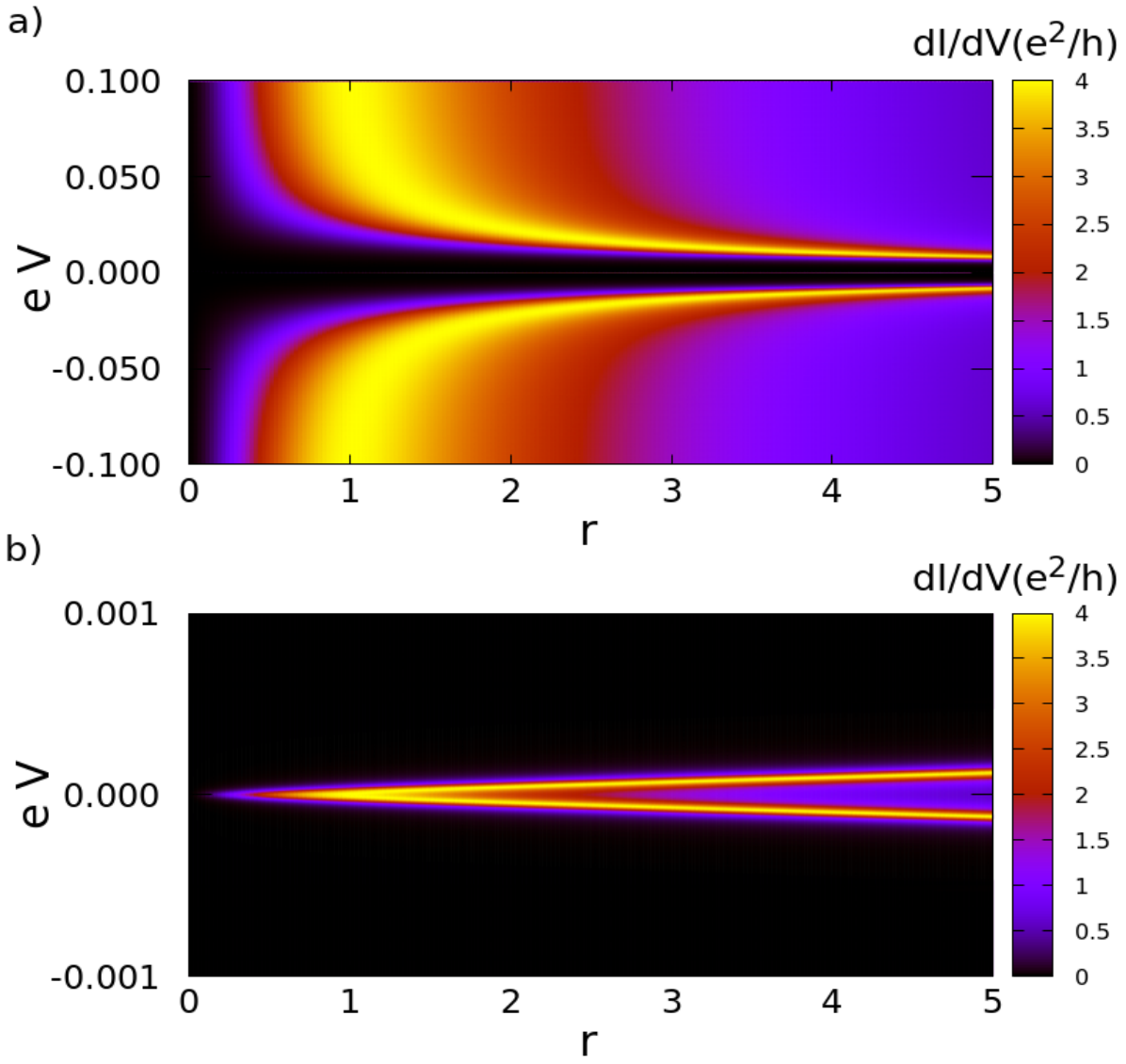


Figure 2.3: Density plot of differential conductance vs $r$ and $eV$ in the noninteracting case, when $\epsilon_d = 0$ in the applied bias range between a) $-0.1\Gamma$ and $0.1\Gamma$ b) Closeup of the central peak in the figure a), in the applied bias range between $-0.001\Gamma$ and $0.001\Gamma$.

$$T_A = \frac{\alpha^4\Gamma^4}{\left[\tilde{\omega} - \frac{\sqrt{3\Gamma}}{2}\alpha\right]^2 \left[\tilde{\omega} + \frac{\sqrt{3\Gamma}}{2}\alpha\right]^2 + \alpha^4\Gamma^4} \tag{2.33}$$

where $\alpha = \frac{(\tilde{\omega}^2-\eta^2)}{(\tilde{\omega}^2-\eta^2-2t^2)}$

This function presents two Fano antiresonances when $\alpha = 0$, that is to say at $\tilde{\omega} = \pm\eta$, and six peaks are symmetrically located on either side of the zero-energy at $\omega = \pm\frac{\sqrt{3}}{2}\alpha$ and $\omega = \pm\frac{\sqrt{3}}{2}\alpha$. To gain a more clear physical insight into the dependence of $T_A$ on $\eta$, we analyze the limit $\eta = 0$. The Hamiltonian $H_{TQD}$ can be diagonalized leading to three effective levels $\omega_1 = \epsilon_d + \sqrt{2t^2}$ , and $\omega_2 = \epsilon_d$ and $\omega_3 = \epsilon_d - \sqrt{2t^2}$ . Since the system of three one-level QDs has three molecular-like states (denoted by index 1, 2, and 3 for increasing energy), one could also expect three peaks in the conductance. However, the matrix elements of the coupling between the molecular state $|2\rangle$ and the left and right leads vanish, that is, the molecular state $|2\rangle$ decouples from the leads when $\eta = 0$ and the central peak disappears. The Andreev transmittance shows only two peaks at the positions $\tilde{\omega} = \pm\sqrt{2t^2}$ and it is zero at $\tilde{\omega} = 0$. On the other side, when $\eta \neq 0$, the molecular-like levels $\omega_1$ and $\omega_3$ located symmetrically on both sides of $\mu_R$ and the AR conductance reveals a well-defined central peak due to two-level Andreev reflection, where the conventional resonant tunneling is forbidden due to $\omega_i(i = 1, 3)$ in the gap. On the other hand, when $\omega_i(i = 1, 3)$ aligns with the chemical potential of the superconducting lead, $\mu_R = 0$, i.e., $\omega_i(i = 1, 3) = 0$ two side-peaks appear in $\tilde{\omega} = \pm\sqrt{\eta^2 + 2t^2}$ due to the Andreev reflection (AR) through a single level. When this happens, an electron coming from the left lead with the energy $\epsilon_d$ can tunnel into the i-state of the QD, leaving a hole propagating back to the i-state in the QD and the creation of a Cooper pair in the right superconducting lead.

### 2.3.2 Interacting case

#### Andreev conductance vs gate voltage

In this section, we study the impact of the electronic charging induced by intradot Coulomb interaction on the transport properties of the TQD system in the linear regime. Figures 2.4 and 2.5 show occupation and linear conductance versus the QD energy level $\epsilon_d$ for the interferometric regime ( $t$, $\eta \ll \Gamma$). We can observe that the Coulomb interaction splits the Dicke spectrum into two sets symmetric to the electron-hole symmetry point $\epsilon_d = U/2$, and their centers are located approximately at $\epsilon_d = 0$ and $-U$. The DOS graph in Fig. 2.5 confirms this behavior. In addition, four Fano antiresonances in the conductance appear at the electron-hole symmetry because of the destructive quantum interference. Additionally, we can observe the features of the occupation numbers to determine the corresponding linear conductance behavior. Interestingly, the occupation number presents a staircase-like form, with abrupt changes around $\epsilon_d = 0$ and $\epsilon_d = -U$. This behavior of the charge is due to the Dicke-like spectrum, as we can see in the DOS (Fig. 2.6), in which a structure of levels with supertunneling (broad states) and subtunneling states (sharp states) develops around $\omega = 0$ and $\omega = U$. As $\varepsilon_d$ or $\varepsilon_d + U$ fall slightly below the Fermi energy, the sharp sub-tunneling state completely enters the Fermi sea, and consequently the charge changes abruptly.

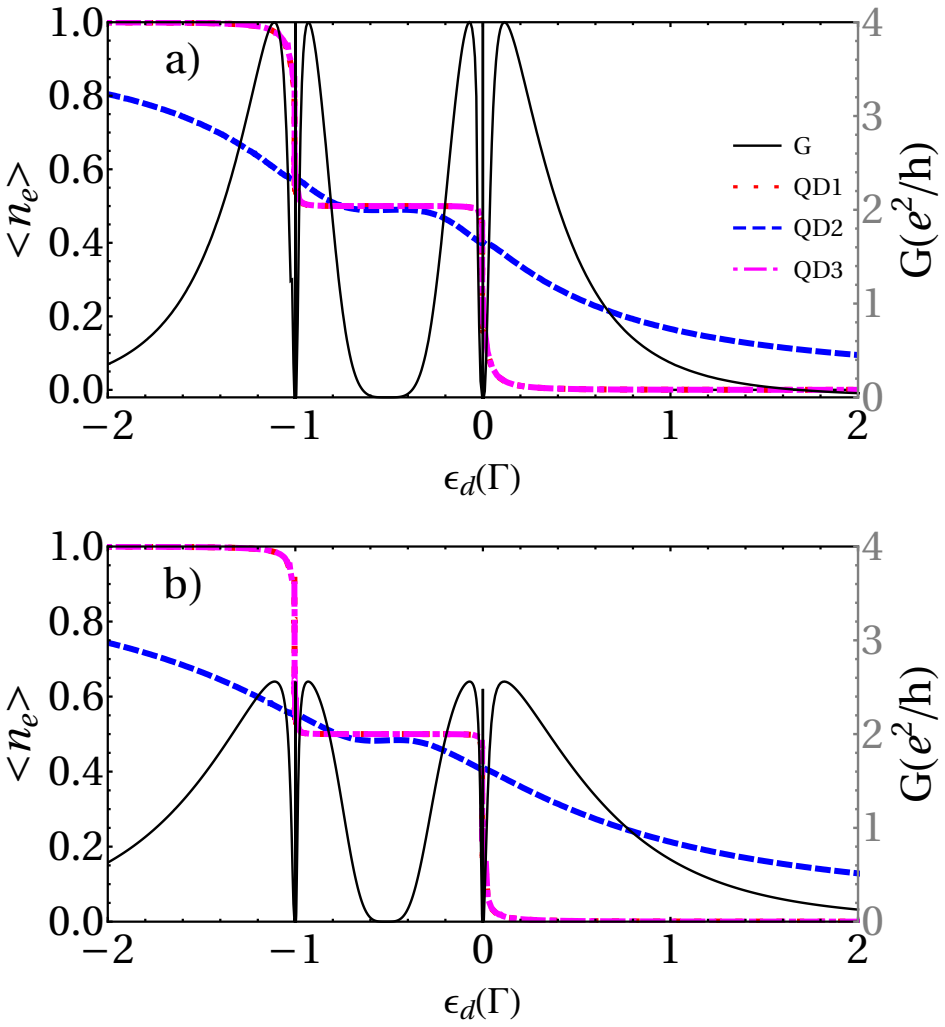


Figure 2.4: Electronic occupation and linear conductance of a TQD system calculated as a function of the dot's level energy for a) $r = 1$ and b) r = 2. Fixed parameters: $U = 1\,\Gamma$, $t = 0.1\Gamma$, and $\eta = 0.001\Gamma$

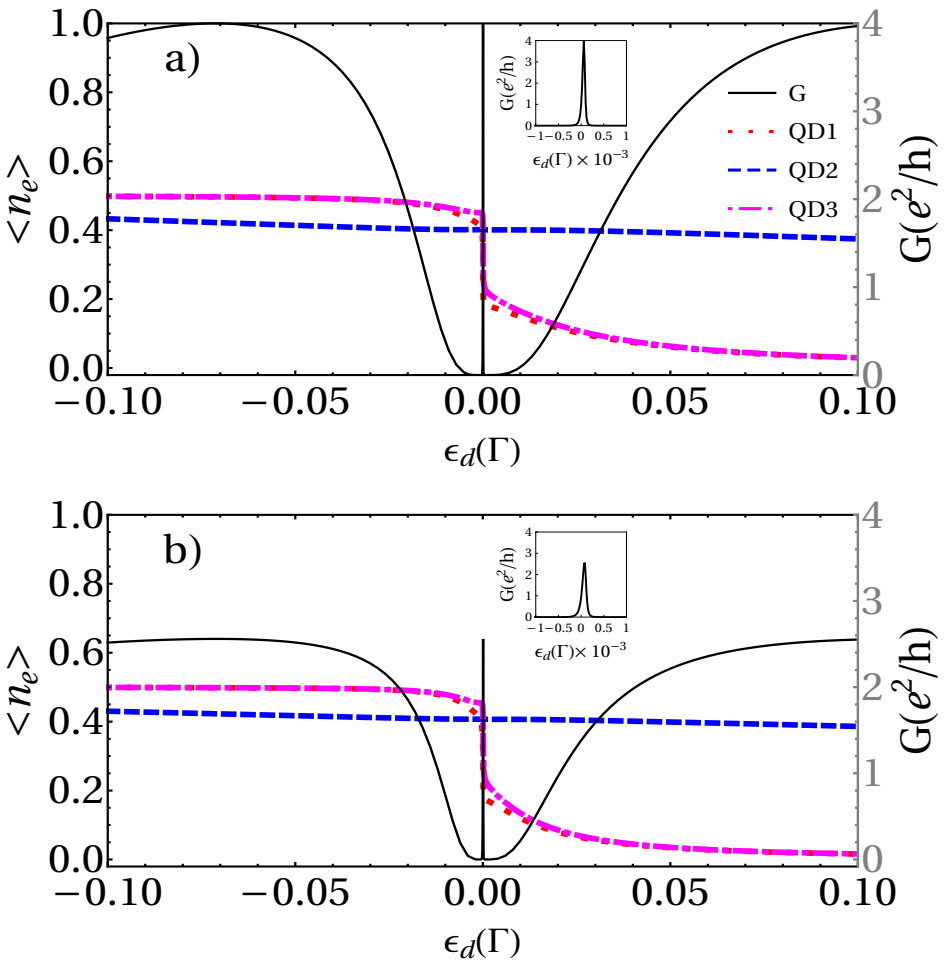


Figure 2.5: Electronic occupation and linear conductance of a TQD system calculated as a function of the dot's level energy around $\omega = 0\Gamma$, for a) $r = 1$ and b) r = 2. Fixed parameters: $U = 1\,\Gamma$, $t = 0.1\Gamma$, and $\eta = 0.001\Gamma$

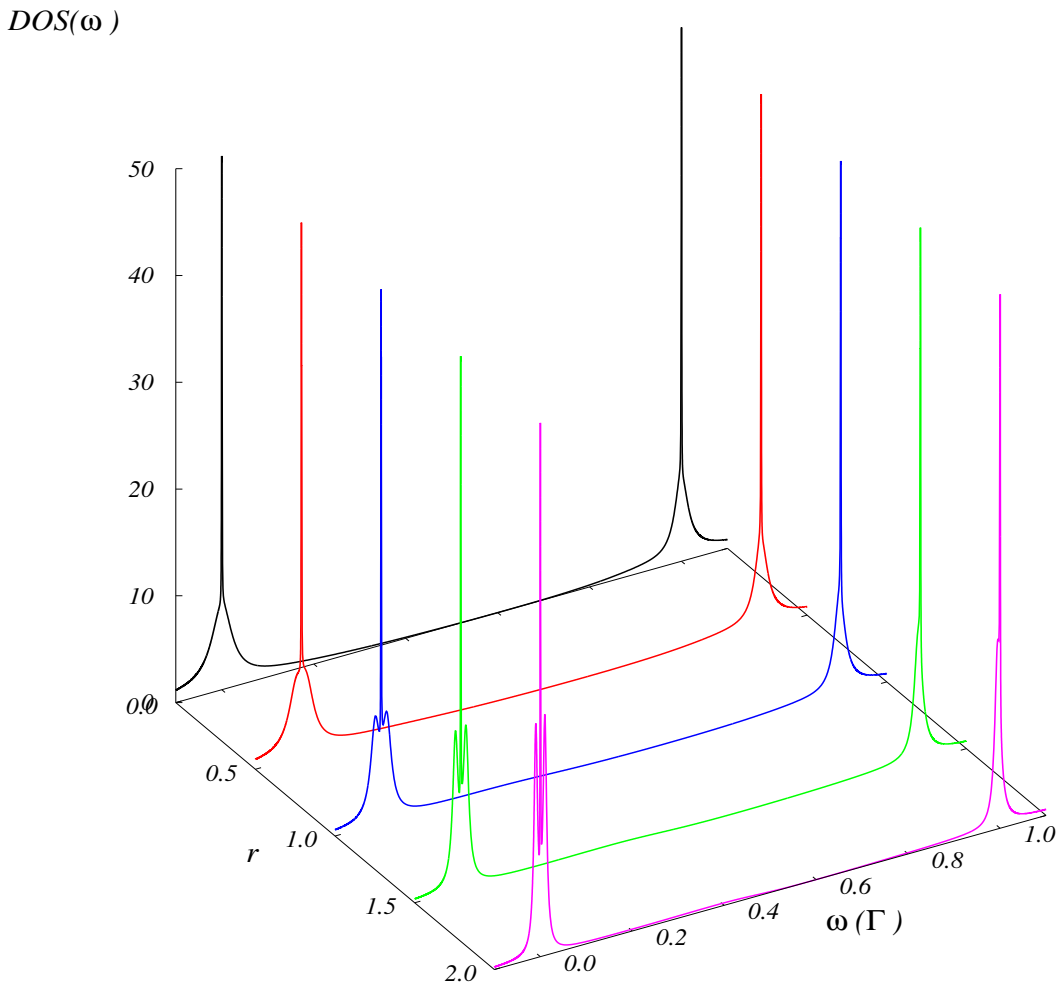


Figure 2.6: Total DOS in the interacting case, calculated as a function of the energy and $r$ for indicated values of rate of coupling: $r = 0$ (black), $r = 0.5$ (red), $r = 1.0$ (blue), $r = 1.5$ (green), $r = 2.0$ (magenta). Fixed parameters: $U = 1\Gamma$, $\epsilon_d = 0$ , $\eta = 0.001\Gamma$, $t = 0.1\Gamma$.

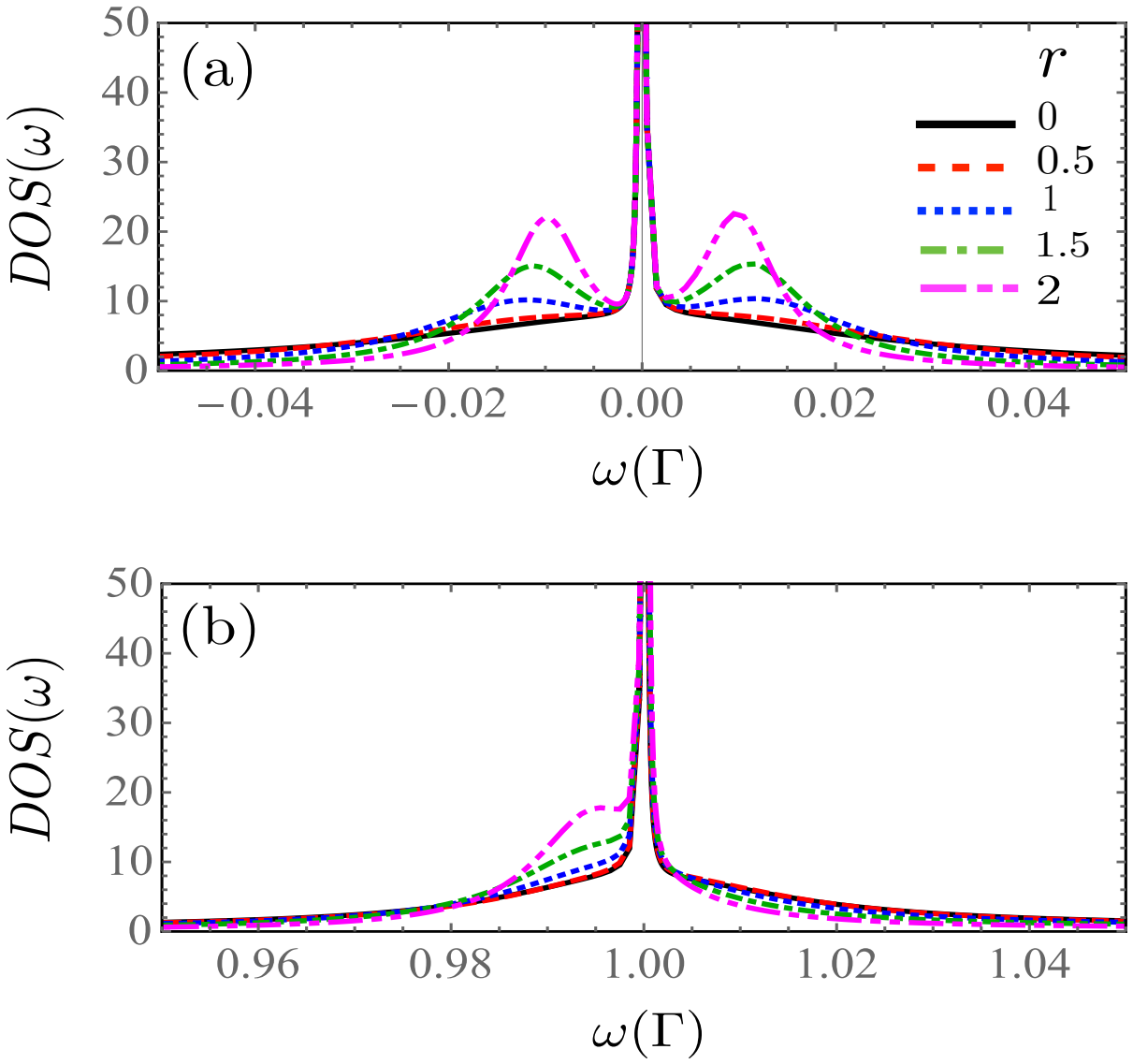


Figure 2.7: Total DOS calculated as a function of the energy in the interacting case ( $U = 1\Gamma$), when $\epsilon_d = 0$ is in a range of energy very near a) $\omega = 0\Gamma$ and b) $\omega = 1\Gamma$, and the indicated values of the rate of coupling: $r = 0$ (black), $r = 0.5$ (red), $r = 1.0$ (blue), $r = 1.5$ (green), $r = 2.0$ (magenta). Fixed parameters: $\eta = 0.001\Gamma$, $t = 0.1\Gamma$.

The DOS in Fig. 2.7 may be written roughly as:

$$\rho(\omega) \approx \frac{1}{\pi} \sum_{\alpha} \Big( \frac{\Gamma_+}{(\omega - e_\alpha)^2 + \Gamma_+^2} + \frac{\Gamma_-}{(\omega - e_\alpha)^2 + \Gamma_-^2} \Big). \tag{2.34}$$

In the limit where $\eta \to 0$, the second term in the sum tends to a Dirac$\delta$ function. Then, by integrating the above equation at Fermi energy and zero temperature, we obtain:

$$n_{di}(\varepsilon_d) \approx \frac{1}{2}\theta(\mu - \varepsilon_d) + \frac{1}{2}\theta(\mu - \varepsilon_d - U). \tag{2.35}$$

From Eq. (2.35), we can understand the charging behavior as a function of the energy level $\varepsilon_d$. As $\varepsilon_d$ decreases and falls below the Fermi energy $\mu$, the charge jumps abruptly in steps of 1/2. Furthermore, since each of these steps in the occupation graph reveals electronic tunneling, three more peaks in the linear conductance plot appear. Each step in electron occupation represents an electron filling from the left normal lead, which occurs when $\epsilon_{di}$ or $\epsilon_{di} + U$ lines up with $\mu_N = \mu_S$. From Eq.(2.8) one can understand that the interlevel interaction results in an energy level splitting, in the simpler case with only one central QD ($t = 0$) : from the original one single-electron spin-degenerate level $\epsilon_d$ splitting into two spin-degenerate levels, $\epsilon_d$ with probability $1 - \langle n \rangle$ and $(\epsilon_d + U)$ with probability $\langle n \rangle$. Of particular interest are the sharp peaks seen in both $\epsilon_d = 0$ and $\epsilon_d = -U$. At $\epsilon_d = 0$, $\epsilon_d$ aligns with the Fermi surface $\mu$ (here we have set $\mu_N = \mu_S = \mu = 0$), so $\langle n \rangle$ jumps from 0 to 0.5, describing the first electron filling; then each of both levels, $\epsilon_d$ and $\epsilon_d + U$, has a probability of being occupied 50%. At $\epsilon_d = -\Gamma$, $\epsilon_d + U$ lines up with the Fermi surface $\mu$, and $\langle n \rangle$ jumps from 0.5 to 1, describing the second electron filling; then level $\epsilon_d + U$ has 100% probability of being occupied while level $\epsilon_d$ has 0% probability.

Additionally, Fig. 2.5 displays a zoom-in of the Andreev conductance vs. the energy level for $r = 1$ and $r = 2$ around $\epsilon_d = 0$. We can see that as $r$ increases, the height of the peaks decreases, and, on the contrary, their width increases in the same way as in the noninteracting case. Also, as we can see in this figure, for small values of $\eta$, the width of the central peak becomes sharper. Moreover, the insets in the above figure show the details of the sharp resonances. This structure of resonances resembles the Dicke resonance in the optical emission spectra of atoms.

### Differential Andreev conductance vs bias voltage

Next, we investigate the effect of the electronic charging induced by the intradot Coulomb interaction on the AR process within the non-equilibrium regime. Figure 2.8 shows the differential conductance as a function of the bias voltage. The central peak, appearing near $eV = 0$, is split due to the proximity effect to the superconductor (Andreev reflection). When $r = 2$ in this figure, one again observes the splitting of the central peak, but now the separation of each of these peaks from the $eV = 0$ is no longer symmetrical as in the noninteracting case. In addition, if we choose $\epsilon_d = 0$ the height of the peaks decreases as $r$ increases, similarly to the noninteracting case (cf. Fig. 2.2(b)), but in Fig. 2.8 we chose to plot $dI/dV$ the value of $\epsilon_d$ in which the differential conductance is maximum, so that effect is not observable.

The shape of the differential conductance may be understood by noticing the quantum interference among the electron trajectories entering and leaving the side-attached

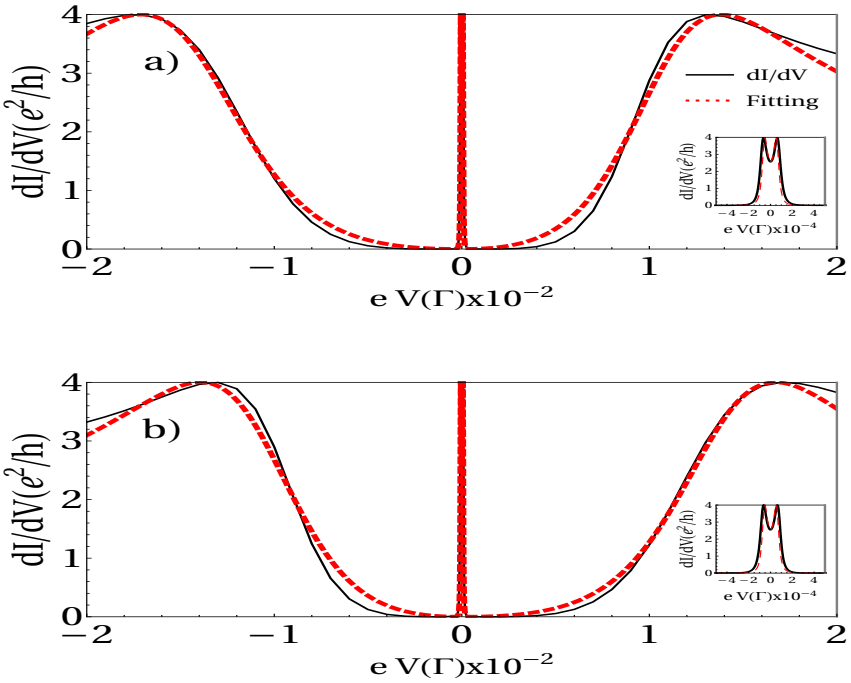


Figure 2.8: a) The differential conductance (black line) as a function of the bias voltage of a TQD system and the fitting (red line) by the sum of the Fano and BW functions when $\epsilon_d = 0.000075\Gamma$ $r = 2$ b) Differential conductance (solid line) calculated as a function of the bias voltage of a TQD system and the proposed fitting (dashed line) when $\epsilon_d = -1.000075\Gamma$ and $r = 2$. The zoom of both figures shows the differential conductance and the fitting proposed by the function BW in the low energy limit. Fixed parameters: $U = 1\,\Gamma$, $t = 0.1\Gamma$, $\eta = 0.001\Gamma$.

quantum dots. These interferences give rise to the so-called Fano-Andreev antiresonances [6, 23, 57]. On the other hand, the states of two side-attached quantum dots interfere with each other, giving rise to a Dicke-like effect.

The equation for $dI/dV$ may be written as a superposition of two Fano- and Breit-Wigner-like line-shapes:

$$\frac{dI}{dV} \approx \frac{1}{1+q_+^2}\frac{(\xi_+ + q_+)^2}{\xi_+^2+1} + \frac{1}{1+q_-^2}\frac{(\xi_- + q_-)^2}{\xi_-^2+1} + \frac{4r^2}{|\varepsilon^2 - r^2|^2} \tag{2.36}$$

where $\xi_\pm = (V \pm q_\pm \Gamma_{S_\pm})/\Gamma_{S_\pm}$ , $\varepsilon = (V + i\Gamma_-)/\Gamma_-$, and $\Gamma_- = \eta^2/\Gamma_N$. It is worth noting that the last term in the above equation does not contain adjustable parameters. The above equation is explained in Fig. 2.9, where the first terms take into account the destructive interference given by the Fano-Andreev effect. The last term represents a process equivalent to the transmission through a double quantum dot in a series configuration with a coupling given by $r\eta$. The fitting of the above equation is shown in Fig. 2.8 (red line). A similar behavior of the differential conductance can be found in the quantum dot coupled to a topological superconductor nanowire. In this case, tuning the nonlocal gate produces hybridization of the two topological states in the superconductor, producing a split of the zero bias peak in the differential conductance. [58]

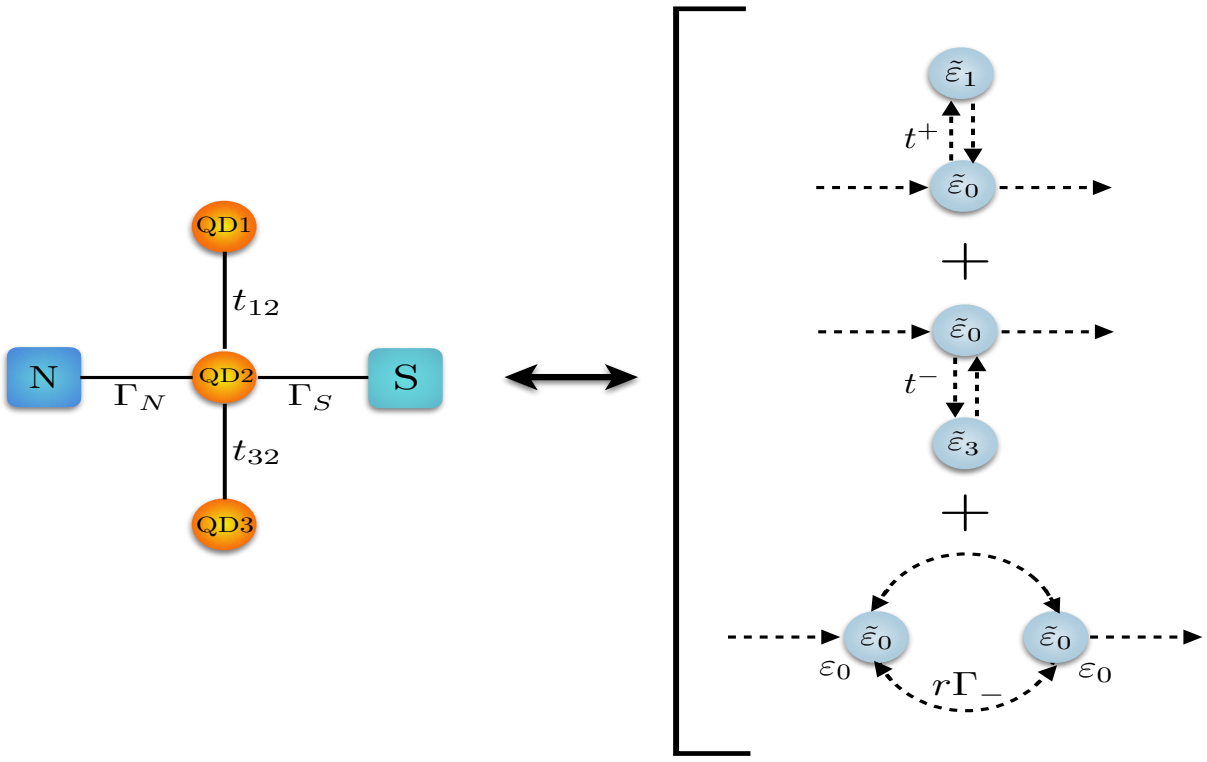


Figure 2.9: Scheme of the Andreev processes: Equivalent path for the Fano-Andreev and Dicke-Andreev transmission. The complete process can be divided into two Fano effects and transmission through equivalent quantum dots in series.

## 2.4 Kondo effect in Equilibrium

Fig. 2.10 shows the the spectral function $\rho(\omega)$ of the correlated QD $U = 10\Gamma$ in the equilibrium situation($V = 0$),for several values of interdot tunneling $t$. When $t = O$ appears a Kondo resonance at $\omega = 0$ for low temperatures, smaller than Kondo temperature ($T_K$ ). We can observe the appearance of a Fano antiresonance in the spectral function at $\epsilon = \epsilon_d$ when $t \neq 0$, due to the destructive interference of electron wavefunctions going through different paths in a laterally coupled triple-quantum dot. It can also be seen in the same figure that as $t$ increases, the antiresonance in $\epsilon = \epsilon_d$ becomes broader.

Fig. 2.11 shows the spectral function measured for various couplings to the superconducting electrode $r = \Gamma_S/\Gamma_N$ when $t = 0\Gamma$, i.e., when the lateral quantum dots are decoupled from the central quantum dot. For $r = 0$ the spectral function present peaks at $\epsilon = \epsilon_d$ and $\epsilon = \epsilon_d + U$ due to the charging effect and the appearance of the Kondo resonance at $\epsilon = 0$ for low temperatures, smaller than $T_K$. By increasing the rate coupling $r$ to the superconducting lead we observe a progressive emergence of the particle-hole features accompanied by a suppression of the Kondo resonance.

By considering the coupling of the two side quantum dots, i.e., when $t = 0.2$, Fig. 2.12 shows the spectral function measured for various couplings to the superconducting electrode $r = \Gamma_S/\Gamma$ we the spectral function present two deep symmetrically located on either side of $\epsilon = \epsilon_d$ and a gradual suppression of the Kondo resonance. Finally, Fig. 2.13 shows the spectral function for different values of shift energy $\eta$. When $\eta \neq 0$ can two observe two sharp deeps located at $\epsilon \approx \epsilon_d \pm \eta$, and two slight deeps located at $\epsilon \approx -\epsilon_d \pm \eta$.

## 2.5 Kondo effect in non-quilibrium

Outside the linear voltage regime we calculate currents and differential conductances taking full voltage dependence of the Fermi functions in the current formulas. Fig. 2.14 present the differential conductance as a function of the bias VL for different values of inter-dot tunneling $t$. In this figure we can observe the enhancement of zero-bias Andreev conductance. Besides this low-temperature we notice also the quasiparticle peak at $eV = \epsilon_d$ and another weaker one at $eV = U$ coming from the upper Coulomb satellite in the spectral function. With increase of the ratio $\Gamma_S/\Gamma_N$ the particle-hole splitting forces the QD into the mixed-valence regime and thereby the zero-bias enhancement gradually vanishes. Additionaly in this figure we can observe the appearance of a Fano antiresonance in the differential conductance at $V = \epsilon_d$ when $t \neq 0$ , which appear just where the peaks were when $t = 0$. On other hand, we can observe that as $t$ grows, zero-bias conductance peak suppression occurs.

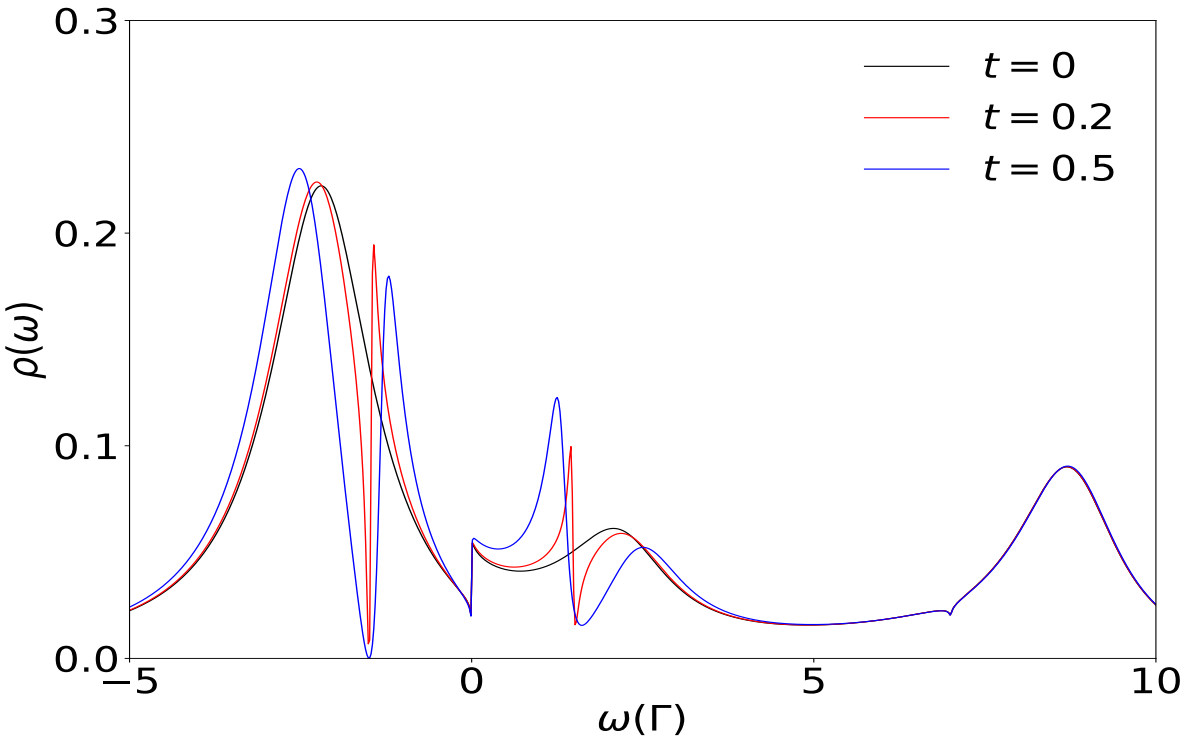


Figure 2.10: Spectral function $\rho(\omega)$ of the correlated QD in the equilibrium situation $V = 0$ obtained for $\epsilon_d = -1.5\Gamma_N$, $r = \Gamma_S/\Gamma = 5$, $U = 10\Gamma_N$, $k_BT = 0.001\Gamma$, and indicated values of the interdot tunneling $t$: $t = 0(black)$, $t = 0.2(red)$ and $t = 0.5(blue)$.

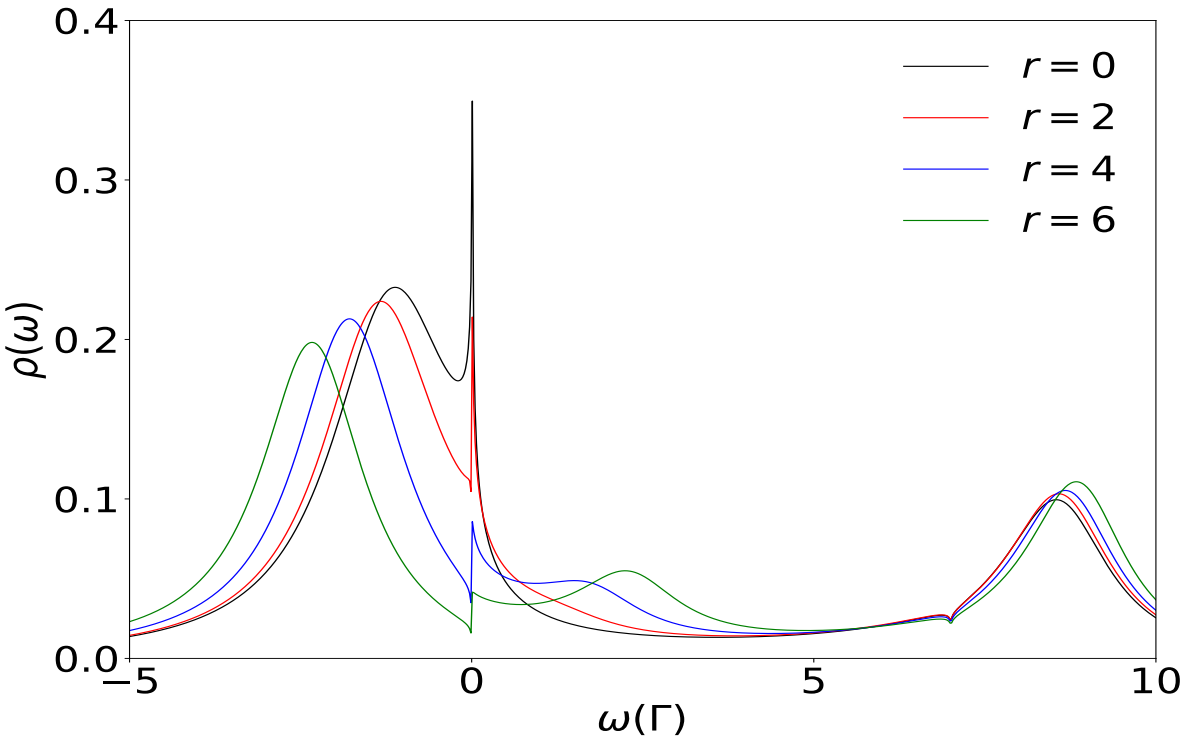


Figure 2.11: Spectral function $\rho(\omega)$ of the correlated QD in the equilibrium situation $V = 0$ obtained for $t = 0\Gamma_N$, $\eta = 0\Gamma_N$,$\epsilon_d = -1.5\Gamma$, $U = 10\Gamma$, $k_BT = 0.001\Gamma$, and indicated values of the ratio $r = \Gamma_S/\Gamma$: $r = 0(black)$, $r = 2(red)$, $r = 4(blue)$ and $r = 6(green)$.

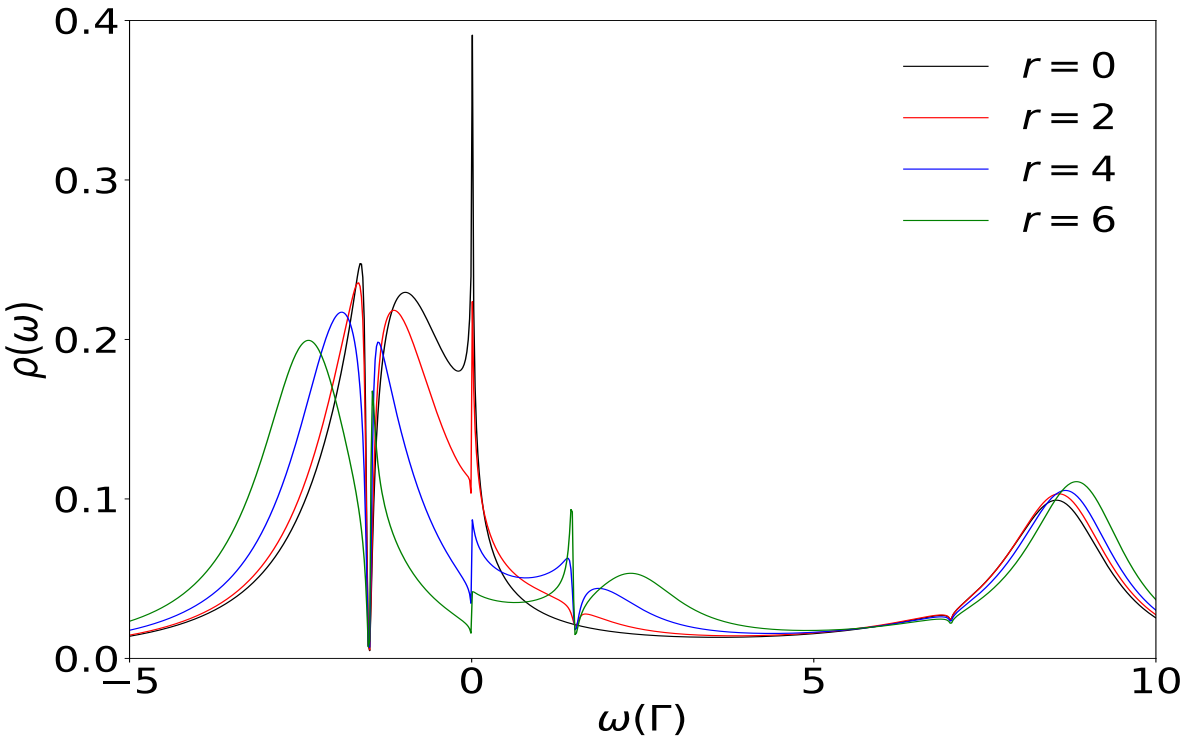


Figure 2.12: Spectral function $\rho(\omega)$ of the correlated QD in the equilibrium situation $V = 0$ obtained for $t = 0.2\Gamma_N$, $\eta = 0\Gamma_N$,$\epsilon_d = -1.5\Gamma_N$, $U = 10\Gamma_N$, $k_BT = 0.001\Gamma_N$, and indicated values of the ratio $r = \Gamma_S/\Gamma_N$: $r = 0(black)$, $r = 2(red)$, $r = 4(blue)$ and $r = 6(green)$.

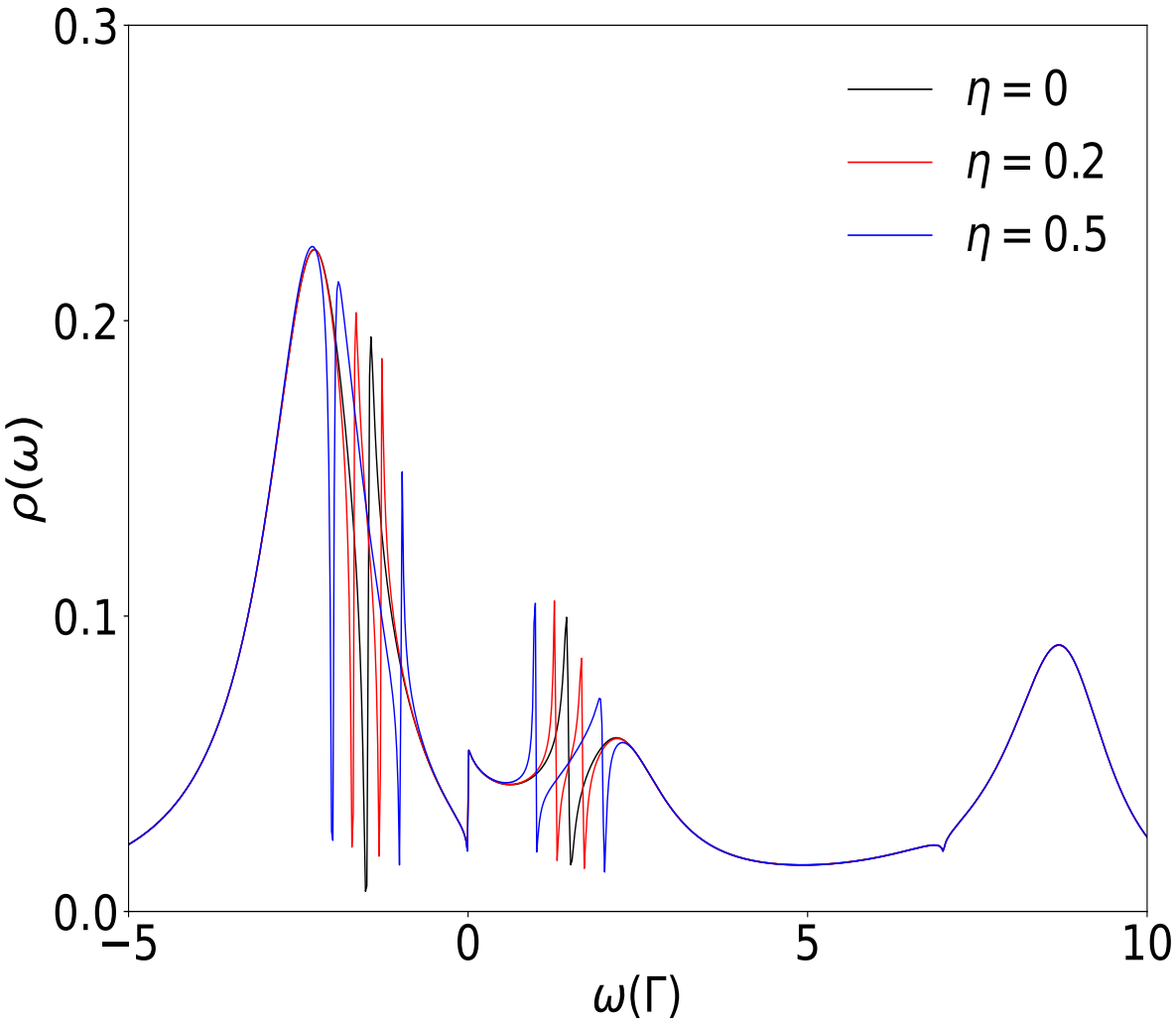


Figure 2.13: Spectral function $\rho(\omega)$ of the correlated QD in the equilibrium situation $V = 0$ obtained for $t = 0.2\Gamma_N$,$r = \Gamma_S/\Gamma_N = 1$, $\epsilon_d = -1.5\Gamma_N$, $U = 10\Gamma_N$, $k_BT = 0.001\Gamma_N$, and indicated values of the shift energy $\eta$: $\eta = 0(black)$, $\eta = 0.3(red)$ and $\eta = 0.5(blue)$.

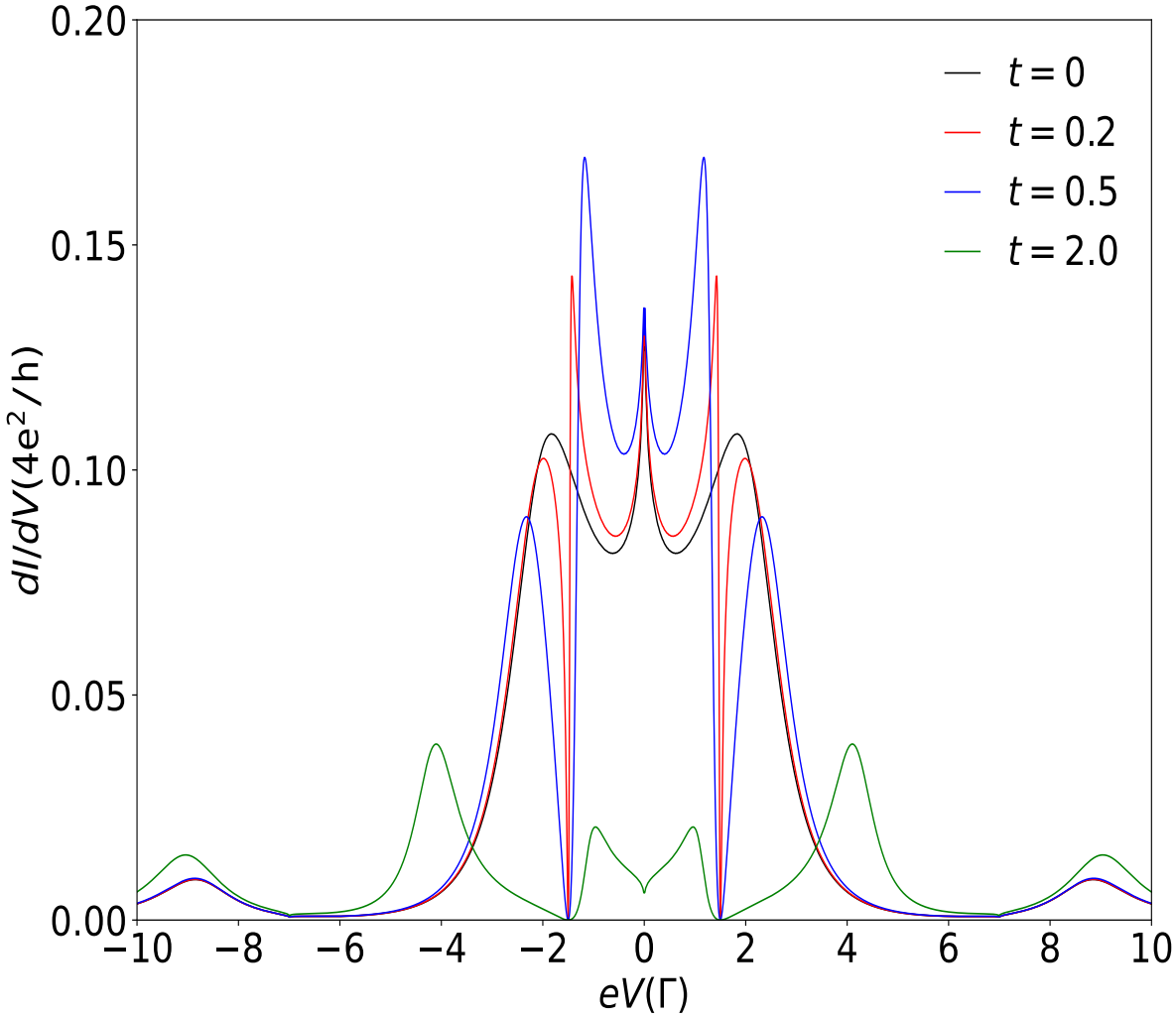


Figure 2.14: The differential conductance $dI/dV$ of the correlated QD in the non-equilibrium situation $V \neq 0$ obtained for $r = \Gamma_S/\Gamma_N = 5$, $\epsilon_d = -1.5\Gamma_N$, $U = 10\Gamma_N$, $k_BT = 0.001\Gamma_N$, and indicated values of the inter-dot tunneling $t$: $t = 0(black)$, $t = 0.2(red)$, $t = 0.5(blue)$ and $t = 2(green)$.

# 3

# Fano-Andreev effect in a T-shaped double quantum dot in the Coulomb-blockade regime

## 3.1 Introduction

The investigation of hybrid structures where normal conductors are connected to superconductors has attracted much attention because these structures exhibit interesting phenomena with potential applications in electronic, spintronics, and quantum information processing [59]. When a normal metal is coupled to a superconductor lead, the superconducting order can leak into the normal metal, inducing pairing correlations and a superconducting gap due to the so-called proximity effect [16]. The mechanism responsible for the proximity effect is known as Andreev reflection [17]. In this process, an electron is reflected as a hole at the interface between the leads. The missing charge in the normal lead appears as a Cooper pair within the superconductor. Since the electrons in the superconductor side and the hole in the normal lead are correlated, these are represented by bound states. In effect, the two charges coming from the normal lead cannot penetrate deep into the superconductor side being absorbed into the superconductor condensate. In hybrid systems composed of quantum dots (QDs), these bound states, called Andreev bound states (ABS), appear as resonances in the QD transmission spectrum, with energies within the superconductor gap. The presence of ABSs is the key ingredient to many different features exhibited by QD-based systems [23, 35, 36, 60–69]. The ABSs modify the so-called Fano effect [70, 71], a well-known phenomenon resulting from quantum interference between discrete and continuum states. In QDs-based systems, the Fano effect signature is an asymmetric resonance pattern arising in the transmission spectrum of the QD or double quantum dots (DQDs). Several authors studying the effect of quantum decoherence on the Fano lineshapes have introduced a normal floating lead directly coupled to the DQD, finding that the floating lead coupled to the lateral QD plays a crucial role in destroying the Fano lineshape. [20, 72]. Other authors have studied T-shaped QDs structure coupled to two normal or ferromagnetic leads left and right and a superconducting lead [73–78]. In particular, A. M. Calle et al. [22] have shown that, in a non-interacting T-shaped double quantum dot coupled to two normal metals, the trans-

mission between the normal leads (ET) exhibits Fano resonances due to the appearance of ABSs in the non-interacting DQD, due to the presence of the superconducting lead. By using a mean-field treatment of Coulomb correlations, E. C. Siqueira *et al.*. [79] have shown complementary patterns of resonances between AR and ET transmittance when a superconductor lead is coupled to a QD, which itself is coupled to two ferromagnetic leads. The effect was shown to be a result of the interplay between the ABSs and the spin polarization provided by the ferromagnets. At low enough temperatures (when the charging energy is sufficiently large compared to the thermal energy of the charge carriers) and under weak coupling of the QD to the leads, the influence of Coulomb correlations becomes increasingly significant. In this regime, called the Coulomb blockade regime, the dot occupation number is fixed, the transport through the quantum dot is blocked (the sequential tunneling is suppressed), and the transport is only favored in the transition regions where the energy of the state $|N_i>|$ is aligned with the chemical potential of the leads. As a consequence, the linear conductance through the dot shows a succession of peaks associated with the degeneracy regions (Coulomb peaks), separated by regions of low conductance. However, by lowering the temperature, the coupling of the electron within the QD to the electrons of the leads gives rise to virtual quantum states within the QD, which allows for an additional transport channel through the QD. This manifests as a narrow resonance peak in the transmission spectrum of the QD, called Kondo resonance. On the other hand, when one of the leads is a superconductor in a three-terminal system, it is possible to probe the interplay between the Fano effect, ET transmission, and ABS states. The interplay between ABS and Kondo effect in hybrid superconductor nanostructures has been extensively studied [80–82]. For the T-shape DQDs structure, A. M. Calle *et al.*. [6] found that the Kondo resonance modifies the ABS resonances. For systems composed of DQDs, the interplay among these effects has not been studied in depth in the literature despite the potential for original effects that may be obtained in these systems.

In this work, we investigate the electronic transport properties of a T-shaped DQD system. As shown in Fig. 2.1, the central QD, $\mathrm{QD}_a$, is connected to the normal leads while the other QD, $\mathrm{QD}_b$, is coupled to a superconductor lead (S). We focus our analysis on the Coulomb blockade regime, with the same values for the onsite Coulomb interaction parameters in both QDs ($U_a = U_b$). The equation-of-motion (EOM) method is used, and our results are obtained using the Hubbard-I approximation by which the relevant Green's functions are obtained. We study the influence of the inter-dot coupling, the coupling between QD and leads, and the Coulomb interaction on the quantum interferometric and molecular features of ET and AR transmission. We address these effects by using the non-equilibrium Green's function formalism.

This paper is organized as follows: in Sec. II, we present the model and formulation for the system displayed in Fig. 1, in Sec. III, the numerical results are presented and discussed. Finally, a summary and the main conclusions are presented in Sec. IV.

## 3.2 Model and Formulation

In Fig. 3.1, the T-shape double quantum-dot system is illustrated. It consists of a central quantum dot, $QD_a$, coupled to the two normal leads, $L_1$ and $L_2$, and a side $QD_b$,

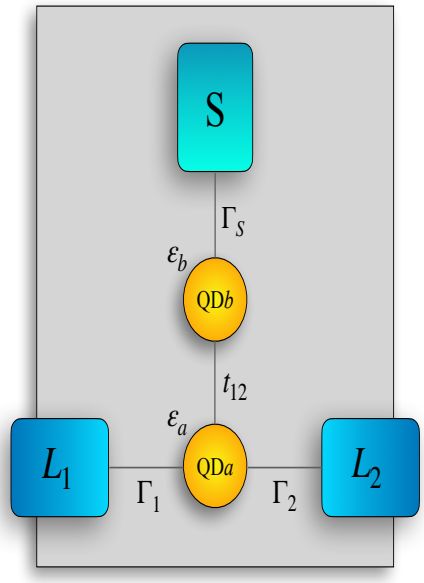


Figure 3.1: The T-shape double QD system studied in this work. It is composed of two quantum dots in which the $QD_a$ is coupled to two normal metals $L_1$ and $L_2$, with the coupling strength being determined by the parameters $\Gamma_1$ and $\Gamma_2$. The second quantum dot, $QD_b$ is coupled to the superconductor $S$, with the coupling strength being modeled by the parameter $\Gamma_S$. The coupling between the QDs is modeled by the $t_{12}$ parameter.

connected to a superconductor $S$. The Hamiltonian of the system is given by:

$$H = H_1 + H_2 + H_S + H_{DQD} + H_T. \tag{3.1}$$

The first and the second terms are the Hamiltonians for the normal leads at the left (1) and right (2) sides of $QD_a$. These are modeled by Eqs. (3.2) and (3.3):

$$H_1 = \sum_k \sum_\sigma \epsilon_{1k\sigma} c^\dagger_{1k\sigma} c_{1k\sigma} \tag{3.2}$$

and

$$H_2 = \sum_k \sum_\sigma \epsilon_{2k\sigma} c^\dagger_{2k\sigma} c_{2k\sigma} \tag{3.3}$$

where $c^\dagger_{\alpha k\sigma}$ ($c_{\alpha k\sigma}$) is the electron creation (annihilation) operator of an electron with spin $\sigma$ and energy $\epsilon_{k\sigma}$ in the $\alpha$ electrode.

The second term stands for the BCS Hamiltonian [41] of the superconducting ($S$) lead and reads:

$$H_S = \sum_k \sum_\sigma \epsilon_{kS} c^\dagger_{kS\sigma} c_{kS\sigma} + \sum_k (\Delta^* c_{kS\downarrow} c_{-kS\uparrow} + \Delta c^\dagger_{-kS\uparrow} c^\dagger_{kS\downarrow}), \tag{3.4}$$

where $c^{\dagger}_{kS\sigma}$ ($c_{kS\sigma}$) is the electron creation (annihilation) operator of an electron with spin $\sigma$ and energy $\epsilon_{kS}$ in the superconducting electrode, and $\Delta$ denotes pair potential, whose absolute value gives the superconducting energy gap.

The $H_{DQD}$ term is given by Eq. (3.5), and takes into account the coupling between the QDs, modeled by the variable $t_{12} = t$, and the Coulomb interaction at each QD, whose strength is modeled by $U_m$, $m = a, b$. The QDs are assumed to have a single spin degenerated level, whose value is determined by $\epsilon_{dm,\sigma}$, $m = a, b$.

$$\begin{aligned} H_{DQD} = \sum_{m=a,b,\sigma} \epsilon_{dm,\sigma} d^{\dagger}_{m,\sigma} d_{m,\sigma} \\ + \sum_{\sigma} t \left[ d^{\dagger}_{a\sigma} d_{b\sigma} + d^{\dagger}_{a\sigma} d_{b\sigma} \right] \\ + \sum_{m=a,b} U_m n_{m\sigma} n_{m\bar{\sigma}} \end{aligned} \tag{3.5}$$

### 3.2.1 Green's functions

To obtain the transport properties for the system modeled by Eq. (3.1), we have used the well-known non-equilibrium Green's function approach [83,84] along with the equation-of-motion method. This formalism has been extensively applied to nanostructured systems. The presence of the superconductor has been taken into account by expressing Green's functions within the Nambu space. In this way, Green's functions are represented by $4 \times 4$ matrices resulting from the tensor product between spin and electron-hole subspaces. By using this formalism, we have obtained a system of coupled Dyson equations for the retarded Green's functions matrices $\mathbf{G}^r_{aa}$ and $\mathbf{G}^r_{bb}$, for $QD_a$ and $QD_b$, respectively:

$$\mathbf{G}^r_{aa} = \mathbf{G}^{ro}_{aa} + \mathbf{G}^r_{aa} \mathbf{t}^{\dagger}_{ab} \mathbf{G}^{ro}_{bb} \mathbf{t}_{ab} \mathbf{G}^{ro}_{aa}, \tag{3.6}$$

and

$$\mathbf{G}^r_{bb} = \mathbf{G}^{ro}_{bb} + \mathbf{G}^r_{bb} \mathbf{t}^{\dagger}_{ab} \mathbf{G}^{ro}_{aa} \mathbf{t}_{ab} \mathbf{G}^{ro}_{bb}, \tag{3.7}$$

with

$$\mathbf{G}^{ro}_{aa} = \mathbf{g}^r_{aa} (1 - \mathbf{\Sigma}^r_L \mathbf{g}^r_{aa})^{-1}, \tag{3.8}$$

and

$$\mathbf{G}^{ro}_{bb} = \mathbf{g}^r_{bb} (1 - \mathbf{\Sigma}^r_S \mathbf{g}^r_{bb})^{-1}. \tag{3.9}$$

In Eqs. (3.6) to (3.9), $\mathbf{g}^r_{aa}$ and $\mathbf{g}^r_{bb}$ are the $QD_a$ and $QD_b$ Green's functions, respectively, when the QDs are isolated from the leads; $\mathbf{t}_{ab}$ describes the tunneling between $QD_a$ and $QD_b$. The coupling to the normal and superconducting leads are modeled by retarded/advanced self-energies $\mathbf{\Sigma}^r_L = \mathbf{\Sigma}^r_1 + \mathbf{\Sigma}^r_2$ and $\mathbf{\Sigma}^r_S$, respectively.

The self-energy for the coupling to the normal leads ($L_1$ and $L_2$) is given by Eq. (3.10):

$$\mathbf{\Sigma}^{r,a}_L = \mp \frac{i}{2} (\Gamma_1 + \Gamma_2) \begin{bmatrix} 1 & 0 & 0 & 0 \\ 0 & 1 & 0 & 0 \\ 0 & 0 & 1 & 0 \\ 0 & 0 & 0 & 1 \end{bmatrix}, \tag{3.10}$$

where $\Gamma_i = \Gamma_{i\uparrow} + \Gamma_{i\downarrow}$ and $\Gamma_{i\sigma} = 2\pi|t_i|^2 N_i$, $(i = 1, 2)$ being the coupling strength, with $t_i$ being amplitude for an electron with spin $\sigma$ of $QD_a$ to be transferred to the lead $L_i$; $N_i$ is the density of states at Fermi level for the normal lead, $L_i$. Since we have assumed both normal leads as non-magnetic, the density of states is the same for both spins.

The retarded/advanced self-energy of the superconductor is given by Eq. (3.11):

$$\mathbf{\Sigma}_S^{r,a} = \mp\frac{i}{2}\rho_S(\epsilon)\Gamma_S \begin{bmatrix} 1 & -\dfrac{\Delta}{\epsilon} & 0 & 0 \\ -\dfrac{\Delta}{\epsilon} & 1 & 0 & 0 \\ 0 & 0 & 1 & \dfrac{\Delta}{\epsilon} \\ 0 & 0 & \dfrac{\Delta}{\epsilon} & 1 \end{bmatrix}. \tag{3.11}$$

In Eq. (3.11), $\Gamma_S = 2\pi|t_s|^2 N_s$ is the coupling strength between the superconductor lead and $QD_b$, defined in terms of the amplitude of tunneling $|t_s|$ and the normal density of states of $N_s$. The $\Delta$ appearing in some of the matrix elements stands for the energy gap of the superconductor and accounts for the electron-hole coupling. The energy gap plays a central role in this model and also modifies the self-energy through $\rho_S$, the dimensionless modified BCS density of states, whose expression is given by:

$$\rho_S(\epsilon) = \frac{|\epsilon|\theta(|\epsilon| - \Delta)}{\sqrt{\epsilon^2 - \Delta^2}} - i\frac{\epsilon\theta(\Delta - |\epsilon|)}{\sqrt{\Delta^2 - \epsilon^2}}, \tag{3.12}$$

with the imaginary part accounting for the Andreev bound states (ABS), within the superconductor gap.

The presence of electronic correlations associates the QDs energy levels with the electronic occupations, which, in turn, depend on external parameters like gate and bias voltages. As a result, Eqs. (3.6) and (3.7) must be solved in a self-consistent way, together with the occupations of the QDs. Such occupations are obtained from the diagonal matrix elements of the "lesser" Green's function matrix, which is obtained through the Keldysh equation. For the $QD_a$, the expression reads:

$$\mathbf{G}_{aa}^{<} = \mathbf{G}_{aa}^{r}(\omega)\mathbf{\Sigma}_{Ta}^{<}\mathbf{G}_{aa}^{a}(\omega), \tag{3.13}$$

with

$$\mathbf{\Sigma}_{Ta}^{<} = \mathbf{\Sigma}_L^{<}(\epsilon) + \mathbf{t}_{ab}^{\dagger}\mathbf{G}_{bb}^{ro}\mathbf{\Sigma}_S^{<}(\epsilon)\mathbf{G}_{bb}^{ao}\mathbf{t}_{ab}. \tag{3.14}$$

The expression for $QD_b$ can be obtained by exchanging the indices $a$ and $b$. In Eq. (3.13), $\mathbf{\Sigma}_{Ta}^{<}$ represents the "lesser" self-energy, which is expressed in terms of the self-energies of the leads: $\mathbf{\Sigma}_L^{<} = \mathbf{\Sigma}_1^{<} + \mathbf{\Sigma}_2^{<}$ and $\mathbf{\Sigma}_S^{<}$. Assuming that the leads are in equilibrium with well-defined chemical potential and temperature, the self-energies of the leads can be obtained using the fluctuation-dissipation theorem: $\mathbf{\Sigma}_i^{<} = \mathbf{F}_i\left[\mathbf{\Sigma}_i^{a} - \mathbf{\Sigma}_i^{r}\right]$, where the Fermi matrix $\mathbf{F}_i$ is given by

$$\mathbf{F}_i = i\begin{bmatrix} f_i & 0 & 0 & 0 \\ 0 & \bar{f}_i & 0 & 0 \\ 0 & 0 & f_i & 0 \\ 0 & 0 & 0 & \bar{f}_i \end{bmatrix}, \tag{3.15}$$

with $f_i = f(\epsilon - eV_i)$ and $\bar{f}_i = f(\epsilon + eV_i)$ $(i = 1, 2, S)$ being the Fermi functions for electrons and holes, respectively. Since the superconductor is assumed to be grounded, $f_i = f(\epsilon)$ for $i = s$.

### 3.2.2 Transmittance and current

The presence of Coulomb correlations leads to a self-consistent problem when solving Eqs. (3.6) and (3.7), since the dependency on the occupations wraps the Green's functions to the occupancies of the QDs. Within the equation-of-motion approach used in this work, this results in an infinite set of equations with Green's functions of increasing order of complexity. To obtain a closed set of equations, one needs to resort to some approximation on the Coulomb correlations. In this work, we have used the so-called Hubbard-I approximation [85], which allows us to derive a simple expression for the electrical current in terms of the different transmission amplitudes that contribute to the electronic transport for this system. In fact, the current $I_j$, flowing in the lead $L_j$ $(j = 1, 2)$, is given by the following expression:

$$I_j = \frac{e}{\hbar} \int d\epsilon \, [\mathbf{G}^r_{aa}(\epsilon)\mathbf{\Sigma}^<_j(\epsilon) + \mathbf{G}^<_{aa}(\epsilon)\mathbf{\Sigma}^a_j(\epsilon) + \text{H.c.}]_{(11+33)}, \qquad j = 1, 2. \tag{3.16}$$

where $11 + 33$ stands for the sum of the 11 and 33 matrix elements of the current matrix. By substituting the Green's functions and self-energies into Eq. (3.16), one obtains the main expression for the electric current in lead $L_1$, written in terms of the transmittances:

$$I_1 = \frac{e}{h} \int [T^{DAR}_{11}(f_1 - \bar{f}_1) + T^{ET}_{12}(f_1 - f_2) + T^{CAR}_{12}(f_1 - \bar{f}_2) + T^{QP}_{1S}(f_1 - f_S)] d\epsilon, \tag{3.17}$$

The first term in Eqs. (3.17) , $T^{DAR}_{11}$, corresponds to direct Andreev reflection transmittances through the paths $(L_1 - QD_a - QD_b - S)$, i.e., an electron of $L_1$ is reflected by $S$ into a hole of $L_1$. The second term, $T^{ET}_{12}$, represents electron tunneling (ET) between the normal leads via $(L_1 - QD_a - QD_b - L_2)$ path. The next term, $T^{CAR}_{11}$, accounts for the transmittances of crossed Andreev reflection through the path $((L_1, L_2) - QD_a - QD_b - S)$, i.e., an electron of $L_1$ is reflected by $S$ into a hole of $L_2$. Finally, the last term, $T^{QP}_{11}$, corresponds to quasiparticles tunneling through the $(L_1 - QD_a - QD_b - S)$ path.

The expressions of the amplitudes in terms of Green's functions are given by:

$$\begin{aligned}
T_{11}^{DAR} &= \Gamma_1^2(|G^r_{aa,14}|^2 + |G^r_{aa,12}|^2 + |G^r_{aa,34}|^2 + |G^r_{aa,32}|^2) \\
T_{12}^{CAR} &= \Gamma_1\Gamma_2(|G^r_{aa,14}|^2 + |G^r_{aa,12}|^2 + |G^r_{aa,34}|^2 + |G^r_{aa,32}|^2) \\
T_{12}^{ET} &= \Gamma_1\Gamma_2(|G^r_{aa,33}|^2 + |G^r_{aa,31}|^2 + |G^r_{aa,13}|^2 + |G^r_{aa,11}|^2) \\
T_{1S}^{QP} &= \bar{\rho}\Gamma_1\Gamma_S\{Y^-_{21}|G^r_{aa,12}|^2 + X^+_{34}|G^r_{aa,13}|^2 + Y^+_{43}|G^r_{aa,14}|^2 \\
&\quad + X^-_{12}|G^r_{aa,11}|^2 - Z^+_{34}G^r_{aa,13}[G^r_{aa,14}]^* - [Z^+_{34}]^*[G^r_{aa,13}]^*G^r_{aa,14} \\
&\quad - Z^-_{12}G^r_{aa,11}[G^r_{aa,12}]^* - [Z^-_{12}]^*[G^r_{aa,11}]^*G^r_{aa,12} \\
&\quad + Y^-_{21}|G^r_{aa,32}|^2 + X^+_{34}|G^r_{aa,33}|^2 + Y^+_{43}|G^r_{aa,34}|^2 \\
&\quad + X^-_{32}|G^r_{aa,31}|^2 - Z^+_{34}G^r_{aa,33}[G^r_{aa,34}]^* \\
&\quad - [Z^+_{34}]^*[G^r_{aa,33}]^*G^r_{aa,34} - Z^-_{12}G^r_{aa,31}[G^r_{aa,32}]^* \\
&\quad - [Z^-_{12}]^*[G^r_{aa,31}]^*G^r_{aa,32}\}
\end{aligned} \tag{3.18}$$

where

$$\begin{aligned}
X^{\pm}_{ij} &\equiv t^2[|G^{ro}_{bb,ii}|^2 + |G^{ro}_{bb,ij}|^2 \pm \frac{\Delta}{\epsilon}(G^{ro}_{bb,ii}[G^{ro}_{bb,ij}]^* + G^{ro}_{bb,ij}[G^{ro}_{bb,ii}]^*), \\
Y^{\pm}_{ij} &\equiv t^2[|G^{ro}_{bb,ii}|^2 + |G^{ro}_{bb,ji}|^2 \pm \frac{\Delta}{\epsilon}(G^{ro}_{bb,ii}[G^{ro}_{bb,ji}]^* + G^{ro}_{bb,ji}[G^{ro}_{bb,ii}]^*)], \\
Z^{\pm}_{ij} &\equiv t^2[G^{ro}_{bb,ij}[G^{ro}_{bb,jj}]^* + [G^{ro}_{bb,ij}]^*G^{ro}_{bb,ii} \\
&\qquad \pm \frac{\Delta}{\epsilon}(|G^{ro}_{bb,ij}|^2 + [G^{ro}_{bb,jj}]^*G^{ro}_{bb,ii})].
\end{aligned} \tag{3.19}$$

(The current flowing and transmittances in $L_2$ can be obtained by interchanging the indexes 1 and 2 in the above equation).

### 3.2.3 Self-consistent calculations

Regarding the occupations of the QDs, they are determined by the "lesser" Green's function. In the case of normal leads with no polarization, the average occupation number remains independent of spin. This allows us to set, for each QD, $\langle n_{i,\sigma}\rangle = \langle n_i\rangle$ where $i = a, b$. These occupation numbers are obtained by solving the following self-consistent system of integral equations:

$$\langle n_{a\uparrow}\rangle = -i\int \frac{d\epsilon}{2\pi}\, G^<_{aa,11}[\epsilon, \langle n_{a\uparrow}\rangle, \langle n_{a\downarrow}\rangle, \langle n_{b\uparrow}\rangle, \langle n_{b\downarrow}\rangle], \tag{3.20a}$$

$$\langle n_{a\downarrow}\rangle = -i\int \frac{d\epsilon}{2\pi}\, G^<_{aa,33}[\epsilon, \langle n_{a\uparrow}\rangle, \langle n_{a\downarrow}\rangle, \langle n_{b\uparrow}\rangle, \langle n_{b\downarrow}\rangle], \tag{3.20b}$$

$$\langle n_{b\uparrow}\rangle = -i\int \frac{d\epsilon}{2\pi}\, G^<_{bb,11}[\epsilon, \langle n_{a\uparrow}\rangle, \langle n_{a\downarrow}\rangle, \langle n_{b\uparrow}\rangle, \langle n_{b\downarrow}\rangle], \tag{3.20c}$$

$$\langle n_{b\downarrow}\rangle = -i\int \frac{d\epsilon}{2\pi}\, G^<_{bb,33}[\epsilon, \langle n_{a\uparrow}\rangle, \langle n_{a\downarrow}\rangle, \langle n_{b\uparrow}\rangle, \langle n_{b\downarrow}\rangle]. \tag{3.20d}$$

In the electron-hole symmetry point, i.e., when $\epsilon_d = -U/2$, the occupation is independent of bias voltage and equal to 1/2 ($n_{a,\sigma} = n_{b,\sigma} = 0.5$, with $\sigma = \uparrow, \downarrow$). In this way,

the exact expression for $(dI/dV)^{ET}$ and $(dI/dV)^{AR}$ in the function of bias voltage can be calculated analytically, and is equal to:

$$\frac{dI^{ET}}{dV} = 2\frac{(4G\,A - 2F\,B\Gamma_S^2 + \frac{1}{4}C\Gamma_S^4)}{(K)} \tag{3.21}$$

and

$$\frac{dI^{AR}}{dV} = 4\frac{t^4\,\Gamma_S^2}{(K)} \tag{3.22}$$

where

$$K = 4D\,A - 2(-t^4\Gamma_L^2 + G\,F\,B - F(t^2 - \Gamma_L^2)B)\Gamma_S^2 + \frac{1}{4}E\,C\Gamma_S^4 \tag{3.23}$$

with

$$\begin{aligned}
A &= \left[(\bar{g}^r_{1,12})^2 - t^2\right]^2 + (\bar{g}^r_{1,12})^2\Gamma_L \\
B &= (\bar{g}^r_{1,12})^2 - t^2 + \Gamma_L^2 \\
C &= (\bar{g}^r_{1,12})^2 + \Gamma_L^2 \\
D &= [(\bar{g}^r_{1,11})^2 - t^2]^2 + (\bar{g}^r_{1,11})^2\,\Gamma_L^2 \\
E &= (\bar{g}^r_{1,11})^2 + \Gamma_L^2 \\
F &= \bar{g}^r_{1,11}\bar{g}^r_{1,12} \\
G &= (\bar{g}^r_{1,11})^2
\end{aligned} \tag{3.24}$$

while $\bar{g}^r_{1,11}$ and $\bar{g}^r_{1,12}$ are the components 11 and 12 of the inverse Green function of $QD_1$ isolated in the Hubbard-I approximation, evaluated in the bias voltage $V$, i.e.:

$$\bar{g}^r_{i,11} = \frac{((V - \epsilon_d - U)(V - \epsilon_d))}{(V - \epsilon_d + U(n_1 - 1))} \tag{3.25}$$

$$\bar{g}^r_{i,12} = \frac{((V + \epsilon_d + U)(V + \epsilon_d))}{(V + \epsilon_d - U(n_1 - 1))} \tag{3.26}$$

$$\tag{3.27}$$

The analysis of these curves is complemented by the local density of states of the QDs, $\rho_a$ and $\rho_b$, defined according to:

$$\rho(\epsilon)_i = -\frac{1}{\pi}\mathrm{Im}(\mathbf{G}^r_{ii,11} + \mathbf{G}^r_{ii,33}), \qquad i = a, b. \tag{3.28}$$

## 3.3 Results and Discussion

In what follows, we consider $\Gamma_1$ as the energy unit. We assume that the QDs levels are spin degenerate and that the intradot Coulomb interaction is the same in both QDs, i.e.,

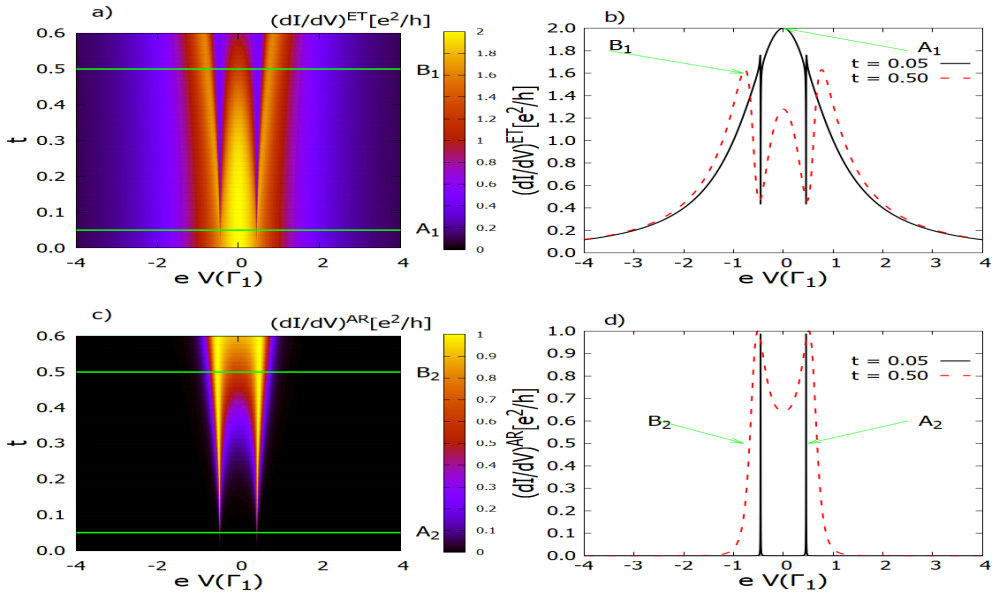


Figure 3.2: Left panel: Contour plot of $(dI/dV)^{ET}$ and $(dI/dV)^{AR}$ in terms of $t$ and $V$, figures a) and c), respectively ; Right panel:$(dI/dV)^{ET}$ and $(dI/dV)^{AR}$ in terms of the energy when $t = 0.05$ (black solid line) or $t = 0.5$(red dashed line), figures b) and d), respectively. Their location at the contour plot is indicated by the horizontal lines labeled by $A_1$ and $A_2$ for $t = 0.05$ and by $B_1$ and $B_2$ for $t = 0.5$, respectively. Other parameters are chosen as $U = 0$, $k_BT = 0\Gamma_1$, $\Gamma_1 = \Gamma_2 = \Gamma_S$ and $\epsilon_a = \epsilon_b = -U/2$

$U_a = U_b = U$. We denoted $r$ as the ratio of leads coupling $\Gamma_S/\Gamma_1$ through which we control the efficiency of the proximity effect, as well as, the interdot tunneling as $t$. Also, we set the gate voltage for each QD in the electron-hole symmetry point, i.e., $\epsilon_a = \epsilon_b = -U/2$. In our work, we focus on the non-equilibrium regime, and the analysis of the results is split into two parts: interferometric regime (when $t < \Gamma_1$ ) and molecular regime (when $t \geq \Gamma_1$ ). In our analysis, we present the results for the differential conductance ET ( $(dI/dV)^{ET}_{12}$ ) and the differential conductance AR $(dI/dV)^{DAR}_{12}$ in terms of the bias voltage applied to the leads, which we will refer to for simplicity as $(dI/dV)^{ET}$ and $(dI/dV)^{DAR}$, respectively. The chemical potential of the normal leads are set with opposite bias voltage, i.e. $\mu_1 = -\mu_2 = eV$, while the superconductor is kept grounded, $\mu_S = 0$. With the normal leads with opposite bias voltage, $(dI/dV)^{CAR}_{12}$ (or $I^{CAR}_{12}$) and $(dI/dV)^{CAR}_{21}$ (or $I^{CAR}_{21}$) are zero since they are proportional to the factor $(f_1 - \bar{f}_2)$ and $(f_2 - \bar{f}_1)$, respectively, which are identically zero. It is worth saying that we are assuming that $|eV| < \Delta$, and therefore the contribution of the quasiparticle current $I^{QP}$ and transmittance $T^{QP}$ is zero within the energy range we are considering. Finally, it is important to note that our calculations were obtained out of the Kondo regime.

### 3.3.1 Interferometric regime

We begin the analysis of the linear regime by focusing on the interdot tunneling effects on $(dI/dV)^{ET}$ and $(dI/dV)^{AR}$, within the interferometric regime ($t \leq \Gamma_1$). For clarity's sake, we start by focusing on the noninteracting regime ($U = 0$). In this case, the behavior

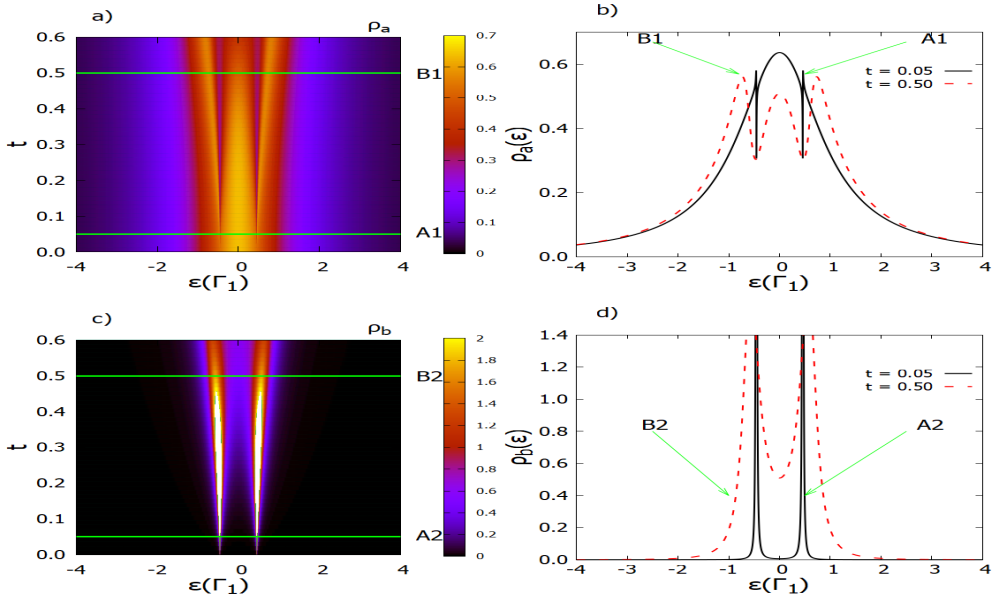


Figure 3.3: Left panel: Contour plot of $\rho_a$ and $\rho_b$ in terms of $t$ and $\epsilon$, figures a) and c), respectively ; Right panel:$\rho_a$ and $\rho_b$ in terms of the energy when $t = 0.05$(black solid line) or $t = 0.5$(red dashed line), figures b) and d), respectively. Their location at the contour plot is indicated by the horizontal lines labeled by $A_1$ and $A_2$ for $t = 0.05$ and by $B_1$ and $B_2$ for $t = 0.5$, respectively. Other parameters are chosen as $U = 0$, $k_BT = 0\Gamma_1$, $\Gamma_1 = \Gamma_2 = \Gamma_S$ and $\epsilon_a = \epsilon_b = -U/2$

of $(dI/dV)^{ET}$ and $(dI/dV)^{AR}$ as functions of $t$ and $V$, are shown in the contour plots of Figs. 3.2(a) and 3.2(c), respectively. For $t = 0$, the $QD_a$ is decoupled from $QD_b - S$ part of the system and, as a result,$(dI/dV)^{ET}$ exhibits a well-known Lorentzian shape, while the $(dI/dV)^{AR}$ remains equal to zero. As $t$ increases, the superconducting correlations start to leak into $QD_a$ and the Andreev bound states (ABSs) emerge as two resonances equidistant from $V = 0$. At the same bias voltage values, two equidistant deeps appear in the $(dI/dV)^{AR}$ curves. The correspondence between these two lineshapes can be better observed in Figs. 3.2(b) and 3.2(d) where cuts of the contour plots for $t = 0.05$ ($\mathsf{A}_1$ and $\mathsf{A}_2$ lines) and and $t = 0.5$ ($\mathsf{B}_1$ and $\mathsf{B}_2$ lines) are shown. It is also worth noting that the central peak at $V = 0$ is preserved in $(dI/dV)^{ET}$ curves, as a manifestation of electron-hole symmetry of the ABSs on the QDs spectra. As $t$ increases, the hybridization between the discrete ABSs with the continuum states, stemming from the normal leads, causes the lineshapes to broaden. This interpretation is based on the fact that the differential conductance curves follow the behavior of the local density of states of the QDs for zero bias voltage, as shown in Fig. 3.3. The very same behavior can be observed from the contour plots for $\rho_a$ and $\rho_b$, at zero bias voltage, as shown in Figs. 3.3(a) and 3.3(c), respectively.

A more detailed line shape can be seen in the cuts for $t = 0.05$ ($\mathsf{A}_1$ and $\mathsf{A}_2$ lines) and $t = 0.5$ ($\mathsf{B}_1$ and $\mathsf{B}_2$ lines), which readily show the same behavior observed in the transmission curves.

In Fig. 3.4, the differential conductance $(dI/dV)^{ET}$ and $(dI/dV)^{AR}$ are shown for $U = 2$. The other parameters remain the same as those used in Figs. 3.2 and 3.3. The

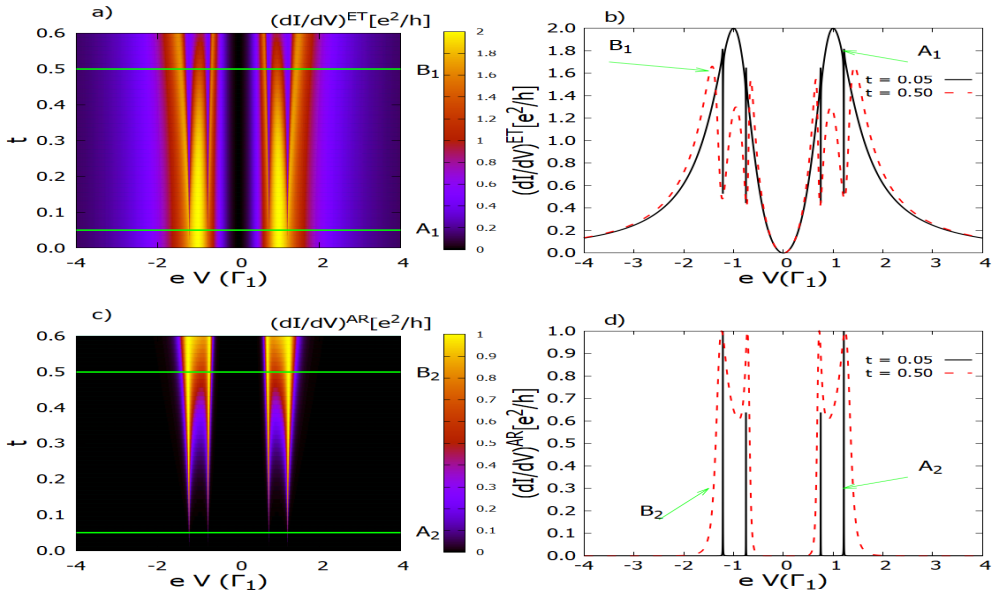


Figure 3.4: Left panel: Contour plot of $(dI/dV)^{ET}$ and $(dI/dV)^{AR}$ in terms of $t$ and $V$, figures a) and c), respectively ; Right panel:$(dI/dV)^{ET}$ and $(dI/dV)^{AR}$ in terms of the bias voltage V, when $t = 0.05$ (solid line) or $t = 0.5$(dashed line), figures b) and d), respectively. Their location at the contour plot is indicated by the horizontal lines labeled by $A_1$ and $A_2$ for $t = 0.05$ and by $B_1$ and $B_2$ for $t = 0.5$, respectively. Other parameters are chosen as $U = 2$, $k_BT = 0\Gamma_1$, $\Gamma_1 = \Gamma_2 = \Gamma_S$ and $\epsilon_a = \epsilon_b = -U/2$

main difference, in this case, is the splitting of the peaks due to the Coulomb correlation. In fact, for $t = 0.05$, two Lorentzian peaks are observed, as is evident from the cut $A_1$, shown in Fig. 3.4(b). The ABSs are also evident at this small value of $t$ as antiresonances superimposed on the peaks despite the presence of Coulomb correlations. As $t$ increases, the broadening of peaks increases, as is evident from the contour plots of Figs. 3.4(a) and 3.4(c) and the corresponding cuts shown in Figs. 3.4 (b) and 3.4 (d). In contrast to the broadening of the peaks, their location is fixed by the Coulomb interaction with the two Lorentzian peaks located at $\pm U/2$, which is also the center of symmetry of the ABSs. A similar behavior is observed for the local density of states for zero bias voltage, as shown in Fig. 3.5. This figure shows in the left panel the contour plot of $\rho_a$ and $\rho_b$ as a function of $\epsilon$ and $t$ [Figs 5 (a) and 5(c), respectively] and shows in the right panel the curves of $\rho_a(\epsilon)$ and $\rho_b(\epsilon)$ in terms of energy [Figs. 5 (b) and 5 (d), respectively], when $t = 0.05$ (solid line) or $t = 0.5$ (dashed line). Their location in the contour plot is indicated by the horizontal lines labeled $A_1$ and $A_2$ for $t = 0.05$ and $B_1$ and $B_2$ for $t = 0.5$. As we can see in figures 5 a) and 5 c), $\rho_a$ takes the form of two Lorentzian curves centered at $\epsilon = \pm U/2$ when $t = 0$, while $\rho_b$ equals zero. However, when $t = 0.05$, we observe the appearance of two pairs of narrow deeps in $\rho_a$ [see lines $A_1$, in Figs. 5 (a) and 5 (b)] revealing the leakage of ABS in the density of states of $QD_a$ , expressed in the two pairs of sharp resonances in $\rho_b$ [see lines $A_2$ , in Figs. 5(c) and 5(d)]. However, as the value of $t$ increases, for example, when $t = 0.5$ the deeps in the $\rho_a$ [see lines $B_1$, in Figs. 5 (a) and 5 (b)], and the resonances in $\rho_b$ [see lines $B_2$, in Figs. 5 (c) and 5 (d))] become progressively wider.

In Fig. (3.6) we study the role of the superconductor in $(dI/dV)^{ET}$ by varying the

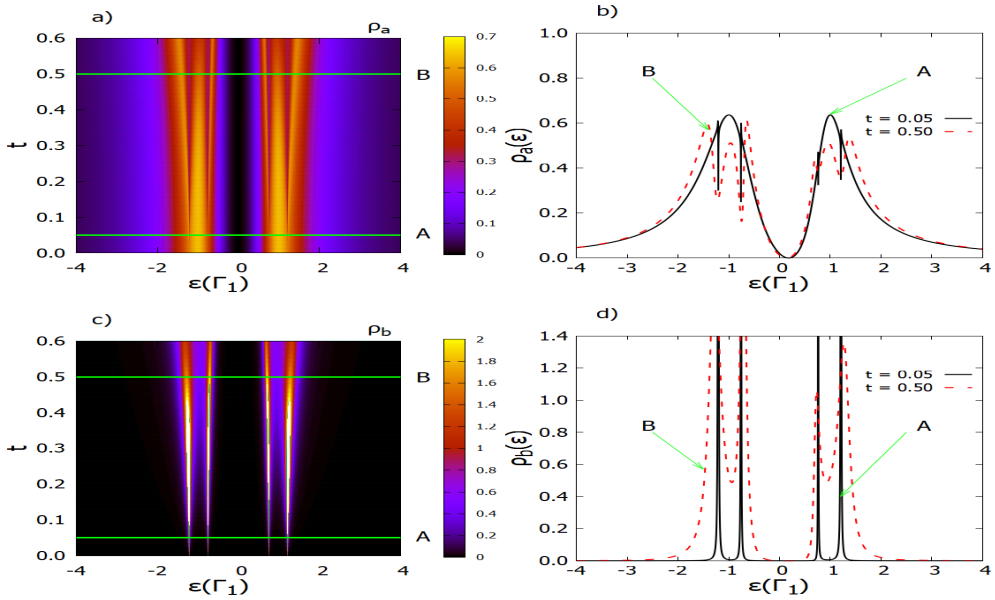


Figure 3.5: Left panel: Contour plot of $\rho_a$ and $\rho_b$, at zero bias voltage, in terms of $t$ and $\epsilon$, figures a) and c), respectively ; Right panel:$\rho_a(\epsilon)$ and $\rho_b(\epsilon)$ in terms of the energy when $t = 0.05$(solid line) or $t = 0.5$(dashed line), figures b) and d), respectively.Their location at the contour plot is indicated by the horizontal lines labeled by $A_1$ and $A_2$ for $t = 0.05$ and by $B_1$ and $B_2$ for $t = 0.5$, respectively. Other parameters are chosen as $U = 2$, $k_BT = 0\Gamma_1$, $\Gamma_1 = \Gamma_2 = \Gamma_S$ and $\epsilon_a = \epsilon_b = -U/2$

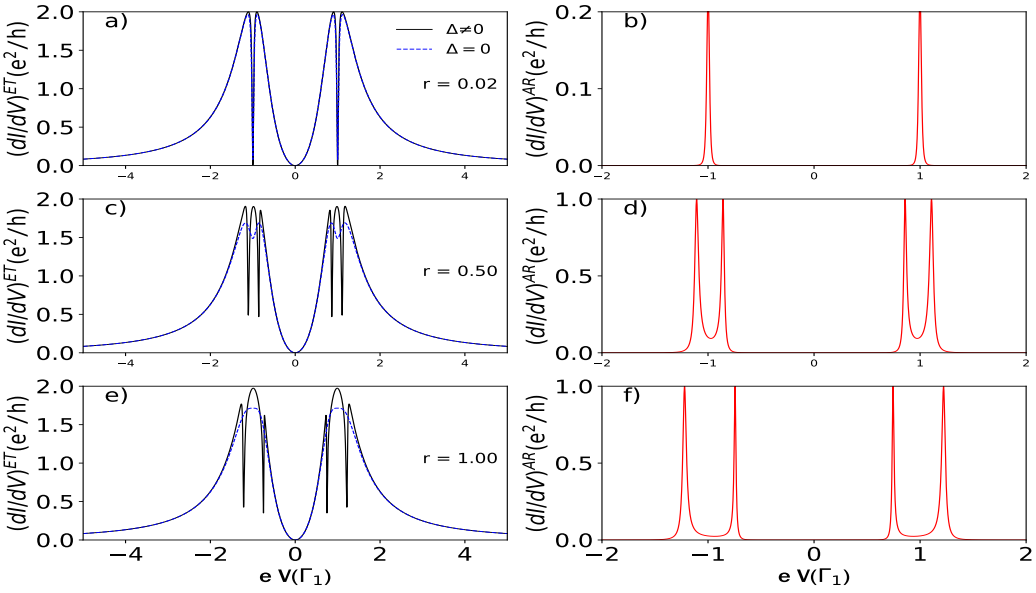


Figure 3.6: The differential conductance $(dI/dV)^{ET}$ (solid black line) and $(dI/dV)^{AR}$ (dashed red line) as a function of the bias voltage $V$ for a) $r = 0.02$, b) $r = 0.50$ and c) $r = 1$. The dashed line in the left panel corresponds to the $(dI/dV)^{ET}$ for $\Delta = 0$, i.e. for a system with three normal contacts. Other parameters are chosen as: $\Delta = 5\Gamma_1$, $U = 2\Gamma_1$, $t = 0.2\Gamma_1$, $k_BT = 0\Gamma_1$, $\Gamma_1 = \Gamma_2$ and $\epsilon_a = \epsilon_b = -U/2$

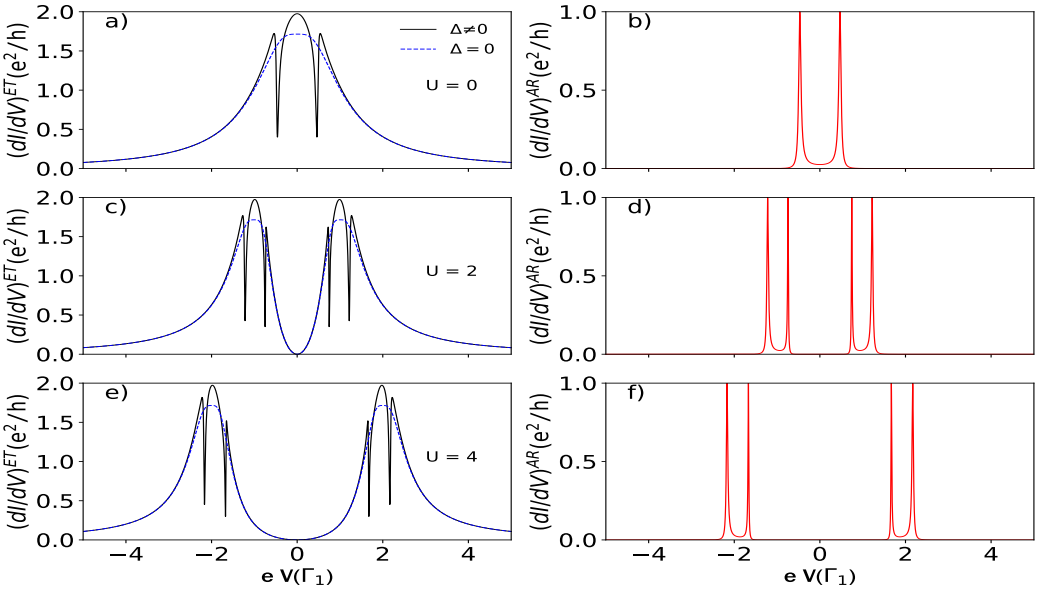


Figure 3.7: In the Left panel, the differential conductance $(dI/dV)^{ET}$ (black solid line ) as a function of the bias voltage $V$ and in the right panel $(dI/dV)^{DAR}$ (red solid line ) as a function of the bias voltage $V$ when $U = 0$ for a) and b), $U = 2$ for c) and d), and $U = 4$ for e) and f). The dashed line on the left panel corresponds to $(dI/dV)^{ET}$ for $\Delta = 0$, that is, for a system with three normal contacts. Other parameters are chosen as $t = 0.2\Gamma_1$ , $\Delta = 5\Gamma_1$ , $k_BT = 0\Gamma_1$, $\Gamma_1 = \Gamma_2 = \Gamma_S$ and $\epsilon_a = \epsilon_b = -U/2$.

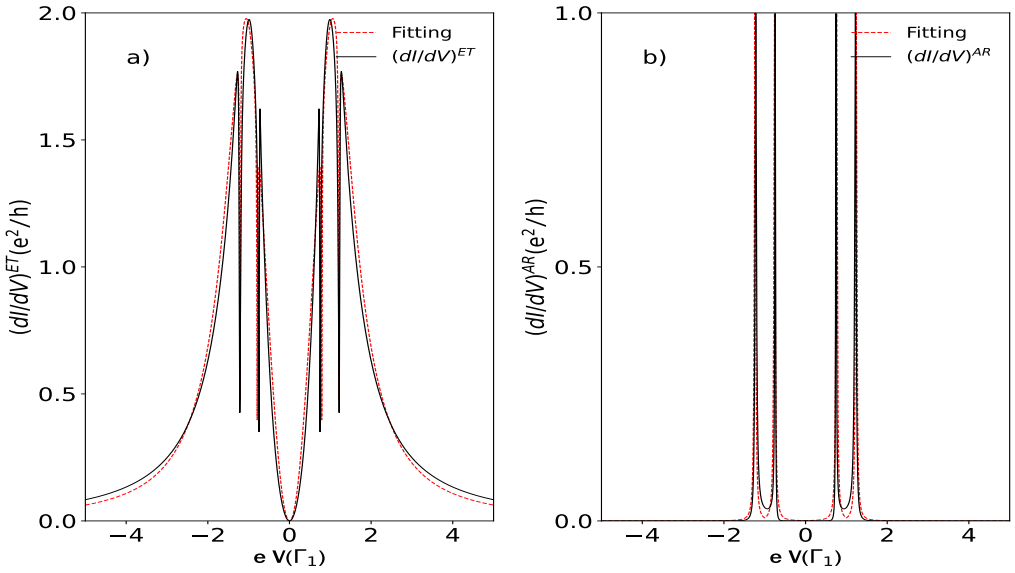


Figure 3.8: a) The differential conductance $(dI/dV)^{ET}$ (black solid line ) and the fitting (red dashed line) as a function of the bias voltage $V$ when $t = 0.2$. b) The differential conductance $(dI/dV)^{AR}$ (solid black line) and the fitting (red dashed line) as a function of the bias voltage $V$ when $t = 0.2$. Other parameters are chosen as $\Delta = 5\Gamma_1$ , $k_BT = 0\Gamma_1$, $\Gamma_1 = \Gamma_2 = \Gamma_S$ and $\epsilon_a = \epsilon_b = -U/2$.

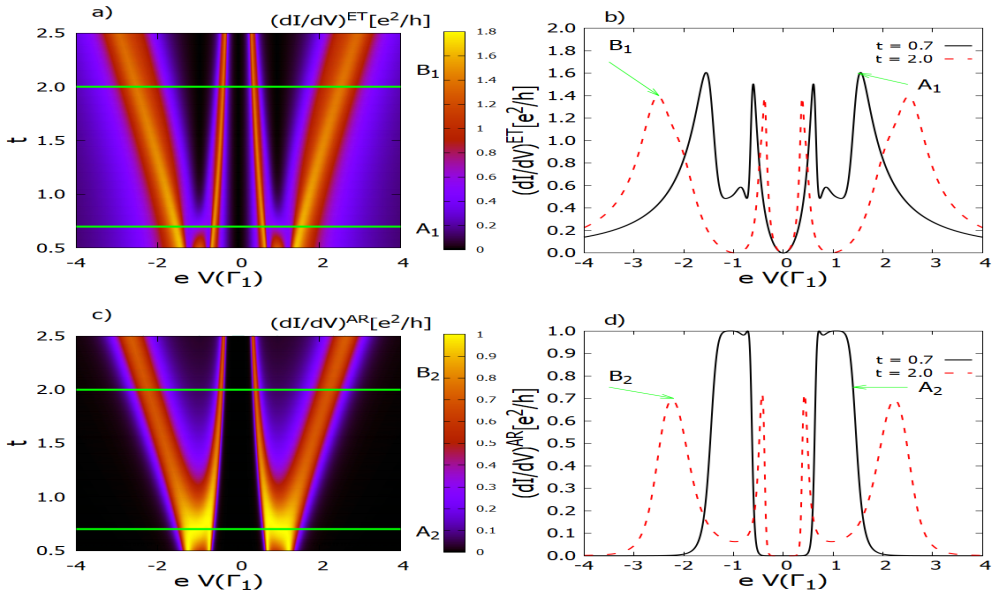


Figure 3.9: Left panel: Contour plot of $(dI/dV)^{ET}$ and $(dI/dV)^{AR}$ in terms of $t$ and $V$, figures a) and c), respectively ; Right panel:$(dI/dV)^{ET}$ and $(dI/dV)^{AR}$ in terms of bias voltage when $t = 0.7$ (solid line) or $t = 2$(dashed line), figures b) and d), respectively. Their location in the contour plot is indicated by the horizontal lines labeled by $A_1$ and $A_2$ for $t = 0.7$ and by $B_1$ and $B_2$ for $t = 2.0$, respectively. Other parameters are chosen as $U = 2$, $k_BT = 0\Gamma_1$, $\Gamma_1 = \Gamma_2 = \Gamma_S$ and $\epsilon_a = \epsilon_b = -U/2$

coupling ratio, $r = \Gamma_S/\Gamma_1$, and $\Delta$, the superconductor gap. While $r$ measures the coupling strength between $QD_b$ and $S$, $\Delta$ carries information on superconductor correlations. The differential conductance $(dI/dV)^{ET}$ and $(dI/dV)^{AR}$, as a function of bias voltage, are shown in the left and right panels of the Fig. (3.6), respectively, for $r$ changing from 0 to 2.0. For $\Delta = 0$, the blue dotted lines represent $(dI/dV)^{ET}$. First, we can note when $r = 0.02$, i.e., when the DQD can be considered decoupled from the third lead, the difference conductance ET shows two deep Fano antiresonances, which reveals the existence of quantum interference due to the effect of the additional channel opened by the second QD coupled to the system. As the value of $r$ increases, Fano antiresonances in the differential conductance ET disappear when the third lead is normal ($\Delta = 0$), due to hybridization of the discrete state of $QD_b$ with the continuum spectrum of $S$ in its normal state. In contrast, when $\Delta \neq 0$ and $r \neq 0$, the lead $S$ becomes a superconductor and the energy gap is revealed at the Fermi level with the presence of ABSs, and two pairs of Fano antiresonances appear in the differential conductance ET, corresponding to the Fano resonances appearing in the differential conductance AR for the same value of $V$, which is a clear manifestation of quantum interference. For example, when $r = 0.02$, the coupling to $S$ is too small, and $(dI/dV)^{ET}$ exhibits the Fano antiresonance pattern. In contrast, for $r \geq 0.50$, the ABSs become pronounced enough to change the shape of $(dI/dV)^{ET}$; this can be seen from the $(dI/dV)^{AR}$ shown by the red curves in Fig. 3.6. As in the non-interacting case, the resonances of $(dI/dV)^{AR}$ correspond to two anti-resonances in $(dI/dV)^{ET}$ curves, equidistant from $\pm U/2$ with a central peak located at $\pm U/2$. In contrast to the normal state, this effect is robust with respect to the increase of

$r$, being preserved for all values of $r$. The main effect of $r$, in this case, is to displace the ABSs on the bias axis. Despite similar effects pointed out in the literature [6, 20], here it is clear that this interference pattern is robust against Coulomb correlations, which, in general, have a detrimental effect on Andreev interference.

Finally, Fig. 3.7 displays in the left panel the electron-tunneling differential conductance($(dI/dV)^{ET}$) (black solid line) and in the right panel the Andreev differential conductance ($(dI/dV)^{AR}$) (red solid line) for different values of intra-dot Coulomb interaction $U$. The dashed line on the left panel also corresponds to the $(dI/dV)^{ET}$ for $\Delta = 0$, that is, for a system with three normal contacts. We can see in Fig. 3.7 that when $t = 0.2$, $U = 0$ and $\Delta = 0$, the differential conductance ET has the form of a Lorentzian centered on the zero bias voltage and does not present antiresonances. On the contrary, when $U = 0$ and $\Delta \neq 0$ the differential conductance ET shows two Fano antiresonances, which coincide with the two resonances in the differential conductance AR. Conversely, when $U \neq 0$ and $\Delta \neq 0$, the two antiresonances in the differential conductance ET and the two resonances in the differential conductance AR are subdivided on either side of the zero bias with the symmetry point located at $\pm U/2$, by the effect of the Coulomb interaction. The separation between the resonances in the differential conductance ET and AR increases as $U$ increases.

One way to better comprehend the tunneling mechanism in different transmission processes is to analyze the differential conductance $(dI/dV)^{ET}$. It can be expressed as a convolution of two Breit-Wigner and two Fano line shapes, as shown in Fig. 3.12 a).

$$\frac{dI^{ET}}{dV} \approx \frac{|\tilde{V}_1 + q|^2}{|\tilde{V}_1|^2 + 1}\left(\frac{1}{\epsilon_1^2 + 1} + \frac{1}{\epsilon_2^2 + 1}\right)\frac{|\tilde{V}_2|^2}{|\tilde{V}_2|^2 + 1}, \tag{3.29}$$

where $\tilde{V}_1 = (||V| - U/2| - \Gamma_S/4)/\eta$ with $\eta = t^2/(\Gamma_S)$, $\tilde{V}_2 = |V|/(\Gamma_{L1}/2)$ , $\epsilon_1 = \frac{|V|-\epsilon_d}{(\Gamma_{L1}/2)}$,$\epsilon_2 = \frac{|V|-(\epsilon_d+U)}{(\Gamma_{L1}/2)}$and $q = q_r + i\, q_i$. The complex Fano parameter, $q$, and the coupling value, $\Gamma_{L1}$, are relevant to understand the differential conductance. On the basis of the above equation, the conductance has two resonances at $V = \epsilon_d$ and $V = \epsilon_d + U$. Each resonance has two dips at $V = \epsilon_d \pm \Gamma_S/4$ and $V = (\epsilon_d + U) \pm \Gamma_S/4$, with $\epsilon_d = -U/2$. Additionally, a single antiresonance appears at $V = 0$. The interference of electrons through different tunneling paths, including Andreev bound-states, explains the Fano effect observed in our results. Due to the presence of Andreev bound states, the electron suffers a change in its phase, and this is reflected in a complex $q$-parameter as we see in Eq.(3.29). Furthermore, the Andreev differential conductance, $(dI/dV)^{AR}$, can be expressed as two Breit-Wigner line shapes (shown in Fig. 3.12 b)).

$$\frac{dI^{AR}}{dV} \approx \left(\frac{1}{\epsilon_3^2 + 1} + \frac{1}{\epsilon_4^2 + 1}\right), \tag{3.30}$$

where $\epsilon_3 = \frac{|V-\epsilon_d|-\Gamma_S/4}{(t^2/\Gamma_S)}$ and $\epsilon_4 = \frac{|V-(\epsilon_d+U)|-\Gamma_S/4}{(t^2/\Gamma_S)}$. The above equation shows that the Andreev differential conductance has four resonances at $V = \epsilon_d \pm \Gamma_S/4$ and $V = (\epsilon_d + U) \pm \Gamma_S/4$, with $\epsilon_d = -U/2$, which coincide exactly with the dips of the differential conductance ET mentioned above. From the fits, we can conclude that the Fano-Andreev effect is robust in the presence of Coulomb interaction. Additionally, in the interferometric regime, Andreev transmission is a resonant tunneling process through Andreev-bound

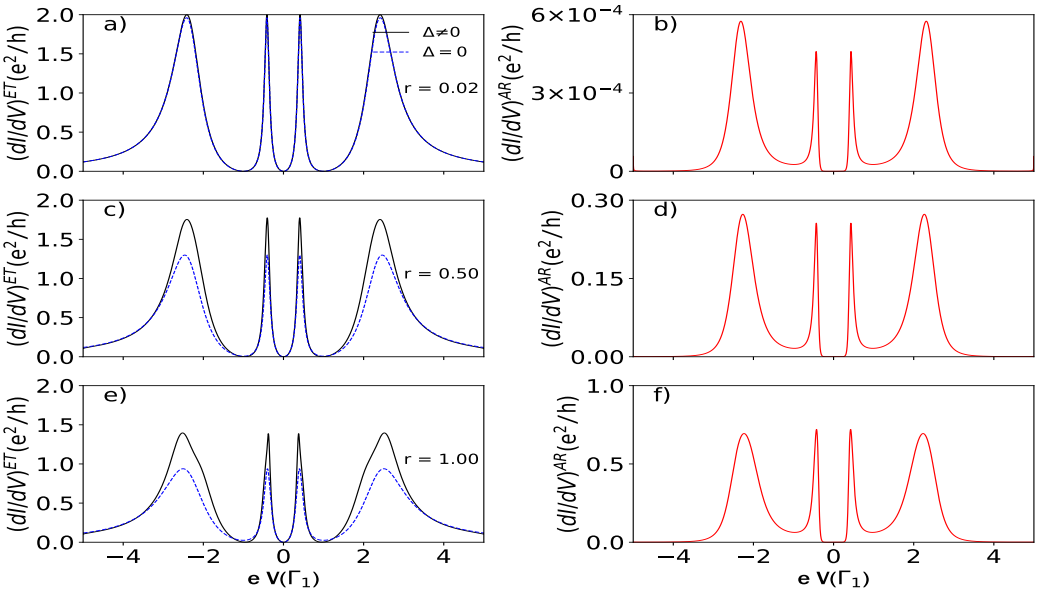


Figure 3.10: In Left panel, the differential conductance $(dI/dV)^{ET}$ (black solid line) as a function of the bias voltage $V$ and in the right panel $(dI/dV)^{AR}$ (red solid line ) as a function of the bias voltage $V$ when $r = 1$ for a) and b), $r = 2$ for c) and d), and $r = 4$ for e) and f). The blue dashed line in the left panel corresponds to $(dI/dV)^{ET}$ for $\Delta = 0$, that is, for a system with three normal contacts. Other parameters are chosen as $t = 2\Gamma_1$ , $\Delta = 5\Gamma_1$ , $U = 2\Gamma_1$, $k_BT = 0\Gamma_1$, $\Gamma_1 = \Gamma_2$ and $\epsilon_a = \epsilon_b = -U/2$.

states, which causes the Fano effect in normal transmission.

### 3.3.2 Molecular regime

In Fig. 3.9,the behavior of $(dI/dV)^{ET}$ and $(dI/dV)^{AR}$ as functions of $t$ and $V$, when $0.5\Gamma_1 <= t <= 2.5\Gamma_1$, are shown in the contour plots of Figs. 3.9(a) and 3.9(c), respectively. The other parameters remain the same as those used in Figs. 3.4 and 3.5. This figure shows the progressive vanishing of antiresonances in the differential conductance ET as $t$ increases from 0.5 to 2.5. This figure shows the progressive disappearance of the antiresonances in the differential conductance ET as $t$ increases from 0.5 to 2.5. As seen in the black solid line in Fig. 9 (a) or line $\mathsf{A}_1$ in 9 (b), when $t = 0.7$ the antiresonances in the differential conductance ET have almost disappeared. Therefore, we can consider that the value of $t$ is the threshold value that separates the interferometric regime from the molecular one. On the other hand, when $t > 0.7$, specifically at $t = 2$ (see line B1 in Fig. 9 a), or red dashed line in Fig. 9 b) ), the differential conductance ET becomes zero at $\pm U/2$, with two asymmetrically located resonances around this point: two lateral resonances moving away from $eV = 0$, and two central resonances approaching each other toward the point of zero bias voltage. On the other hand, similar behavior is shown by the differential conductance AR. When $t = 0.7$ (see black solid line in Fig. 9 d) or line A2 in Fig. 9 c) ), the double structure of the peaks has almost disappeared, to reappear again, for $t > 0.7$(see red dashed line in Fig. 9 d) or line B2 in Fig. 9 c) ). However, now the resonances in the differential Andreev conductance approximately coincide with

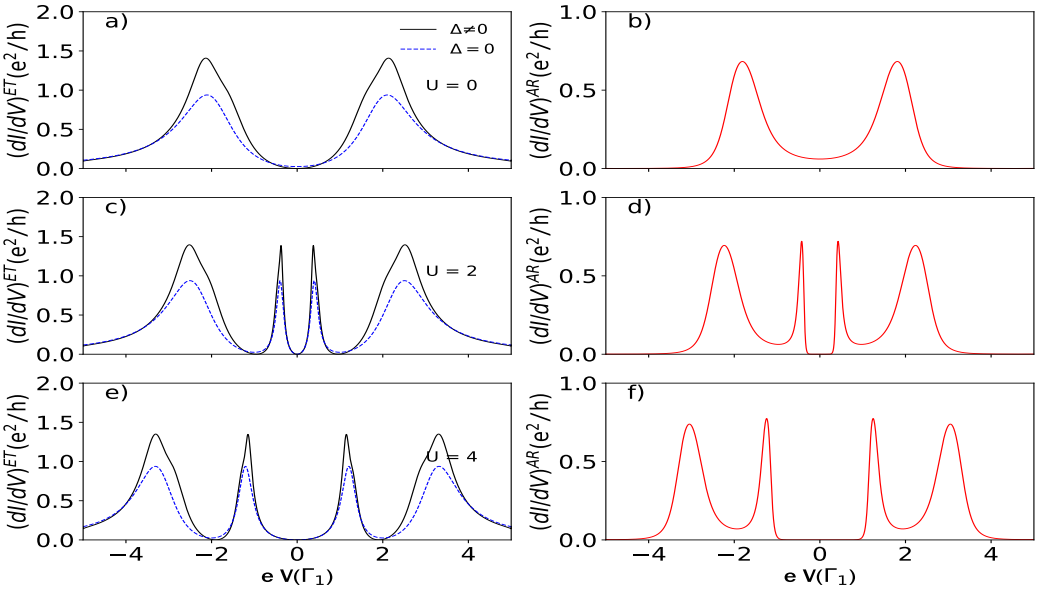


Figure 3.11: In the left panel the differential conductance $(dI/dV)^{ET}$ (black solid line ) as a function of the bias voltage $V$ and in the right panel $(dI/dV)^{DAR}$ (red solid line ) as a function of the bias voltage $V$ when $U = 0$ for a) and b), $U = 2$ for c) and d), and $U = 4$ for e) and f). The blue dashed line on the left panel corresponds to $(dI/dV)^{ET}$ for $\Delta = 0$, that is, for a system with three normal contacts. Other parameters are chosen as $t = 2\Gamma_1$, $\Delta = 5\Gamma_1$, $k_BT = 0\Gamma_1$, $\Gamma_1 = \Gamma_2 = \Gamma_S$, and $\epsilon_a = \epsilon_b = -U/2$.

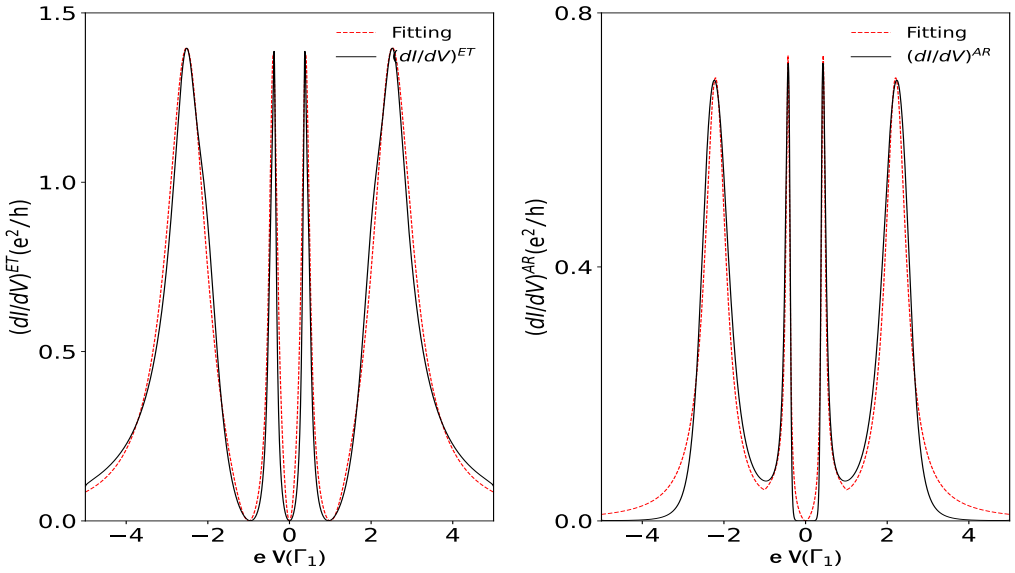


Figure 3.12: a) The differential conductance $(dI/dV)^{ET}$ (black solid line ) and the fitting (red dashed line) as a function of the bias voltage $V$ when $t = 2$. b) The differential conductance $(dI/dV)^{AR}$ (black solid line ) and the fitting (red dashed line) as a function of the bias voltage $V$ when $t = 0.2$. Other parameters are chosen as $\Delta = 5\Gamma_1$ , $k_BT = 0\Gamma_1$, $\Gamma_1 = \Gamma_2 = \Gamma_S$ and $\epsilon_a = \epsilon_b = -U/2$.

those in the differential ET conductance (see line B2 in Fig. 9 c) ).

Now, we study the effect of the coupling ratio, $r$, on the differential conductance ET and AR in the molecular regime ($t \geq \Gamma_1$). Fig. 3.10 shows in the left panel the electron-tunneling differential conductance($(dI/dV)^{ET}$) (black solid line), and in the right panel the Andreev differential conductance ($(dI/dV)$) (red solid line), for different values of rate coupling $r$ when $\Delta = 5$. The blue dashed line in the left panel also corresponds to the $(dI/dV)^{ET}$ for $\Delta = 0$, that is, for a system with three normal contacts. First, we can note that, by changing $r$ from 0.05 to 1, the shape of the differential conductance curve ET does not change significantly when the lead S is in its normal state ($\Delta = 0$) or when it is in its superconducting state ($\Delta \neq 0$). The only noticeable effect on the differential conductance of the presence of lead S in its superconducting state is the decrease in the height of the resonances and the progressive splitting of the lateral peaks. On the other hand, the differential conductance AR presents two resonances on each side of the zero bias voltage, asymmetrically located around $\pm U/2$, which are located approximately around the same bias voltage values as the resonances in the differential conductance ET, and these resonances turn out to be visible even for small values of $r$. However, it is possible to appreciate a remarkable reduction in the height of the AR differential conductance resonances when we are in the molecular regime for the interferometric regime (see Figs. 10 b, d), and f) ).

Fig. 3.11 shows in the left panel the electron-tunneling differential conductance ET (black solid line) and in the right panel the Andreev differential conductance (red solid line), in the molecular regime, for different values of the Coulomb interaction between dots $U$. The blue dashed line in the left panel also corresponds to the $(dI/dV)^{ET}$ for $\Delta = 0$, that is, for a system with three normal contacts. We can see in Fig. 3.11 that when $t = 2$, $U = 0$, in contrast to the interferometric regime, the differential conductance ET and AR have the form of two Lorentzian curves, localized close to $\pm t$ with the center of symmetry located at zero bias voltage, irrespective of whether the lead S is in its normal state ($\Delta = 0$) or its superconducting state ($\Delta \neq 0$), and unlike in the interferometric case, there are no antiresonances present in $(dI/dV)^{ET}$ when ($\Delta \neq 0$). On the other hand, when $U$ is nonzero, whether $\Delta = 0$ or $\Delta \neq 0$, the resonances in $(dI/dV)^{ET}$ and $(dI/dV)^{AR}$ are doubled, and are located approximately around the bias voltage $\epsilon_d$ and $\epsilon_d + U$, by the effect of the Coulomb interaction. The separation between the resonances in the differential conductance ET and AR increases as U increases.

The differential conductance $(dI/dV)^{ET}$ can be represented by combining two Breit-Wigner and two Fano line shapes, in the range $0.7 \leq t \leq 2$ and $r \leq 1$, as shown in Figure 12a.

$$\frac{dI^{ET}}{dV} \approx \frac{\epsilon_1^2}{\epsilon_1^2+1}\left(\frac{1}{\omega_1^2+1}+\frac{1}{\omega_2^2+1}\right)\frac{\epsilon_2^2}{\epsilon_2^2+1} \tag{3.31}$$

where $\omega_1 = ||V| - \gamma_1|/\eta_1$, $\omega_2 = (||V| - \gamma_2|)/\eta_2$, $\epsilon_1 = ||V| - U/2|/(\Gamma_1/2)$, $\epsilon_2 = |V|/\Gamma_1$. Where $\gamma_i = (-\epsilon_d \mp t/2 - U/2 + (1/2)\sqrt{t^2+U^2})$ with $i = 1, 2$ ( in the molecular limit $((t/\Gamma_{L1}) > 1)$ and at the electron-hole symmetry point) and on the other hand,$\eta_1$ and $\eta_2$ are fitting parameters. Note that from the above expression the differential conductance vanishes at $V = \pm U/2$ and $V = 0$. The $q$-parameter in molecular regimes is real, unlike in interferometric regimes. Also, the differential conductance shows resonances at $V \approx$

$\pm\gamma_1$ and $V \approx \pm(\gamma_2)$. Furthermore, it is interesting to note that by making a Taylor approximation concerning $t/U$, the values of $\gamma_1$ and $\gamma_2$ become $\gamma_1 = U^2/(4t)$ and $\gamma_2 = t+U^2/(4t)$, respectively. That is, when $t >> U$ the central peaks tend to approach $V = 0$, and the lateral peaks tend to lie at $V = t$.

In addition, the equation for $(dI/dV)^{AR}$ may be written as the superposition of two Breit-Wigner and one Fano line shapes. [Fig. 3.12(b)]:

$$\frac{dI^{AR}}{dV} \approx \frac{\xi^2}{\xi^2+1}\left(\frac{1}{\nu_1^2+1} + \frac{1}{\nu_2^2+1}\right) \tag{3.32}$$

where $\nu_1 = ||V| - \gamma_1|/(\bar{\xi_1})$ , $\nu_2 = (||V| - \gamma_2|)/(\bar{\xi_2})$, and $\xi = |V|/(\bar{\xi_3})$. Here, as before,$\gamma_i = (-\epsilon_d \mp t/2 - U/2 + (1/2)\sqrt{t^2+U^2})$ with $i = 1, 2$ ( in the molecular limit $((t/\Gamma_{L1}) > 1)$ and at the electron-hole symmetry point) and on other hand,$\bar{\xi_1}$,$\bar{\xi_2}$ and $\bar{\xi_3}$ are fitting parameters.

The fitting presented above offers a reasonable understanding of the shape of the Andreev differential conductance shown in Figure 11. The Andreev states undergo a split caused by $t$ and as a result of this tunneling coupling, the Andreev bound states acquire widths that manifest themselves in the Andreev differential conductance.

# 4

# Thermoelectric transport properties of a T-shaped double quantum dot system in the Coulomb blockade regime

## Introduction

The need to manufacture thermoelectric devices that convert heat into electricity (and vice versa) with high thermoelectric efficiency, based on thermoelectric phenomena such as Seebeck and Peltier effects, has pushed the search for materials with new properties. The usual way to measure efficiency is through the merit figure ($Z$), which is defined as $Z = S^2GT/(\kappa)$, where S, G, T, $\kappa$ are the Seebeck coefficient, electronic conductance, absolute temperature, and thermal conductance (which is equal to the sum of electron thermal conductance ($\kappa_e$) and phonon thermal conductance $\kappa_p$). For technological applications, it is required that the value of Z be as large as possible, and therefore it is clear that if you want to increase the value of Z, you must increase the Seebeck coefficient and the electrical conductance, and reduce both the thermal conductance. Additionally, the thermal and electronic conductances for most bulk materials at very low or room temperature obey Wiedemann–Franz law [86] $\kappa/GT = L_0$, where $L_0$ is a constant known as Lorentz number given by $L_0 = k_B^2\pi^3/3e^2$ with $k_B$ the Boltzmann constant and e the electron charge. Consequently, an increase in electrical conductance will cause an increase in thermal conductance. In turn, due to Mott's law [87] ($S \sim T\partial lnG/\partial E$ an increase in the electronic conductance will cause a decrease in the Seebeck coefficient. Consequently, in conventional solids, the merit figure rarely exceeds the value 1 $ZT \leq 1$. This difficulty of bulk materials can be overcome in mesoscopic systems (such as a QD) as suggested by Hicks and Dresselhaus [88, 89]. Due to its low dimensionality, the physics properties of these systems are strongly affected by quantum confinement (level quantization) as well as by Coulomb blockade effects, which can lead to violation of the Wiedemann-Franz law and failure of the Mott relation [90–96]. Moreover, in these low dimensional systems, the thermal conductance is rather small [97] due to the increase of the phonon scattering which allows according to the Wiedemann–Franz law to reach high values of ZT. On the

other hand, Mahan and Sofo [98] show that the sharp features of the electronic density of states ( $\delta$-like DOS) resulting from the quantum size effect can improve the thermoelectric efficiency, i.e., maximization of ZT. For this reason, quantum dots (QD) systems are promising candidates for high-efficiency thermoelectric devices. Consequently, many experimental and theoretical groups have devoted themselves to the thermoelectric properties of QD systems, as a result, some interesting phenomena were reported [99–106].

On the other hand, some researchers, in recent years, have focused their attention on the thermoelectric phenomena in a QD system modulated by Fano and Kondo effects. Specifically, single quantum dot systems are subject to the Kondo effect when the spin of the electron on the localized levels of the quantum dot is screened by the conduction electrons in the normal lead below a characteristic temperature (the Kondo temperature). Also, electron transport in single quantum dot systems is characterized by Fano-like resonances attributed to the interference between the quantum amplitudes for the two possible electron channels in the system: a direct conduction pathway through the leads and an indirect conduction pathway that involves the localized levels in the quantum dot. These two phenomena are characterized by the peaked configuration of the DOS or electrical conductance.

Electric transport through multiple-quantum dots coupled to normal and superconducting leads has already been widely studied [107–125]. These studies have confirmed that the thermoelectric properties of hybrid QD systems coupled with one conventional lead (metallic or ferromagnetic lead) and one superconducting lead are remarkably better than those coupled with two conventional leads [123,126–129]. It has been found that the thermoelectric efficiency of the former can even reach several times or even tens of times of the latter by comprehensively regulating the superconducting gap, interdot coupling, and asymmetric parameters, which can also be additionally enhanced by the interference effect and intradot Coulomb interaction. This is mainly attributed to unique tunneling mechanisms and a high density of state distributions near the edges of the superconducting gap. The Andreev tunneling of Cooper pairs is allowed only inside the superconducting gap, while the tunneling of single electrons is allowed outside the superconducting gap, both of which have a significant impact on the thermoelectric properties. The very high density of states near superconducting gap edges changes rapidly with energy, which is mainly responsible for the high thermopower and low thermal conductivity near superconducting gap edges.

In particular, in this work, we study the subgap thermoelectric properties, such as conductance and Seebeck coefficient, and the influence exerted on these properties by the different parameters that define this system, such as intradot correlation (U), interdot tunneling (t) between the central and lateral QD, rate of coupling with the superconductor lead and the temperature. Because the usual definition of the Seebeck coefficient for two leads, is not directly applicable to the multiterminal system due to other currents flowing in adjacent branches, we use definitions of the local and nonlocal Seebeck coefficients valid for the three-terminal normal and hybrid device given by G. Michałek et al [130]. In particular, we are interested in the influence of the superconducting electrode on the subgap thermoelectric properties of this system, because the superconducting electrode is responsible for strong nonlocal effects, and it may also cause the negative conductance resulting from a competition between the crossed Andreev reflections and the direct electron

tunneling involving normal electrodes.

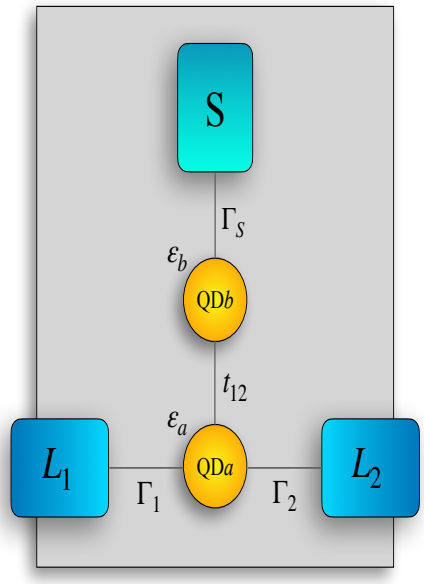


Figure 4.1: The T-shape double QD system studied in this work. It is composed of two quantum dots in which the $QD_a$ is coupled to two normal metals $L_1$ and $L_2$, with the coupling strength being determined by the parameters $\Gamma_1$ and $\Gamma_2$. The second quantum dot, $QD_b$ is coupled to the superconductor $S$, with the coupling strength being modeled by the parameter $\Gamma_S$. The coupling between the QDs is modeled by the $t_{12}$ parameter.

## 4.1 Model and Formulation

In Fig. 4.1, the T-shape double quantum-dot system is illustrated. It consists of a central quantum dot, $QD_a$, coupled to the two normal leads, $L_1$ and $L_2$, and a side $QD_b$, connected to a superconductor $S$. The Hamiltonian of the system is given by:

$$H = H_1 + H_2 + H_S + H_{DQD} + H_T. \tag{4.1}$$

The first and the second terms are the Hamiltonians for the normal leads at the left (1) and right (2) sides of $QD_a$. These are modeled by Eqs. (4.2) and (4.3):

$$H_1 = \sum_k \sum_\sigma \epsilon_{1k\sigma} c^\dagger_{1k\sigma} c_{1k\sigma}, \tag{4.2}$$

and

$$H_2 = \sum_k \sum_\sigma \epsilon_{2k\sigma} c^\dagger_{2k\sigma} c_{2k\sigma}, \tag{4.3}$$

where $c^{\dagger}_{\alpha k\sigma}$ ($c_{\alpha k\sigma}$) is the electron creation (annihilation) operator of an electron with spin $\sigma$ and energy $\epsilon_{k\sigma}$ in the $\alpha$ electrode.

The second term stands for the BCS Hamiltonian [41] of the superconducting ($S$) lead and reads:

$$H_S = \sum_k \sum_\sigma \epsilon_{kS} c^{\dagger}_{kS\sigma} c_{kS\sigma} + \sum_k (\Delta^* c_{kS\downarrow} c_{-kS\uparrow} + \Delta c^{\dagger}_{-kS\uparrow} c^{\dagger}_{kS\downarrow}), \tag{4.4}$$

where $c^{\dagger}_{kS\sigma}$ ($c_{kS\sigma}$) is the electron creation (annihilation) operator of an electron with spin $\sigma$ and energy $\epsilon_{kS}$ in the superconducting electrode, and $\Delta$ denotes pair potential, whose absolute value gives the superconducting energy gap.

The $H_{DQD}$ term is given by Eq. (4.5), and takes into account the coupling between the QDs, modeled by the variable $t_{12} = t$, and the Coulomb interaction at each QD, whose strength is modeled by $U_m$, $m = a, b$. The QDs are assumed to have a single spin degenerated level, whose value is determined by $\epsilon_{dm,\sigma}$, $m = a, b$.

$$\begin{aligned} H_{DQD} = & \sum_{m=a,b,\sigma} \epsilon_{dm,\sigma} d^{\dagger}_{m,\sigma} d_{m,\sigma} \\ & + \sum_\sigma t \left[ d^{\dagger}_{a\sigma} d_{b\sigma} + d^{\dagger}_{a\sigma} d_{b\sigma} \right] \\ & + \sum_{m=a,b} U_m n_{m\sigma} n_{m\bar{\sigma}} \end{aligned} \tag{4.5}$$

### 4.1.1 Green's functions

To obtain the transport properties for the system modeled by Eq. (4.1), we have used the well-known non-equilibrium Green's function approach [83,84] along with the equation-of-motion method. This formalism has been extensively applied to nanostructured systems. The presence of the superconductor has been taken into account by expressing Green's functions within the Nambu space. In this way, Green's functions are represented by $4 \times 4$ matrices resulting from the tensor product between spin and electron-hole subspaces. By using this formalism, we have obtained a system of coupled Dyson equations for the retarded Green's functions matrices $\mathbf{G}^r_{aa}$ and $\mathbf{G}^r_{bb}$, for $QD_a$ and $QD_b$, respectively:

$$\mathbf{G}^r_{aa} = \mathbf{G}^{ro}_{aa} + \mathbf{G}^r_{aa} \mathbf{t}^{\dagger}_{ab} \mathbf{G}^{ro}_{bb} \mathbf{t}_{ab} \mathbf{G}^{ro}_{aa}, \tag{4.6}$$

and

$$\mathbf{G}^r_{bb} = \mathbf{G}^{ro}_{bb} + \mathbf{G}^r_{bb} \mathbf{t}^{\dagger}_{ab} \mathbf{G}^{ro}_{aa} \mathbf{t}_{ab} \mathbf{G}^{ro}_{aa}, \tag{4.7}$$

with

$$\mathbf{G}^{ro}_{aa} = \mathbf{g}^r_{aa} (1 - \mathbf{\Sigma}^r_L \mathbf{g}^r_{aa})^{-1}, \tag{4.8}$$

and

$$\mathbf{G}^{ro}_{bb} = \mathbf{g}^r_{bb} (1 - \mathbf{\Sigma}^r_S \mathbf{g}^r_{bb})^{-1}. \tag{4.9}$$

In Eqs. (4.6) to (4.9), $\mathbf{g}^r_{aa}$ and $\mathbf{g}^r_{bb}$ are the $QD_a$ and $QD_b$ Green's functions, respectively, when the QDs are isolated from the leads; $\mathbf{t}_{ab}$ describes the tunneling between

$QD_a$ and $QD_b$. The coupling to the normal and superconducting leads are modeled by retarded/advanced self-energies $\mathbf{\Sigma}_L^r = \mathbf{\Sigma}_1^r + \mathbf{\Sigma}_2^r$ and $\mathbf{\Sigma}_S^r$, respectively.

The self-energy for the coupling to the normal leads ($L_1$ and $L_2$) is given by Eq. (4.10):

$$\mathbf{\Sigma}_L^{r,a} = \mp\frac{i}{2}(\Gamma_1 + \Gamma_2)\begin{bmatrix}1 & 0 & 0 & 0\\ 0 & 1 & 0 & 0\\ 0 & 0 & 1 & 0\\ 0 & 0 & 0 & 1\end{bmatrix}, \tag{4.10}$$

where $\Gamma_i = \Gamma_{i\uparrow} + \Gamma_{i\downarrow}$ and $\Gamma_{i\sigma} = 2\pi|t_i|^2 N_i$, $(i = 1, 2)$ being the coupling strength, with $t_i$ being amplitude for an electron with spin $\sigma$ of $QD_a$ to be transferred to the lead $L_i$; $N_i$ is the density of states at Fermi level for the normal lead, $L_i$. Since we have assumed both normal leads as non-magnetic, the density of states is the same for both spins.

The retarded/advanced self-energy of the superconductor is given by Eq. (4.11):

$$\mathbf{\Sigma}_S^{r,a} = \mp\frac{i}{2}\rho_S(\epsilon)\Gamma_S\begin{bmatrix}1 & -\dfrac{\Delta}{\epsilon} & 0 & 0\\ -\dfrac{\Delta}{\epsilon} & 1 & 0 & 0\\ 0 & 0 & 1 & \dfrac{\Delta}{\epsilon}\\ 0 & 0 & \dfrac{\Delta}{\epsilon} & 1\end{bmatrix}. \tag{4.11}$$

In Eq. (4.11), $\Gamma_S = 2\pi|t_s|^2 N_s$ is the coupling strength between the superconductor lead and $QD_b$, defined in terms of the amplitude of tunneling $|t_s|$ and the normal density of states of $N_s$. The $\Delta$ appearing in some of the matrix elements stands for the energy gap of the superconductor and accounts for the electron-hole coupling. The energy gap plays a central role in this model and also modifies the self-energy through $\rho_S$, the dimensionless modified BCS density of states, whose expression is given by:

$$\rho_S(\epsilon) = \frac{|\epsilon|\theta(|\epsilon| - \Delta)}{\sqrt{\epsilon^2 - \Delta^2}} - i\frac{\epsilon\theta(\Delta - |\epsilon|)}{\sqrt{\Delta^2 - \epsilon^2}}, \tag{4.12}$$

with the imaginary part accounting for the Andreev bound states (ABS), within the superconductor gap.

The presence of electronic correlations associates the QDs energy levels with the electronic occupations, which, in turn, depend on external parameters like gate and bias voltages. As a result, Eqs. (4.6) and (4.7) must be solved in a self-consistent way, together with the occupations of the QDs. Such occupations are obtained from the diagonal matrix elements of the "lesser" Green's function matrix, which is obtained through the Keldysh equation. For the $QD_a$, the expression reads:

$$\mathbf{G}_{aa}^{<} = \mathbf{G}_{aa}^{r}(\omega)\mathbf{\Sigma}_{Ta}^{<}\mathbf{G}_{aa}^{a}(\omega), \tag{4.13}$$

with

$$\mathbf{\Sigma}_{Ta}^{<} = \mathbf{\Sigma}_L^{<}(\epsilon) + \mathbf{t}_{ab}^{\dagger}\mathbf{G}_{bb}^{ro}\mathbf{\Sigma}_S^{<}(\epsilon)\mathbf{G}_{bb}^{ao}\mathbf{t}_{ab}. \tag{4.14}$$

The expression for $QD_b$ can be obtained by exchanging the indices $a$ and $b$. In Eq. (4.13), $\mathbf{\Sigma}_{Ta}^{<}$ represents the "lesser" self-energy, which is expressed in terms of the self-energies of the leads: $\mathbf{\Sigma}_L^{<} = \mathbf{\Sigma}_1^{<} + \mathbf{\Sigma}_2^{<}$ and $\mathbf{\Sigma}_S^{<}$. Assuming that the leads are in equilibrium

with well-defined chemical potential and temperature, the self-energies of the leads can be obtained using the fluctuation-dissipation theorem: $\mathbf{\Sigma}_i^< = \mathbf{F}_i\,[\mathbf{\Sigma}_i^a - \mathbf{\Sigma}_i^r]$, where the Fermi matrix $\mathbf{F}_i$ is given by

$$\mathbf{F}_i = i \begin{bmatrix} f_i & 0 & 0 & 0 \\ 0 & \bar{f}_i & 0 & 0 \\ 0 & 0 & f_i & 0 \\ 0 & 0 & 0 & \bar{f}_i \end{bmatrix}, \tag{4.15}$$

with $f_i = f(\epsilon - eV_i)$ and $\bar{f}_i = f(\epsilon + eV_i)$ $(i = 1, 2, S)$ being the Fermi functions for electrons and holes, respectively. Since the superconductor is assumed to be grounded, $f_i = f(\epsilon)$ for $i = s$.

### 4.1.2 Transmittance and current

The presence of Coulomb correlations leads to a self-consistent problem when solving equations (4.6) and (4.7), since the dependency on the occupations wraps the Green's functions to the occupancies of the QDs. Within the equation-of-motion approach used in this work, this results in an infinite set of equations with Green's functions of increasing order of complexity. To obtain a closed set of equations, one needs to resort to some approximation on the Coulomb correlations. In this work, we have used the so-called Hubbard-I approximation [85], which allows us to derive a simple expression for the electrical current in terms of the different transmission amplitudes that contribute to the electronic transport for this system. In fact, the current $I_j$, flowing in the lead $L_j$ $(j = 1, 2)$, is given by the following expression:

$$I_j = \frac{e}{\hbar} \int d\epsilon\, [\mathbf{G}^r_{aa}(\epsilon)\mathbf{\Sigma}^<_j(\epsilon) + \mathbf{G}^<_{aa}(\epsilon)\mathbf{\Sigma}^a_j(\epsilon) + \text{H.c.}]_{(11+33)}, \qquad j = 1, 2. \tag{4.16}$$

where $11 + 33$ stands for the sum of the 11 and 33 matrix elements of the current matrix. By substituting the Green's functions and self-energies into Eq. (4.16), one obtains the main expression for the electric current, written in terms of the transmittances:

$$I_1 = \frac{e}{h} \int [T_{11}^{DAR}(f_1 - \bar{f}_1) + T_{12}^{ET}(f_1 - f_2) + T_{12}^{CAR}(f_1 - \bar{f}_2) + T_{1S}^{QP}(f_1 - f_S)]d\epsilon, \tag{4.17}$$

for the current flowing in lead $L_1$, and

$$I_2 = \frac{e}{h} \int [T_{22}^{DAR}(f_2 - \bar{f}_2) + T_{21}^{ET}(f_2 - f_1) + T_{21}^{CAR}(f_2 - \bar{f}_1) + T_{2S}^{QP}(f_2 - f_S)]d\epsilon, \tag{4.18}$$

for the current flowing in $L_2$.

The first terms appearing in Eqs. (4.17) and (4.18), $T_{11}^{DAR}$ and $T_{22}^{DAR}$, correspond to direct Andreev reflection transmittances through the paths $(L_1 - QD_a - S)$ and $(L_2 - QD_a - S)$, respectively. The second terms $T_{12}^{ET}$ and $T_{21}^{ET}$ are due to electron tunneling (ET) between the normal leads, i.e., through the path $(L_1 - QD_a - L_2)$ and $(L_1 - QD_a - L_2 S)$, respectively. Notice that these fluxes cancel each other when performing the sum of the currents $I = I_1 + I_2$, which is the current entering into the superconductor. The next two terms, $T_{11}^{CAR}$ and $T_{22}^{CAR}$, account for the crossed Andreev reflection transmittances through $((L_1, L_2) - QD_a - S)$ and $((L_2, L_1) - QD_a - S)$ paths, respectively. Finally, the last terms, $T_{11}^{QP}$ and $T_{22}^{QP}$, correspond to the quasiparticles tunneling through $(L_1 - QD_a - S)$ and $(L_2 - QD_a - S)$ paths, respectively.

The expressions of the amplitudes in terms of Green's functions are given by:

$$
\begin{aligned}
T_{11}^{DAR} &= \Gamma_1^2(|G^r_{aa,14}|^2 + |G^r_{aa,12}|^2 + |G^r_{aa,34}|^2 + |G^r_{aa,32}|^2) \\
T_{12}^{CAR} &= \Gamma_1\Gamma_2(|G^r_{aa,14}|^2 + |G^r_{aa,12}|^2 + |G^r_{aa,34}|^2 + |G^r_{aa,32}|^2) \\
T_{12}^{ET} &= \Gamma_1\Gamma_2(|G^r_{aa,33}|^2 + |G^r_{aa,31}|^2 + |G^r_{aa,13}|^2 + |G^r_{aa,11}|^2) \\
T_{1S}^{QP} &= \bar{\rho}\Gamma_1\Gamma_S\{Y_{21}^-|G^r_{aa,12}|^2 + X_{34}^+|G^r_{aa,13}|^2 + Y_{43}^+|G^r_{aa,14}|^2 \\
&\quad + X_{12}^-|G^r_{aa,11}|^2 - Z_{34}^+G^r_{aa,13}[G^r_{aa,14}]^* - [Z_{34}^+]^*[G^r_{aa,13}]^*G^r_{aa,14} \\
&\quad - Z_{12}^-G^r_{aa,11}[G^r_{aa,12}]^* - [Z_{12}^-]^*[G^r_{aa,11}]^*G^r_{aa,12} \\
&\quad + Y_{21}^-|G^r_{aa,32}|^2 + X_{34}^+|G^r_{aa,33}|^2 + Y_{43}^+|G^r_{aa,34}|^2 \\
&\quad + X_{32}^-|G^r_{aa,31}|^2 - Z_{34}^+G^r_{aa,33}[G^r_{aa,34}]^* \\
&\quad - [Z_{34}^+]^*[G^r_{aa,33}]^*G^r_{aa,34} - Z_{12}^-G^r_{aa,31}[G^r_{aa,32}]^* \\
&\quad - [Z_{12}^-]^*[G^r_{aa,31}]^*G^r_{aa,32}\} \\
T_{22}^{DAR} &= \Gamma_2^2(|G^r_{aa,14}|^2 + |G^r_{aa,12}|^2 + |G^r_{aa,34}|^2 + |G^r_{aa,32}|^2) \\
T_{21}^{CAR} &= \Gamma_1\Gamma_2(|G^r_{aa,14}|^2 + |G^r_{aa,12}|^2 + |G^r_{aa,34}|^2 + |G^r_{aa,32}|^2) \\
T_{21}^{ET} &= \Gamma_1\Gamma_2(|G^r_{aa,33}|^2 + |G^r_{aa,31}|^2 + |G^r_{aa,13}|^2 + |G^r_{aa,11}|^2) \\
T_{2S}^{QP} &= \bar{\rho}\Gamma_2\Gamma_S\{Y_{21}^-|G^r_{aa,12}|^2 + X_{34}^+|G^r_{aa,13}|^2 + Y_{43}^+|G^r_{aa,14}|^2 \\
&\quad + X_{12}^-|G^r_{aa,11}|^2 - Z_{34}^+G^r_{aa,13}[G^r_{aa,14}]^* - [Z_{34}^+]^*[G^r_{aa,13}]^*G^r_{aa,14} \\
&\quad - Z_{12}^-G^r_{aa,11}[G^r_{aa,12}]^* - [Z_{12}^-]^*[G^r_{aa,11}]^*G^r_{aa,12} \\
&\quad + Y_{21}^-|G^r_{aa,32}|^2 + X_{34}^+|G^r_{aa,33}|^2 + Y_{43}^+|G^r_{aa,34}|^2 \\
&\quad + X_{32}^-|G^r_{aa,31}|^2 - Z_{34}^+G^r_{aa,33}[G^r_{aa,34}]^* \\
&\quad - [Z_{34}^+]^*[G^r_{aa,33}]^*G^r_{aa,34} - Z_{12}^-G^r_{aa,31}[G^r_{aa,32}]^* \\
&\quad - [Z_{12}^-]^*[G^r_{aa,31}]^*G^r_{aa,32}\}
\end{aligned}
\tag{4.19}
$$

where

$$
\begin{aligned}
X_{ij}^{\pm} &\equiv t^2[|G^{ro}_{bb,ii}|^2 + |G^{ro}_{bb,ij}|^2 \pm \frac{\Delta}{\epsilon}(G^{ro}_{bb,ii}[G^{ro}_{bb,ij}]^* + G^{ro}_{bb,ij}[G^{ro}_{bb,ii}]^*), \\
Y_{ij}^{\pm} &\equiv t^2[|G^{ro}_{bb,ii}|^2 + |G^{ro}_{bb,ji}|^2 \pm \frac{\Delta}{\epsilon}(G^{ro}_{bb,ii}[G^{ro}_{bb,ji}]^* + G^{ro}_{bb,ij}[G^{ro}_{bb,ii}]^*), \\
Z_{ij}^{\pm} &\equiv t^2[G^{ro}_{bb,ij}[G^{ro}_{bb,jj}]^* + [G^{ro}_{bb,ij}]^*G^{ro}_{bb,ii} \\
&\qquad \pm \frac{\Delta}{\epsilon}(|G^{ro}_{bb,ij}|^2 + [G^{ro}_{bb,jj}]^*G^{ro}_{bb,ii})].
\end{aligned}
\tag{4.20}
$$

### 4.1.3 Self-consistent calculations

Regarding the occupations of QDs, they are determined by the "lesser" Green's function. In the case of normal leads with no polarization, the average occupation number remains independent of spin. This allows us to set, for each QD, $\langle n_{i,\sigma}\rangle = \langle n_i\rangle$ where $i = a, b$. These occupation numbers are obtained by solving the following self-consistent system of integral equations:

$$\langle n_{a\uparrow}\rangle = -i\int \frac{d\epsilon}{2\pi}\, G^{<}_{aa,11}[\epsilon, \langle n_{a\uparrow}\rangle, \langle n_{a\downarrow}\rangle, \langle n_{b\uparrow}\rangle, \langle n_{b\downarrow}\rangle], \tag{4.21a}$$

$$\langle n_{a\downarrow}\rangle = -i\int \frac{d\epsilon}{2\pi}\, G^{<}_{aa,33}[\epsilon, \langle n_{a\uparrow}\rangle, \langle n_{a\downarrow}\rangle, \langle n_{b\uparrow}\rangle, \langle n_{b\downarrow}\rangle], \tag{4.21b}$$

$$\langle n_{b\uparrow}\rangle = -i\int \frac{d\epsilon}{2\pi}\, G^{<}_{bb,11}[\epsilon, \langle n_{a\uparrow}\rangle, \langle n_{a\downarrow}\rangle, \langle n_{b\uparrow}\rangle, \langle n_{b\downarrow}\rangle], \tag{4.21c}$$

$$\langle n_{b\downarrow}\rangle = -i\int \frac{d\epsilon}{2\pi}\, G^{<}_{bb,33}[\epsilon, \langle n_{a\uparrow}\rangle, \langle n_{a\downarrow}\rangle, \langle n_{b\uparrow}\rangle, \langle n_{b\downarrow}\rangle]. \tag{4.21d}$$

## 4.2 Thermoelectric Properties in linear regime

Measurement of voltage $\Delta\mu$ induced by the temperature difference $\Delta T$ gives the Seebeck coefficient. Let us recall that the standard definition of the Seebeck coefficients, in the two- terminal system is the vanishing of the current.

By definition, the thermopower, or Seebeck-coefficient, S is given by the difference in chemical potential $\Delta\mu$ which arises due to a small temperature difference $\Delta T$ under open circuit conditions ($I \to 0$) between two voltage probes, divided by $\Delta T$ :

$$S = -\left.\frac{\Delta\mu}{e\Delta T}\right|_{I=0} \tag{4.22}$$

In multiterminal devices, there exist a large number of various possibilities. In this paper, we will follow the proposal made by G. Michałek et al. [130], that is, we measure open-circuit conditions(imposing $J_i = 0$ for all electrodes). Note that this assumption makes our condition similar to that of Mazza et al. [131].

Once the local and non-local resistances of the hybrid system are determined under isothermal conditions, we can express the local and nonlocal thermopowers as

$$S_{RL} = -\left.\frac{\Delta\mu_{RL}}{e\Delta T_{RL}}\right|_{T_{LS}=0} = R_{RL,RL}(\mathcal{L}^{ET}_{LR,T} + \mathcal{L}^{CAR}_{LR,T}) + \mathcal{L}^{QP}_{RS,T} \tag{4.23}$$

with

$$\mathcal{L}^{\kappa}_{\alpha\beta,\mu} = \frac{2e}{h}\int dE\ \mathcal{T}^{\kappa}(E)\left(-\frac{\partial f_0}{\partial E}\right), \tag{4.24}$$

$$\mathcal{L}^{\kappa}_{\alpha\beta,T} = \frac{2e}{h}\int dE\ \frac{(E-\mu)}{T}\mathcal{T}^{\kappa}(E)\left(-\frac{\partial f_0}{\partial E}\right), \tag{4.25}$$

with $\alpha, \beta = \{L, R, S\}$ and $\kappa = \{QP, ET, CAR, DAR\}$. whereas

$$R_{RL,RL} = \frac{2\mathcal{L}^{CAR}_{LR,\mu} + \mathcal{L}^{DAR}_{LL,\mu} + \mathcal{L}^{DAR}_{RR,\mu} + \frac{1}{2}(\mathcal{L}^{QP}_{LS,\mu} + \mathcal{L}^{QP}_{RS,\mu})}{eD} = \frac{1}{G_{RL}} \tag{4.26}$$

with

$$\begin{aligned} D =& \mathcal{L}^{ET}_{LR,\mu}(\mathcal{L}^{DAR}_{LL,\mu} + 2\mathcal{L}^{CAR}_{LR,\mu} + \mathcal{L}^{DAR}_{RR,\mu}) + \mathcal{L}^{CAR}_{LR,\mu}(\mathcal{L}^{DAR}_{LL,\mu} + \mathcal{L}^{DAR}_{RR,\mu}) + 2\mathcal{L}^{DAR}_{LL,\mu}\mathcal{L}^{DAR}_{RR,\mu} \\ &+ \frac{1}{2}(\mathcal{L}^{QP}_{LS,\mu} + \mathcal{L}^{QP}_{RS,\mu})(\mathcal{L}^{ET}_{LR,\mu} + \mathcal{L}^{CAR}_{LR,\mu}) \\ &+ (\mathcal{L}^{DAR}_{LL,\mu}\mathcal{L}^{QP}_{RS,\mu} + \mathcal{L}^{DAR}_{RR,\mu}\mathcal{L}^{QP}_{LS,\mu}) \\ &+ \frac{1}{2}\mathcal{L}^{QP}_{LS,\mu}\mathcal{L}^{QP}_{RS,\mu} \end{aligned} \tag{4.27}$$

in the subgap regime, it can be shown that the equations for $G_{RL,RL}$ and $S_{RL}$ are given by:

$$G_{RL,RL} = \frac{1}{R_{RL,RL}} = e(\mathcal{L}^{ET}_{LR,\mu} + \mathcal{L}^{CAR}_{LR,\mu}) \tag{4.28}$$

$$S_{RL} = R_{RL,RL}(\mathcal{L}^{ET}_{LR,T} + \mathcal{L}^{CAR}_{LR,T}) \tag{4.29}$$

## 4.3 Results and Discussion

### 4.3.1 Effect of superconducting energy gap $\Delta$

The corresponding Thermopower as a function of QD level $\epsilon_d$ is plotted in Fig. 4.2. When $t \neq 0$ the electrical conductance $G_{RL}$, as shown in Fig. 4.2(a), exhibits two sharp side peaks in $\epsilon_d \approx -t - U + \delta(\Sigma^r)$ and $\epsilon_d \approx t + \delta(\Sigma^r)$ where $\delta(\Sigma^r)$is a small self-energy correction that is due to the coupling between the QDs and electrodes, while the central peak appears in the middle between them at $\epsilon_d = -U/2$ (which coincides with one of the zeros of $S$ ). which become two peaks as the value of U increases. Separation of the side peaks is approximately equal to $2t$. However, the height of the side peaks of the conductance $G_{RL}$ increases as the energy gap of the superconductor increases. In turn, the height of the central peak at $\epsilon_d = -U/2$ decreases with increasing $\Delta$ while the value of $S_{RL}$ remains equal to zero. The explanation of this behavior for the central peaks can be obtained from Fig.4.3 which shows the plots of the different transmissions as a function of $\epsilon$ for the value of $\epsilon_d = -U/2$ in the case where $\Delta = 0$ and in the case where $\Delta = 1$. As can be seen in Fig. 4.3(a), in the case where $\Delta$ is zero, there is an important contribution made by the transmission $T_{RS}^{ET}$ to the integral $L_{RS,\mu}^{ET}$ present in the equation for $G_{RL}$ when the energy is close to zero and $\epsilon_d = -U/2$ (see Eq. (5.28). On the other hand, when the delta is nonzero, an energy gap is opened in which transmission $T_{RS}^{QP}$ is forbidden and only $T_{RL}^{ET}$ contributes to the value of $G_{RL}$ near zero energy so that its value is smaller than when $\Delta = 0$ (see Fig.4.3). However, when $\epsilon_d = -U/2$ the symmetric distribution of $T_{RL}^{ET}$ and $T_{RL}^{CAR}$ around zero causes the integrals $L_{RL,T}^{ET}$ and $L_{RL,T}^{CAR}$ to become identically zero in both cases( because the integrand is the product of an even function by $\epsilon df/d\epsilon$), which explains the zero value of the thermopower for $\epsilon_d = -U/2$ when $\Delta = 0$ or $\Delta \neq 0$. The thermopower $S_{RL}$ as a function of $\epsilon_d$ for different values of $\Delta$ is shown in Fig. 4.2(b). The two zeros of $S_{LR}$ coincide with the side maxima of $G_{RL}$ (resonances). Furthermore, the maximum value of $|S_{RL}|$ is reached on both sides of $\epsilon_d = -U/2$ ( near $\epsilon_d = 0$ or $\epsilon_d = -U$ when $G_{RL}$ is close to its minimum value (see Fig. 4.3 (b). Furthermore, $S_{RL}$ increases rapidly when the superconductor energy gap increases and reaches its maximum value when the delta is close to $\Delta = 1\Gamma_L$. The explanation for this behavior is based on the fact that when $\Delta = 1\Gamma_L$ the conductance $G_{RL}$ is reduced to zero at $\epsilon_d = 0$ or $-U$ and $L_{RL,T}^{ET}$ decreases more smoothly than when $\Delta = 0$ for these values of $\epsilon_d$, which explains the significant increase in $S_{RL}$ when $\Delta = 1$.

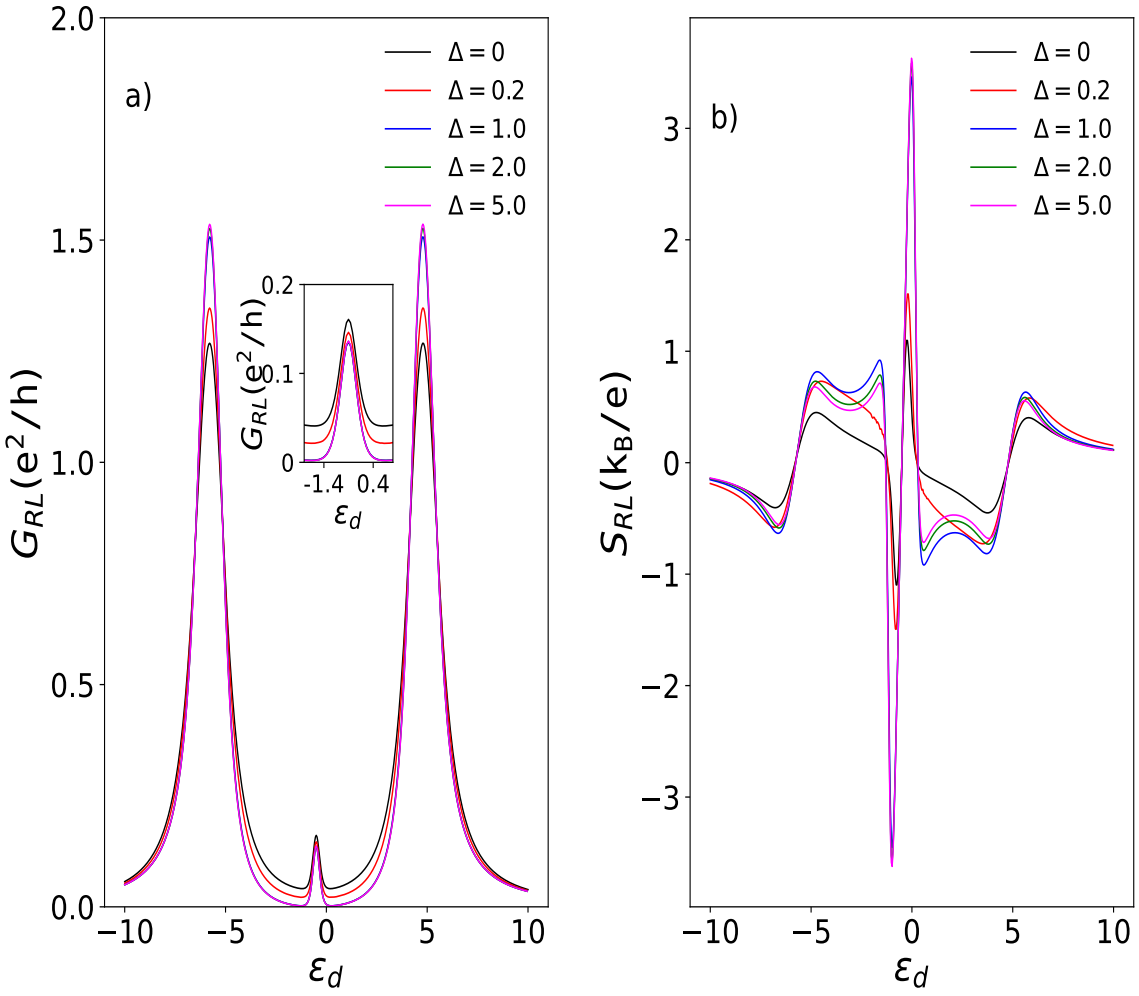


Figure 4.2: The electronic conductance $G_{RL}$ (a) and the Seebeck coefficient $S_{RL}$ (b) in units $k_B/e$ as a function of the QD level position $\epsilon_d$ for differents values of the superconducting energy gap $\Delta$. Other parameters are chosen as $\Gamma_L = \Gamma_R = \Gamma_S$ , $t = 2\Gamma_L$, $K_BT = 0.1\Gamma_L$,and $U = 1\Gamma_L$.

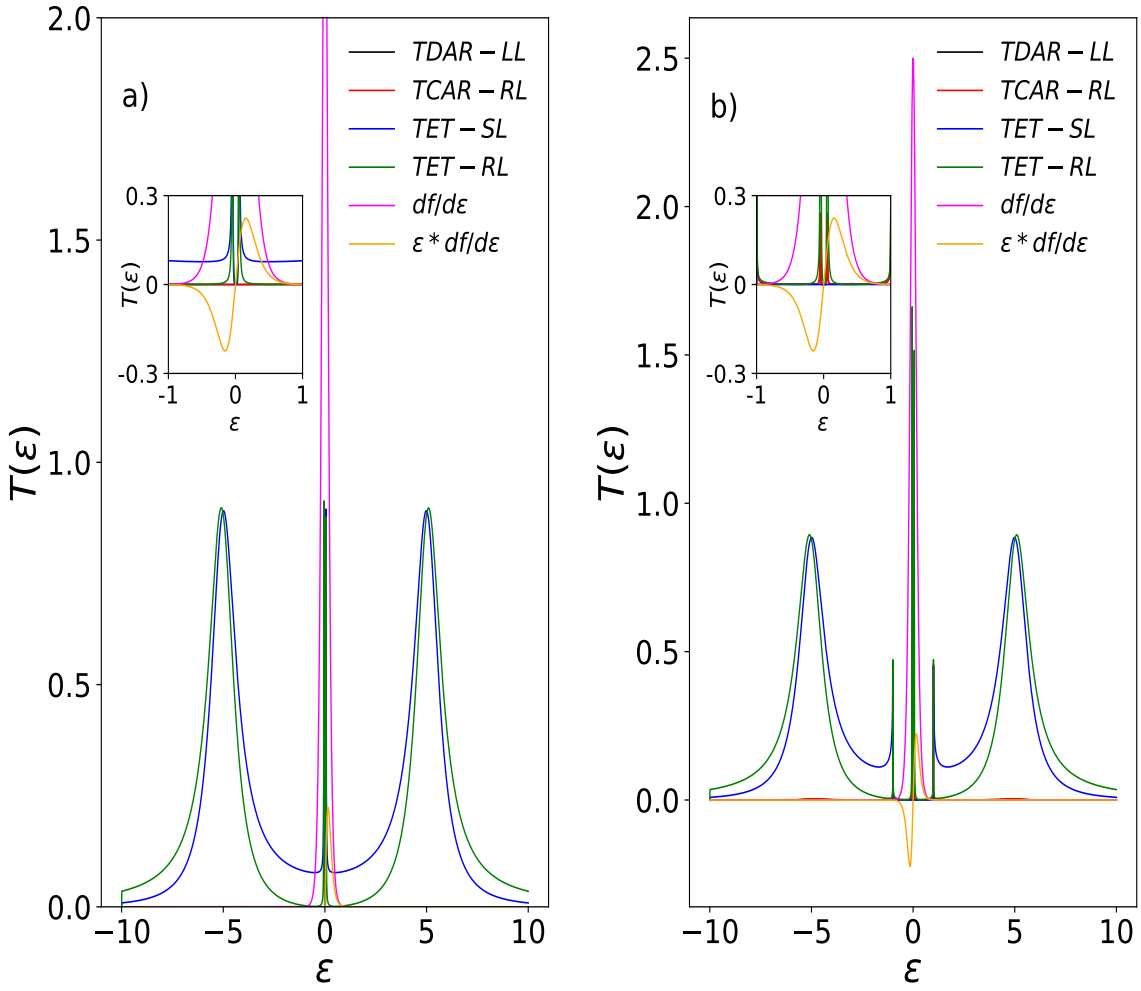


Figure 4.3: The transmittance $T_{LR}^{ET}$ and other thermolectric parameters as function of the energy $\epsilon$, when $\Delta = 0$ (a) or $\Delta = 1$(b). Other parameters are chosen as $\epsilon_d = -U/2$, $t = 5$, $U = 1\Gamma_L$, $k_BT = 0.1\Gamma_L$ and $\Gamma_L = \Gamma_R = \Gamma_S$.

### Influence of intradot Coulomb interactions

The electronic conductance $G_{RL}$ as a function of $\epsilon_d$ for different values of $U$ is shown in Fig. 4.4 a). We can observe that the Coulomb interaction splits the electronic conductance spectrum into two sets symmetric to the electron-hole symmetry point $\epsilon_d = -U/2$, and their centers are located approximately at $\epsilon_d = 0$ and $\epsilon_d = -U$. The height of the two lateral peaks of the conductance $G_{RL}$ does not change appreciably with the change of $U$. In turn, the height of the two central peaks increases as $U$ increases.

The thermopower $S_{RL}$ as a function of $\epsilon_d$ for different values of $U$ is shown in Fig. 4.4 b). The thermopower is antisymmetric to the thermopower zeros that coincide, as mentioned above, with the electronic conductance peaks, where $S$ has a maximum and a minimum on each side of these. The height of the thermopower peaks $S_{RL}$ does not change appreciably with the change of $U$.

The Coulomb interaction strongly affects the thermopower in a valley between the conductance peaks. In particular, an additional sharp structure appears close to the electron/hole symmetry point $\epsilon_d = -U/2$. This effect is related to the Fano resonance and is a signature of the destructive interference between the activated QD levels. It leads to a reduction of total transmission to zero and, as a consequence, to a reduction of $G_{RL}$ and $L^{ET}_{RL,T}$. Since the reduction of $G_{RL}$ is stronger than $L^{ET}_{RL,T}$, the reduction of $S_{RL}$ is increased.

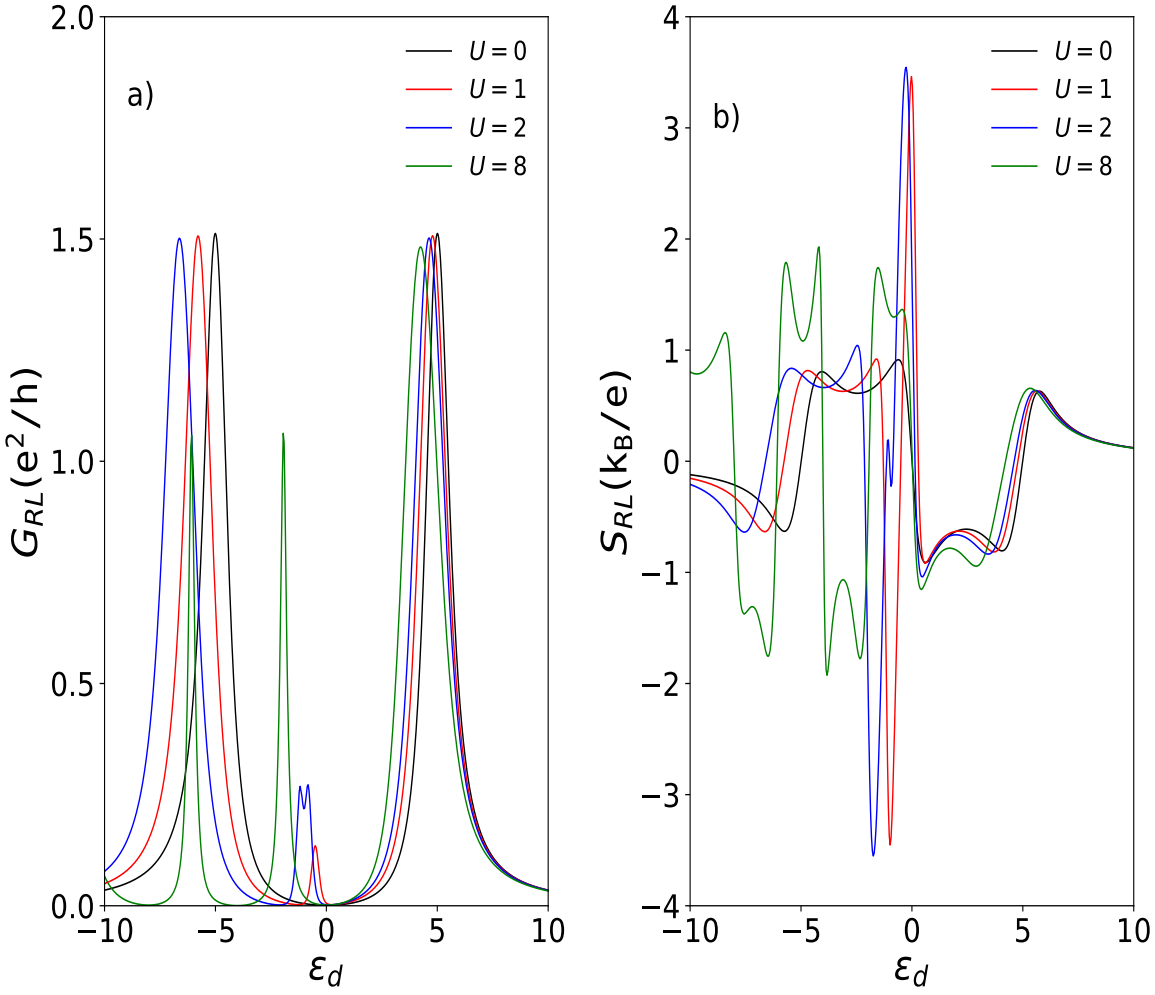


Figure 4.4: The electronic conductance $G_{LR}$ (a) and the Seebeck coefficient $S_{RL}$ (b) in units $k_B/e$ as a function of the QD level position $\epsilon_d$ for differents values of the coulomb interaction $U$ . Other parameters are chosen as $\Delta = 1\Gamma_L$ $\Gamma_L = \Gamma_R = \Gamma_S$ , $t = 2\Gamma_L$, $K_BT = 0.1\Gamma_L$,and $U = 1\Gamma_L$.

**Effect of Temperature**

The corresponding behavior of the electronic conductance $G_{RL}$ and thermopower $S_{RL}$ with temperature and gate voltage is shown in Fig. 4.5. As the temperature increases, the height of the lateral peaks of the electronic conductance $G_{RL}$ decreases while the central peaks gradually disappear. The explanation for this behavior lies in the flattening of the derivative of the fermi function as the temperature increases which reduces the contribution of $T_{RL}^{ET}$ to the integral $L_{LR,\mu}^{ET}$, and consequently reduces the electronic conductance $G_{RL}$(See Fig.8). On the other hand, when the temperature is higher, due to the flattening of the fermi derivative function, the variation of the $L_{RL,\mu}^{ET}$ integral is less abrupt in the vicinity of $\epsilon_d = -U/2$ which explains the disappearance of the central peak of $G_{RL}$. (See Fig. 4.5 a)). On the other hand, the height of the |S| peaks decreases with increasing temperature. This is because at higher temperatures the peak of the derivative of the Fermi function is broadened, which allows for a greater overlap with the transmission $T_{RL,\mu}^{ET}$ which allows the integral $L_{RL,\mu}^{ET}$ to reach a larger value than at low temperatures, and therefore $G_{RL}$ never becomes very small, at the same time the integral $L_{RL,T}^{ET}$ is reduced. Additionally, as the temperature increases, an increase in the contribution of the $L_{RS,T}^{QP}$ integral to the Thermopower can be observed, because the broadening of the peak of the derivative of the Fermi function allows a greater overlap of the Fermi function with the $T_{RS}^{QP}$ transmission outside the energy gap of the superconductor (See Fig. 4.5 b)).

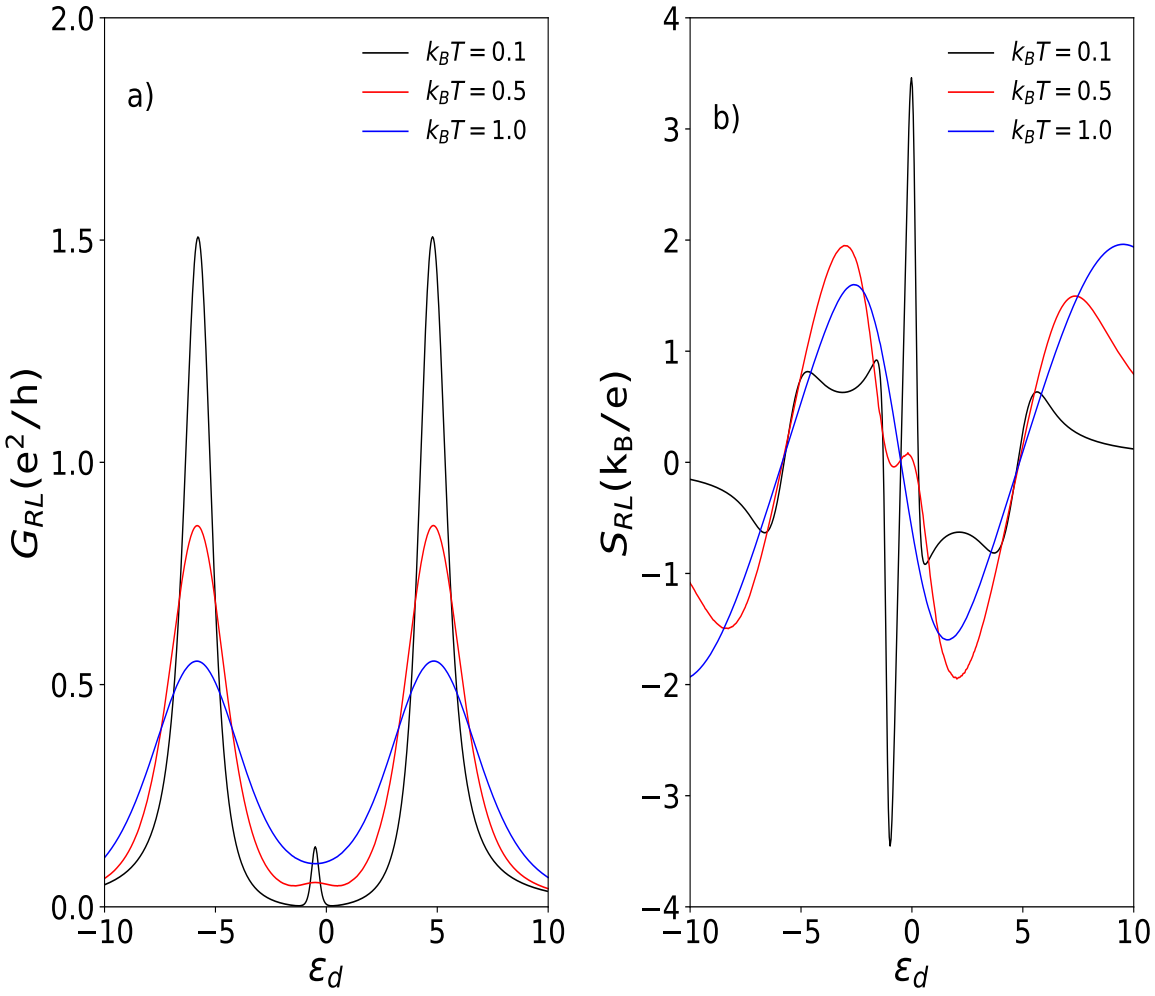


Figure 4.5: The electronic conductance $G_{RL}$ and Seebeck coefficient $S_{RL}$ in unit $k_B/e$ as function of the QD level position $\epsilon$ for different values of the temperature $K_BT$. Other parameters are chosen as $t = 5\Gamma_L$, $U = 1\Gamma_L$, $\Delta = 1\Gamma_L$ and $\Gamma_S = \Gamma_L = \Gamma_R$.

### Effect interdot tunneling

The electronic conductance $G_{RL}$ and the thermopower $S_{RL}$ as a function of $\epsilon_d$ for different values of interdot tunneling $t$ are shown in Fig. 4.6. Fig. 4.6 (a) shows that the lateral peaks of $G_{RL}$ move away from each other as the value of $t$ increases. When $t = 0$ there are only 2 peaks of $G_{RL}$. When $t \neq 0$ a narrow peak appears, whose height decreases as $t$ increases. The reduction of the height of the central peak is due to the progressive decrease of the overlap between the fermi function and the transmission $T^{ET}_{RL}$ as $t$ increases.

On the other hand, in Fig.4.6(b) one can observe the increase of the maximum of $|S|$ as $t$ increases. This is mainly due to the decrease of $G_{RL}$ near the Fermi energy as $t$ increases due to the progressive reduction of the overlap between the Fermi derivative function and the two narrow central peaks of $T^{ET}_{RL}$ located within the superconductor energy gap and the increase of the quotient $L^{ET}_{RL,T}/G_{RL}$ as t increases.

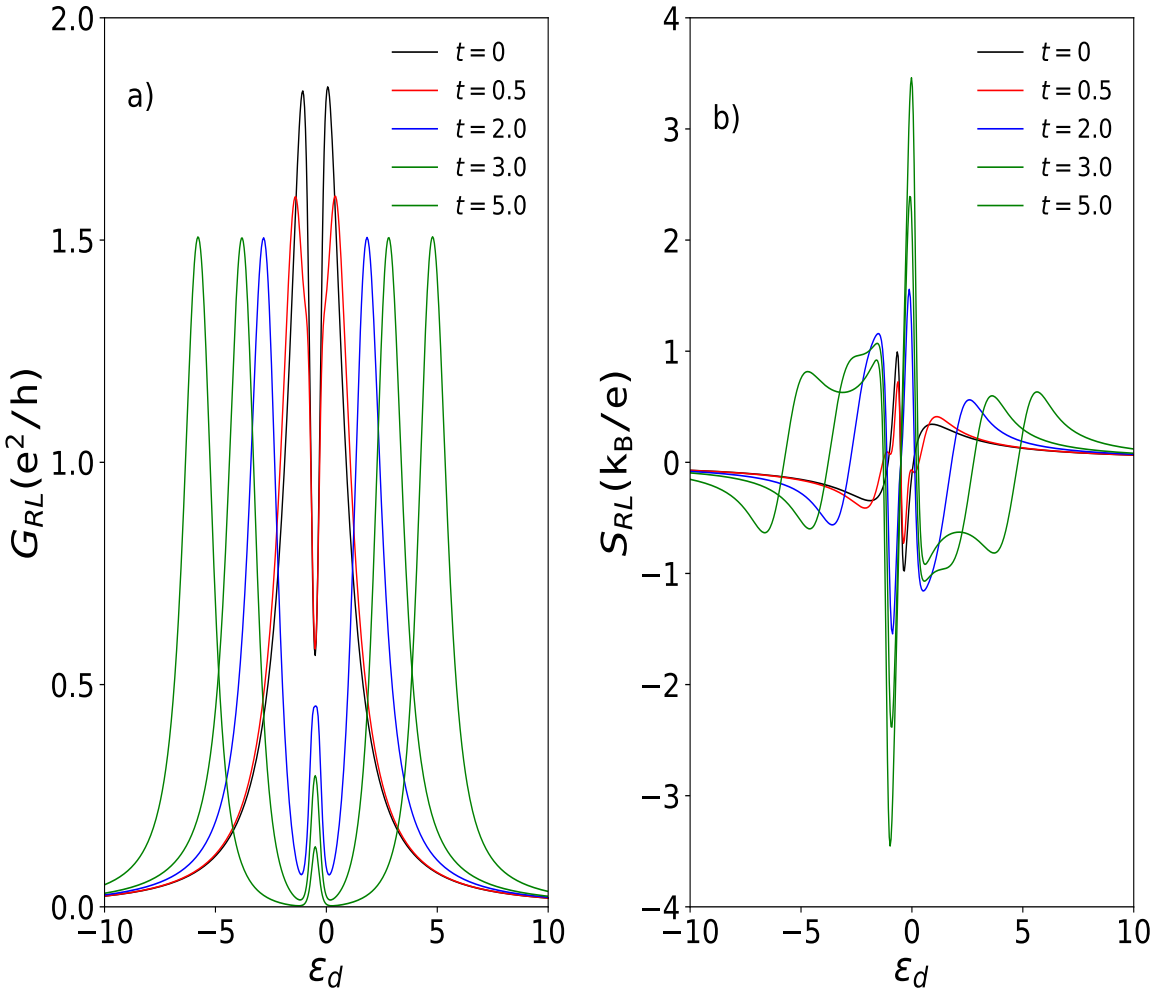


Figure 4.6: The electronic conductance $G_{RL}$ (a))and The Seebeck coefficient $S_{RL}$ (b)) in unit $k_B/e$ as function of the QD level position $\epsilon$ for different values of the interdot tunneling. Other parameters are chosen as $\Delta = 1\Gamma_L$, $U = 1\Gamma_L$, $k_BT = 0.1\Gamma_L$ and $\Gamma_L = \Gamma_R = \Gamma_S$.

**Effect of** $r = \Gamma_S/\Gamma_N$

Electronic conductance $G_{RL}$ and thermopower $S_{RL}$ as a function of $\epsilon_d$ for different values of interdot tunneling $t$ are shown in Fig. 4.7. It can be seen in Fig. 4.7 a) that the height of the lateral peaks of $G_{RL}$ decreases as the coupling rate $\Gamma_S/\Gamma_L$ increases. On the contrary, the maximum height of $G_{RL}$ in $\epsilon_d = -U/2$ grows slightly as $\Gamma_S/\Gamma_L$ grows. Interestingly, $G_{RL}$ rapidly decreases to zero in the neighborhood of $\epsilon_d = -U/2$ when $\Gamma_S/\Gamma_L \leq 1$, however, when $\Gamma_S/\Gamma_L > 1$, the conductance $G_{RL}$ does not become zero at any point within the Coulomb blockade region. However, the maximum value of thermopower as a function of $\epsilon_d$ decreases as $r$ increases (see Fig. 4.7b).

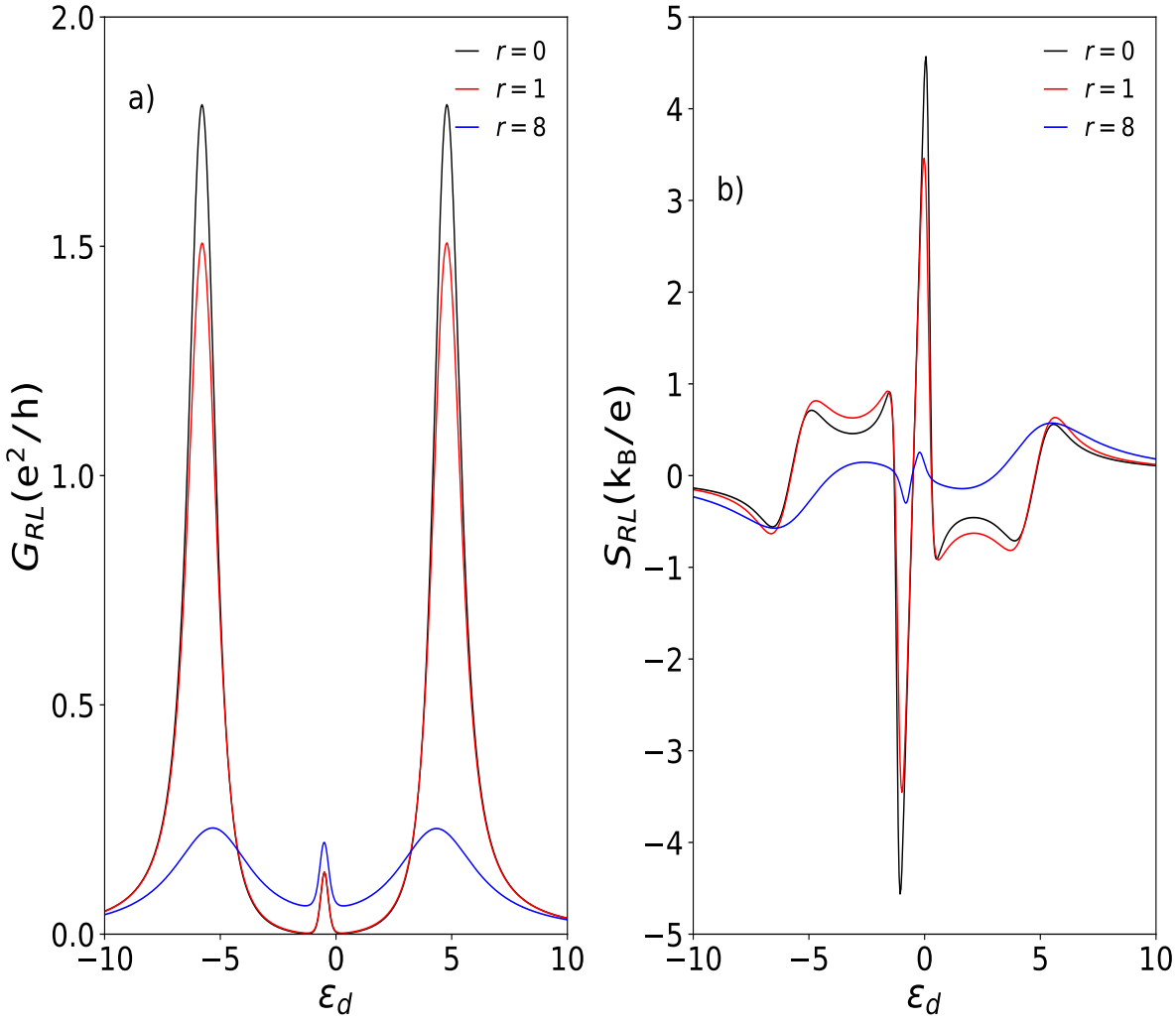


Figure 4.7: The electronic conductance $G_{RL}$ (a))and The Seebeck coefficient $S_{RL}$ (b)) in unit $k_B/e$ as function of the QD level position $\epsilon$ for different values of the coupling ratio $\Gamma_S/\Gamma_L$ . Other parameters are chosen as $t = 5\Gamma_L$, $\Delta = 1\Gamma_L$, $U = 1\Gamma_L$, $k_BT = 0.1\Gamma_L$, and $\Gamma_L = \Gamma_R$.

# 5

# Summary

In summary in this work, we have investigated the electronic transport through a hybrid nanostructures such as a parallel triple quantum-dot system coupled to normal and superconducting leads or T-shaped double quantum dot (DQD) system . In the first place we study the the electronic transport through a parallel triple quantum-dot system coupled to normal and superconducting leads. The main focus was to study the Andreev features appearing in both the differential conductance and QD occupations under Coulomb correlations in the QDs. Within the interferometric regime (small $t$), we have studied the impact on the sub-gap transport properties by varying the coupling ratio with the leads, $r$, when the level spacing between two side-QDs and the central QD is small $\eta \ll 1$. We found that the conductance, both in the interacting and in the non-interacting case, shows the presence Fano-Andreev reflactions and a sharp central peak resembling the Dicke resonance in the optical emission spectra of atoms, in which the role of the distance between atoms is played by the space in energy levels $\eta$. In particular, in the interacting case we show a splitting due to the Andreev reflection of the subradiant and superradiant quasiparticles states whenever the coupling ratio exceeds the certain critical value. On other hand, we explain the shape of the differential conductance near of zero-bias voltage as a result of the two equivalent quantum interference processes: the first, among the electron trajectories entering and leaving the side-attached quantum dots, the one that giving rise, to the so-called Fano-Andreev antiresonances, and the second, the interference between the states of two side-attached quantum dots, the one that giving rise to a Dicke-like effect. Additionaly,we have studied the electronic transport properties in function of different parameters of this system such as inter-dot tunneling, Coulomb interaction, coupling ratio with the superconductor lead and the temperature, when the temperature is lower than the Kondo temperature, which allowed us to capture two important effects of the Coulomb interaction, such as the charge effect and appearance of the Kondo resonance at $\omega = 0$. To complement this, we have also analyzed the case of the the non-equilibrium regime, where we were able to observe the enhancement of zero-bias Andreev conductance driven by the Kondo effect for low temperatures, smaller than $T_K$ . Subsequently, we study a T-shaped double quantum dot (DQD) system under non-equilibrium conditions in the Coulomb blockade regime. We utilized a non-equilibrium Green's function calculation and the equation of motion method using the Hubbard-I approximation to do this. Our findings indicate superconducting interference effects on transport between normal leads, which can be detected as Fano-like anti-resonances in

the QD transmission spectrum. We identified two different regimes, called interferometric and molecular. In both cases, the differential conductance (ET) can be expressed as a convolution of Fano and Breit Wigner lines shape. However, in the interferometric case, the Fano lines shapes are centered on the energies of the Andreev bound states with finite complex $q$-parameter, while in the molecular case, it vanishes. On the other hand, the Andreev reflection shows maxima corresponding to the Andreev bound states. Therefore, we conclude that the interference effect is robust against Coulomb correlations and can be probed experimentally under non-equilibrium conditions. Finally, we study the subgap thermoelectric properties, such as conductance and Seebeck coefficient,and the influence exerted on these properties by the different parameters that define this system, such as intradot correlation ($U$), interdot tunneling ($t$) between the central and lateral QD, rate of coupling with the superconductor lead and the temperature. The Coulomb interaction strongly affects the thermopower in a valley between the conductance peaks. In particular, it can be observed that the Seebeck coefficient increases rapidly when the energy gap of the superconductor increases and reaches its maximum value when delta is close to $\Delta = 1\Gamma_L$. Moreover, an additional sharp structure appears close to the electron-hole symmetry point. This effect is related to the Fano resonance and is a signature of the destructive interference between the activated QD levels. On other hand, the height of the $|S|$ peaks decreases with increasing temperature. And finally as the inter-dot tunneling $t$ increases one can observe the increase of the maximum of $|S|$ due to the progressive reduction of the overlap between the fermi derivative function and the two narrow central peaks of $T_{RL}^{ET}$ that are located inside the superconductor energy gap.

# 6

# Appendix

## 6.1 $T_A$ in the limit $\Delta \gg \epsilon$

Here we present the Andreev transmittance for a TQD between normal and superconducting leads in the limit $\Delta \gg \epsilon$ and zero inter-dot tunneling ($t = 0$).

$$T(\omega) = 2T_A(\omega) + T_Q(\omega) \tag{6.1}$$

$$T_A(\omega) = \Gamma_N^2(|G_{12}^r|^2) \tag{6.2}$$

$$T_Q = \Gamma_N \Gamma_S \, \bar{\rho} \left( |G_{11}^r|^2 + |G_{12}^r|^2 - \frac{2\Delta}{|\epsilon|} Re\left[ G_{11}^r (G_{12}^r)^* \right] \right) \tag{6.3}$$

with

$$\bar{\rho}(\omega) = \frac{|\omega|\theta(|\omega| - \Delta)}{\sqrt{\omega^2 - \Delta^2}}. \tag{6.4}$$

On other side

$$G_{12}(\omega) = \frac{i\Gamma_S \Delta \rho(\omega)}{2\omega D} \tag{6.5}$$

where

$$\rho(\omega) = \frac{|\omega|\theta(|\omega| - \Delta)}{\sqrt{\omega^2 - \Delta^2}} - i\frac{\omega\theta(\Delta - |\omega|)}{\sqrt{\Delta^2 - \omega^2}}$$

and

$$D = \left( g_{11}^{-1} - \Sigma_{NS} \right) \left( g_{22}^{-1} - \Sigma_{NS} \right) + \frac{\Gamma^2 \Delta^2 \rho^2}{4\omega^2},$$

where $\Sigma_{NS} = -\frac{1}{2} i \left( \Gamma_N + \Gamma_S \rho \right)$ is the self-energy of the leads, and

$$g_{11}^{-1} = \omega - \epsilon_d - \frac{t^2}{\omega - \epsilon_1} - \frac{t^2}{\omega - \epsilon_3} \tag{6.6}$$

$$g_{22}^{-1} = \omega - \epsilon_d - \frac{t^2}{\omega + \epsilon_1} - \frac{t^2}{\omega + \epsilon_3} \tag{6.7}$$

with $\epsilon_1 = \epsilon_d + \eta$ and $\epsilon_3 = \epsilon_d - \eta$

If the real part of $\rho(\omega)$ is named "a" and its imaginary part "b", we can write the above equation as:

$$G_{12}^r(\omega) = \frac{(a - b\,i)\Gamma_S\Delta/2\omega}{[c + d\,i]} \tag{6.8}$$

where

$$\begin{aligned} c &= \frac{\Gamma_S^2\Delta^2}{4\omega^2}(a^2 - b^2) - \frac{1}{4}\left(\Gamma_N + \Gamma_S a\right)^2 \\ &\quad + (g_{11} - b\,\Gamma_S/2)\left(g_{22}^{-1} - b\,\Gamma_S/2\right) \\ d &= \frac{(\Gamma_N + a\,\Gamma_S)}{2}\left(g_{11}^{-1} + g_{22}^{-1} - b\Gamma_S\right) \\ &\quad + \frac{\Gamma_S^2\Delta^2 a\,b}{2\omega^2} \end{aligned} \tag{6.9}$$

Consequently, we have

$$|G_{12}|^2 = \frac{\Gamma_S\Delta}{2\omega}\frac{(a^2 + b^2)}{[c^2 + d^2]} \tag{6.10}$$

## 6.2 Symmetric Coupling $\Gamma_N = \Gamma_S$

Substituting these expressions into the equation into $G_{12}$ and considering $t \neq 0$, and $\Gamma_N = \Gamma_S = \Gamma$ at the limit of $\Delta \gg \omega$ we have:

$$\begin{aligned} T_A &= \Gamma_N^2|G_{12}^\sigma|^2 \\ &= \Gamma_N^2|G_{12}^\sigma|^2 = \frac{\Gamma^4(\omega^2 - \eta^2)^4}{\Gamma^4\left[\omega^2 - \eta^2\right]^4 + 4\omega^4\left[(\omega^2 - \eta^2 - 2t^2\right]^4} \end{aligned} \tag{6.11}$$

Then, the first maximum occurs when $\omega = 0$ and the two other maxima values of $T(\epsilon)$ occur when $\omega = \pm\sqrt{\eta^2 + 2t^2}$.

## 6.3 Asymmetric Coupling $\Gamma_S = 2\Gamma$

Substituting these expressions into the equation into $G_{12}$, considering $t \neq 0$, and $\Gamma_S = 2\Gamma$ at the limit of $\Delta \gg \omega$, we have:

$$\begin{aligned} T_A &= \Gamma_N^2|G_{12}^\sigma|^2 \\ &= \frac{\Gamma^4}{\left[\frac{\omega\Gamma(\omega^2 - \eta^2 - 2t^2)}{(\omega^2 - \eta^2)}\right]^2 + \left[\omega^2\frac{(\omega^2 - \eta^2 - 2t^2)^2}{(\omega^2 - \eta^2)^2} - \frac{5\Gamma^2}{4}\right]^2} \end{aligned} \tag{6.12}$$

In this case, because of this functional structure, $T_A$ presents six peaks located symmetrically on each side of $\omega = 0$. As before, when the coupling to the leads was symmetric, the zeros of $T(\omega)$ occur when $\omega = \pm\eta$. In the particular case $t = 0$ and $\eta = 0$, we have:

$$T_A(\omega) = \frac{\Gamma^4}{[\Gamma^2\epsilon^2 + (\omega^2 - 5\Gamma^2/4)^2]} \tag{6.13}$$

Then, the maximum value of $T(\omega)$ occurs close to $\omega = \pm\Gamma$:

$$\begin{aligned} T_A(\pm\Gamma) &= \frac{\Gamma^4}{[\Gamma^2\Gamma^2 + (\Gamma^2 - 5\Gamma^2/4)^2]} \\ &= \frac{\Gamma^4}{[\Gamma^4 + (\Gamma^2/4)^2]} \\ &= \frac{16\Gamma^4}{17\Gamma^4} \\ &\approx 1 \end{aligned}$$

## 6.4 Linear and differential conductance in the limit of low temperature

Linear conductance $G$ in the subgap limit ($eV \ll \Delta$) is written as:

$$G = \frac{4e^2}{h}\int \frac{\partial f}{\partial \omega} T_A(\omega) d\omega \tag{6.14}$$

If $k_B\tau \to 0$, then $\frac{\partial f}{\partial \omega} \to \delta(\omega - \mu)$, so that

$$G = \frac{4e^2}{h}\int \delta(\omega - \mu) T_A(\omega) d\omega = \frac{4e^2}{h} T_A(\mu) \tag{6.15}$$

Consequently, the peaks of $T_A$ as a function of the energy $\epsilon$ for a fixed value of $\epsilon_d$ are the same for $G$ as a function of $\mu$ for a fixed value of $\epsilon_d$. For this reason, as expected, the graph of $G$ as a function of the Fermi energy $\mu$, in the case of a quantum dot asymmetric coupling with the leads, presents two peaks as the case of $T_A$ as a function of the energy.

### 6.4.1 $dI/dV$ vs $T_A$

The general form for the electronic current in the sub-gap limit ($eV \ll \Delta$) is

$$I = \frac{2e}{h}\int d\omega\, T_A\left[f_L(\omega - eV) - f_L(\omega + eV)\right] \tag{6.16}$$

In the limit of low temperature $k_B\tau \to 0$

$$I = \frac{2e}{h}\int\ d\omega\, T_A\left[\Theta(eV - \omega) - \Theta(-\omega - eV)\right] \tag{6.17}$$

$$I = \frac{2e}{h}\int d\omega\, T_A\left[1 - \Theta(\omega - eV) - 1 + \Theta(\omega + eV)\right] \tag{6.18}$$

$$I = \frac{2e}{h} \int d\omega \, T_A \left[ \Theta(\omega + eV) - \Theta(\omega - eV) \right] \tag{6.19}$$

$$I = \frac{2e}{h} \int_{-eV}^{eV} d\omega \, T_A(\omega) \tag{6.20}$$

Then

$$\frac{dI}{dV} = \frac{2e}{h} \int d\omega \, T_A \frac{\partial}{\partial V} \left[ \Theta(\omega + eV) - \Theta(\omega - eV) \right] \tag{6.21}$$

$$\frac{dI}{dV} = \frac{2e}{h} \int d\omega \, T_A \left[ \delta(\omega + eV) + \delta(\omega - eV) \right] \tag{6.22}$$

$$\frac{dI}{dV} = \frac{2e^2}{h} \left[ T_A(-eV) + T_A(eV) \right] = \frac{4e^2}{h} T_A(eV) \tag{6.23}$$

Consequently, for a fixed value of $\epsilon_d$, the peaks of $T_A$ as a function of $eV$ are the same as $\partial I / \partial V$ as a function of $eV$.

scientific reports

Check for updates

OPEN

# Dicke and Fano-Andreev reflections in a triple quantum-dot system

A. González I.[1]✉, M. Pacheco[1,3], A. M. Calle[1,3], E. C. Siqueira[2,3] & P. A. Orellana[1]✉

**This article studies quantum interference effects and their influence on the electronic transport through a parallel triple quantum-dot system coupled to normal and superconducting leads in the linear response and non-equilibrium regime. We model the system by a triple impurity Anderson Hamiltonian including the Coulomb intra-dot correlations in all quantum-dots. Using the non-equilibrium Green's function formalism, we calculate the Andreev conductance and the transmittance for energies within the superconductor gap. Our results show that the Andreev reflection spectra, both in the presence and absence of Coulomb interaction, reveal Fano and Dicke-like resonances in analogy to the Fano and Dicke effects in atomic physics. As one of the main results, we obtain that the charge shows abrupt changes due to the Dicke effect.**

Electron transport through multiple quantum dots systems exhibits exciting interference effects such as Fano[1–7] and Aharonov-Bohm[8–12]. The interference phenomenon, which resembles the well-known Dicke resonance in atomic physics, appears to be of particular importance[13]. It manifests itself by a narrow (subradiant) and a broad (superradiant) line-shape, spontaneously emitted by closely linked atoms, separated by a distance smaller than the wavelength of the emitted light[14]. In the electronic case, the decay rates (level broadening) are produced by the couplings between localized levels and the conduction channel, and the proximity and effective couplings give rise to fast (super-tunneling) and slow (sub-tunneling) modes[15].

The presence of the Dicke effect has been predicted theoretically and experimentally in different nanoscopic systems[16–24]. On the other hand, Fano effect is another quantum interference phenomena that has been studied in quantum transport for some time. This effect is due to the quantum interference from localized states and continuum states. It yields characteristic asymmetric Fano lineshape, characterized by the Fano factor $q$, which is a measure of the coupling strength between the continuum and the localized state.

The electronic transport through quantum dots (QDs), double quantum dots (DQDs) and triple quantum dots (TQDs) coupled to normal/ferromagnetic and superconductor leads, has been studied recently[25–30]. The Cooper pairs[31] transport, along with interference effects among electrons and holes, gives rise to novel and interesting phenomena[32,33]. Within this context, several features of the Dicke effect have been considered under the presence of superconductor correlations. In particular, it has been found that the Dicke effect occurs in the Andreev conductance spectrum by modulating the interdot coupling and the side-dot levels[34,35]. A description of the relationship between the induced electron pairing and the Dicke effect has been studied[36] by focusing specifically on how the electron pairing and correlation effects are affected by the side-attached quantum dots, ranging from the interferometric to the molecular limits. However, a detailed description of the interplay between Dicke effects and the charging effect induced by the Coulomb intra-dot correlations, is still missing.

In this paper, we present an investigation of the influence of the Dicke and Fano effects on electronic transport through a coupled triple quantum dot system coupled to normal and superconducting leads in a linear and non-linear regime.

In particular, we study the interplay between the proximity effect due to the superconducting lead and the conjunction of two phenomena: Dicke and Fano-Andreev reflections. We shall focus on the electronic properties of TQDs within the regime of low temperatures and sub-gap energies ($eV \ll \Delta$), where the electronic transport is mainly carried by Andreev reflection (AR). We consider Coulomb correlations in all the quantum-dots and study their influence on the electronic conductance. The inter-dot Coulomb interaction is assumed to be much smaller than the corresponding intra-dot interaction and, in consequence, is omitted. Transport characteristics, such as the Andreev conductance and the electrical current of the system at the low-temperature limit, are derived using the non-equilibrium Green function method, in the linear and non-linear response regime. We use the Hubbard I approximation[37] to obtain the relevant Green's functions from the equations of motion. Our results show that

[1]Departamento de Física, Universidad Técnica Federico Santa María, 110 V Valparaíso, Casilla, Chile. [2]Departamento Acadêmico de Física, Universidade Tecnológica Federal do Paraná, Curitiba, Brazil. [3]These authors contributed equally: M. Pacheco, A. M. Calle and E. C. Siqueira. ✉email: alejandro.gonzalezi@usm.cl; pedro.orellana@usm.cl

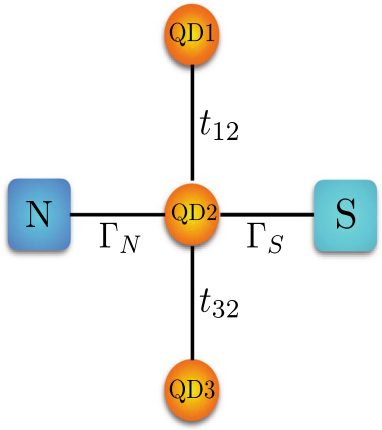


**Figure 1.** A sketch of triple-QD system coupled to normal metal and superconducting leads.

the Andreev reflection spectra, both in the presence and absence of Coulomb interaction, reveal Dicke and Fano-like resonances in analogy to their counterpart effects in atomic physics. As one of the main effects, we obtain that the charge shows abrupt changes due to the Dicke effect, which has not been shown in previous reports.

The paper is organized as follows. "Results" introduces the model and describes the general background of the transport properties in the TQD system. Next, "Summary" presents the corresponding numerical results in the equilibrium and non-equilibrium regime for both non-interacting and interacting cases. Finally, "Appendix" closes with a summary and general conclusions.

## Results

### Model

The system under consideration consists of a single-level central quantum dot (QD2) attached to one normal metallic and one superconducting lead and two side quantum dots (QD1 and QD3) as shown schematically in Fig. 1. The following Hamiltonian models the system (N-TQD-S):

$$H = H_N + H_S + H_{TQD} + H_T. \tag{1}$$

The first term is the Hamiltonian for the normal electrode and it is given by:

$$H_N = \sum_k \sum_\sigma \epsilon_{kN\sigma} c^\dagger_{kN\sigma} c_{kN\sigma}, \tag{2}$$

where $c^\dagger_{kN\sigma}$ ($c_{kN\sigma}$) is the electron creation (annihilation) operator of an electron with spin $\sigma$ and energy $\epsilon_{kN\sigma}$ in the normal electrode.

The second term stands for the *BCS* Hamiltonian[31] of the superconducting (right) lead and reads:

$$H_S = \sum_k \sum_\sigma \epsilon_{kS} c^\dagger_{kS\sigma} c_{kS\sigma} + \sum_k (\Delta^* c_{kS\downarrow} c_{-kS\uparrow} + \Delta c^\dagger_{-kS\uparrow} c^\dagger_{kS\downarrow}), \tag{3}$$

where $c^\dagger_{kS\sigma}$ ($c_{kS\sigma}$) is the electron creation (annihilation) operator of an electron with spin $\sigma$ and energy $\epsilon_{kS}$ in the superconducting electrode, and $\Delta$ denotes the superconducting energy gap.

The third term is the Hamiltonian of three coupled *QDs*, given by

$$H_{TQD} = \sum_{m,\sigma} \epsilon_{dm,\sigma} d^\dagger_{m,\sigma} d_{m,\sigma} + \sum_\sigma \sum_{j=1,3} \left[ t_{j2} d^\dagger_{2\sigma} d_{j\sigma} + H.c \right] + \sum_m U_m n_{m\sigma} n_{m\bar{\sigma}}, \tag{4}$$

where $d^\dagger_{m\sigma}$ ($d_{m\sigma}$) is the electron creation (annihilation) operator of an electron with spin $\sigma$ and energy $\epsilon_{dm}$ in the $m$-th quantum dot with $m = 1, 2, 3$. We assume that each quantum dot has only a single-electron spin-degenerate level, with $\epsilon_{dm\uparrow} = \epsilon_{dm\downarrow}$; $U_m$ is the strength of the Coulomb interaction in the $m$-th quantum dot while $t_{j2} (j = 1, 3)$ stands for the interdot coupling parameter.

The last term in Eq. (1) describes tunneling of electrons between the leads ($N$, $S$) and the central quantum dot ($QD2$) :

$$H_T = \sum_{k\sigma} \sum_{\beta=N,S} (V_{k\beta\sigma} c^\dagger_{k\beta\sigma} d_{2\sigma} + H.c), \tag{5}$$

where $V_{k\beta\sigma} (\beta = N, S)$ is the tunneling matrix element between the central $QD2$ and the electrode $\beta$. In the wide-band limit approximation, one can introduce the coupling constants with the leads: $\Gamma_\beta = 2\pi \sum_k |V_{k\beta}|^2 \delta(\omega - \epsilon^\beta_k)$.

The retarded Green's function $\mathbf{G}^r_\sigma$ in the generalized $6 \times 6$ Nambu representation is obtained from the Dyson equation:

$$\mathbf{G}^r = \mathbf{g}^r + \mathbf{g}^r \mathbf{\Sigma}^r \mathbf{G}^r, \tag{6}$$

where $\mathbf{g}^r$ denotes the retarded Green's function of the triple quantum dot isolated from the leads being written as:

$$\mathbf{g}^r = \begin{bmatrix} \left[\mathbf{g}_1^r\right]^{-1} & \mathbf{t} & \mathbf{0} \\ \mathbf{t}^* & \left[\mathbf{g}_2^r\right]^{-1} & \mathbf{t} \\ \mathbf{0} & \mathbf{t}^* & \left[\mathbf{g}_3^r\right]^{-1} \end{bmatrix}^{-1}, \tag{7}$$

where $\mathbf{g}_m^r$ matrices are defined as:

$$\mathbf{g}_m^r = \begin{bmatrix} \dfrac{1-n_m}{\omega-\epsilon_{dm}} + \dfrac{n_m}{\omega-\epsilon_{dm}-U_m} & 0 \\ 0 & \dfrac{1-n_m}{\omega+\epsilon_{dm}} + \dfrac{n_m}{\omega+\epsilon_{dm}+U_m} \end{bmatrix}, \tag{8}$$

with $m = 1, 2, 3$. The interdot coupling matrix $\mathbf{t}$ is given by:

$$\mathbf{t} = \begin{bmatrix} -t & 0 \\ 0 & t \end{bmatrix}. \tag{9}$$

The retarded self-energy of the leads, in the wide-band approximation, acquires the following form:

$$\mathbf{\Sigma}^r = \begin{bmatrix} \mathbf{0} & \mathbf{0} & \mathbf{0} \\ \mathbf{0} & \mathbf{\Sigma}_N^r + \mathbf{\Sigma}_S^r & \mathbf{0} \\ \mathbf{0} & \mathbf{0} & \mathbf{0}, \end{bmatrix} \tag{10}$$

where

$$\mathbf{\Sigma}_N^r = -\frac{i}{2}\Gamma_N \begin{bmatrix} 1 & 0 \\ 0 & 1 \end{bmatrix} \tag{11}$$

and

$$\mathbf{\Sigma}_S^r = -\frac{i}{2}\rho_s(\omega)\Gamma_S \begin{bmatrix} 1 & -\frac{\Delta}{\omega} \\ -\frac{\Delta}{\omega} & 1 \end{bmatrix}, \tag{12}$$

where $\rho_s$ denotes the dimensionless modified BCS density of states in the superconductor given by:

$$\rho_s(\omega) = \frac{|\omega|\theta(|\omega|-\Delta)}{\sqrt{\omega^2-\Delta^2}} - i\frac{\omega\theta(\Delta-|\omega|)}{\sqrt{\Delta^2-\omega^2}}. \tag{13}$$

We have adopted the equation of motion method and the Hubbard-I decoupling scheme to find the Green's functions. The general expression for the charge current through a barrier from the normal lead to the *QDs* can be calculated in terms of non-equilibrium Green's function $G^{r,a}$. The charge current $I$ flowing in a biased system from left to right can be calculated from the following expression:

$$I = -e\left\langle \frac{dN}{dt} \right\rangle \tag{14}$$

with $N = \sum_{k\sigma} c_{k\sigma}^\dagger c_{k\sigma}$.

By using the equation of motion (EOM), we can obtain

$$I = \frac{2e}{\hbar}\sum \int d\omega \left[\mathbf{G}_2^r(\omega)\mathbf{\Sigma}_N^<(\omega) + \mathbf{G}_2^<(\omega)\mathbf{\Sigma}_N^a(\omega) + H.c.\right]_{(11)}, \tag{15}$$

where $\mathbf{G}^{r,<}(\omega)$ is the Fourier transform of retarded and lesser Green's function of the system, and $\mathbf{\Sigma}_N^{<,a}$ is the Fourier transform of lesser, advanced self-energy of the normal lead.

In order to obtain the lesser Green's function $G_\sigma^<(\omega)$, we use the Keldysh equation

$$\mathbf{G}^< = \mathbf{G}^r(\omega)\mathbf{\Sigma}^<\mathbf{G}^a(\omega), \tag{16}$$

where the lesser self-energy is given by

$$\mathbf{\Sigma}^<(\omega) = \mathbf{\Sigma}_N^< + \mathbf{\Sigma}_S^< = \begin{bmatrix} \mathbf{0} & \mathbf{0} & \mathbf{0} \\ \mathbf{0} & \mathbf{f}_N(\omega)\mathbf{\Gamma}_N + \mathbf{f}_S(\omega)\mathbf{\Gamma}_S & \mathbf{0} \\ \mathbf{0} & \mathbf{0} & \mathbf{0}, \end{bmatrix} \tag{17}$$

while $\mathbf{f}_i$ is the Fermi matrix, given by

$$\mathbf{f}_i = \begin{bmatrix} f_i & 0 \\ 0 & \bar{f}_i \end{bmatrix} \tag{18}$$

with the Fermi functions for electrons and holes defined as $f_i = f(\omega - V_i)$ and $\bar{f}_i = f(\omega + V_i)$, respectively. For $i = N$ and $f_i = \bar{f}_i = f(\omega)$ for $i = S$. Also,

$$\mathbf{\Gamma}_N = \begin{bmatrix} \Gamma_N & 0 \\ 0 & \Gamma_N \end{bmatrix} \tag{19}$$

and

$$\mathbf{\Gamma}_S = \bar{\rho}_s(\omega)\Gamma_S \begin{bmatrix} 1 & -\frac{\Delta}{\omega} \\ -\frac{\Delta}{\omega} & 1 \end{bmatrix} \tag{20}$$

denotes the couplings constants in the matrix form of the leads, while $\bar{\rho}_s$ denotes the density of states in the superconductor given by

$$\bar{\rho}_s(\omega) = \frac{|\omega|\theta(|\omega| - \Delta)}{\sqrt{\omega^2 - \Delta^2}}. \tag{21}$$

Finally, by substituting the matrix elements previously calculated, the current in the sub-gap regime ($e|V| < \Delta$), i.e., the Andreev current in the limit of low temperature, can be written as

$$I_A = \frac{2e}{h}\int_{-eV}^{eV} d\omega\, T_A(\omega), \tag{22}$$

where $V$ is the bias voltage, and $T_A$ is the Andreev transmittance, given by:

$$T_A = \Gamma_N^2 |G^r_{2,12}(\omega)|^2. \tag{23}$$

It is important to note that the Coulomb correlations make $T_A$ dependent on the average occupations of the QDs. For the non-magnetic case, the averaged occupation number does not depend on spin, which allows us to set for each QD: $\langle n_{i,\sigma}\rangle = \langle n_i\rangle$, $i = 1, 2, 3$. These occupation numbers are obtained by solving the following system of equations:

$$\langle n_1\rangle = -i\int \frac{d\omega}{2\pi} G^<_{1,11}[\omega, \langle n_1\rangle, \langle n_2\rangle, \langle n_3\rangle], \tag{24a}$$

$$\langle n_2\rangle = -i\int \frac{d\omega}{2\pi} G^<_{2,11}[\omega, \langle n_1\rangle, \langle n_2\rangle, \langle n_3\rangle], \tag{24b}$$

$$\langle n_3\rangle = -i\int \frac{d\omega}{2\pi} G^<_{3,11}[\omega, \langle n_1\rangle, \langle n_2\rangle, \langle n_3\rangle]. \tag{24c}$$

As one may notice by inspecting Eqs. (24a), (24b) and (24c), they form a system of equations for $\langle n_1\rangle$, $\langle n_2\rangle$ and $\langle n_3\rangle$ which must be solved in a self-consistent way.

The LDOS of the quantum dots come from of matrix elements of the retarded Green's function matrix (electron components in Nambu space). The LDOS for dots 1, 2 and 3 are, respectively:

$$\rho_1(\omega) = -\frac{1}{\pi} Im(G^r_{1,11}[\omega, \langle n_1\rangle, \langle n_2\rangle, \langle n_3\rangle]), \tag{25a}$$

$$\rho_2(\omega) = -\frac{1}{\pi} Im(G^r_{2,11}[\omega, \langle n_1\rangle, \langle n_2\rangle, \langle n_3\rangle]), \tag{25b}$$

$$\rho_3(\omega) = -\frac{1}{\pi} Im(G^r_{3,11}[\omega, \langle n_1\rangle, \langle n_2\rangle, \langle n_3\rangle]). \tag{25c}$$

Then, the total DOS of the triple quantum-dot is given by the addition of LDOS of each QD:

$$\rho(\omega) = \rho_1(\omega) + \rho_2(\omega) + \rho_3(\omega). \tag{26}$$

## Results

We now discuss the transport properties within the Andreev regime. Within this regime, the range for the Fermi energy and QD levels is restricted in the range of the superconductor gap, $\Delta$. We denoted $r$ as the ratio of leads coupling $\Gamma_S/\Gamma_N$ and assumed that the quantum-dot levels are spin degenerate, $\epsilon_{di,\sigma} = \epsilon_{di}$ (for $i = 1, 2, 3$). In addition, we have introduced the parameter $\eta$, which describes the separation of the levels $\epsilon_{d1}$ and $\epsilon_{d3}$ from the level $\epsilon_{d2} = \epsilon_d$. We have supposed that the energy levels of the side dots (QD1 and QD3) are located symmetrically with respect to the energy level of the central dot (QD2), i.e. $\epsilon_{d1} = \epsilon_d + \eta$ and $\epsilon_{d3} = \epsilon_d - \eta$. Furthermore, unless stated otherwise, we set the coupling between the two side dots to the central dot to be symmetric ( $t_{12} = t_{32} = t$ ), and we consider two regimes: interferometric regime (when $t$ is very small in respect to $\Gamma$ ) and the molecular regime (when $t$ is very near to the value of $\Gamma$ ). In the linear response regime, the chemical potentials of the leads

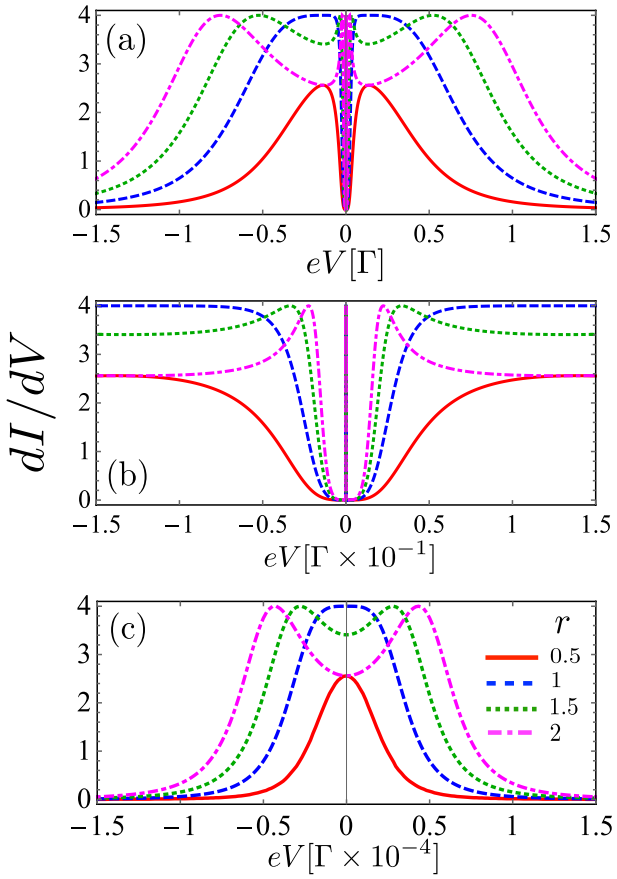


**Figure 2.** Differential conductance in the noninteracting case, calculated as a function of the bias voltage when $\epsilon_d = 0$ and indicated values of $r$: $r = 0.5$(*red*), $r = 1.0$(*blue*), $r = 1.5$(*green*), $r = 2.0$(*magenta*). Fixed parameters: $\eta = 0.001\Gamma, t = 0.1\Gamma$. (**b**) Closeup of central peak presented in panel (**a**). (**c**) Closeup of central peak presented in panel (**b**).

are set to zero, $\mu_N = \mu_S = 0$. On the other side, in the non-linear regime we set the chemical potential of the leads as $\mu_N = eV$ and $\mu_S = 0$, therefore, $\mu_N - \mu_S = eV$, where $V$ is the applied voltage. In addition, we assume in all our calculations that $k_B\tau = 0$, where $\tau$ is the temperature. Finally, we assume that the intradot Coulomb interaction is equal at all quantum dots, i.e., $U_m = U$, for $m = 1, 2, 3$. In what follows, we rename $\Gamma_N = \Gamma$.

**Noninteracting case.** Let us first consider the limit where the Coulomb interaction is neglected, $U_i = 0$ for $i = 1, 2, 3$.

In Fig. 2 we show the differential conductance as a function of the bias voltage for different values of $r = \Gamma_S/\Gamma_N$, by choosing a small $t$ (interferometric regime) and an even smaller value of $\eta$ in order to investigate the Dicke resonances. We can observe that when $r$ does not exceed a certain critical value, the differential conductance exhibits one very narrow central peak and two broader and smaller side peaks symmetrically located with respect to the zero energy. However, for higher values of $r$, we observe that $dI/dV$ presents six peaks in this interval of energy. In other words, these peaks split as $r$ increases from a specific critical value (see inset in Fig. 2). Also, we note from Fig. 3 that the spacing of these peaks increases with the value of $r$ when $eV$ is very near zero and conversely, they move closer when the range of $eV$ increases. In order to have a better understanding of Fig. 2, we will analyze the effect of $r$ and $\eta$ on the differential conductance. For that purpose we will study the expression for $T_A$ given by Eq. (23), in the limit of $\Delta \to \infty$ with $\tilde{\omega} = \omega - \epsilon_d$, for which we obtain,

$$T_A = \frac{r^2\Gamma^4(\tilde{\omega}^2 - \eta^2)^2}{S} \tag{27}$$

with

$$S = 4\Gamma^2\tilde{\omega}^2\left(\tilde{\omega}^2 - \eta^2 - 2t^2\right)^2 + \frac{\left(4\tilde{\omega}^2\left(\tilde{\omega}^2 - \eta^2 - 2t^2\right)^2 - \left(1 + r^2\right)\Gamma^2\left(\tilde{\omega}^2 - \eta^2\right)^2\right)^2}{4(\tilde{\omega}^2 - \eta^2)^2}.$$

From Eq. (27) we can deduce that the roots of $T_A$ are $\tilde{\omega} = \pm\eta$. In the case of symmetric coupling with the leads ($\Gamma_S = \Gamma$), the Andreev transmittance is given by the expression:

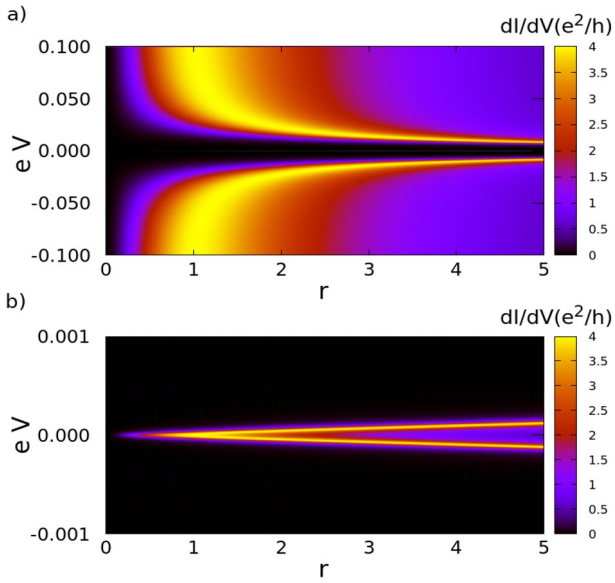


**Figure 3.** Density plot of differential conductance vs $r$ and $eV$ in the noninteracting case, when $\epsilon_d = 0\Gamma$ in the applied bias range between (**a**) $-0.1\Gamma$ and $0.1\Gamma$ (**b**) Closeup of the central peak in the figure (**a**), in the applied bias range between $-0.001\Gamma$ and $0.001\Gamma$.

$$T_A = \frac{\Gamma^4(\tilde{\omega}^2 - \eta^2)^4}{\Gamma^4\left[\tilde{\omega}^2 - \eta^2\right]^4 + 4\tilde{\omega}^4\left[(\tilde{\omega}^2 - \eta^2 - 2t^2\right]^4}. \tag{28}$$

Equation (28) shows that in the transmittance function there are resonant peaks appearing at $\tilde{\omega} = \pm\sqrt{\eta^2 + 2t^2}$, $\tilde{\omega} = 0$, and two Fano antiresonances located at $\tilde{\omega} = \pm\eta$. The narrow central peak in the transmittance may be considered as a long-lived (subradiant) state, while the other two peaks correspond to short-lived (superradiant) states. Since the central peak is located at zero, the width of the central peak is defined by the value of $\eta$. For small values of $\eta$, the width of the central peak becomes much narrower. With $\eta$ increasing, the width of the central line also increases, while the two satellite peaks become broader with $\eta$. This effect resembles the Dicke effect in atomic physics, where a strong narrow emission line appears when the distance between atoms is smaller than the Fermi wavelength of the corresponding radiation. In the present case, the difference of energy between the levels, $\eta$, plays the role of the distance between atoms.

On the other hand, when we consider an asymmetric coupling to the leads, for instance, $r = 2$, the Andreev transmittance function is given by Eq. (29) :

$$T_A = \frac{\alpha^4\Gamma^4}{\left[\tilde{\omega} - \frac{\sqrt{3\Gamma}}{2}\alpha\right]^2\left[\tilde{\omega} + \frac{\sqrt{3\Gamma}}{2}\alpha\right]^2 + \alpha^4\Gamma^4}, \tag{29}$$

where $\alpha = \frac{(\tilde{\omega}^2 - \eta^2)}{(\tilde{\omega}^2 - \eta^2 - 2t^2)}$

This function presents two Fano antiresonances when $\alpha = 0$, that is to say at $\tilde{\omega} = \pm\eta$, and six peaks are symmetrically located on either side of the zero-energy at $\omega = \pm\frac{\sqrt{3}}{2}\alpha$ and $\omega = \pm\frac{\sqrt{3}}{2}\alpha$. To gain a more clear physical insight into the dependence of $T_A$ on $\eta$, we analyze the limit $\eta = 0$. The Hamiltonian $H_{TQD}$ can be diagonalized leading to three effective levels $\omega_1 = \epsilon_d + \sqrt{2t^2}$ , and $\omega_2 = \epsilon_d$ and $\omega_3 = -\sqrt{2t^2}$ . Since the system of three one-level QDs has three molecular-like states (denoted by index 1, 2, and 3 for increasing energy), one could also expect three peaks in the conductance. However, the matrix elements of the coupling between the molecular state $|2\rangle$ and the left and right leads vanish, that is, the molecular state $|2\rangle$ decouples from the leads when $\eta = 0$ and the central peak disappears. The Andreev transmittance shows only two peaks at the positions $\tilde{\omega} = \pm\sqrt{2t^2}$ and it is zero at $\tilde{\omega} = 0$. On the other side, when $\eta \neq 0$, the molecular-like levels $\omega_1$ and $\omega_3$ locate symmetrically on both sides of $\mu_R$ and the AR conductance reveals a well-defined central peak due to two-level Andreev reflection, where the conventional resonant tunneling is forbidden due to $\omega_i (i = 1, 3)$ in the gap. On other hand, when $\omega_i (i = 1, 3)$ aligns with the chemical potential of the superconducting lead, $\mu_R = 0$, i.e., $\omega_i (i = 1, 3) = 0$ two side-peaks appear in $\tilde{\omega} = \pm\sqrt{\eta^2 + 2t^2}$ due to the Andreev reflection (AR) through a single level. When this happens, an electron coming from the left lead with the energy $\epsilon_d$ can tunnel into the i-state of the QD, leaving a hole propagating back to the i-state in the QD and the creation of a Cooper pair in the right superconducting lead.

**Interacting case.** *Andreev conductance vs gate voltage.* In this section, we study the impact of the electronic charging induced by intradot Coulomb interaction on the transport properties of the TQD system in the

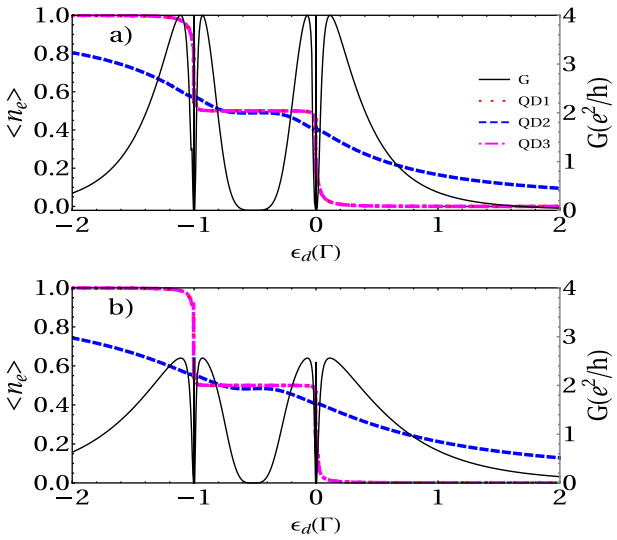


**Figure 4.** Electronic occupation and linear conductance of a TQD system calculated as a function of the dot's level energy for (**a**) $r = 1$ and (**b**) r = 2. Fixed parameters: $U = 1\,\Gamma, t = 0.1\Gamma$, and $\eta = 0.001\Gamma$.

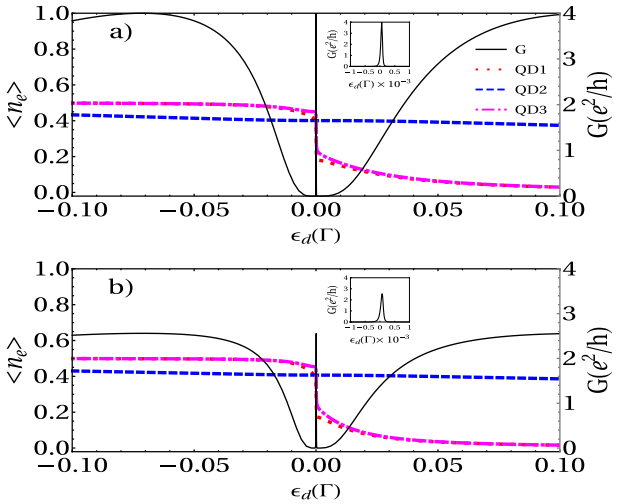


**Figure 5.** Electronic occupation and linear conductance of a TQD system calculated as a function of the dot's level energy around $\omega = 0\Gamma$, for (**a**) $r = 1$ and (**b**) r = 2. Fixed parameters: $U = 1\,\Gamma, t = 0.1\Gamma$, and $\eta = 0.001\Gamma$.

linear regime. Figures 4 and 5 display the occupation and linear conductance versus the QD energy level $\epsilon_d$ for the interferometric regime ( $t, \eta \ll \Gamma$). We can observe that the Coulomb interaction splits the Dicke spectrum into two sets symmetric with respect to the electron-hole symmetry point $\epsilon_d = U/2$, and their centers are located approximately at $\epsilon_d = 0$ and $-U$. The graph of DOS in Fig. 5 confirms this behavior. Besides, four Fano antiresonances in the conductance appear at the electron-hole symmetry due to the destructive quantum interference. Additionally, we can observe the occupation numbers' features to determine the corresponding linear conductance behavior. It is remarkable that the occupation number presents a staircase-like form, with abrupt changes around $\epsilon_d = 0$ and $\epsilon_d = -U$. This behavior of the charge is due to the Dicke-like spectrum, as we can see in the DOS (Fig. 6), in which a structure of levels with super-tunneling (broad states) and sub-tunneling states (sharp states) develops around $\omega = 0$ and $\omega = U$. As $\varepsilon_d$ or $\varepsilon_d + U$ fall slightly below the Fermi energy, the sharp sub-tunneling state completely enters the Fermi sea, and consequently, the charge changes abruptly.

The DOS in Fig. 7 may be written roughly as:

$$\rho(\omega) \approx \frac{1}{\pi} \sum_{\alpha} \Big( \frac{\Gamma_+}{(\omega - e_\alpha)^2 + \Gamma_+^2} + \frac{\Gamma_-}{(\omega - e_\alpha)^2 + \Gamma_-^2} \Big). \tag{30}$$

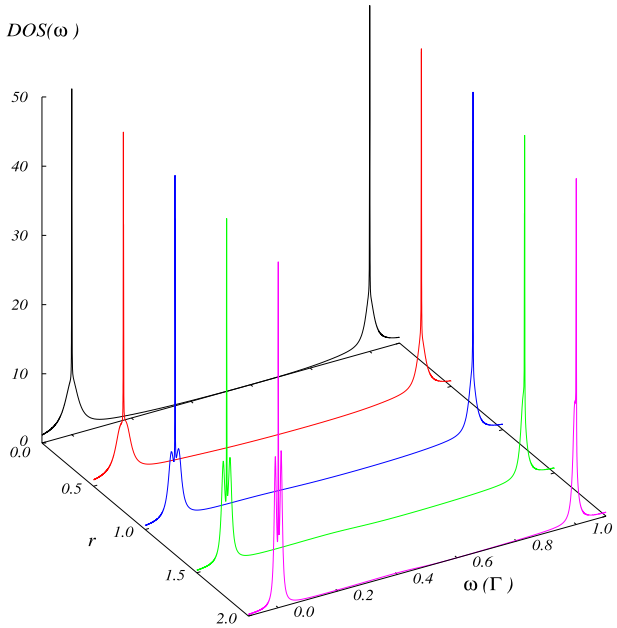


**Figure 6.** Total DOS in the interacting case, calculated as a function of the energy and $r$ for indicated values of rate of coupling: $r = 0$ (black), $r = 0.5$ (red), $r = 1.0$ (blue), $r = 1.5$ (green), $r = 2.0$ (magenta). Fixed parameters: $U = 1\Gamma, \epsilon_d = 0\,, \eta = 0.001\Gamma, t = 0.1\Gamma$.

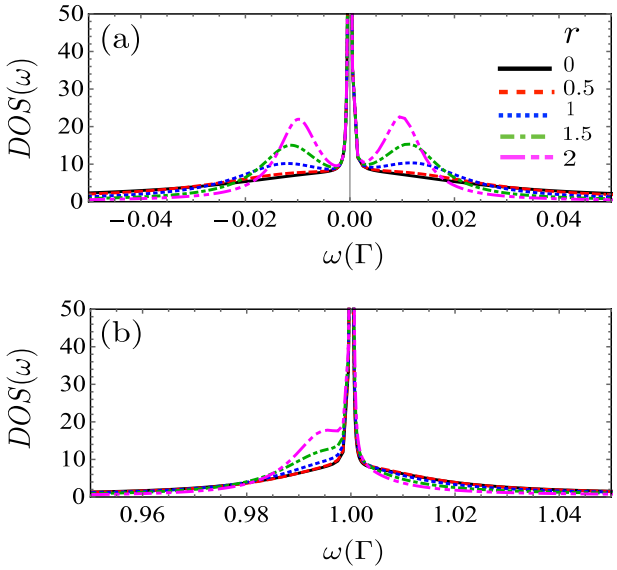


**Figure 7.** Total DOS calculated as a function of the energy in the interacting case ( $U = 1\Gamma$), when $\epsilon_d = 0$ is in a range of energy very near (**a**) $\omega = 0\Gamma$ and (**b**) $\omega = 1\Gamma$ , and the indicated values of the rate of coupling: $r = 0$ (black), $r = 0.5$ (red), $r = 1.0$ (blue), $r = 1.5$ (green), $r = 2.0$ (magenta). Fixed parameters: $\eta = 0.001\Gamma$, $t = 0.1\Gamma$.

In the limit when $\eta \to 0$, the second term in the sum tends to a Dirac-$\delta$ function. Then, by integrating the above equation at Fermi energy and zero temperature, we obtain:

$$n_{di}(\varepsilon_d) \approx \frac{1}{2}\theta(\mu - \varepsilon_d) + \frac{1}{2}\theta(\mu - \varepsilon_d - U). \tag{31}$$

From Eq. (31), we can understand the charge behavior as a function of the energy level $\varepsilon_d$. As $\varepsilon_d$ decreases and falls below the Fermi energy $\mu$, the charge jumps abruptly in steps of 1/2. Besides, since each of these steps in the occupation graph reveals electronic tunneling, three more peaks in the linear conductance plot appear. Each step in electron occupation represents an electron filling from the left normal lead, which occurs when $\epsilon_{di}$ or

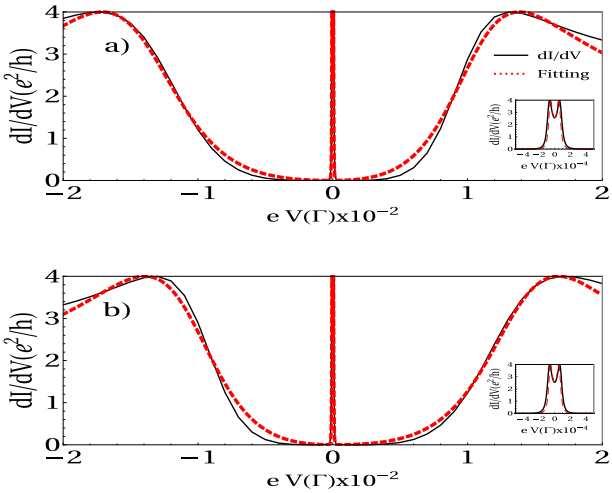


**Figure 8.** (**a**) The differential conductance (black line) as a function of the bias voltage of a TQD system and the fitting (red line) by the sum of the Fano and BW functions when $\epsilon_d = 0.000075\Gamma\, r = 2$. (**b**) Differential conductance (solid line) calculated as a function of the bias voltage of a TQD system and the proposed fitting (dashed line) when $\epsilon_d = -1.000075\Gamma$ and $r = 2$. The zoom of both figures shows the differential conductance and the fitting proposed by the function BW in the low energy limit. Fixed parameters: $U = 1\,\Gamma, t = 0.1\Gamma$, $\eta = 0.001\Gamma$.

$\epsilon_{di} + U$ lines up with $\mu_N = \mu_S$. From Eq. (8) one can understand that the intra-level interaction results in an energy level splitting, in the simpler case with only one central QD ($t = 0$) : from the original one single-electron spin-degenerate level $\epsilon_d$ splitting into two spin-degenerate levels, $\epsilon_d$ with the probability $1 - \langle n\rangle$ and $(\epsilon_d + U)$ with the probability $\langle n\rangle$. Of particular interest are the sharp peaks seen at both $\epsilon_d = 0$ and $\epsilon_d = -U$. At $\epsilon_d = 0$, $\epsilon_d$ lines up with the Fermi surface $\mu$ (here we have set $\mu_N = \mu_S = \mu = 0$), so $\langle n\rangle$ jumps from 0 to 0.5, describing the first electron filling; then each of both levels, $\epsilon_d$ and $\epsilon_d + U$ , has 50% probability of being occupied. At $\epsilon_d = -\Gamma, \epsilon_d + U$ lines up with the Fermi surface $\mu$, and $\langle n\rangle$ jumps from 0.5 to 1, describing the second electron filling; then level $\epsilon_d + U$ has 100% probability of being occupied while level $\epsilon_d$ has 0% probability.

Additionally, Fig. 5 displays a zoom of the Andreev conductance vs the energy level for $r = 1$ and $r = 2$ around $\epsilon_d = 0$. We can see that as $r$ increases, the height of the peaks decreases and, on the contrary, their width increases, in the same way as in the non-interacting case. Besides, as we can see in this figure, for small values of $\eta$, the central peak's width becomes sharper. Moreover, the insets in the above figure show the details of the sharp resonances. This structure of resonances resembles the Dicke resonance in the optical emission spectra of atoms.

*Differential Andreev conductance vs bias voltage.* Next, we investigate the effect of the electronic charging induced by intra-dot Coulomb interaction on the AR process within the non-equilibrium regime. Figure 8 displays the differential conductance as a function of the bias voltage. The central peak, appearing near $eV = 0$, is split due to the proximity effect to the superconductor (Andreev reflection). When $r = 2$ in this figure, one again observes the splitting of the central peak, but now the separation of each of these peaks from the $eV = 0$ is no longer symmetrical as in the non-interacting case. In addition, if we choose $\epsilon_d = 0$ the height of the peaks decreases as $r$ increases, similarly to the non-interacting case (c.f. Fig. 2b), but in Fig. 8 we chose to plot $dI/dV$ the value of $\epsilon_d$ in which the differential conductance is maximum, so that effect is not observable.

The shape of the differential conductance may be understood by noticing the quantum interference among the electron trajectories entering and leaving the side-attached quantum dots. These interferences give rise to the so-called Fano-Andreev antiresonances[5–7]. On the other hand, the states of two side-attached quantum dots interfere with each other, giving rise to a Dicke-like effect.

The equation for $dI/dV$ may be written as a superposition of two Fano and Breit–Wigner like line-shapes:

$$\frac{dI}{dV} \approx \frac{1}{1+q_+^2}\frac{(\xi_+ + q_+)^2}{\xi_+^2+1} + \frac{1}{1+q_-^2}\frac{(\xi_- + q_-)^2}{\xi_-^2+1} + \frac{4r^2}{|\varepsilon^2 - r^2|^2}, \tag{32}$$

where $\xi_\pm = (V \pm q_\pm\Gamma_{S_\pm})/\,\Gamma_{S_\pm}$ , $\varepsilon = (V + i\Gamma_-)/\,\Gamma_-$, and $\Gamma_- = \eta^2/\,\Gamma_N$. It is worth noting that the last term in the above equation does not contain adjustable parameters. The above equation is explained in Fig. 9, where the first terms take into account the destructive interference given by the Fano-Andreev effect. The last term represents a process equivalent to the transmission through a double quantum-dot in a series configuration with a coupling given by $r\eta$. The fitting of the above equation is shown in Fig. 8 (red line). Similar behavior of the differential conductance can be found in the a quantum dot coupled to a topological superconductor nanowire. In this case, tuning the non-local gate produce the hybridization of the two topological states in the superconductor producing a split of the zero bias peak in the differential conductance[38].

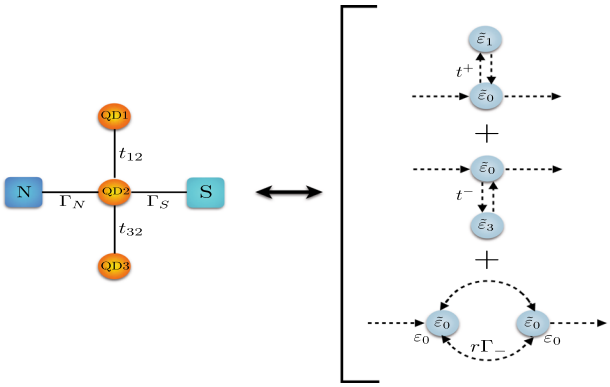


**Figure 9.** Scheme of the Andreev processes: equivalent path for the Fano-Andreev and Dicke-Andreev transmission. The complete process can be divided in two Fano effects and a transmission through equivalent quantum-dots in series.

## Summary

In summary, we have investigated the electronic transport through a triple quantum-dot device coupled to normal and superconductor leads. The main focus was to study the Andreev features appearing in both the differential conductance and QD occupations under Coulomb correlations in the QDs. Within the interferometric regime (small $t$), we have studied the impact on the sub-gap transport properties by varying the coupling ratio with the leads, $r$, when the level spacing between two side-QDs and the central QD is small $\eta \ll 1$. We found that the conductance, both in the interacting and in the non-interacting case, shows the presence Fano-Andreev reflactions and a sharp central peak resembling the Dicke resonance in the optical emission spectra of atoms, in which the role of the distance between atoms is played by the space in energy levels $\eta$. In particular, in the interacting case we show a splitting due to the Andreev reflection of the subradiant and superradiant quasiparticles states whenever the coupling ratio exceeds the certain critical value. On other hand, we explain the shape of the differential conductance near of zero-bias voltage as a result of the two equivalent quantum interference processes: the first, among the electron trajectories entering and leaving the side-attached quantum dots, the one that giving rise, to the so-called Fano-Andreev antiresonances, and the second, the interference between the states of two side-attached quantum dots, the one that giving rise to a Dicke-like effect.

Additionally, we found that when we consider the intradot interaction, the Dicke spectrum split into two symmetric sets equidistant to the electron-hole symmetry point. On the other hand, dramatic changes in the charge are produced when a subradiant state falls below the Fermi energy. This property could be used to store charge in quantum dots.

## Appendix

**$T_A$ in the limit $\Delta \gg \epsilon$.** Here we present the Andreev transmittance for a TQD between normal and superconducting leads in the limit $\Delta \gg \epsilon$ and zero inter-dot tunneling ($t = 0$).

$$T(\omega) = 2T_A(\omega) + T_Q(\omega) \tag{33}$$

$$T_A(\omega) = \Gamma_N^2(|G_{12}^r|^2) \tag{34}$$

$$T_Q = \Gamma_N\Gamma_S\,\tilde{\rho}\left(|G_{11}^r|^2 + |G_{12}^r|^2 - \frac{2\Delta}{|\epsilon|}Re\left[G_{11}^r(G_{12}^r)^*\right]\right) \tag{35}$$

with

$$\tilde{\rho}(\omega) = \frac{|\omega|\theta(|\omega| - \Delta)}{\sqrt{\omega^2 - \Delta^2}}. \tag{36}$$

On other side

$$G_{12}(\omega) = \frac{i\Gamma_S\Delta\rho(\omega)}{2\omega D}, \tag{37}$$

where

$$\rho(\omega) = \frac{|\omega|\theta(|\omega| - \Delta)}{\sqrt{\omega^2 - \Delta^2}} - i\frac{\omega\theta(\Delta - |\omega|)}{\sqrt{\Delta^2 - \omega^2}}$$

and

$$D = \left(g_{11}^{-1} - \Sigma_{NS}\right)\left(g_{22}^{-1} - \Sigma_{NS}\right) + \frac{\Gamma^2\Delta^2\rho^2}{4\omega^2},$$

where $\Sigma_{NS} = -\frac{1}{2}i(\Gamma_N + \Gamma_S\rho)$ is the self-energy of the leads, and

$$g_{11}^{-1} = \omega - \epsilon_d - \frac{t^2}{\omega - \epsilon_1} - \frac{t^2}{\omega - \epsilon_3} \tag{38}$$

$$g_{22}^{-1} = \omega - \epsilon_d - \frac{t^2}{\omega + \epsilon_1} - \frac{t^2}{\omega + \epsilon_3} \tag{39}$$

with $\epsilon_1 = \epsilon_d + \eta$ and $\epsilon_3 = \epsilon_d - \eta$

If the real part of $\rho(\omega)$ is named "a" and his imaginary part "b", we can write the above equation as:

$$G_{12}^r(\omega) = \frac{(a - b\,i)\Gamma_S\Delta/2\omega}{[c + d\,i]}, \tag{40}$$

where

$$\begin{aligned} c &= \frac{\Gamma_S^2\Delta^2}{4\omega^2}(a^2 - b^2) - \frac{1}{4}(\Gamma_N + \Gamma_S a)^2 \\ &\quad + \left(g_{11} - b\,\Gamma_S/2\right)\left(g_{22}^{-1} - b\,\Gamma_S/2\right) \\ d &= \frac{(\Gamma_N + a\,\Gamma_S)}{2}\left(g_{11}^{-1} + g_{22}^{-1} - b\Gamma_S\right) \\ &\quad + \frac{\Gamma_S^2\Delta^2 a\,b}{2\omega^2}. \end{aligned} \tag{41}$$

Consequently, we have

$$|G_{12}|^2 = \frac{\Gamma_S\Delta}{2\omega}\frac{(a^2 + b^2)}{\left[c^2 + d^2\right]}. \tag{42}$$

*Symmetric Coupling* $\Gamma_N = \Gamma_S$. Substituting these expressions in the equation to $G_{12}$ and considering $t \neq 0$, and $\Gamma_N = \Gamma_S = \Gamma$ at the limit of $\Delta \gg \omega$ we have:

$$\begin{aligned} T_A &= \Gamma_N^2|G_{12}^\sigma|^2 \\ &= \Gamma_N^2|G_{12}^\sigma|^2 = \frac{\Gamma^4(\omega^2 - \eta^2)^4}{\Gamma^4\left[\omega^2 - \eta^2\right]^4 + 4\omega^4\left[(\omega^2 - \eta^2 - 2t^2\right]^4}. \end{aligned} \tag{43}$$

Then, the first maximum occurs when $\omega = 0$ and the two other maxima values of $T(\epsilon)$ occur when $\omega = \pm\sqrt{\eta^2 + 2t^2}$.

*Asymmetric Coupling* $\Gamma_S = 2\Gamma$. Substituting these expressions in the equation to $G_{12}$, considering $t \neq 0$, and $\Gamma_S = 2\Gamma$ at the limit of $\Delta \gg \omega$ we have:

$$\begin{aligned} T_A &= \Gamma_N^2|G_{12}^\sigma|^2 \\ &= \frac{\Gamma^4}{\left[\frac{\omega\Gamma(\omega^2 - \eta^2 - 2t^2)}{(\omega^2 - \eta^2)}\right]^2 + \left[\omega^2\frac{(\omega^2 - \eta^2 - 2t^2)^2}{(\omega^2 - \eta^2)^2} - \frac{5\Gamma^2}{4}\right]^2}. \end{aligned} \tag{44}$$

In this case because of this functional structure, $T_A$ presents six peaks located symmetrically each side of $\omega = 0$. As before when the coupling to the leads was symmetric, the zeros of $T(\omega)$ occur when $\omega = \pm\eta$. At the particular case $t = 0$ and $\eta = 0$, we have:

$$T_A(\omega) = \frac{\Gamma^4}{\left[\Gamma^2\epsilon^2 + (\omega^2 - 5\Gamma^2/4)^2\right]}. \tag{45}$$

Then, the maximum value of $T(\omega)$ occurs close to $\omega = \pm\Gamma$:

$$
\begin{aligned}
T_A(\pm\Gamma) &= \frac{\Gamma^4}{\left[\Gamma^2\Gamma^2 + (\Gamma^2 - 5\Gamma^2/4)^2\right]} \\
&= \frac{\Gamma^4}{\left[\Gamma^4 + (\Gamma^2/4)^2\right]} \\
&= \frac{16\Gamma^4}{17\Gamma^4} \\
&\approx 1.
\end{aligned}
$$

**Linear and differential conductance in the limit of low temperature.** Linear conductance $G$ in the sub-gap limit ($eV \ll \Delta$) is written as:

$$G = \frac{4e^2}{h}\int \frac{\partial f}{\partial \omega} T_A(\omega) d\omega. \tag{46}$$

If $k_B\tau \to 0$ then $\frac{\partial f}{\partial \omega} \to \delta(\omega - \mu)$, so that

$$G = \frac{4e^2}{h}\int \delta(\omega - \mu) T_A(\omega) d\omega = \frac{4e^2}{h} T_A(\mu). \tag{47}$$

Consequently, the peaks of $T_A$ as a function of the energy $\epsilon$ for a fixed value of $\epsilon_d$ are the same for $G$ as a function of $\mu$ for a fixed value of $\epsilon_d$. For this reason, as expected, the graph of $G$ in function of the Fermi energy $\mu$, in the case of a quantum dot asymmetric coupling with the leads, presents two peaks as the case of $T_A$ as a function of the energy.

***dI/dV* vs $T_A$.** The general form for the electronic current in the sub-gap limit ($eV \ll \Delta$) is

$$I = \frac{2e}{h}\int d\omega\, T_A\left[f_L(\omega - eV) - f_L(\omega + eV)\right]. \tag{48}$$

In the limit of low temperature $k_B\tau \to 0$

$$I = \frac{2e}{h}\int d\omega\, T_A[\Theta(eV - \omega) - \Theta(-\omega - eV)] \tag{49}$$

$$I = \frac{2e}{h}\int d\omega\, T_A[1 - \Theta(\omega - eV) - 1 + \Theta(\omega + eV)] \tag{50}$$

$$I = \frac{2e}{h}\int d\omega\, T_A[\Theta(\omega + eV) - \Theta(\omega - eV)] \tag{51}$$

$$I = \frac{2e}{h}\int_{-eV}^{eV} d\omega\, T_A(\omega). \tag{52}$$

Then

$$\frac{dI}{dV} = \frac{2e}{h}\int d\omega\, T_A \frac{\partial}{\partial V}[\Theta(\omega + eV) - \Theta(\omega - eV)] \tag{53}$$

$$\frac{dI}{dV} = \frac{2e}{h}\int d\omega\, T_A[\delta(\omega + eV) + \delta(\omega - eV)] \tag{54}$$

$$\frac{dI}{dV} = \frac{2e^2}{h}[T_A(-eV) + T_A(eV)] = \frac{4e^2}{h} T_A(eV). \tag{55}$$

Consequently, for a fixed value of $\epsilon_d$, the peaks of $T_A$ as a function of $eV$ are the same as $\partial I/\partial V$ in function of $eV$.

Received: 6 November 2020; Accepted: 29 January 2021
Published online: 16 February 2021

## References

1. Guevara, M. L., Claro, F. & Orellana, P. A. Ghost Fano resonance in a double quantum dot molecule attached to leads. *Phys. Rev. B* **67**, 195335. https://doi.org/10.1103/PhysRevB.67.195335 (2003).
2. Lu, H., Lu, R. & Zhu, B. F. Tunable Fano effect in parallel-coupled double quantum dot system. *J. Phys. Condens. Matter* **18**, 8961. https://doi.org/10.1103/PhysRevB.71.235320 (2006).

3. Baranski, J. & Domanski, T. Decoherence effect on the Fano lineshapes in double quantum dots coupled between normal and superconducting leads. *Phys. Rev. B* **85**, 205451. https://doi.org/10.1103/PhysRevB.85.205451 (2012).
4. Ding, G. H., Kim, C. K. & Nahm, K. Fano resonance in electron transport through parallel double quantum dots in the Kondo regime. *Phys. Rev. B* **71**, 205313. https://doi.org/10.1103/PhysRevB.71.205313 (2005).
5. Calle, M. *et al.* Fano-Andreev effect in a T-shape double quantum dot in the Kondo regime. *J. Phys. Condens. Matter* **29**, 135301 (2017).
6. Calle, A. M., Pacheco, M. & Orellana, P. A. Fano effect and Andreev bound states in T-shape double quantum dots. *Phys. Lett. A* **377**, 1474. https://doi.org/10.1088/1361-648X/aa58c1/meta (2013).
7. Barański, J., Zienkiewicz, T., Barańska, M. & Kapcia, K. J. Anomalous Fano resonance in double quantum dot system coupled to superconductor. *Sci. Rep.* **10**, 2881. https://doi.org/10.1038/s41598-020-59498-y (2020).
8. Gómez, I., Domínguez-Adame, F. & Orellana, P. A. Fano-like resonances in three-quantum-dot Aharonov–Bohm rings. *J. Phys. Condens. Matter* **16**, 1613. https://doi.org/10.1088/0953-8984/16/9/009 (2004).
9. Ye, C.-Z., Li, Z.-J., Nie, Y.-H. & Liang, J.-Q. Rashba spin-orbit interaction induced spin-polarized Andreev-reflection current through a double Aharonov-Bohm interferometer. *J. Appl. Phys.* **104**, 053721. https://doi.org/10.1063/1.2977685 (2008).
10. Trocha, P. & Barnaś, J. Quantum interference and Coulomb correlation effects in spin-polarized transport through two coupled quantum dots. *J. Phys. Rev. B* **76**, 165432. https://doi.org/10.1103/PhysRevB.76.165432 (2007).
11. Sztenkiel, D. & Świrkowicz, R. Interference effects in a double quantum dot system with inter-dot Coulomb correlations. *J. Phys. Condens. Matter* **19**, 176202. https://doi.org/10.1103/PhysRevB.67.1953350 (2007).
12. Liu, Y.-S., Chen, H. & Yang, X.-F. Transport properties of an Aharonov–Bohm ring with strong interdot coulomb interaction. *J. Phys. Condens. Matter* **19**, 246201. https://doi.org/10.1103/PhysRevB.67.1953351 (2007).
13. Dicke, R. H. The effect of collisions upon the Doppler width of spectral lines. *Phys. Rev.* **89**, 472. https://doi.org/10.1103/PhysRevB.67.1953352 (1953).
14. Dicke, R. H. Coherence in spontaneous radiation processes. *Phys. Rev.* **93**, 99. https://doi.org/10.1103/PhysRevB.67.1953353 (1954).
15. Brandes, T. Coherent and collective quantum optical effects in mesoscopic systems. *Phys. Rep.* **408**, 315. https://doi.org/10.1103/PhysRevB.67.1953354 (2005).
16. Shahbazyan, T. V. & Raikh, M. E. Two-channel resonant tunneling. *Phys. Rev. B* **49**, 17123. https://doi.org/10.1103/PhysRevB.67.1953355 (1994).
17. Shahbazyan, T. V. & Ulloa, S. E. Localized states in a strong magnetic field: Resonant scattering and the Dicke effect. *Phys. Rev. B* **57**, 6642. https://doi.org/10.1103/PhysRevB.67.1953356 (1998).
18. Vorrath, T. & Brandes, T. Dicke effect in the tunnel current through two double quantum dots. *Phys. Rev. B* **68**, 035309. https://doi.org/10.1103/PhysRevB.67.1953357 (2003).
19. Wunsch, B. & Chudnovskiy, A. Quasistates and their relation to the Dicke effect in a mesoscopic ring coupled to a reservoir. *Phys. Rev. B* **68**, 245317. https://doi.org/10.1103/PhysRevB.67.1953358 (2003).
20. Orellana, P. A., Ladrón de Guevara, M. L. & Claro, F. Controlling Fano and Dicke effects via a magnetic flux in a two-site Anderson model. *Phys. Rev. B* **70**, 233315. https://doi.org/10.1103/PhysRevB.67.1953359 (2004).
21. Trocha, P. & Barnaś, J. Dicke-like effect in spin-polarized transport through coupled quantum dots. *J. Phys. Condens. Matter* **20**, 125220. https://doi.org/10.1103/PhysRevB.71.2353200 (2008).
22. Trocha, P. & Barnaś, J. Kondo–Dicke resonances in electronic transport through triple quantum dots. *Phys. Rev. B* **78**, 075424. https://doi.org/10.1103/PhysRevB.71.2353201 (2008).
23. Vernek, E., Orellana, P. A. & Ulloa, S. E. Suppression of Kondo screening by the Dicke effect in multiple quantum dots. *Phys. Rev. B* **82**, 165304. https://doi.org/10.1103/PhysRevB.71.2353202 (2010).
24. Wang, Q., Xie, H., Nie, Y.-H. & Ren, W. Enhancement of thermoelectric efficiency in triple quantum dots by the Dicke effect. *Phys. Rev. B* **87**, 075102. https://doi.org/10.1103/PhysRevB.71.2353203 (2013).
25. Sun, Q.-F., Wang, J. & Lin, T.-H. Resonant Andreev reflection in a normal-metal-quantum-dot-superconductor system. *Phys. Rev. B* **59**, 5. https://doi.org/10.1103/PhysRevB.71.2353204 (1999).
26. Yu, Z., Qing-Feng, S. & Tsung-Han, L. Effect of intra-dot coulomb interaction on Andreev reflection in normal-metal/quantum-dot/superconductor system. *Commun. Theor. Phys. (Beijing, China)* **36**, 101 (2001).
27. Siqueira, E. C. & Cabrera, G. G. Andreev tunneling through a double quantum-dot system coupled to a ferromagnet and a superconductor: Effects of mean-field electronic correlations. *Phys. Rev. B* **81**, 094526. https://doi.org/10.1103/PhysRevB.71.2353205 (2010).
28. Trocha, P. & Barnaś, J. Spin-polarized Andreev transport influenced by Coulomb repulsion through a two-quantum-dot system. *Phys. Rev. B* **89**, 245418. https://doi.org/10.1103/PhysRevB.71.2353206 (2014).
29. Trocha, P. & Barnaś, J. Spin-dependent thermoelectric phenomena in a quantum dot attached to ferromagnetic and superconducting electrodes. *Phys. Rev. B* **95**, 165439. https://doi.org/10.1103/PhysRevB.71.2353207 (2017).
30. Bai, L., Zhang, R. & Duan, C.-L. Andreev reflection tunneling through a triangular triple quantum dot system. *Phys. B* **405**, 23. https://doi.org/10.1103/PhysRevB.71.2353208 (2010).
31. Bardeen, J., Cooper, L. N. & Schrieffer, J. R. Microscopic theory of superconductivity. *Phys. Rev.* **106**, 162. https://doi.org/10.1103/PhysRevB.71.2353209 (1957).
32. Orellana, P. A., Lara, G. A. & Anda, E. V. Kondo and Dicke effect in quantum dots side coupled to a quantum wire. *Phys. Rev. B* **74**, 193315. https://doi.org/10.1103/PhysRevB.85.2054510 (2006).
33. de Guevara, M. L. & Orellana, P. A. Electronic transport through a parallel-coupled triple quantum dot molecule: Fano resonances and bound states in the continuum. *Phys. Rev. B* **73**, 205303. https://doi.org/10.1103/PhysRevB.85.2054511 (2006).
34. Bai, L., Wu, Y.-J. & Wang, B. Andreev reflection in a triple quantum dot system coupled with a normal-metal and a superconductor. *Phys. Status Solidi B* **247**, 335. https://doi.org/10.1103/PhysRevB.85.2054512 (2010).
35. Xu, W.-P., Zhang, Y.-Y., Wang, Q., Li, Z.-J. & Nie, Y.-H. Thermoelectric effects in triple quantum dots coupled to a normal and a superconducting leads. *Phys. Lett. A* **380**, 958. https://doi.org/10.1103/PhysRevB.85.2054513 (2016).
36. Glodzik, S., Wójcik, K. P., Weymann, I. & Domański, T. Interplay between electron pairing and Dicke effect in triple quantum dots structures. *Phys. Rev. B* **95**, 125419. https://doi.org/10.1103/PhysRevB.85.2054514 (2017).
37. Hubbard, J. & Flowers, B. H. Electron correlations in narrow energy bands. *Proc. R. Soc. Lond. A* **276**, 238 (1963).
38. Zhang, H., Liu, D. E., Wimmer, M. & Kouwenhoven, L. P. Next steps of quantum transport in Majorana nanowire devices. *Nat. Commun.* **10**, 5128 (2019).


## Acknowledgements

This work has been partially supported by Universidad Santa María Grant USM-DGIIP PI-LI 1925 and 1919 and FONDECYT Grant 1201876.

## Author contributions

A.G.I. derived the analytic expressions, performed numerical calculations and wrote the paper in its final form. P.A.O., E.C.S., M.P. and A.M.C. contributed to the discussions and analysis of the results. All authors reviewed the manuscript.All authors accepted it.

## Funding

Funding was funded by Universidad Técnica Federico Santa María (Grant No: USM-DGIIP PI-LI 1925, 1919), FONDECYT (Grant No: 1201876)).

## Competing interests

The authors declare no competing interests.

## Additional information

**Correspondence** and requests for materials should be addressed to A.G.I. or P.A.O.

**Reprints and permissions information** is available at www.nature.com/reprints.

**Publisher's note** Springer Nature remains neutral with regard to jurisdictional claims in published maps and institutional affiliations.

# Fano-Andreev effect in a T-shaped Double Quantum Dot in the Coulomb-blockade regime

A. González I.,[1] A. M. Calle,[2] M. Pacheco,[1] E. C. Siqueira,[3] and Pedro A. Orellana[1]

[1] *Departamento de Física, Universidad Técnica Federico Santa María, Casilla 110 V, Valparaíso, Chile*
[2] *Departamento de Física, Universidad Católica del Norte, Antofagasta, Chile*
[3] *Departamento Acadêmico de Física, Universidade Tecnológica Federal do Paraná, Brazil*

We studied the effects of superconducting quantum correlations in a system consisting of two quantum dots, two normal leads, and a superconductor. Using the non-equilibrium Green's functions method, we analyzed the transmission, density of states, and differential conductance of electrons between the normal leads. We found that the superconducting correlations resulted in Fano-Andreev interference, which is characterized by two anti-resonance line shapes in all of these quantities. This behavior was observed in both equilibrium and non-equilibrium regimes and persisted even when Coulomb correlations were taken into account using the Hubbard-I approximation. It is worth noting that the robustness of this behavior against these conditions has not been studied previously in the literature.

## I. INTRODUCTION

The investigation of hybrid structures, where normal conductors are connected to superconductors, has garnered significant interest due to their potential for applications in electronics, spintronics, and quantum information processing [1]. When a normal metal is connected to a superconductor lead, the superconducting order can leak into the normal metal. This causes pairing correlations and a superconducting gap due to the proximity effect[2]. The mechanism responsible for the proximity effect is known as Andreev reflection[3]. In this process, an electron is reflected as a hole at the interface between the leads. The missing charge in the normal lead appears as a Cooper pair within the superconductor. Since the electrons in the superconductor side and the hole in the normal lead are correlated, these are represented by bound states. In effect, the two charges coming from the normal lead cannot penetrate deep into the superconductor side, being absorbed into the superconductor condensate. In hybrid systems composed of quantum dots (QDs), these bound states, called Andreev bound states (ABS), appear as resonances in the QD transmission spectrum, with energies within the superconductor gap. The presence of ABSs is the key ingredient to many different features exhibited by QD-based systems[4–16]. The ABSs modify the so-called Fano effect[17, 18], a well-known phenomenon resulting from quantum interference between discrete and continuum states. In QDs-based systems, the Fano effect signature is an asymmetric resonance pattern arising in the transmission spectrum of the QDs or double quantum dots (DQDs). Several authors have studied the effect of quantum decoherence on Fano lineshapes. To this end, they introduced a normal floating lead directly coupled to the double quantum dot (DQD). Their findings show that the floating lead coupled to the lateral QD plays a crucial role in destroying the Fano lineshape. [19, 20]. Other authors have studied the structure of T-shaped QDs coupled to two normal or ferromagnetic leads left and right and a superconducting lead [21–26]. In particular, A. M. Calle et al. [27] have shown that, in a noninteracting T-shaped double quantum dot coupled to two normal metals, the transmission between the normal leads (ET) exhibits Fano resonances due to the appearance of ABSs in the non-interacting DQD, due to the presence of the superconducting lead (Fano-Andreev effect). Using a mean-field treatment of Coulomb correlations, E. C. Siqueira *et al.*. [28] have shown complementary resonance patterns between AR and ET transmittance when a superconductor lead is coupled to a QD, which itself is coupled to two ferromagnetic leads. The effect was shown to be a result of the interplay between the ABSs and the spin polarization provided by the ferromagnets. When the charging energy is much larger than the thermal energy of the charge carriers and the QD is only weakly coupled to the leads, Coulomb correlations become increasingly significant at low temperatures. This is known as the Coulomb blockade regime, where the number of electrons in the dot is fixed. Sequential tunneling is suppressed and transport is only possible when the energy of the state $|N_i>|$ is aligned with the chemical potential of the leads. As a result, the linear conductance through the quantum dot shows a series of peaks that correspond to the degeneracy regions (Coulomb peaks). These peaks are separated by regions of low conductance. However, when the temperature is lowered, the coupling of the electron within the QD to the electrons of the leads gives rise to virtual quantum states within the QD, which allows for an additional transport channel through the QD. This manifests itself as a narrow resonance peak in the QD transmission spectrum, called the Kondo resonance. However, when one of the leads is a superconductor in a three-terminal system, it is possible to probe the interaction between the Fano effect, ET transmission, and ABS states. The interaction between ABS and the Kondo effect in hybrid superconductor nanostructures has been extensively studied[14, 29, 30]. For the structure of DQDs of T shape, A. M. Calle *et al.*.[31] found that the Kondo resonance modifies ABS resonances. However, in systems composed of DQDs, the interplay among the Coulomb correlation

within an intermediate range of values, Fano effect, and ABS states, has not been studied in depth in the literature, despite the potential for original effects that may be obtained in these systems.

In this work, we investigate the electronic transport properties of a T-shaped DQD system. Fig. 1 shows the scheme, where the central QD, $QD_a$, is connected to normal leads, while the other QD, $QD_b$, is coupled to a superconductor lead (S).In our analysis, we focus on the Coulomb blockade regime, with identical values for the onsite Coulomb interaction parameters in both quantum dots (QD), namely $U_a = U_b$. To obtain our results, we use the equation-of-motion (EOM) method to calculate the relevant Green's functions. The intradot Coulomb correlation is considered in the Hubbard-I approximation, which provides a reliable description of the Coulomb blockade regime. We investigate in the nonequilibrium regime and at zero temperature the impact of the Coulomb interaction (U), inter-dot coupling, and coupling between QD and leads on the Fano-Andreev effect in both molecular and interferometric regimes. To study these effects, we employ the nonequilibrium Green function formalism.

This paper is organized as follows: in Sec. II, we present the model and formulation for the system displayed in Fig. 1, in Sec. III, the numerical results are presented and discussed. Finally, a summary and the main conclusions are presented in Sec. IV.

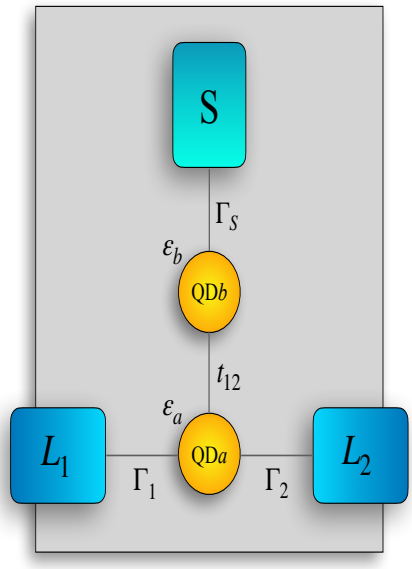


FIG. 1. The T-shape double QD system studied in this work. It is composed of two quantum dots in which the $QD_a$ is coupled to two normal metals $L_1$ and $L_2$, with the coupling strength being determined by the parameters $\Gamma_1$ and $\Gamma_2$. The second quantum dot, $QD_b$, is coupled to the superconductor $S$, with the coupling strength being modeled by the parameter $\Gamma_S$. The coupling between the QDs is modeled by the $t_{12}$ parameter.

## II. MODEL AND FORMULATION

In Fig. 1, the T-shape double quantum-dot system is illustrated. It consists of a central quantum dot, $QD_a$, coupled to the two normal leads, $L_1$ and $L_2$, and a side $QD_b$, connected to a superconductor $S$. The Hamiltonian of the system is given by:

$$H = H_1 + H_2 + H_S + H_{DQD} + H_T. \tag{1}$$

The first and the second terms are the Hamiltonians for the normal leads at the left (1) and right (2) sides of $QD_a$. These are modeled by Eqs. (2) and (3):

$$H_1 = \sum_k \sum_\sigma \epsilon_{1k\sigma} c^\dagger_{1k\sigma} c_{1k\sigma}, \tag{2}$$

and

$$H_2 = \sum_k \sum_\sigma \epsilon_{2k\sigma} c^\dagger_{2k\sigma} c_{2k\sigma}, \tag{3}$$

where $c^\dagger_{\alpha k\sigma}$ ($c_{\alpha k\sigma}$) is the electron creation (annihilation) operator of an electron with spin $\sigma$ and energy $\epsilon_{k\sigma}$ in the $\alpha$ electrode.

The second term stands for the BCS Hamiltonian[32] of the superconducting ($S$) lead and reads:

$$H_S = \sum_k \sum_\sigma \epsilon_{kS} c^\dagger_{kS\sigma} c_{kS\sigma} + \sum_k (\Delta^* c_{kS\downarrow} c_{-kS\uparrow} + \Delta c^\dagger_{-kS\uparrow} c^\dagger_{kS\downarrow}), \tag{4}$$

where $c^\dagger_{kS\sigma}$ ($c_{kS\sigma}$) is the electron creation (annihilation) operator of an electron with spin $\sigma$ and energy $\epsilon_{kS}$ in the superconducting electrode, and $\Delta$ denotes pair potential, whose absolute value gives the superconducting energy gap.

The $H_{DQD}$ term is given by Eq. (5) and takes into account the coupling between the QDs, modeled by the variable $t_{12} = t$, and the Coulomb interaction at each QD, whose strength is modeled by $U_m$, $m = a, b$. The QDs are assumed to have a single spin degenerated level, whose value is determined by $\epsilon_{dm,\sigma}$, $m = a, b$.

$$H_{DQD} = \sum_{m=a,b,\sigma} \epsilon_{dm,\sigma} d^{\dagger}_{m,\sigma} d_{m,\sigma} + \sum_{\sigma} t \left[ d^{\dagger}_{a\sigma} d_{b\sigma} + d^{\dagger}_{a\sigma} d_{b\sigma} \right] + \sum_{m=a,b} U_m n_{m\sigma} n_{m\bar{\sigma}} \tag{5}$$

### A. Green's functions

In order to obtain the transport properties for the system modeled by Eq. (1), we have used the well-known non-equilibrium Green's function approach[33, 34] along with the equation-of-motion method. This formalism has been extensively applied to nanostructured systems. The presence of the superconductor has been taken into account by expressing Green's functions within the Nambu space. In this way, Green's functions are represented by $4 \times 4$ matrices resulting from the tensor product between spin and electron-hole subspaces. By using this formalism, we have obtained a system of coupled Dyson equations for the retarded Green's functions matrices $\mathbf{G}^r_{aa}$ and $\mathbf{G}^r_{bb}$, for $QD_a$ and $QD_b$, respectively:

$$\mathbf{G}^r_{aa} = \mathbf{G}^{ro}_{aa} + \mathbf{G}^r_{aa} \mathbf{t}^{\dagger}_{ab} \mathbf{G}^{ro}_{bb} \mathbf{t}_{ab} \mathbf{G}^{ro}_{aa}, \tag{6}$$

and

$$\mathbf{G}^r_{bb} = \mathbf{G}^{ro}_{bb} + \mathbf{G}^r_{bb} \mathbf{t}^{\dagger}_{ab} \mathbf{G}^{ro}_{aa} \mathbf{t}_{ab} \mathbf{G}^{ro}_{bb}, \tag{7}$$

with

$$\mathbf{G}^{ro}_{aa} = \mathbf{g}^r_{aa} (1 - \mathbf{\Sigma}^r_L \mathbf{g}^r_{aa})^{-1}, \tag{8}$$

and

$$\mathbf{G}^{ro}_{bb} = \mathbf{g}^r_{bb} (1 - \mathbf{\Sigma}^r_S \mathbf{g}^r_{bb})^{-1}. \tag{9}$$

In Eqs. (6) to (9), $\mathbf{g}^r_{aa}$ and $\mathbf{g}^r_{bb}$ are the $QD_a$ and $QD_b$ Green's functions, respectively, when the QDs are isolated from the leads; $\mathbf{t}_{ab}$ describes the tunneling between $QD_a$ and $QD_b$. The coupling to the normal and superconducting leads are modeled by retarded/advanced self-energies $\mathbf{\Sigma}^r_L = \mathbf{\Sigma}^r_1 + \mathbf{\Sigma}^r_2$ and $\mathbf{\Sigma}^r_S$, respectively.

The self-energy for the coupling to the normal leads ($L_1$ and $L_2$) is given by Eq. (10):

$$\mathbf{\Sigma}^{r,a}_L = \mp \frac{i}{2} (\Gamma_1 + \Gamma_2) \begin{bmatrix} 1 & 0 & 0 & 0 \\ 0 & 1 & 0 & 0 \\ 0 & 0 & 1 & 0 \\ 0 & 0 & 0 & 1 \end{bmatrix}, \tag{10}$$

where $\Gamma_i = \Gamma_{i\uparrow} + \Gamma_{i\downarrow}$ and $\Gamma_{i\sigma} = 2\pi |t_i|^2 N_i$, $(i = 1, 2)$ being the coupling strength, with $t_i$ being amplitude for an electron with spin $\sigma$ of $QD_a$ to be transferred to the lead $L_i$; $N_i$ is the density of states at Fermi level for the normal lead, $L_i$. Since we have assumed both normal leads as non-magnetic, the density of states is the same for both spins.

The retarded/advanced self-energy of the superconductor is given by Eq. (11):

$$\mathbf{\Sigma}^{r,a}_S = \mp \frac{i}{2} \rho_S(\epsilon) \Gamma_S \begin{bmatrix} 1 & -\frac{\Delta}{\epsilon} & 0 & 0 \\ -\frac{\Delta}{\epsilon} & 1 & 0 & 0 \\ 0 & 0 & 1 & \frac{\Delta}{\epsilon} \\ 0 & 0 & \frac{\Delta}{\epsilon} & 1 \end{bmatrix}. \tag{11}$$

In Eq. (11), $\Gamma_S = 2\pi |t_s|^2 N_s$ is the coupling strength between the superconductor lead and $QD_b$, defined in terms of the amplitude of tunneling $|t_s|$ and the normal density of states of $N_s$. The $\Delta$ appearing in some of the matrix elements stands for the energy gap of the superconductor and accounts for the electron-hole coupling. The energy gap plays a central role in this model and also modifies the self-energy through $\rho_S$, the dimensionless modified BCS density of states, whose expression is given by:

$$\rho_S(\epsilon) = \frac{|\epsilon| \theta(|\epsilon| - \Delta)}{\sqrt{\epsilon^2 - \Delta^2}} - i \frac{\epsilon \theta(\Delta - |\epsilon|)}{\sqrt{\Delta^2 - \epsilon^2}}, \tag{12}$$

with the imaginary part accounting for the Andreev bound states (ABS), within the superconductor gap.

The presence of electronic correlations associates the QD energy levels with the electronic occupations, which, in turn, depend on external parameters like gate and bias voltages. As a result, Eqs. (6) and (7) must be solved in a self-consistent way, together with the occupations of the QDs. Such occupations are obtained from the diagonal matrix elements of the "lesser" Green's function matrix, which is obtained through the Keldysh equation. For the $QD_a$, the expression reads:

$$\mathbf{G}^<_{aa} = \mathbf{G}^r_{aa}(\omega) \mathbf{\Sigma}^<_{Ta} \mathbf{G}^a_{aa}(\omega), \tag{13}$$

with

$$\mathbf{\Sigma}^<_{Ta} = \mathbf{\Sigma}^<_L(\epsilon) + \mathbf{t}^{\dagger}_{ab} \mathbf{G}^{ro}_{bb} \mathbf{\Sigma}^<_S(\epsilon) \mathbf{G}^{ao}_{bb} \mathbf{t}_{ab}. \tag{14}$$

The expression for $QD_b$ can be obtained by exchanging the indices $a$ and $b$. In Eq. (13), $\mathbf{\Sigma}^<_{Ta}$ represents the "lesser" self-energy, which is expressed in terms of the self-energies of the leads: $\mathbf{\Sigma}^<_L = \mathbf{\Sigma}^<_1 + \mathbf{\Sigma}^<_2$ and $\mathbf{\Sigma}^<_S$. Assuming that the leads are in equilibrium with well-defined chemical potential and temperature, the self-energies of the leads can be obtained using the fluctuation-dissipation theorem: $\mathbf{\Sigma}^<_i = \mathbf{F}_i [\mathbf{\Sigma}^a_i - \mathbf{\Sigma}^r_i]$, where the Fermi matrix $\mathbf{F}_i$ is given by

$$\mathbf{F}_i = i \begin{bmatrix} f_i & 0 & 0 & 0 \\ 0 & \bar{f}_i & 0 & 0 \\ 0 & 0 & f_i & 0 \\ 0 & 0 & 0 & \bar{f}_i \end{bmatrix}, \tag{15}$$

with $f_i = f(\epsilon - eV_i)$ and $\bar{f}_i = f(\epsilon + eV_i)$ $(i = 1, 2, S)$ being the Fermi functions for electrons and holes, respectively. Since the superconductor is assumed to be grounded, $f_i = f(\epsilon)$ for $i = s$.

### B. Transmittance and current

The presence of Coulomb correlations leads to a self-consistent problem when solving Eqs. (6) and (7), since the dependency on the occupations wraps the Green's functions to the occupancies of the QDs. Within the equation-of-motion approach used in this work, this results in an infinite set of equations with Green's functions of increasing order of complexity. To obtain a closed set of equations, one needs to resort to some approximation on the Coulomb correlations. In this work, we have used the so-called Hubbard-I approximation[35], which allows us to derive a simple expression for the electrical current in terms of the different transmission amplitudes that contribute to the electronic transport for this system. In fact, the current $I_j$, flowing in the lead $L_j$ $(j = 1, 2)$, is given by the following expression:

$$I_j = \frac{e}{\hbar}\int d\epsilon\,[\mathbf{G}^r_{aa}(\epsilon)\mathbf{\Sigma}^<_j(\epsilon) + \mathbf{G}^<_{aa}(\epsilon)\mathbf{\Sigma}^a_j(\epsilon) + \text{H.c.}]_{(11+33)}, \qquad j = 1, 2. \tag{16}$$

where $11 + 33$ stands for the sum of the 11 and 33 matrix elements of the current matrix. By substituting the Green's functions and self-energies into Eq. (16), one obtains the main expression for the electric current flowing in the lead $L_1$, written in terms of the transmittances:

$$I_1 = \frac{e}{h}\int [T^{DAR}_{11}(f_1 - \bar{f}_1) + T^{ET}_{12}(f_1 - f_2) + T^{CAR}_{12}(f_1 - \bar{f}_2) + T^{QP}_{1S}(f_1 - f_S)]d\epsilon, \tag{17}$$

The first term in Eqs. (17) , $T^{DAR}_{11}$, corresponds to direct Andreev reflection transmittances through the paths $(L_1 - QD_a - QD_b - S)$, i.e., an electron of $L_1$ is reflected by $S$ into a hole of $L_1$. The second term, $T^{ET}_{12}$, represents electron tunneling (ET) between the normal leads via $(L_1 - QD_a - QD_b - L_2)$ path. The next term, $T^{CAR}_{11}$, accounts for the transmittances of crossed Andreev reflection through the path $((L_1, L_2) - QD_a - QD_b - S)$, i.e., an electron of $L_1$ is reflected by $S$ into a hole of $L_2$. Finally, the last term, $T^{QP}_{11}$, corresponds to quasiparticles tunneling through the $(L_1 - QD_a - QD_b - S)$ path.

The amplitudes can be expressed in terms of Green's functions, which are given as follows:

$$\begin{aligned}
T^{DAR}_{11} &= \Gamma_1^2(|G^r_{aa,14}|^2 + |G^r_{aa,12}|^2 + |G^r_{aa,34}|^2 + |G^r_{aa,32}|^2)\\
T^{CAR}_{12} &= \Gamma_1\Gamma_2(|G^r_{aa,14}|^2 + |G^r_{aa,12}|^2 + |G^r_{aa,34}|^2 + |G^r_{aa,32}|^2)\\
T^{ET}_{12} &= \Gamma_1\Gamma_2(|G^r_{aa,33}|^2 + |G^r_{aa,31}|^2 + |G^r_{aa,13}|^2 + |G^r_{aa,11}|^2)\\
T^{QP}_{1S} &= \bar{\rho}\Gamma_1\Gamma_S\{Y^-_{21}|G^r_{aa,12}|^2 + X^+_{34}|G^r_{aa,13}|^2 + Y^+_{43}|G^r_{aa,14}|^2\\
&\quad + X^-_{12}|G^r_{aa,11}|^2 - Z^+_{34}G^r_{aa,13}[G^r_{aa,14}]^* - [Z^+_{34}]^*[G^r_{aa,13}]^*G^r_{aa,14}\\
&\quad - Z^-_{12}G^r_{aa,11}[G^r_{aa,12}]^* - [Z^-_{12}]^*[G^r_{aa,11}]^*G^r_{aa,12}\\
&\quad + Y^-_{21}|G^r_{aa,32}|^2 + X^+_{34}|G^r_{aa,33}|^2 + Y^+_{43}|G^r_{aa,34}|^2\\
&\quad + X^-_{32}|G^r_{aa,31}|^2 - Z^+_{34}G^r_{aa,33}[G^r_{aa,34}]^*\\
&\quad - [Z^+_{34}]^*[G^r_{aa,33}]^*G^r_{aa,34} - Z^-_{12}G^r_{aa,31}[G^r_{aa,32}]^*\\
&\quad - [Z^-_{12}]^*[G^r_{aa,31}]^*G^r_{aa,32}\}
\end{aligned} \tag{18}$$

where

$$\begin{aligned}
X^\pm_{ij} &\equiv t^2[|G^{ro}_{bb,ii}|^2 + |G^{ro}_{bb,ij}|^2 \pm \frac{\Delta}{\epsilon}(G^{ro}_{bb,ii}[G^{ro}_{bb,ij}]^* + G^{ro}_{bb,ij}[G^{ro}_{bb,ii}]^*),\\
Y^\pm_{ij} &\equiv t^2[|G^{ro}_{bb,ii}|^2 + |G^{ro}_{bb,ji}|^2 \pm \frac{\Delta}{\epsilon}(G^{ro}_{bb,ii}[G^{ro}_{bb,ji}]^* + G^{ro}_{bb,ji}[G^{ro}_{bb,ii}]^*)],\\
Z^\pm_{ij} &\equiv t^2[G^{ro}_{bb,ij}[G^{ro}_{bb,jj}]^* + [G^{ro}_{bb,ij}]^*G^{ro}_{bb,ii}\\
&\qquad \pm \frac{\Delta}{\epsilon}(|G^{ro}_{bb,ij}|^2 + [G^{ro}_{bb,jj}]^*G^{ro}_{bb,ii})],
\end{aligned} \tag{19}$$

(The current flowing and transmittances in $L_2$ can be obtained by interchanging the indexes 1 and 2 in the above equation).

### C. Self-consistent calculations

Regarding the occupations of QDs, they are determined by the "lesser" Green function. In the case of normal leads with no polarization, the average occupation number remains independent of spin. This allows us to set, for each QD, $\langle n_{i,\sigma}\rangle = \langle n_i\rangle$ where $i = a, b$. These occupation numbers are obtained by solving the following self-consistent system of integral equations:

$$\langle n_{a\uparrow}\rangle = -i\int \frac{d\epsilon}{2\pi}\, G^<_{aa,11}[\epsilon, \langle n_{a\uparrow}\rangle, \langle n_{a\downarrow}\rangle, \langle n_{b\uparrow}\rangle, \langle n_{b\downarrow}\rangle], \tag{20a}$$

$$\langle n_{a\downarrow}\rangle = -i\int \frac{d\epsilon}{2\pi}\, G^<_{aa,33}[\epsilon, \langle n_{a\uparrow}\rangle, \langle n_{a\downarrow}\rangle, \langle n_{b\uparrow}\rangle, \langle n_{b\downarrow}\rangle], \tag{20b}$$

$$\langle n_{b\uparrow}\rangle = -i\int \frac{d\epsilon}{2\pi}\, G^<_{bb,11}[\epsilon, \langle n_{a\uparrow}\rangle, \langle n_{a\downarrow}\rangle, \langle n_{b\uparrow}\rangle, \langle n_{b\downarrow}\rangle], \tag{20c}$$

$$\langle n_{b\downarrow}\rangle = -i\int \frac{d\epsilon}{2\pi}\, G^<_{bb,33}[\epsilon, \langle n_{a\uparrow}\rangle, \langle n_{a\downarrow}\rangle, \langle n_{b\uparrow}\rangle, \langle n_{b\downarrow}\rangle]. \tag{20d}$$

At the electron hole symmetry point, that is, when $\epsilon_d = -U/2$, the occupation is independent of the bias voltage and equal to 1/2 ($n_{a,\sigma} = n_{b,\sigma} = 0.5$, with $\sigma = \uparrow, \downarrow$). In this way, the exact expression for $(dI/dV)^{ET}$ and $(dI/dV)^{AR}$ as a function of the bias voltage can be calculated analytically and is equal to:

$$\frac{dI^{ET}}{dV} = 2\frac{(4G\,A - 2F\,B\Gamma_S^2 + \frac{1}{4}C\Gamma_S^4)}{(K)} \tag{21}$$

and

$$\frac{dI^{AR}}{dV} = 4\frac{t^4\,\Gamma_S^2}{(K)} \tag{22}$$

where

$$K = 4D\,A - 2(-t^4\Gamma_L^2 + G\,F\,B - F(t^2 - \Gamma_L^2)B)\Gamma_S^2 + \frac{1}{4}E\,C\Gamma_S^4 \tag{23}$$

with

$$\begin{aligned} A &= \left[(\bar{g}^r_{1,12})^2 - t^2\right]^2 + (\bar{g}^r_{1,12})^2\Gamma_L \\ B &= (\bar{g}^r_{1,12})^2 - t^2 + \Gamma_L^2 \\ C &= (\bar{g}^r_{1,12})^2 + \Gamma_L^2 \\ D &= [(\bar{g}^r_{1,11})^2 - t^2]^2 + (\bar{g}^r_{1,11})^2\,\Gamma_L^2 \\ E &= (\bar{g}^r_{1,11})^2 + \Gamma_L^2 \\ F &= \bar{g}^r_{1,11}\bar{g}^r_{1,12} \\ G &= (\bar{g}^r_{1,11})^2 \end{aligned} \tag{24}$$

while $\bar{g}^r_{1,11}$ and $\bar{g}^r_{1,12}$ are the components 11 and 12 of the inverse Green function of $QD_1$ isolated in the Hubbard-I approximation, evaluated in the bias voltage $V$, i.e.:

$$\bar{g}^r_{i,11} = \frac{((V - \epsilon_d - U)(V - \epsilon_d))}{(V - \epsilon_d + U(n_1 - 1))} \tag{25}$$

$$\bar{g}^r_{i,12} = \frac{((V + \epsilon_d + U)(V + \epsilon_d))}{(V + \epsilon_d - U(n_1 - 1))} \tag{26}$$

$$\tag{27}$$

The analysis of these curves is complemented by the local density of states of the QDs, $\rho_a$ and $\rho_b$, defined according to:

$$\rho(\epsilon)_i = -\frac{1}{\pi}\mathrm{Im}(\mathbf{G}^r_{ii,11} + \mathbf{G}^r_{ii,33}), \qquad i = a, b. \tag{28}$$

## III. RESULTS AND DISCUSSION

In what follows, we consider $\Gamma_1$ as the energy unit. We assume that the QDs levels are spin degenerate and that the intradot Coulomb interaction is the same in both QDs, that is, $U_a = U_b = U$. We denote $r$ as the ratio of leads coupling $\Gamma_S/\Gamma_1$ through which we control the efficiency of the proximity effect, as well as the tunneling between dots as $t$. In addition, we set the gate voltage for each QD in the electron-hole symmetry point, that is, $\epsilon_a = \epsilon_b = -U/2$. In our work, we focus on the nonequilibrium regime, and the analysis of the results is split into two parts: the interferometric regime (when $t < \Gamma_1$ ) and the molecular regime (when $t \geq \Gamma_1$ ). In our analysis, we present the results for the differential conductance ET ( $(dI/dV)^{ET}_{12}$ ) and the differential conductance AR $(dI/dV)^{DAR}_{12}$ in terms of the bias voltage applied to the leads, which we will refer to for simplicity as $(dI/dV)^{ET}$ and $(dI/dV)^{DAR}$, respectively. The chemical potentials of the normal leads are set with opposite bias voltage, i.e. $\mu_1 = -\mu_2 = eV$, while the superconductor is kept grounded, $\mu_S = 0$. With normal leads with opposite bias voltage, $(dI/dV)^{CAR}_{12}$ (or $I^{CAR}_{12}$) and $(dI/dV)^{CAR}_{21}$ (or $I^{CAR}_{21}$) are zero since they are proportional to the factors $(f_1 - \bar{f}_2)$ and $(f_2 - \bar{f}_1)$, respectively, which are identically zero. It is worth saying that we assume that $|eV| < \Delta$, and therefore the contribution of the quasiparticle current $I^{QP}$ and transmittance $T^{QP}$ is zero within the energy range that we are considering. Finally, it is important to note that our calculations were obtained out of the Kondo regime.

### A. Interferometric regime

We begin the analysis of the non-equilibrium regime by focusing on the effects of interdot tunneling on $(dI/dV)^{ET}$ and $(dI/dV)^{AR}$, within the interferometric regime ($t \leq \Gamma_1$). For clarity's sake, we start by focusing on the noninteracting regime ($U = 0$). In this case, the behaviors of $(dI/dV)^{ET}$ and $(dI/dV)^{AR}$ as functions of $t$ and $V$, are shown in the contour plots of Figs. 2(a) and 2(c), respectively. For $t = 0$, the $QD_a$ is decoupled from the $QD_b - S$ part of the system and, as a result,$(dI/dV)^{ET}$ exhibits a well-known Lorentzian shape, while $(dI/dV)^{AR}$ remains equal to zero. As $t$ increases, the superconducting correlations start to leak into $QD_a$, and the Andreev bound states (ABSs) emerge as two resonances equidistant from $V = 0$. At the same bias voltage values, two equidistant depths appear in the $(dI/dV)^{AR}$ curves. The correspondence between these two lineshapes can be better observed in Figs. 2(b) and 2(d) where cuts of the contour plots for $t = 0.05$ ($\mathsf{A}_1$ and $\mathsf{A}_2$ lines) and $t = 0.5$ ($\mathsf{B}_1$ and $\mathsf{B}_2$ lines) are shown. It is also worth noting that the central peak at $V = 0$ is preserved in the $(dI/dV)^{ET}$ curves, as a manifestation of the electron-hole symmetry of the ABSs in the QD spectra. As $t$ increases, hybridization between discrete ABSs and continuum states, originating from normal leads, causes the lineshapes to broaden. This interpretation is based on the fact that the differential conductance curves follow the behavior of the local density of states of the QDs

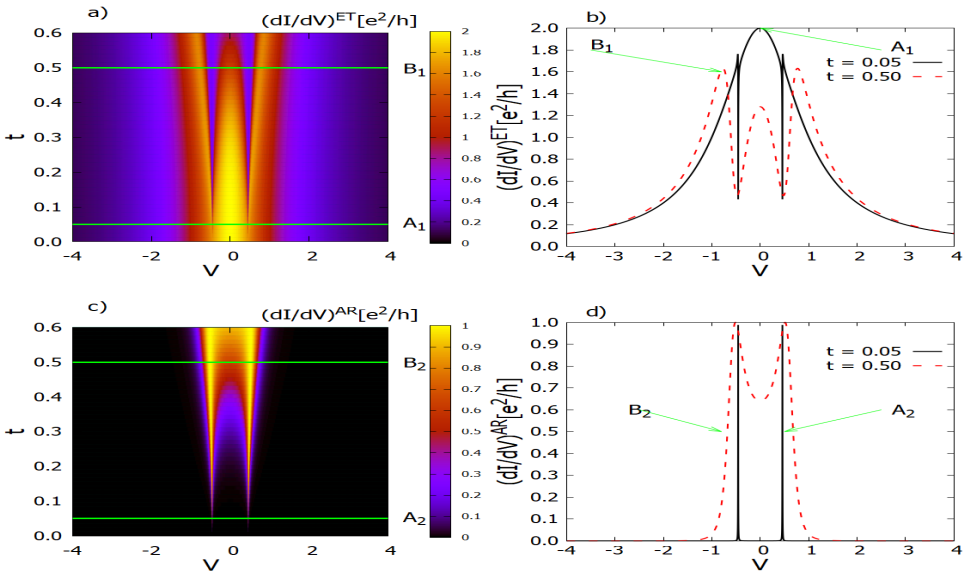


FIG. 2. Left panel: Contour plot of $(dI/dV)^{ET}$ and $(dI/dV)^{AR}$ in terms of $t$ and $V$, figures a) and c), respectively; Right panel:$(dI/dV)^{ET}$ and $(dI/dV)^{AR}$ in terms of the energy when $t = 0.05$ (solid black line) or $t = 0.5$ (red dashed line), figures b) and d), respectively. Their location in the contour plot is indicated by the horizontal lines marked by $A_1$ and $A_2$ for $t = 0.05$ and by $B_1$ and $B_2$ for $t = 0.5$, respectively. Other parameters are chosen as $U = 0$, $k_BT = 0\Gamma_1$, $\Gamma_1 = \Gamma_2 = \Gamma_S$ and $\epsilon_a = \epsilon_b = -U/2$

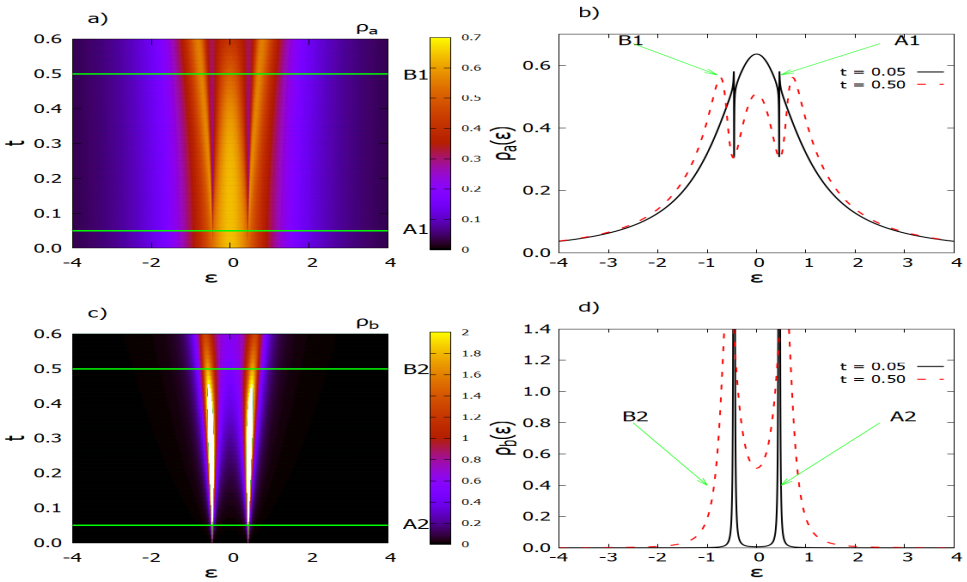


FIG. 3. Left panel: Contour plot of $\rho_a$ and $\rho_b$ in terms of $t$ and $\epsilon$, figures a) and c), respectively; Right panel:$\rho_a$ and $\rho_b$ in terms of energy when $t = 0.05$ (solid black line) or $t = 0.5$ (red dashed line), figures b) and d), respectively. Their location in the contour plot is indicated by the horizontal lines labeled $A_1$ and $A_2$ for $t = 0.05$ and by $B_1$ and $B_2$ for $t = 0.5$, respectively. Other parameters are chosen as $U = 0$, $k_BT = 0\Gamma_1$, $\Gamma_1 = \Gamma_2 = \Gamma_S$ and $\epsilon_a = \epsilon_b = -U/2$

for zero bias voltage, as shown in Fig. 3. The very same behavior can be observed from the contour plots for $\rho_a$ and $\rho_b$, at zero bias voltage, as shown in Figs. 3(a) and 3(c), respectively.

A more detailed line shape can be seen in the cuts for $t = 0.05$ ($A_1$ and $A_2$ lines) and $t = 0.5$ ($B_1$ and $B_2$ lines), which readily show the same behavior observed in the transmission curves.

In Fig. 4, the differential conductance $(dI/dV)^{ET}$ and $(dI/dV)^{AR}$ are shown for $U = 2$. The other parameters remain the same as those used in Figs. 2 and 3. The main difference, in this case, is the splitting of the peaks due to the Coulomb correlation. In fact, for $t = 0.05$, two Lorentzian peaks are observed, as is evident from the cut

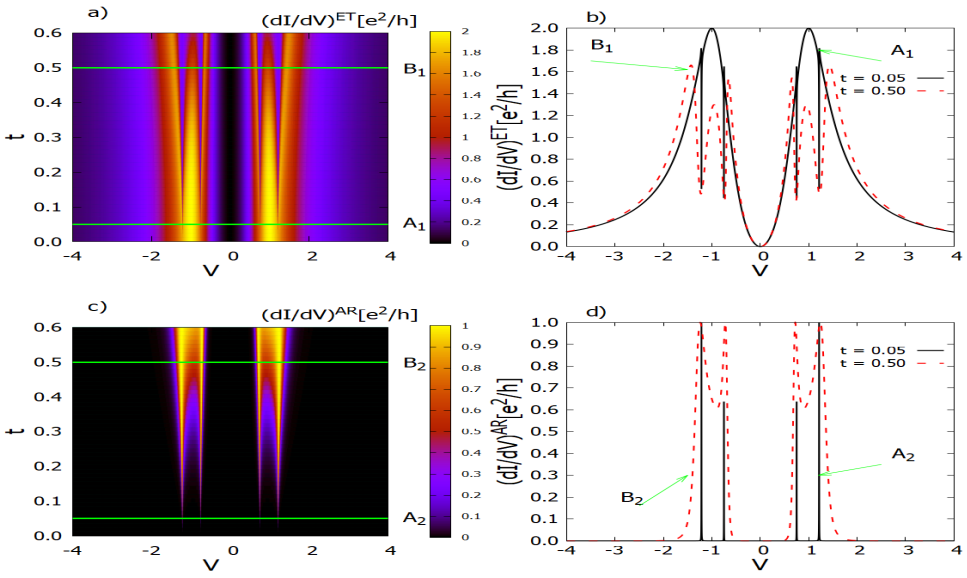


FIG. 4. Left panel: Contour plot of $(dI/dV)^{ET}$ and $(dI/dV)^{AR}$ in terms of $t$ and $V$, figures a) and c), respectively ; Right panel:$(dI/dV)^{ET}$ and $(dI/dV)^{AR}$ in terms of bias voltage V, when $t = 0.05$ (solid line) or $t = 0.5$(dashed line), figures b) and d), respectively. Their location in the contour plot is indicated by the horizontal lines marked by $A_1$ and $A_2$ for $t = 0.05$ and by $B_1$ and $B_2$ for $t = 0.5$, respectively. Other parameters are chosen as $U = 2$, $k_BT = 0\Gamma_1$, $\Gamma_1 = \Gamma_2 = \Gamma_S$ and $\epsilon_a = \epsilon_b = -U/2$

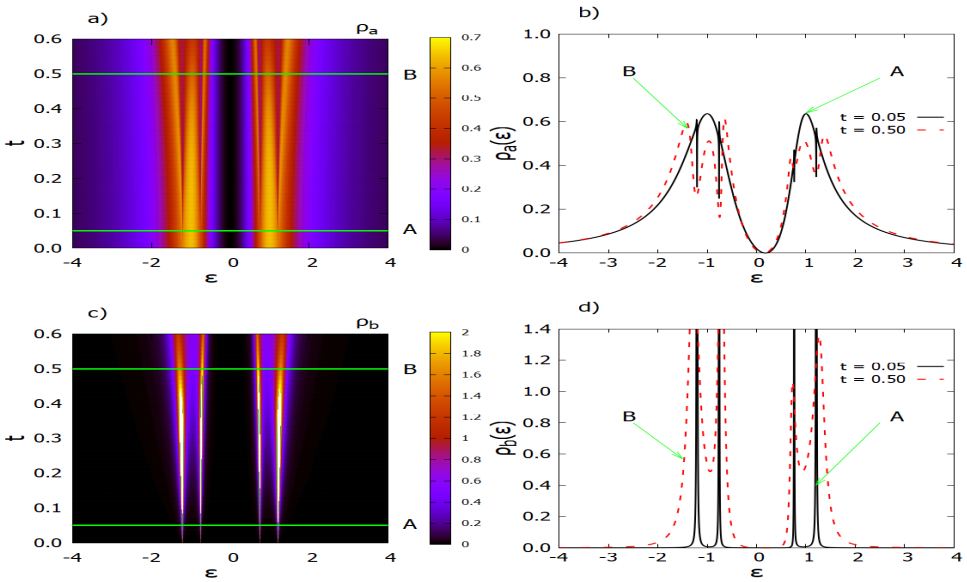


FIG. 5. Left panel: Contour plot of $\rho_a$ and $\rho_b$, at zero bias voltage, in terms of $t$ and $\epsilon$, figures a) and c), respectively ; Right panel:$\rho_a(\epsilon)$ and $\rho_b(\epsilon)$ in terms of the energy when $t = 0.05$(solid line) or $t = 0.5$(dashed line), figures b) and d), respectively. Their location on the contour plot is indicated by the horizontal lines labeled by $A_1$ and $A_2$ for $t = 0.05$ and by $B_1$ and $B_2$ for $t = 0.5$, respectively. Other parameters are chosen as $U = 2$, $k_BT = 0\Gamma_1$, $\Gamma_1 = \Gamma_2 = \Gamma_S$ and $\epsilon_a = \epsilon_b = -U/2$

$A_1$, shown in Fig. 4(b). The ABSs are also evident at this small value of $t$ as antiresonances superimposed on the peaks despite the presence of Coulomb correlations. As $t$ increases, the broadening of peaks increases, as is evident from the contour plots of Figs. 4(a) and 4(c) and the corresponding cuts shown in Figs. 4 (b) and 4 (d). In contrast to the broadening of the peaks, their location is fixed by the Coulomb interaction with the two Lorentzian peaks located at $\pm U/2$, which is also the center of symmetry of the ABSs. A similar behavior is observed for the local density of states for zero bias voltage, as shown in Fig. 5. This figure shows in the left panel the contour plot of $\rho_a$ and $\rho_b$ as a function of $\epsilon$ and $t$ [Figs 5 (a) and 5(c), respectively] and shows in the right panel

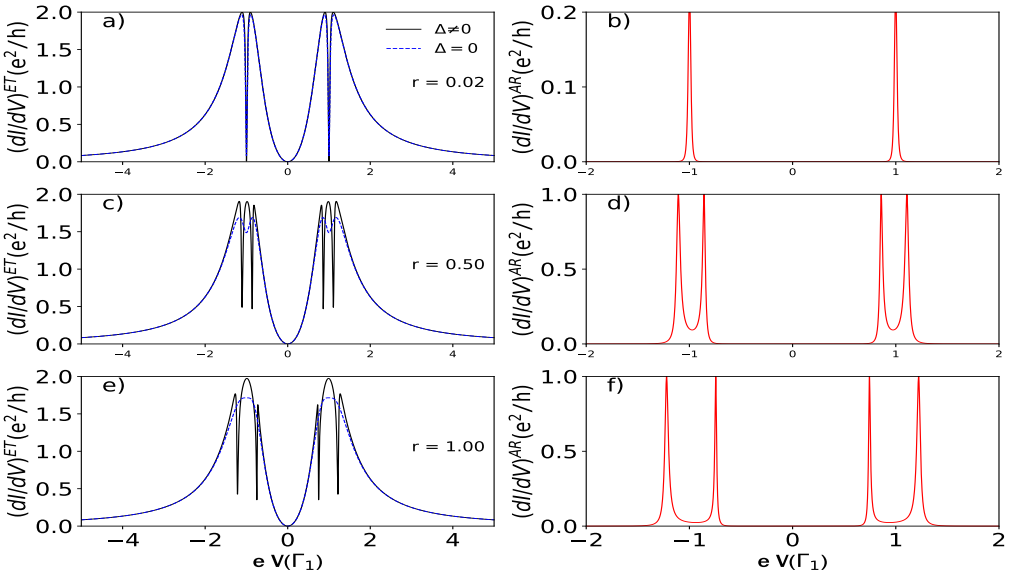


FIG. 6. The differential conductance $(dI/dV)^{ET}$ (solid black line) and $(dI/dV)^{AR}$ (dashed red line) as a function of the bias voltage $V$ for a) $r = 0.02$, b) $r = 0.50$ and c) $r = 1$. The dashed line in the left panel corresponds to the $(dI/dV)^{ET}$ for $\Delta = 0$, i.e., for a system with three normal contacts. Other parameters are chosen as: $\Delta = 5\Gamma_1$, $U = 2\Gamma_1$, $t = 0.2\Gamma_1$, $k_BT = 0\Gamma_1$, $\Gamma_1 = \Gamma_2$ and $\epsilon_a = \epsilon_b = -U/2$

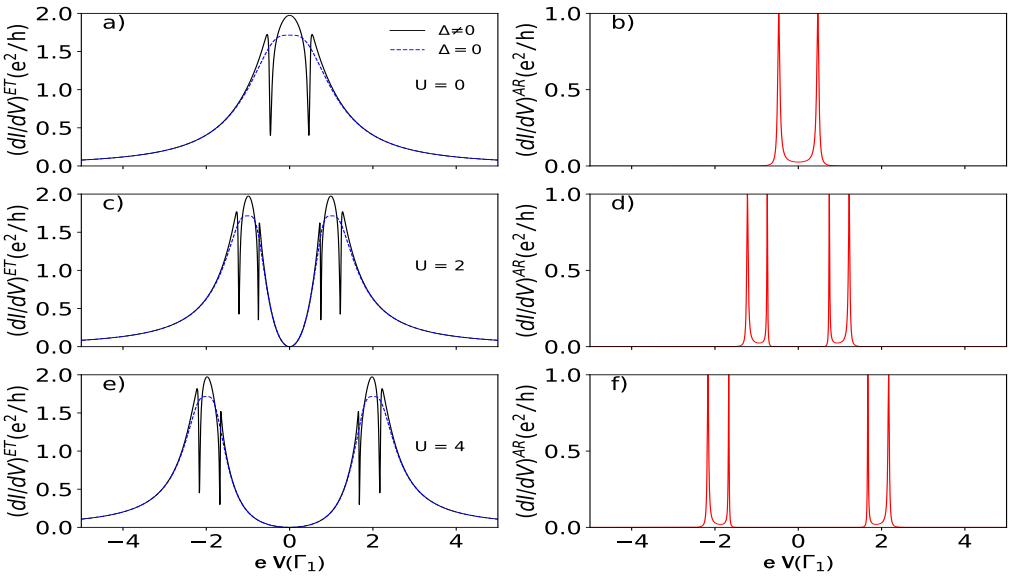


FIG. 7. In the left panel, the differential conductance $(dI/dV)^{ET}$ (black solid line ) as a function of the bias voltage $V$ and in the right panel $(dI/dV)^{DAR}$ (red solid line ) as a function of the bias voltage $V$ when $U = 0$ for a) and b), $U = 2$ for c) and d), and $U = 4$ for e) and f). The dashed line on the left panel corresponds to $(dI/dV)^{ET}$ for $\Delta = 0$, that is, for a system with three normal contacts. Other parameters are chosen as $t = 0.2\Gamma_1$, $\Delta = 5\Gamma_1$, $k_BT = 0\Gamma_1$, $\Gamma_1 = \Gamma_2 = \Gamma_S$, and $\epsilon_a = \epsilon_b = -U/2$.

the curves of $\rho_a(\epsilon)$ and $\rho_b(\epsilon)$ in terms of energy [Figs. 5 (b) and 5 (d), respectively], when $t = 0.05$ (solid line) or $t = 0.5$ (dashed line). Their location in the contour plot is indicated by the horizontal lines labeled $A_1$ and $A_2$ for $t = 0.05$ and $B_1$ and $B_2$ for $t = 0.5$. As we can see in figures 5 a) and 5 c), $\rho_a$ takes the form of two Lorentzian curves centered at $\epsilon = \pm U/2$ when $t = 0$, while $\rho_b$ equals zero. However, when $t = 0.05$, we observe the appearance of two pairs of narrow deeps in $\rho_a$ [see lines $\mathsf{A}_1$, in Figs. 5 (a) and 5 (b)] revealing the leakage of ABS in the density of states of $QD_a$ , expressed in the two pairs of sharp resonances in $\rho_b$ [see lines $\mathsf{A}_2$ , in Figs. 5(c) and 5(d)]. However, as the value of $t$ increases, for example, when $t = 0.5$ the deeps in the $\rho_a$ [see lines $\mathsf{B}_1$, in Figs. 5

(a) and 5 (b)], and the resonances in $\rho_b$ [see lines $\mathsf{B}_2$, in Figs. 5 (c) and 5 (d))] become progressively wider.

In Fig. (6) we study the role of the superconductor in $(dI/dV)^{ET}$ by varying the coupling ratio, $r = \Gamma_S/\Gamma_1$, and $\Delta$, the superconductor gap. While $r$ measures the coupling strength between $QD_b$ and $S$, $\Delta$ carries the information on the superconductor correlations. The differential conductance $(dI/dV)^{ET}$ and $(dI/dV)^{AR}$, as a function of bias voltage, are shown in the left and right panels of the Fig. (6), respectively, for $r$ changing from 0.02 to 1.0. For $\Delta = 0$, the blue dotted lines represent $(dI/dV)^{ET}$. In the first place, we can note that when $r = 0.02$, i.e. when the DQD can be considered decoupled from the third lead, the difference conductance ET shows two deep Fano antiresonances, which reveals the existence of quantum interference due to the effect of the additional channel opened by the second QD coupled to the system. As the value of $r$ increases, Fano antiresonances in the differential conductance ET disappear when the third lead is normal ($\Delta = 0$), due to hybridization of the discrete state of $QD_b$ with the continuum spectrum of $S$ in its normal state. On the contrary, when $\Delta \neq 0$ and $r \neq 0$, the lead $S$ becomes a superconductor, and the energy gap is revealed at the Fermi level with the presence of the ABS, and two pairs of Fano antiresonances appear in the differential conductance ET, corresponding to the Fano resonances appearing in the differential conductance AR for the same value of $V$, which is a clear manifestation of quantum interference. For example, when $r = 0.02$, the coupling to $S$ is too small, and $(dI/dV)^{ET}$ exhibits the Fano antiresonance pattern. In contrast, for $r \geq 0.50$, the ABSs become pronounced enough to change the shape of $(dI/dV)^{ET}$; this can be seen from the $(dI/dV)^{AR}$ shown by the red curves in Fig. 6. As in the non-interacting case, the resonances of $(dI/dV)^{AR}$ correspond to two antiresonances in the $(dI/dV)^{ET}$ curves, equidistant from $\pm U/2$ with a central peak located at $\pm U/2$. In contrast to the normal state, this effect is robust with respect to the increase of $r$, being preserved for all values of $r$. Actually, the main effect of $r$, in this case, is to displace ABSs on the bias axis. Despite similar effects pointed out in the literature[20, 27, 31], here it is clear that such an interference pattern is robust against Coulomb correlations, which, in general, have a detrimental effect on Andreev interference.

Finally, Fig. 7 shows in the left panel the electron tunneling differential conductance ($(dI/dV)^{ET}$) (black solid line) and in the right panel the Andreev differential conductance ($(dI/dV)^{AR}$) (red solid line) for different values of the intradot Coulomb interaction $U$. The dashed line on the left panel also corresponds to $(dI/dV)^{ET}$ for $\Delta = 0$, that is, for a system with three normal contacts. We can see in Fig. 7 that when $t = 0.2$, $U = 0$ and $\Delta = 0$, the differential conductance ET has the form of a Lorentzian centered on the zero bias voltage and does not present antiresonances. In contrast, when $U = 0$ and $\Delta \neq 0$, the differential conductance ET shows two Fano antiresonances, which coincide with the two resonances in the differential conductance AR. On the contrary, when $U \neq 0$ and $\Delta \neq 0$, the two antiresonances in differential conductance ET and the two resonances in the differential conductance AR are subdivided on either side of the zero bias with the symmetry point located at $\pm U/2$, by the effect of the Coulomb interaction. The separation between the resonances in the differential conductance ET and AR increases as $U$ increases.

One way to better understand the tunneling mechanism in different transmission processes is to analyze the differential conductance $(dI/dV)^{ET}$. It can be expressed as a convolution of two Breit-Wigner and two Fano line shapes, as shown in Figure 8a.

$$\frac{dI^{ET}}{dV} \approx \frac{|\tilde{V}_1 + q|^2}{|\tilde{V}_1|^2 + 1}\left(\frac{1}{\epsilon_1^2 + 1} + \frac{1}{\epsilon_2^2 + 1}\right)\frac{|\tilde{V}_2|^2}{|\tilde{V}_2|^2 + 1}, \quad (29)$$

where $\tilde{V}_1 = (||V| - U/2| - \Gamma_S/4)/\eta$ with $\eta = t^2/(\Gamma_S)$, $\tilde{V}_2 = |V|/(\Gamma_{L1}/2)$ , $\epsilon_1 = \frac{|V|-\epsilon_d}{(\Gamma_{L1}/2)}$,$\epsilon_2 = \frac{|V|-(\epsilon_d+U)}{(\Gamma_{L1}/2)}$and $q = q_r + i\,q_i$. The complex Fano parameter, $q$, and the coupling value, $\Gamma_{L1}$, are relevant to understanding the differential conductance. Based on the above equation, the conductance has two resonances at $V = \epsilon_d$ and $V = \epsilon_d + U$. Each resonance has two dips at $V = \epsilon_d \pm \Gamma_S/4$ and $V = (\epsilon_d + U) \pm \Gamma_S/4$, with $\epsilon_d = -U/2$. Additionally, a single antiresonance appears at $V = 0$. The interference of electrons through different tunneling paths, including Andreev bound-states, explains the Fano effect observed in our results. Due to the presence of Andreev bound states, the electron suffers a change in its phase, and this is reflected in a complex $q$-parameter as we see in Eq.(29). In addition, the Andreev differential conductance, $(dI/dV)^{AR}$, can be expressed as two Breit-Wigner line shapes (shown in Figure 8b).

$$\frac{dI^{AR}}{dV} \approx \left(\frac{1}{\epsilon_3^2 + 1} + \frac{1}{\epsilon_4^2 + 1}\right), \quad (30)$$

where $\epsilon_3 = \frac{|V-\epsilon_d|-\Gamma_S/4}{(t^2/\Gamma_S)}$ and $\epsilon_4 = \frac{|V-(\epsilon_d+U)|-\Gamma_S/4}{(t^2/\Gamma_S)}$. The above equation shows that the Andreev differential conductance has four resonances at $V = \epsilon_d \pm \Gamma_S/4$ and $V = (\epsilon_d + U) \pm \Gamma_S/4$, with $\epsilon_d = -U/2$, which coincide exactly with the dips of the differential conductance ET mentioned above. From the fits, we can conclude that the Fano-Andreev effect is robust in the presence of Coulomb interaction. Additionally, in the interferometric regime, Andreev transmission is a resonant tunneling process through Andreev-bound states, which causes the Fano effect in normal transmission.

### B. Molecular regime

In this subsection, we analyze the molecular regime. The contour plots in Fig. 9 a-c display the behavior of

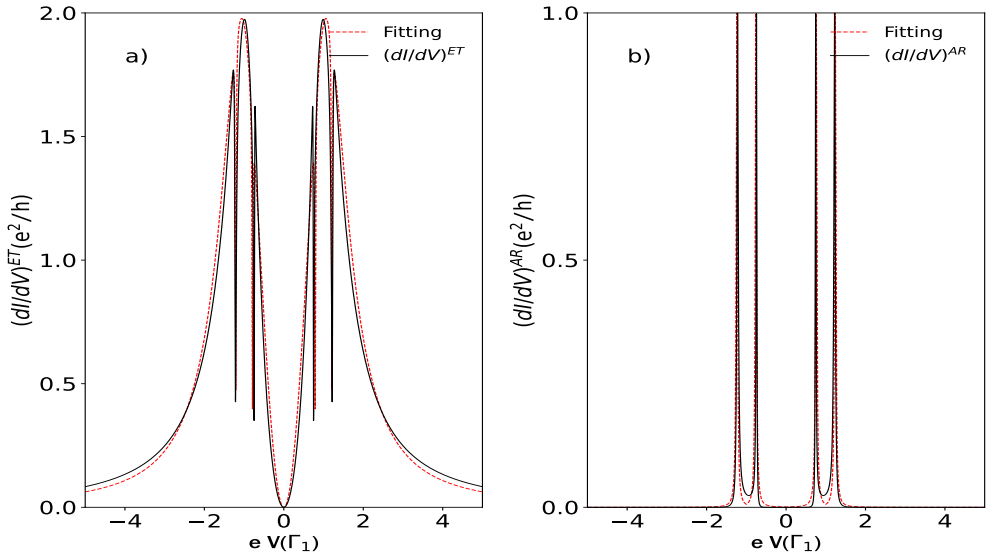


FIG. 8. a) The differential conductance $(dI/dV)^{ET}$ (black solid line ) and the fitting (red dashed line) as a function of the bias voltage $V$ when $t = 0.2$. b) The differential conductance $(dI/dV)^{AR}$ (black solid line ) and the fitting (red dashed line) as a function of the bias voltage $V$ when $t = 0.2$. Other parameters are chosen as $\Delta = 5\Gamma_1$ , $k_BT = 0\Gamma_1$, $\Gamma_1 = \Gamma_2 = \Gamma_S$ and $\epsilon_a = \epsilon_b = -U/2$.

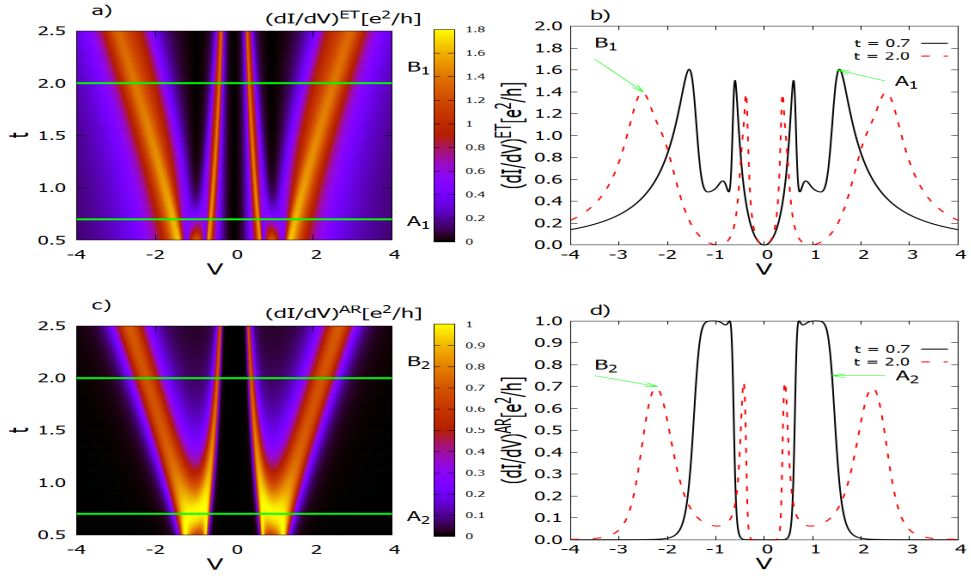


FIG. 9. Left panel: Contour plot of $(dI/dV)^{ET}$ and $(dI/dV)^{AR}$ in terms of $t$ and $V$, figures a) and c), respectively ; Right panel:$(dI/dV)^{ET}$ and $(dI/dV)^{AR}$ in terms of bias voltage when $t = 0.7$ (solid line) or $t = 2$(dashed line), figures b) and d), respectively. Their location in the contour plot is indicated by the horizontal lines labeled $A_1$ and $A_2$ for $t = 0.7$ and by $B_1$ and $B_2$ for $t = 2.0$, respectively. Other parameters are chosen as $U = 2$, $k_BT = 0\Gamma_1$, $\Gamma_1 = \Gamma_2 = \Gamma_S$ and $\epsilon_a = \epsilon_b = -U/2$

$(dI/dV)^{ET}$ and $(dI/dV)^{AR}$ as functions of $t$ and $V$, in the range $0.5\Gamma_1 \leq t \leq 2.5\Gamma_1$, are shown in the contour plots of Figs. 9(a) and 9(c), respectively. The other parameters remain the same as the ones used in Figs. 4 and 5. This figure displays the progressive vanishing of the antiresonances in the differential conductance ET as $t$ increases. As seen in the black solid line in Fig. 9 a or line $A_1$ in 9 b, when $t = 0.7$, the antiresonances in the differential conductance ET have almost disappeared. Therefore, we can consider that this value of $t$ is the threshold value that defines the transition between the interferometric and molecular regimes. On the other hand, when $t > 0.7$, specifically at $t = 2$ (see line B1 in Fig. 9 a, or red dashed line in Fig. 9 b), the differential

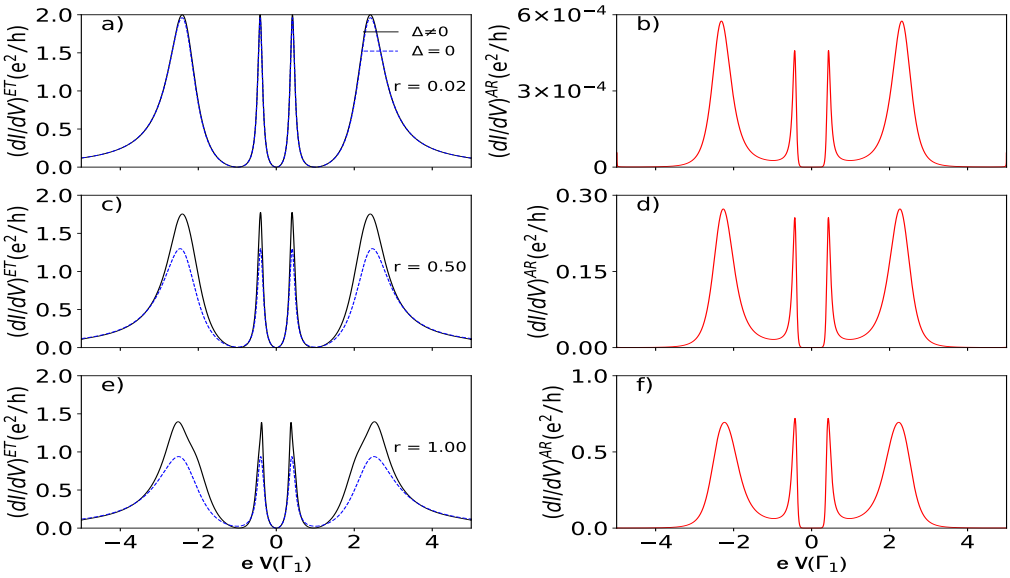


FIG. 10. In the left panel, the differential conductance $(dI/dV)^{ET}$ (black solid line) as a function of the bias voltage $V$ and in the right panel $(dI/dV)^{AR}$ (red solid line ) as a function of the bias voltage $V$ when $r = 1$ for a) and b), $r = 2$ for c) and d), and $r = 4$ for e) and f). The blue dashed line on the left panel corresponds to $(dI/dV)^{ET}$ for $\Delta = 0$, that is, for a system with three normal contacts. Other parameters are chosen as $t = 2\Gamma_1$ , $\Delta = 5\Gamma_1$ , $U = 2\Gamma_1$, $k_BT = 0\Gamma_1$, $\Gamma_1 = \Gamma_2$ and $\epsilon_a = \epsilon_b = -U/2$.

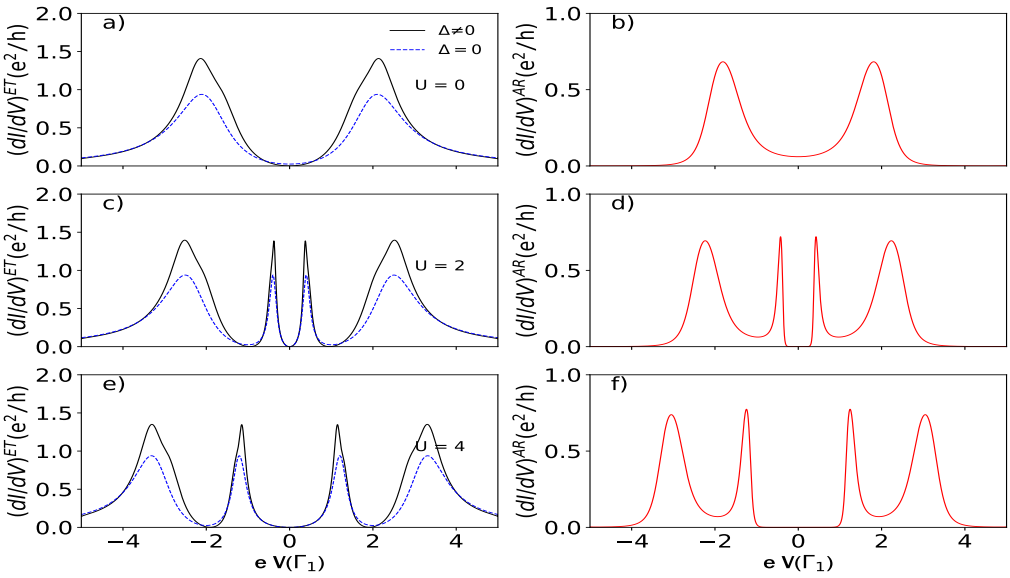


FIG. 11. In the Left panel, the differential conductance $(dI/dV)^{ET}$ (black solid line ) as a function of the bias voltage $V$ and in the right panel $(dI/dV)^{DAR}$ (red solid line ) as a function of the bias voltage $V$ when $U = 0$ for a) and b), $U = 2$ for c) and d), and $U = 4$ for e) and f). The blue dashed line on the left panel corresponds to $(dI/dV)^{ET}$ for $\Delta = 0$, that is, for a system with three normal contacts. Other parameters are chosen as $t = 2\Gamma_1$ , $\Delta = 5\Gamma_1$ , $k_BT = 0\Gamma_1$, $\Gamma_1 = \Gamma_2 = \Gamma_S$ and $\epsilon_a = \epsilon_b = -U/2$.

conductance ET becomes zero at $\pm U/2$, with two asymmetrically located resonances around this point: two lateral resonances moving away from the $eV = 0$, and two central resonances approaching each other towards the point of zero bias voltage. On the other hand, the differential conductance AR exhibits similar behavior. At $t = 0.7$ (indicated by the black solid line in Fig. 9d or line A2 in Fig. 9c), the double peak structure has almost vanished only to reappear again for $t > 1$ (as shown by the red dashed line in Fig. 9d or line B2 in Fig. 9c). However, now the resonances in the differential Andreev conductance align closely with those in the differential ET conductance (as seen in line B2 in Fig. 9c).

Now, we study the effect of the coupling ratio, $r$, on

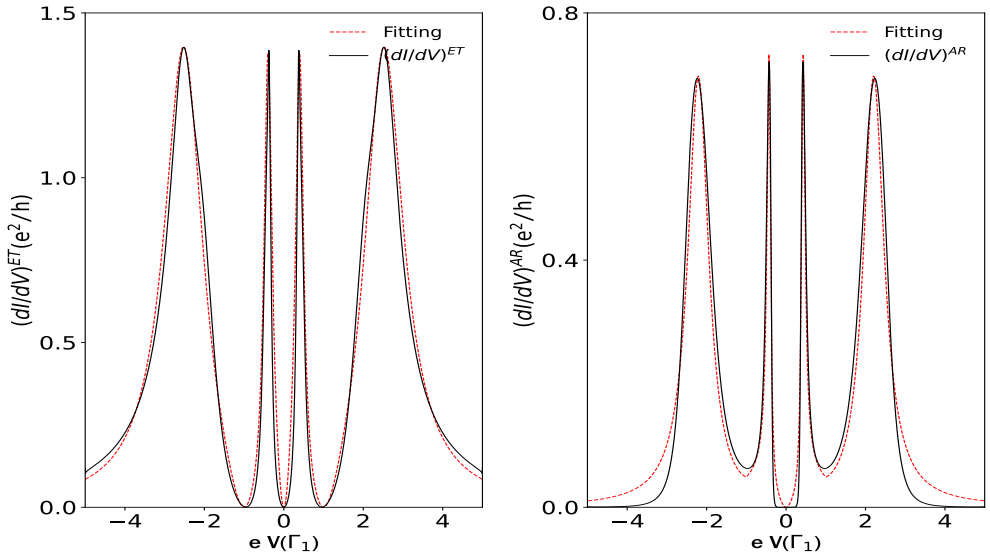


FIG. 12. a) The differential conductance $(dI/dV)^{ET}$ (black solid line ) and the fitting (red dashed line) as a function of the bias voltage $V$ when $t = 2$. b) The differential conductance $(dI/dV)^{AR}$ (black solid line ) and the fitting (red dashed line) as a function of the bias voltage $V$ when $t = 0.2$. Other parameters are chosen as $\Delta = 5\Gamma_1$ , $k_BT = 0\Gamma_1$, $\Gamma_1 = \Gamma_2 = \Gamma_S$ and $\epsilon_a = \epsilon_b = -U/2$.

the differential conductance ET and AR in the molecular regime ($t \geq \Gamma_1$). Fig. 10 displays in the left panel the electron-tunneling differential conductance($(dI/dV)^{ET}$) (black solid line), and in the right panel, the Andreev differential conductance ($(dI/dV)$) (red solid line), for different values of rate coupling $r$ for $\Delta = 5$. The blue dashed line in the left panel also corresponds to the $(dI/dV)^{ET}$ for $\Delta = 0$, i.e., for a system with three normal contacts. In the first place, we can note that by changing $r$ from 0.05 to 1, the shape of the differential conductance curve ET does not change significantly when the lead S is in its normal state ($\Delta = 0$) or when it is in its superconducting state ($\Delta \neq 0$). The only noticeable effect on the differential conductance of the presence of lead S in its superconducting state is the decrease in the height of the resonances and the progressive splitting of the lateral peaks. On the other hand, the differential conductance AR presents two resonances on each side of the zero bias voltage, asymmetrically located around $\pm U/2$, which are located approximately around the same bias voltage values as the resonances in the differential conductance ET, and these resonances turn out to be visible even for small values of $r$. However, it is possible to appreciate a remarkable reduction in the height of the AR differential conductance resonances when we are in the molecular regime for the interferometric regime (see Fig. 10 b, d, and f).

Fig. 11 displays in the left panel the electron-tunneling differential conductance ET (black solid line) and in the right panel the Andreev differential conductance (red solid line), in the molecular regime, for different values of intra-dot Coulomb interaction $U$. The blue dashed line in the left panel also corresponds to the $(dI/dV)^{ET}$ for $\Delta = 0$, i.e., for a system with three normal contacts. We can see in Fig. 11 that when $t = 2$, $U = 0$, in contrast to the interferometric regime, the differential conductance ET and AR have the form of two Lorenzian curves, localized close to $\pm t$ with the center of symmetry located at zero bias voltage, irrespective of whether the lead S is in its normal state ($\Delta = 0$) or its superconducting state ($\Delta \neq 0$), and unlike in the interferometric case, there are no antiresonances present in $(dI/dV)^{ET}$ when ($\Delta \neq 0$). On the other hand, when $U$ is non-zero, whether $\Delta = 0$ or $\Delta \neq 0$, the resonances in $(dI/dV)^{ET}$ and $(dI/dV)^{AR}$ are doubled, and are located approximately around the bias voltage $\epsilon_d$ and $\epsilon_d + U$, by the effect of the Coulomb interaction. The separation between the resonances in the differential conductance ET and AR grows as U increases.

The differential conductance $(dI/dV)^{ET}$ can be represented by combining two Breit-Wigner and two Fano line shapes, in the range $0.7 \leq t \leq 2$ and $r \leq 1$, as shown in Figure 12a.

$$\frac{dI^{ET}}{dV} \approx \frac{\epsilon_1^2}{\epsilon_1^2+1}\Big(\frac{1}{\omega_1^2+1}+\frac{1}{\omega_2^2+1}\Big)\frac{\epsilon_2^2}{\epsilon_2^2+1} \tag{31}$$

where $\omega_1 = ||V| - \gamma_1|/\eta_1$, $\omega_2 = (||V| - \gamma_2|)/\eta_2$, $\epsilon_1 = ||V| - U/2|/(\Gamma_1/2)$, $\epsilon_2 = |V|/\Gamma_1$. Where $\gamma_i = (-\epsilon_d \mp t/2 - U/2 + (1/2)\sqrt{t^2+U^2})$ with $i = 1, 2$ ( in the molecular limit ($(t/\Gamma_{L1}) > 1$) and at the electron-hole symmetry point) and on other hand,$\eta_1$ and $\eta_2$ are fitting parameters. Note that from the above expression, the differential conductance vanishes at $V = \pm U/2$ and $V = 0$. The $q$-parameter in molecular regimes is real, unlike in inter-

ferometric regimes. Furthermore, the differential conductance shows resonances at $V \approx \pm\gamma_1$ and $V \approx \pm(\gamma_2)$. It is interesting to note that by making a Taylor approximation to $t/U$, the values of $\gamma_1$ and $\gamma_2$ become $\gamma_1 = U^2/(4t)$ and $\gamma_2 = t+U^2/(4t)$, respectively. That is, when $t >> U$ the central peaks tend to approach $V = 0$, and the lateral peaks tend to lie at $V = t$.

In addition, the equation for $(dI/dV)^{AR}$ may be written as the superposition of two Breit-Wigner and one Fano line shapes. [Fig. 12(b)]:

$$\frac{dI^{AR}}{dV} \approx \frac{\xi^2}{\xi^2+1}\left(\frac{1}{\nu_1^2+1} + \frac{1}{\nu_2^2+1}\right) \tag{32}$$

where $\nu_1 = ||V| - \gamma_1|/(\bar{\xi_1})$ , $\nu_2 = (||V| - \gamma_2|)/(\bar{\xi_2})$, and $\xi = |V|/(\bar{\xi_3})$. Here, as before,$\gamma_i = (-\epsilon_d \mp t/2 - U/2 + (1/2)\sqrt{t^2+U^2})$ with $i = 1, 2$ ( in the molecular limit $((t/\Gamma_{L1}) > 1)$ and at the electron-hole symmetry point) and on other hand,$\bar{\xi_1}$,$\bar{\xi_2}$ and $\bar{\xi_3}$ are fitting parameters.

The fitting presented above offers a reasonable understanding of the shape of the Andreev differential conductance shown in Figure 11. The Andreev states undergo a split caused by $t$ and as a result of this tunneling coupling, the Andreev bound states acquire widths that manifest themselves in the Andreev differential conductance.

## IV. SUMMARY

We have investigated the electronic transport properties of a T-shaped double quantum dot (DQD) system in the Coulomb blockade regime under nonequilibrium conditions. We employed a non-equilibrium Green's function calculation method and the equation of motion approach using the Hubbard-I approximation to do this. Our results suggest superconducting interference effects on transport between normal leads, which can be identified as Fano-like antiresonances in the QD transmission spectrum.

We have identified two distinct regimes, the interferometric and molecular regimes. In both regimes, the differential conductance (ET) can be expressed as a convolution of the Fano and Breit Wigner lines. However, in the interferometric regime, the Fano line shapes are centered on the energies of the Andreev bound states with a finite complex $q$ parameter, while in the molecular regime, the $q$ parameter takes real values. On the other hand, the Andreev reflection exhibits maxima that correspond to the Andreev bound states. Therefore, we can conclude that the interference effect is robust against Coulomb correlations and can be experimentally probed under nonequilibrium conditions.

## ACKNOWLEDGEMENTS

This work has been partially supported by the Universidad Técnica Federico Santa Mar' ia grant USM-DGIIP PI-LI 1925 and 1919 and the FONDECYT Grant 1201876.

[1] Leo P. Kouwenhoven, Gerd Schön, and Lydia L. Sohn. *Introduction to Mesoscopic Electron Transport*. Springer Netherlands, 1997.

[2] A. I. Buzdin. Proximity effects in superconductor-ferromagnet heterostructures. *Rev. Mod. Phys.*, 77:935–976, 2005.

[3] A F Andreev. Thermal conductivity of the intermediate state of superconductors. *Zh. Eksperim. i Teor. Fiz.*, 46, 1964.

[4] Qing-feng Sun, Jian Wang, and Tsung-han Lin. Resonant andreev reflection in a normal-metal–quantum-dot–superconductor system. *Phys. Rev. B*, 59:3831–3840, Feb 1999.

[5] SUN Qing-Feng ZHU Yu and LIN Tsung-Han. Effect of intra-dot coulomb interaction on andreev reflection in normal-metal/quantum-dot/superconductor system. *Communications in Theoretical Physics*, 36(01):101, 2001.

[6] Xiao-Qi Wang, Shu-Feng Zhang, Yu Han, and Wei-Jiang Gong. Fano-andreev effect in a parallel double quantum dot structure. *Phys. Rev. B*, 100, 2019.

[7] J. Gramich, A. Baumgartner, and C. Schönenberger. Andreev bound states probed in three-terminal quantum dots. *Phys. Rev. B*, 96:195418, Nov 2017.

[8] Jean-Damien Pillet, Charis Quay, Pascal Morfin, Cristina Bena, Alfredo Yeyati, and Philippe Joyez. Andreev bound states in supercurrent-carrying carbon nanotubes revealed. *Nature Physics*, 6:695, 05 2010.

[9] Ajay Chamoli, Tanuj and. Andreev bound states in superconductor-quantum dot josephson junction at infinite-u limit. 2020.

[10] Travis Dirks, Taylor Hughes, Siddhartha Lal, Bruno Uchoa, Yung-Fu Chen, Cesar Chialvo, Paul Goldbart, and Nadya Mason. Transport through andreev bound states in a graphene quantum dot. *Nature Physics*, 7, 05 2010.

[11] Rosario Fazio and Roberto Raimondi. Resonant andreev tunneling in strongly interacting quantum dots. *Phys. Rev. Lett.*, 80:2913–2916, Mar 1998.

[12] Jan Barański, Tomasz Zienkiewicz, Magdalena Barańska, and Konrad Kapcia. Anomalous fano resonance in double quantum dot system coupled to superconductor. *Scientific Reports*, 10:2881, 02 2020.

[13] Jan Barański and T. Domański. Fano-type interference in quantum dots coupled between metallic and superconducting leads. *Phys. Rev. B*, 84:195424, Nov 2011.

[14] T. Domański, A. Donabidowicz, and K. I. Wysokiński. Influence of pair coherence on charge tunneling through a quantum dot connected to a superconducting lead. *Phys. Rev. B*, 76:104514, Sep 2007.

[15] Grzegorz Górski and Krzysztof Kucab. Transport properties of proximitized double quantum dots. *Physica E: Low-dimensional Systems and Nanostructures*, 126:114459, 02 2021.

[16] T. Domański, I. Weymann, M. Barańska, and G. Górski. Constructive influence of the induced electron pairing on the kondo state. *Scientific Reports*, 2016.

[17] U. Fano. Effects of configuration interaction on intensities and phase shifts. *Phys. Rev.*, 124:1866–1878, Dec 1961.

[18] Andrey E. Miroshnichenko, Sergej Flach, and Yuri S. Kivshar. Fano resonances in nanoscale structures. *Rev. Mod. Phys.*, 82:2257–2298, Aug 2010.

[19] Gao Wen-Zhu, Gong Wei-Jiang, Zheng Yi-Song, Liu Yu, and Lü Tian-Quan. Fano effect in t-shaped double quantum dot structure with decoherence effect. *Communications in Theoretical Physics*, 49(3):771, mar 2008.

[20] J. Barański and T. Domański. Decoherence effect on fano line shapes in double quantum dots coupled between normal and superconducting leads. *Phys. Rev. B*, 85:205451, May 2012.

[21] Grzegorz Michałek, Bogdan Bułka, Marcin Urbaniak, Tomasz Domanski, and K. Wysokinski. Andreev spectroscopy in three-terminal hybrid nanostructure. *Acta Physica Polonica Series a*, 127:293, 02 2015.

[22] Grzegorz Michałek, Tomasz Domanski, and K. Wysokinski. Cooper pair splitting efficiency in the hybrid three-terminal quantum dot. *Journal of Superconductivity and Novel Magnetism*, 30, 01 2017.

[23] Yu Zhu, Qing-feng Sun, and Tsung-han Lin. Andreev reflection through a quantum dot coupled with two ferromagnets and a superconductor. *Phys. Rev. B*, 65:024516, Dec 2001.

[24] Grzegorz Michałek, Tomasz Domanski, Bogdan Bułka, and K. Wysokinski. Novel non-local effects in three-terminal hybrid devices with quantum dot. *Scientific Reports*, 5, 05 2015.

[25] E. C. Siqueira and G. G. Cabrera. Andreev tunneling through a double quantum-dot system coupled to a ferromagnet and a superconductor: Effects of mean-field electronic correlations. *Phys. Rev. B*, 81:094526, Mar 2010.

[26] Ezequiel Siqueira, P. Orellana, Antonio Seridonio, R. Cestari, M. Figueira, and Guillermo Cabrera. Interference effects induced by andreev bound states in a hybrid nanostructure composed by a quantum dot coupled to ferromagnetic and superconductor leads. 09 2014.

[27] A M Calle, M Pacheco, G B Martins, V M Apel, G A Lara, and P A Orellana. Fano–andreev effect in a t-shape double quantum dot in the kondo regime. *Journal of Physics: Condensed Matter*, 29(13):135301, feb 2017.

[28] E.C. Siqueira, P.A. Orellana, R.C. Cestari, M.S. Figueira, and G.G. Cabrera. Fano effect and andreev bound states in a hybrid superconductor–ferromagnetic nanostructure. *Physics Letters A*, 379(39):2524–2529, 2015.

[29] Grzegorz Michałek, Bogdan R. Bułka, Tadeusz Domański, and Karol I. Wysokiński. Interplay between direct and crossed andreev reflections in hybrid nanostructures. *Phys. Rev. B*, 88:155425, Oct 2013.

[30] Sachin Verma and Ajay Singh. Non-equilibrium thermoelectric transport across normal metal–quantum dot–superconductor hybrid system within the coulomb blockade regime. *Journal of Physics: Condensed Matter*, 34(15):155601, feb 2022.

[31] A M Calle, M Pacheco, G B Martins, V M Apel, G A Lara, and P A Orellana. Fano–andreev effect in a t-shape double quantum dot in the kondo regime. *Journal of Physics: Condensed Matter*, 29(13):135301, feb 2017.

[32] J. Bardeen, L. N. Cooper, and J. R. Schrieffer. Microscopic theory of superconductivity. *Phys. Rev.*, 106:162–164, Apr 1957.

[33] Hartmut Haug and A. P. Jauho. Quantum kinetics in transport and optics of semiconductors. 2004.

[34] J. Rammer and H. Smith. Quantum field-theoretical methods in transport theory of metals. *Rev. Mod. Phys.*, 58:323–359, Apr 1986.

[35] J Hubbard. Electron correlations in narrow energy bands. *Proc. Roy. Soc. (London), Ser. A*.

# Thermoelectric transport properties of a T-shaped double quantum dot system in the Coulomb blockade regime

**A. González I.[1,*], M. Pacheco[1,+], A. M. Calle[1,+], E. C. Siqueira[2,+], and P. A. Orellana[1,*]**

[1]Departamento de Física, Universidad Técnica Federico Santa María, Valparaíso, Casilla 110 V, Chile
[2]Departamento Acadêmico de Física, Universidade Tecnológica Federal do Paraná, Brazil
[*]alejandro.gonzalezi@usm.cl;pedro.orellana.dinamarca@usm.cl
[+]these authors contributed equally to this work

## ABSTRACT

We investigate the thermoelectric properties of a T-shaped double quantum dot system described by a generalized Anderson Hamiltonian. The system's electrical conduction ($G$) and the fundamental thermoelectric parameters such as the Seebeck coefficient ($S$) and the thermal conductivity ($\kappa$), along with the system's thermoelectric figure of merit ($ZT$) are numerically estimated based on a Green's function formalism that includes contributions up to the Hartree-Fock level. Our results account for finite onsite Coulomb interaction terms in both component quantum dots and discuss various ways leading to an enhanced thermoelectric figure of merit for the system. We demonstrate that the presence of Fano resonances in the Coulomb blockade regime is responsible for a strong violation of the Wiedemann-Franz law and a considerable enhancement of the system's figure of merit ($ZT$ ).

## Introduction

The need for manufacturing thermoelectric devices which can convert heat into electricity (and vice versa) with high thermoelectric efficiency, based on thermoelectric phenomena such as Seebeck and Peltier effects, has pushed the search of materials with new properties. The usual way to measure the efficiency is through the figure of merit ($Z$), which is defined as $Z = S^2GT/(\kappa)$, where S, G, T, $\kappa$ are Seebeck coefficient, electronic conductance, absolute temperature and thermal conductance (which is equal to the sum of electron thermal conductance ($\kappa_e$) and the phonon thermal conductance $\kappa_p$). For technological applications, it is required that the value of Z be as large as possible, and therefore it is clear that if you want to increase the value of Z you must increase the Seebeck coefficient and the electrical conductance, and reduce both the thermal conductance. Additionaly, the thermal and electronic conductances for most bulk materials at very low or room temperature obey Wiedemann–Franz law[1] $\kappa/GT = L_0$, where $L_0$ is a constant known as Lorentz number given by $L_0 = k_B^2\pi^3/3e^2$ with $k_B$ the Boltzmann constant and e the electron charge. Consequently, an increase in electrical conductance will cause an increase in thermal conductance. In turn, due to Mott's law[2] ($S \sim T\partial lnG/\partial E$ an increase in the electronic conductance will cause a decrease in the Seebeck coefficient. Consequently, in conventional solids the figure of merit rarely exceeds the value 1 $ZT \leq 1$. This difficulty of bulk materials can be overcome in mesoscopic systems (such as a QD) as suggested by Hicks and Dresselhaus[3,4]. Due to its low dimensionality , the physics properties of these systems are strongly affected by quantum confinement (level quantization) as well as by Coulomb blockade effects, which can lead to violation of the Wiedemann-Franz law and failure of the Mott relation[5–11]. Moreover, in this low dimensional systems the thermal conductance is rather small[12] due to the increase of the phonon scattering which allows according the Wiedemann–Franz law to reach high values of ZT. On other hand, Mahan and Sofo[13] show that the sharp features of the electronic density of states ( $\delta$-like DOS) resulted from the quantum size effect can improve the thermoelectri efficiency, i.e., a maximization of ZT. For this reason, quantum dot (QD) systems are promising candidates for high efficiency thermoelectric devices. Consequently, many experimental and theoretical groups have devoted themselves to the thermoelectric properties of QD systems, as a result, some interesting phenomena were reported[14–21].

On other hand, some researchers, in recent years, have focused their attention on the thermoelectric phenomena in a QD systems modulated by the Fano and Kondo effects. Especifically, single quantum dot system's are subject to the Kondo effect when the spin of the electron on the localized levels of the quantum dot gets screened by the conduction electrons in the normal lead below a characteristic temperature (the Kondo temperature). Also, electron transport in single quantum dot systems is characterized by Fano-like resonances attributed to the interference between the quantum amplitudes for the two possible

electron channels in the system: a direct conduction pathway through the leads and an indirect conduction pathway that involves the localized levels in the quantum dot. These two phenomena are characterized by the peaked configuration of the DOS or the electrical conductance.

The electric transport through multiple-quantum-dot systems coupled to normal and superconducting leads has already been widely studied[22–40]. These studies have confirmed that the thermoelectric properties of QDs hybrid systems coupled to one conventional lead(metallic or ferromagnetic lead) and one superconducting lead is remarkably better than these coupled to two conventional leads[38,41–44]. It has been found that the thermoelectric efficiency of the former can even reach several times or even tens of times of the latter by comprehensively regulating the superconducting gap, interdot coupling and asymmetric parameters, which also can be additionally enhanced by the interference effect and intredot Coulomb interaction. It mainly attributes to unique tunneling mechanisms and high denstity of state distributions near superconducting gap edges. The Andreev tunneling of Cooper pairs is only allowed inside the superconducting gap, while the tunneling of single electrons is allowed outside the superconducting gap, both of them have significant impact on the thermoelectric properties. The very high density of states near superconducting gap edges changes rapidly with energy, which is mainly responsible for the high thermopower and low thermal conductivity near superconducting gap edges

In particular, in this work we study the subgap thermoelectric properties, such as conductance and Seebeck coefficient,and the influence exerted on these properties by the different parameters that define this system, such as intradot correlation (U), interdot tunneling (t) between the central and lateral QD, rate of coupling with the superconductor lead and the temperature. Because the usual definition of Seebeck coefficient for two lead, is not directly applicable to the multiterminal system due to other currents flowing in adjacent branches, we use definitions of the local and nonlocal Seebeck coefficients valid for the three-terminal normal and hybrid device given by G. Michałek et al[45]. In particular, we are interested in the influence of the superconducting electrode on the subgap thermoelectric properties of this system, because the superconducting electrode is responsible for strong nonlocal effects, and it may also cause the negative conductance resulting from a competition between the crossed Andreev reflections and the direct electron tunneling involving normal electrodes.

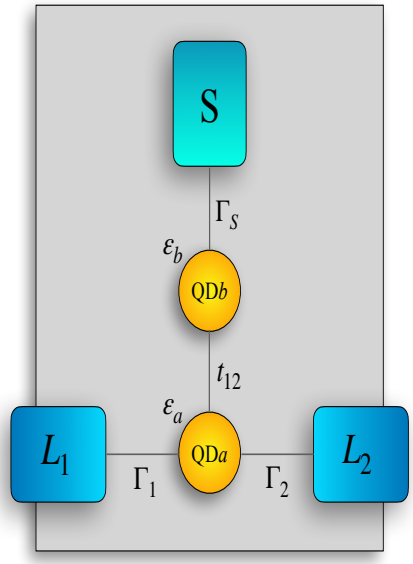


**Figure 1.** The T-shape double QD system studied in this work. It is composed of two quantum dots in which the $QD_a$ is coupled to two normal metals $L_1$ and $L_2$, with the coupling strength being determined by the parameters $\Gamma_1$ and $\Gamma_2$. The second quantum dot, $QD_b$ is coupled to the superconductor $S$, with the coupling strength being modeled by the parameter $\Gamma_S$. The coupling between the QDs is modeled by the $t_{12}$ parameter.

## 1 Model and Formulation

In Fig. 1, the T-shape double quantum-dot system is illustrated. It consists of a central quantum dot, $QD_a$, coupled to the two normal leads, $L_1$ and $L_2$, and a side $QD_b$, connected to a superconductor $S$. The Hamiltonian of the system is given by:

$$H = H_1 + H_2 + H_S + H_{DQD} + H_T. \tag{1}$$

The first and the second terms are the Hamiltonians for the normal leads at the left (1) and right (2) sides of $QD_a$. These are modeled by Eqs. (2) and (3):

$$H_1 = \sum_k \sum_\sigma \varepsilon_{1k\sigma} c^\dagger_{1k\sigma} c_{1k\sigma}, \tag{2}$$

and

$$H_2 = \sum_k \sum_\sigma \varepsilon_{2k\sigma} c^\dagger_{2k\sigma} c_{2k\sigma}, \tag{3}$$

where $c^\dagger_{\alpha k\sigma}$ ($c_{\alpha k\sigma}$) is the electron creation (annihilation) operator of an electron with spin $\sigma$ and energy $\varepsilon_{k\sigma}$ in the $\alpha$ electrode.

The second term stands for the BCS Hamiltonian[?] of the superconducting ($S$) lead and reads:

$$H_S = \sum_k \sum_\sigma \varepsilon_{kS} c^\dagger_{kS\sigma} c_{kS\sigma} + \sum_k (\Delta^* c_{kS\downarrow} c_{-kS\uparrow} + \Delta c^\dagger_{-kS\uparrow} c^\dagger_{kS\downarrow}), \tag{4}$$

where $c^\dagger_{kS\sigma}$ ($c_{kS\sigma}$) is the electron creation (annihilation) operator of an electron with spin $\sigma$ and energy $\varepsilon_{kS}$ in the superconducting electrode, and $\Delta$ denotes pair potential, whose absolute value gives the superconducting energy gap.

The $H_{DQD}$ term is given by Eq. (5), and takes into account the coupling between the QDs, modeled by the variable $t_{12} = t$, and the Coulomb interaction at each QD, whose strength is modeled by $U_m$, $m = a, b$. The QDs are assumed to have a single spin degenerated level, whose value is determined by $\varepsilon_{dm,\sigma}$, $m = a, b$.

$$\begin{aligned} H_{DQD} = & \sum_{m=a,b,\sigma} \varepsilon_{dm,\sigma} d^\dagger_{m,\sigma} d_{m,\sigma} \\ & + \sum_\sigma t \left[ d^\dagger_{a\sigma} d_{b\sigma} + d^\dagger_{a\sigma} d_{b\sigma} \right] \\ & + \sum_{m=a,b} U_m n_{m\sigma} n_{m\bar{\sigma}} \end{aligned} \tag{5}$$

### 1.1 Green's functions

In order to obtain the transport properties for the system modeled by Eq. (1), we have used the well-known non-equilibrium Green's function approach[?,?] along with the equation-of-motion method. This formalism has been extensively applied to nanostructured systems. The presence of the superconductor has been taken into account by expressing Green's functions within the Nambu space. In this way, Green's functions are represented by $4 \times 4$ matrices resulting from the tensor product between spin and electron-hole subspaces. By using this formalism, we have obtained a system of coupled Dyson equations for the retarded Green's functions matrices $\mathbf{G}^r_{aa}$ and $\mathbf{G}^r_{bb}$, for $QD_a$ and $QD_b$, respectively:

$$\mathbf{G}^r_{aa} = \mathbf{G}^{ro}_{aa} + \mathbf{G}^r_{aa} \mathbf{t}^\dagger_{ab} \mathbf{G}^{ro}_{bb} \mathbf{t}_{ab} \mathbf{G}^{ro}_{aa}, \tag{6}$$

and

$$\mathbf{G}^r_{bb} = \mathbf{G}^{ro}_{bb} + \mathbf{G}^r_{bb} \mathbf{t}^\dagger_{ab} \mathbf{G}^{ro}_{aa} \mathbf{t}_{ab} \mathbf{G}^{ro}_{bb}, \tag{7}$$

with

$$\mathbf{G}^{ro}_{aa} = \mathbf{g}^r_{aa} (1 - \mathbf{\Sigma}^r_L \mathbf{g}^r_{aa})^{-1}, \tag{8}$$

and

$$\mathbf{G}^{ro}_{bb} = \mathbf{g}^{r}_{bb}(1 - \mathbf{\Sigma}^{r}_{S}\mathbf{g}^{r}_{bb})^{-1}. \tag{9}$$

In Eqs. (6) to (9), $\mathbf{g}^{r}_{aa}$ and $\mathbf{g}^{r}_{bb}$ are the $QD_a$ and $QD_b$ Green's functions, respectively, when the QDs are isolated from the leads; $\mathbf{t}_{ab}$ describes the tunneling between $QD_a$ and $QD_b$. The coupling to the normal and superconducting leads are modeled by retarded/advanced self-energies $\mathbf{\Sigma}^{r}_{L} = \mathbf{\Sigma}^{r}_{1} + \mathbf{\Sigma}^{r}_{2}$ and $\mathbf{\Sigma}^{r}_{S}$, respectively.

The self-energy for the coupling to the normal leads ($L_1$ and $L_2$) is given by Eq. (10):

$$\mathbf{\Sigma}^{r,a}_{L} = \mp\frac{i}{2}(\Gamma_1 + \Gamma_2)\begin{bmatrix} 1 & 0 & 0 & 0 \\ 0 & 1 & 0 & 0 \\ 0 & 0 & 1 & 0 \\ 0 & 0 & 0 & 1 \end{bmatrix}, \tag{10}$$

where $\Gamma_i = \Gamma_{i\uparrow} + \Gamma_{i\downarrow}$ and $\Gamma_{i\sigma} = 2\pi|t_i|^2 N_i$, $(i = 1, 2)$ being the coupling strength, with $t_i$ being amplitude for an electron with spin $\sigma$ of $QD_a$ to be transferred to the lead $L_i$; $N_i$ is the density of states at Fermi level for the normal lead, $L_i$. Since we have assumed both normal leads as non-magnetic, the density of states is the same for both spins.

The retarded/advanced self-energy of the superconductor is given by Eq. (11):

$$\mathbf{\Sigma}^{r,a}_{S} = \mp\frac{i}{2}\rho_S(\varepsilon)\Gamma_S\begin{bmatrix} 1 & -\frac{\Delta}{\varepsilon} & 0 & 0 \\ -\frac{\Delta}{\varepsilon} & 1 & 0 & 0 \\ 0 & 0 & 1 & \frac{\Delta}{\varepsilon} \\ 0 & 0 & \frac{\Delta}{\varepsilon} & 1 \end{bmatrix}. \tag{11}$$

In Eq. (11), $\Gamma_S = 2\pi|t_s|^2 N_s$ is the coupling strength between the superconductor lead and $QD_b$, defined in terms of the amplitude of tunneling $|t_s|$ and the normal density of states of $N_s$. The $\Delta$ appearing in some of the matrix elements stands for the energy gap of the superconductor and accounts for the electron-hole coupling. The energy gap plays a central role in this model and also modifies the self-energy through $\rho_S$, the dimensionless modified BCS density of states, whose expression is given by:

$$\rho_S(\varepsilon) = \frac{|\varepsilon|\theta(|\varepsilon| - \Delta)}{\sqrt{\varepsilon^2 - \Delta^2}} - i\frac{\varepsilon\theta(\Delta - |\varepsilon|)}{\sqrt{\Delta^2 - \varepsilon^2}}, \tag{12}$$

with the imaginary part accounting for the Andreev bound states (ABS), within the superconductor gap.

The presence of electronic correlations associates the QDs energy levels with the electronic occupations, which, in turn, depend on external parameters like gate and bias voltages. As a result, Eqs. (6) and (7) must be solved in a self-consistent way, together with the occupations of the QDs. Such occupations are obtained from the diagonal matrix elements of the "lesser" Green's function matrix, which is obtained through the Keldysh equation. For the $QD_a$, the expression reads:

$$\mathbf{G}^{<}_{aa} = \mathbf{G}^{r}_{aa}(\omega)\mathbf{\Sigma}^{<}_{Ta}\mathbf{G}^{a}_{aa}(\omega), \tag{13}$$

with

$$\mathbf{\Sigma}^{<}_{Ta} = \mathbf{\Sigma}^{<}_{L}(\varepsilon) + \mathbf{t}^{\dagger}_{ab}\mathbf{G}^{ro}_{bb}\mathbf{\Sigma}^{<}_{S}(\varepsilon)\mathbf{G}^{ao}_{bb}\mathbf{t}_{ab}. \tag{14}$$

The expression for $QD_b$ can be obtained by exchanging the indices $a$ and $b$. In Eq. (13), $\mathbf{\Sigma}^{<}_{Ta}$ represents the "lesser" self-energy, which is expressed in terms of the self-energies of the leads: $\mathbf{\Sigma}^{<}_{L} = \mathbf{\Sigma}^{<}_{1} + \mathbf{\Sigma}^{<}_{2}$ and $\mathbf{\Sigma}^{<}_{S}$. Assuming that the leads are in equilibrium with well-defined chemical potential and temperature, the self-energies of the leads can be obtained using the fluctuation-dissipation theorem: $\mathbf{\Sigma}^{<}_{i} = \mathbf{F}_i[\mathbf{\Sigma}^{a}_{i} - \mathbf{\Sigma}^{r}_{i}]$, where the Fermi matrix $\mathbf{F}_i$ is given by

$$\mathbf{F}_i = i\begin{bmatrix} f_i & 0 & 0 & 0 \\ 0 & \bar{f}_i & 0 & 0 \\ 0 & 0 & f_i & 0 \\ 0 & 0 & 0 & \bar{f}_i \end{bmatrix}, \tag{15}$$

with $f_i = f(\varepsilon - eV_i)$ and $\bar{f}_i = f(\varepsilon + eV_i)$ $(i = 1, 2, S)$ being the Fermi functions for electrons and holes, respectively. Since the superconductor is assumed to be grounded, $f_i = f(\varepsilon)$ for $i = s$.

### 1.2 Transmittance and current

The presence of Coulomb correlations leads to a self-consistent problem when solving Eqs. (6) and (7), since the dependency on the occupations wraps the Green's functions to the occupancies of the QDs. Within the equation-of-motion approach used in this work, this results in an infinite set of equations with Green's functions of increasing order of complexity. In order to obtain a closed set of equations, one needs to resort to some approximation on the Coulomb correlations. In this work, we have used the so-called Hubbard-I approximation[?], which allows us to derive a simple expression for the electrical current in terms of the different transmission amplitudes that contribute to the electronic transport for this system. In fact, the current $I_j$, flowing in the lead $L_j$ ($j = 1,2$), is given by the following expression:

$$I_j = \frac{e}{\hbar}\int d\varepsilon\,[\mathbf{G}^r_{aa}(\varepsilon)\mathbf{\Sigma}^<_j(\varepsilon) + \mathbf{G}^<_{aa}(\varepsilon)\mathbf{\Sigma}^a_j(\varepsilon) + \text{H.c.}]_{(11+33)}, \qquad j = 1,2. \tag{16}$$

where $11+33$ stands for the sum of the 11 and 33 matrix elements of the current matrix. By substituting the Green's functions and self-energies into Eq. (16), one obtains the main expression for the electric current flowing in the lead $L_1$, written in terms of the transmittances:

$$I_1 = \frac{e}{h}\int [T^{DAR}_{11}(f_1 - \bar{f}_1) + T^{ET}_{12}(f_1 - f_2) + T^{CAR}_{12}(f_1 - \bar{f}_2) + T^{QP}_{1S}(f_1 - f_S)]d\varepsilon, \tag{17}$$

The first term appearing in Eqs. (17) , $T^{DAR}_{11}$, correspond to direct Andreev reflection transmittances through the paths $(L_1 - QD_a - QD_b - S)$ and $(L_2 - QD_a - S)$, respectively. The second term $T^{ET}_{12}$ is due to electron tunneling (ET) between the normal leads, i.e., through the path $(L_1 - QD_a - QD_b - L_2)$, respectively. The next two term, $T^{CAR}_{11}$ account for the crossed Andreev reflection transmittances through $((L_1, L_2) - QD_a - QD_b - S)$ path, respectively. Finally, the last term, $T^{QP}_{11}$, correspond to the quasiparticles tunneling through $(L_1 - QD_a - QD_b - S)$ path, respectively.

The expressions of the amplitudes in terms of Green's functions are given by:

$$\begin{aligned}
T^{DAR}_{11} &= \Gamma_1^2(|G^r_{aa,14}|^2 + |G^r_{aa,12}|^2 + |G^r_{aa,34}|^2 + |G^r_{aa,32}|^2)\\
T^{CAR}_{12} &= \Gamma_1\Gamma_2(|G^r_{aa,14}|^2 + |G^r_{aa,12}|^2 + |G^r_{aa,34}|^2 + |G^r_{aa,32}|^2)\\
T^{ET}_{12} &= \Gamma_1\Gamma_2(|G^r_{aa,33}|^2 + |G^r_{aa,31}|^2 + |G^r_{aa,13}|^2 + |G^r_{aa,11}|^2)\\
T^{QP}_{1S} &= \tilde{\rho}\Gamma_1\Gamma_S\{Y^-_{21}|G^r_{aa,12}|^2 + X^+_{34}|G^r_{aa,13}|^2 + Y^+_{43}|G^r_{aa,14}|^2\\
&\quad + X^-_{12}|G^r_{aa,11}|^2 - Z^+_{34}G^r_{aa,13}[G^r_{aa,14}]^* - [Z^+_{34}]^*[G^r_{aa,13}]^*G^r_{aa,14}\\
&\quad - Z^-_{12}G^r_{aa,11}[G^r_{aa,12}]^* - [Z^-_{12}]^*[G^r_{aa,11}]^*G^r_{aa,12}\\
&\quad + Y^-_{21}|G^r_{aa,32}|^2 + X^+_{34}|G^r_{aa,33}|^2 + Y^+_{43}|G^r_{aa,34}|^2\\
&\quad + X^-_{32}|G^r_{aa,31}|^2 - Z^+_{34}G^r_{aa,33}[G^r_{aa,34}]^*\\
&\quad - [Z^+_{34}]^*[G^r_{aa,33}]^*G^r_{aa,34} - Z^-_{12}G^r_{aa,31}[G^r_{aa,32}]^*\\
&\quad - [Z^-_{12}]^*[G^r_{aa,31}]^*G^r_{aa,32}\}
\end{aligned} \tag{18}$$

where

$$\begin{aligned}
X^\pm_{ij} &\equiv t^2[|G^{ro}_{bb,ii}|^2 + |G^{ro}_{bb,ij}|^2 \pm \frac{\Delta}{\varepsilon}(G^{ro}_{bb,ii}[G^{ro}_{bb,ij}]^* + G^{ro}_{bb,ij}[G^{ro}_{bb,ii}]^*),\\
Y^\pm_{ij} &\equiv t^2[|G^{ro}_{bb,ii}|^2 + |G^{ro}_{bb,ji}|^2 \pm \frac{\Delta}{\varepsilon}(G^{ro}_{bb,ii}[G^{ro}_{bb,ji}]^* + G^{ro}_{bb,ji}[G^{ro}_{bb,ii}]^*)],\\
Z^\pm_{ij} &\equiv t^2[G^{ro}_{bb,ij}[G^{ro}_{bb,jj}]^* + [G^{ro}_{bb,ij}]^*G^{ro}_{bb,ii}\\
&\qquad \pm \frac{\Delta}{\varepsilon}(|G^{ro}_{bb,ij}|^2 + [G^{ro}_{bb,jj}]^*G^{ro}_{bb,ii})].
\end{aligned} \tag{19}$$

(The current flowing and transmittances in $L_2$ can be obtained by interchanging the indexes 1 and 2 in the above equation).

### 1.3 Self-consistent calculations

Regarding the occupations of the QDs, they are determined by the "lesser" Green's function. In the case of normal leads with no polarization, the average occupation number remains independent of spin. This allows us to set, for each QD, $\langle n_{i,\sigma}\rangle = \langle n_i\rangle$ where $i = a, b$. These occupation numbers are obtained by solving the following self-consistent system of integral equations:

$$\langle n_{a\uparrow}\rangle = -i\int \frac{d\varepsilon}{2\pi} G^{<}_{aa,11}[\varepsilon, \langle n_{a\uparrow}\rangle, \langle n_{a\downarrow}\rangle, \langle n_{b\uparrow}\rangle, \langle n_{b\downarrow}\rangle], \tag{20a}$$

$$\langle n_{a\downarrow}\rangle = -i\int \frac{d\varepsilon}{2\pi} G^{<}_{aa,33}[\varepsilon, \langle n_{a\uparrow}\rangle, \langle n_{a\downarrow}\rangle, \langle n_{b\uparrow}\rangle, \langle n_{b\downarrow}\rangle], \tag{20b}$$

$$\langle n_{b\uparrow}\rangle = -i\int \frac{d\varepsilon}{2\pi} G^{<}_{bb,11}[\varepsilon, \langle n_{a\uparrow}\rangle, \langle n_{a\downarrow}\rangle, \langle n_{b\uparrow}\rangle, \langle n_{b\downarrow}\rangle], \tag{20c}$$

$$\langle n_{b\downarrow}\rangle = -i\int \frac{d\varepsilon}{2\pi} G^{<}_{bb,33}[\varepsilon, \langle n_{a\uparrow}\rangle, \langle n_{a\downarrow}\rangle, \langle n_{b\uparrow}\rangle, \langle n_{b\downarrow}\rangle]. \tag{20d}$$

## 2 Thermoelectric Properties in linear regime

The measurement of the voltage $\Delta\mu$ induced by the temperature difference $\Delta T$ gives the Seebeck coefficient. Let us recall that the standard definition of the Seebeck coefficients,in the two- terminal system is the vanishing of the current.

By definition, the thermopower, or Seebeck-coefficient, S is given by the difference in chemical potential $\Delta\mu$ which arises due to a small temperature difference $\Delta T$ under open circuit conditions $(I \to 0)$ between two voltage probes, divided by $\Delta T$ :

$$S = -\left.\frac{\Delta\mu}{e\Delta T}\right|_{I=0} \tag{21}$$

In multiterminal devices, there exist a large number of various possibilities.In this paper we will follow the proposal made by G. Michałek et al.[45], i.e. we perform the measurement under open-circuit conditions(imposing $J_i = 0$ for all electrodes). Note that this assumption makes our condition similar to that of Mazza et al.[46].

Once the local and nonlocal resistances of the hybrid system are determined under isothermal conditions, we can express the local and nonlocal thermopowers as

$$S_{RL} = -\left.\frac{\Delta\mu_{RL}}{e\Delta T_{RL}}\right|_{T_{LS}=0} = R_{RL,RL}(\mathscr{L}^{ET}_{LR,T} + \mathscr{L}^{CAR}_{LR,T}) + \mathscr{L}^{QP}_{RS,T} \tag{22}$$

with

$$\mathscr{L}^{\kappa}_{\alpha\beta,\mu} = \frac{2e}{h}\int dE\ \mathscr{T}^{\kappa}(E)\left(-\frac{\partial f_0}{\partial E}\right), \tag{23}$$

$$\mathscr{L}^{\kappa}_{\alpha\beta,T} = \frac{2e}{h}\int dE\ \frac{(E-\mu)}{T}\mathscr{T}^{\kappa}(E)\left(-\frac{\partial f_0}{\partial E}\right), \tag{24}$$

with $\alpha, \beta = \{L, R, S\}$ and $\kappa = \{QP, ET, CAR, DAR\}$.

whereas

$$R_{RL,RL} = \frac{2\mathscr{L}^{CAR}_{LR,\mu} + \mathscr{L}^{DAR}_{LL,\mu} + \mathscr{L}^{DAR}_{RR,\mu} + \frac{1}{2}(\mathscr{L}^{QP}_{LS,\mu} + \mathscr{L}^{QP}_{RS,\mu})}{eD} = \frac{1}{G_{RL}} \tag{25}$$

with

$$\begin{aligned} D =& \mathscr{L}^{ET}_{LR,\mu}(\mathscr{L}^{DAR}_{LL,\mu} + 2\mathscr{L}^{CAR}_{LR,\mu} + \mathscr{L}^{DAR}_{RR,\mu}) + \mathscr{L}^{CAR}_{LR,\mu}(\mathscr{L}^{DAR}_{LL,\mu} + \mathscr{L}^{DAR}_{RR,\mu}) + 2\mathscr{L}^{DAR}_{LL,\mu}\mathscr{L}^{DAR}_{RR,\mu} \\ &+ \frac{1}{2}(\mathscr{L}^{QP}_{LS,\mu} + \mathscr{L}^{QP}_{RS,\mu})(\mathscr{L}^{ET}_{LR,\mu} + \mathscr{L}^{CAR}_{LR,\mu}) \\ &+ (\mathscr{L}^{DAR}_{LL,\mu}\mathscr{L}^{QP}_{RS,\mu} + \mathscr{L}^{DAR}_{RR,\mu}\mathscr{L}^{QP}_{LS,\mu}) \\ &+ \frac{1}{2}\mathscr{L}^{QP}_{LS,\mu}\mathscr{L}^{QP}_{RS,\mu} \end{aligned} \tag{26}$$

in the subgap regime it can be shown that the equations for $G_{RL,RL}$ and $S_{RL}$ are given by :

$$G_{RL,RL} = \frac{1}{R_{RL,RL}} = e(\mathscr{L}^{ET}_{LR,\mu} + \mathscr{L}^{CAR}_{LR,\mu}) \tag{27}$$

$$S_{RL} = R_{RL,RL}(\mathscr{L}^{ET}_{LR,T} + \mathscr{L}^{CAR}_{LR,T}) \tag{28}$$

## 3 Results and Discussion

### 3.1 Effect of superconducting energy gap $\Delta$

The corresponding Thermopower as a function of QD level $\varepsilon_d$ is plotted in Fig. 2. When $t \neq 0$ the electrical conductance $G_{RL}$, as shown in Fig. 2(a), exhibits two sharp side peaks in $\varepsilon_d \approx -t - U + \delta(\Sigma^r)$ and $\varepsilon_d \approx t + \delta(\Sigma^r)$ where $\delta(\Sigma^r)$is a small self-energy correction that is due to the coupling between the QDs and electrodes, while the central peak appears in the middle between them at $\varepsilon_d = -U/2$ (which coincides with one of the zeros of $S$ ). which become two peaks as the value of U increases. Separation of the side peaks is approximately equal to $2t$. However, the height of the side peaks of the conductance $G_{RL}$ increases as the energy gap of the superconductor increases. In turn, the height of the central peak at $\varepsilon_d = -U/2$ decreases with increasing $\Delta$ while the value of $S_{RL}$ remains equal to zero. The explanation of this behavior for the central peaks can be obtained from Fig.3 which shows the plots of the different transmissions as a function of $\varepsilon$ for the value of $\varepsilon_d = -U/2$ in the case where $\Delta = 0$ and in the case where $\Delta = 1$. As can be seen in Fig. 3(a), in the case where $\Delta$ is zero, there is an important contribution made by the transmission $T_{RS}^{ET}$ to the integral $L_{RS,\mu}^{ET}$ present in the equation for $G_{RL}$ when the energy is close to zero and $\varepsilon_d = -U/2$ (see Eq. (5.28). On the other hand, when the delta is nonzero, an energy gap is opened in which transmission $T_{RS}^{QP}$ is forbidden and only $T_{RL}^{ET}$ contributes to the value of $G_{RL}$ near zero energy so that its value is smaller than when $\Delta = 0$ (see Fig.3). However, when $\varepsilon_d = -U/2$ the symmetric distribution of $T_{RL}^{ET}$ and $T_{RL}^{CAR}$ around zero causes the integrals $L_{RL,T}^{ET}$ and $L_{RL,T}^{CAR}$ to become identically zero in both cases( because the integrand is the product of an even function by $\varepsilon df/d\varepsilon$), which explains the zero value of the thermopower for $\varepsilon_d = -U/2$ when $\Delta = 0$ or $\Delta \neq 0$. The thermopower $S_{RL}$ as a function of $\varepsilon_d$ for different values of $\Delta$ is shown in Fig. 2(b). The two zeros of $S_{LR}$ coincide with the side maxima of $G_{RL}$ (resonances). Furthermore, the maximum value of $|S_{RL}|$ is reached on both sides of $\varepsilon_d = -U/2$ ( near $\varepsilon_d = 0$ or $\varepsilon_d = -U$ when $G_{RL}$ is close to its minimum value (see Fig. 3 (b). Furthermore, $S_{RL}$ increases rapidly when the superconductor energy gap increases and reaches its maximum value when the delta is close to $\Delta = 1\Gamma_L$. The explanation for this behavior is based on the fact that when $\Delta = 1\Gamma_L$ the conductance $G_{RL}$ is reduced to zero at $\varepsilon_d = 0$ or $-U$ and $L_{RL,T}^{ET}$ decreases more smoothly than when $\Delta = 0$ for these values of $\varepsilon_d$, which explains the significant increase in $S_{RL}$ when $\Delta = 1$.

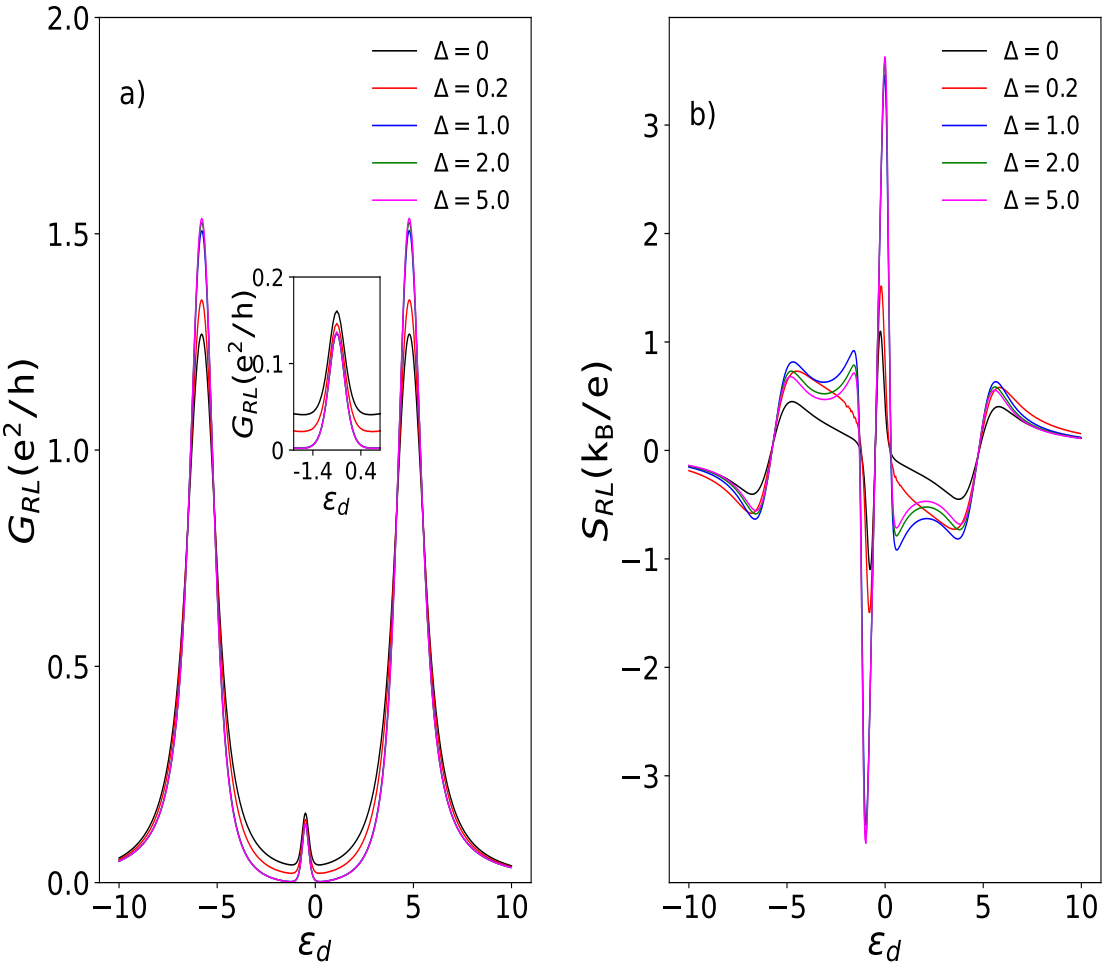


**Figure 2.** The electronic conductance $G_{RL}$ (a) and the Seebeck coefficient $S_{RL}$ (b) in units $k_B/e$ as a function of the QD level position $\varepsilon_d$ for differents values of the superconducting energy gap $\Delta$. Other parameters are chosen as $\Gamma_L = \Gamma_R = \Gamma_S$ , $t = 2\Gamma_L$, $K_BT = 0.1\Gamma_L$,and $U = 1\Gamma_L$.

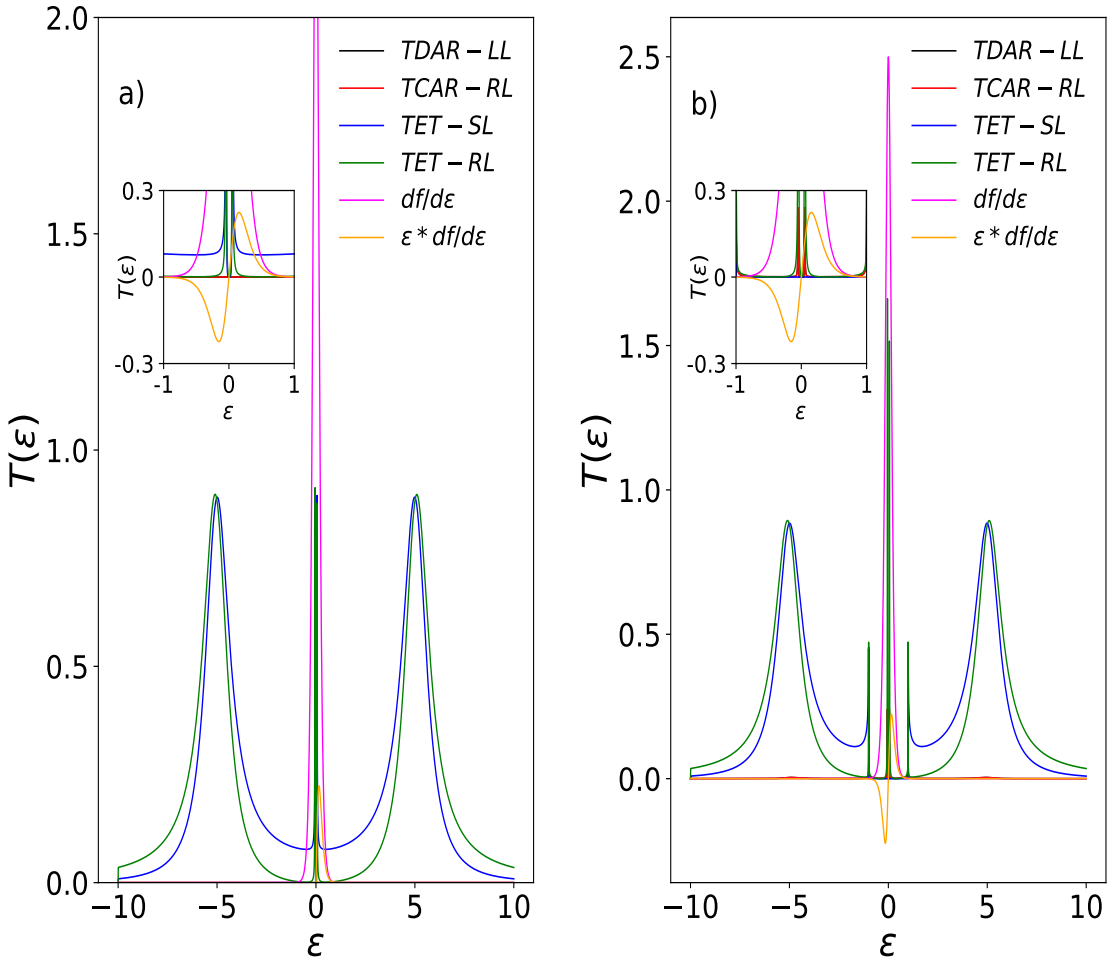


**Figure 3.** The transmittance $T_{LR}^{ET}$ and other thermolectric parameters as function of the energy $\varepsilon$, when $\Delta = 0$ (a) or $\Delta = 1$(b). Other parameters are chosen as $\varepsilon_d = -U/2$, $t = 5$, $U = 1\Gamma_L$, $k_BT = 0.1\Gamma_L$ and $\Gamma_L = \Gamma_R = \Gamma_S$.

### 3.1.1 Influence of intradot Coulomb interactions

The electronic conductance $G_{RL}$ as a function of $\varepsilon_d$ for different values of $U$ is shown in Fig. 4 a). We can observe that the Coulomb interaction splits the electronic conductance spectrum into two sets symmetric to the electron-hole symmetry point $\varepsilon_d = -U/2$, and their centers are located approximately at $\varepsilon_d = 0$ and $\varepsilon_d = -U$. The height of the two lateral peaks of the conductance $G_{RL}$ does not change appreciably with the change of $U$. In turn, the height of the two central peaks increases as $U$ increases.

The thermopower $S_{RL}$ as a function of $\varepsilon_d$ for different values of $U$ is shown in Fig. 4 b). The thermopower is antisymmetric to the thermopower zeros that coincide, as mentioned above, with the electronic conductance peaks, where $S$ has a maximum and a minimum on each side of these. The height of the thermopower peaks $S_{RL}$ does not change appreciably with the change of $U$.

The Coulomb interaction strongly affects the thermopower in a valley between the conductance peaks. In particular, an additional sharp structure appears close to the electron/hole symmetry point $\varepsilon_d = -U/2$. This effect is related to the Fano resonance and is a signature of the destructive interference between the activated QD levels. It leads to a reduction of total transmission to zero and, as a consequence, to a reduction of $G_{RL}$ and $L^{ET}_{RL,T}$. Since the reduction of $G_{RL}$ is stronger than $L^{ET}_{RL,T}$, the reduction of $S_{RL}$ is increased.

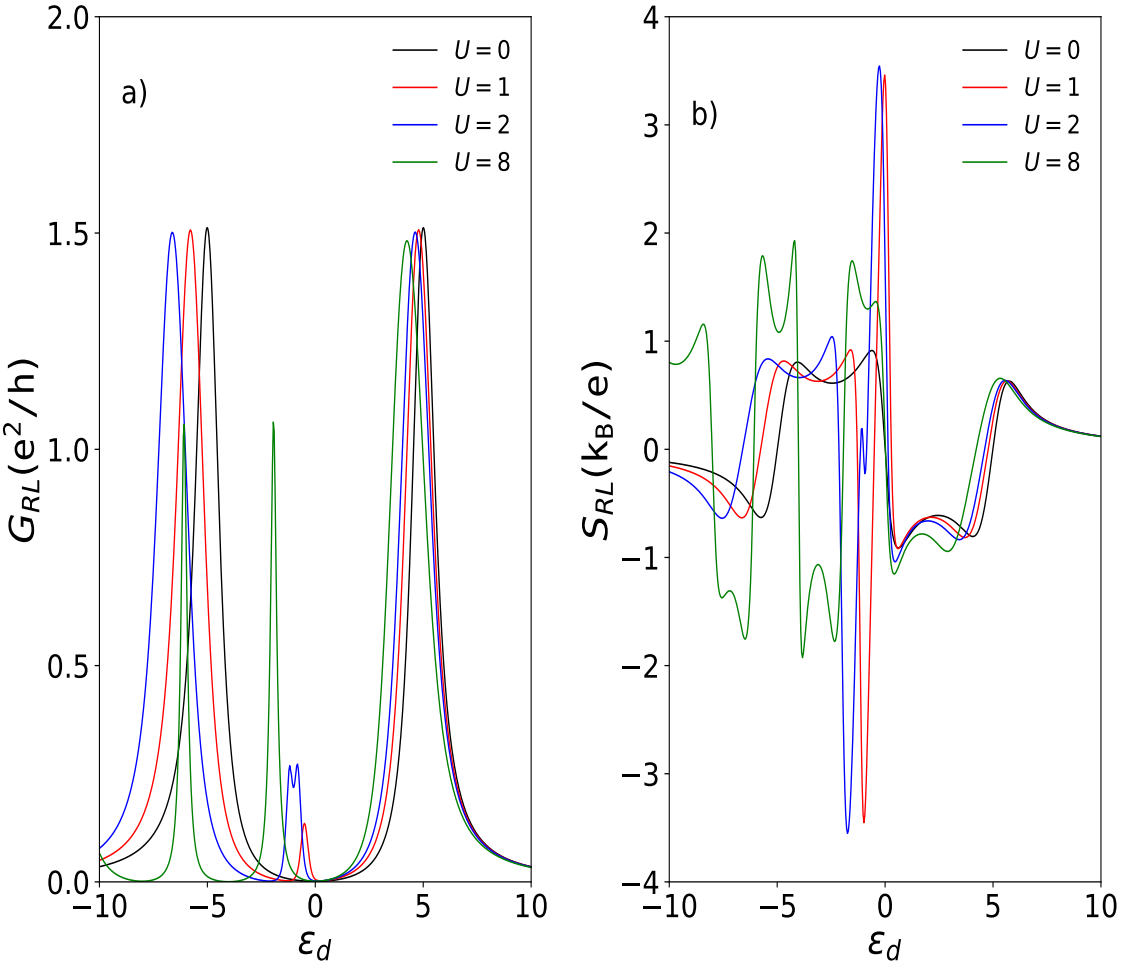


**Figure 4.** The electronic conductance $G_{LR}$ (a) and the Seebeck coefficient $S_{RL}$ (b) in units $k_B/e$ as a function of the QD level position $\varepsilon_d$ for differents values of the coulomb interaction $U$ . Other parameters are chosen as $\Delta = 1\Gamma_L$ $\Gamma_L = \Gamma_R = \Gamma_S$ , $t = 2\Gamma_L$, $K_BT = 0.1\Gamma_L$,and $U = 1\Gamma_L$.

### 3.1.2 Effect of Temperature

The corresponding behavior of the electronic conductance $G_{RL}$ and thermopower $S_{RL}$ with temperature and gate voltage is shown in Fig. 5. As the temperature increases, the height of the lateral peaks of the electronic conductance $G_{RL}$ decreases while the central peaks gradually disappear. The explanation for this behavior lies in the flattening of the derivative of the fermi function as the temperature increases which reduces the contribution of $T_{RL}^{ET}$ to the integral $L_{LR,\mu}^{ET}$, and consequently reduces the electronic conductance $G_{RL}$(See Fig.8). On the other hand, when the temperature is higher, due to the flattening of the fermi derivative function, the variation of the $L_{RL,\mu}^{ET}$ integral is less abrupt in the vicinity of $\varepsilon_d = -U/2$ which explains the disappearance of the central peak of $G_{RL}$. (See Fig. 5 a)). On the other hand, the height of the |S| peaks decreases with increasing temperature. This is because at higher temperatures the peak of the derivative of the Fermi function is broadened, which allows for a greater overlap with the transmission $T_{RL,\mu}^{ET}$ which allows the integral $L_{RL,\mu}^{ET}$ to reach a larger value than at low temperatures, and therefore $G_{RL}$ never becomes very small, at the same time the integral $L_{RL,T}^{ET}$ is reduced. Additionally, as the temperature increases, an increase in the contribution of the $L_{RS,T}^{QP}$ integral to the Thermopower can be observed, because the broadening of the peak of the derivative of the Fermi function allows a greater overlap of the Fermi function with the $T_{RS}^{QP}$ transmission outside the energy gap of the superconductor (See Fig. 5 b)).

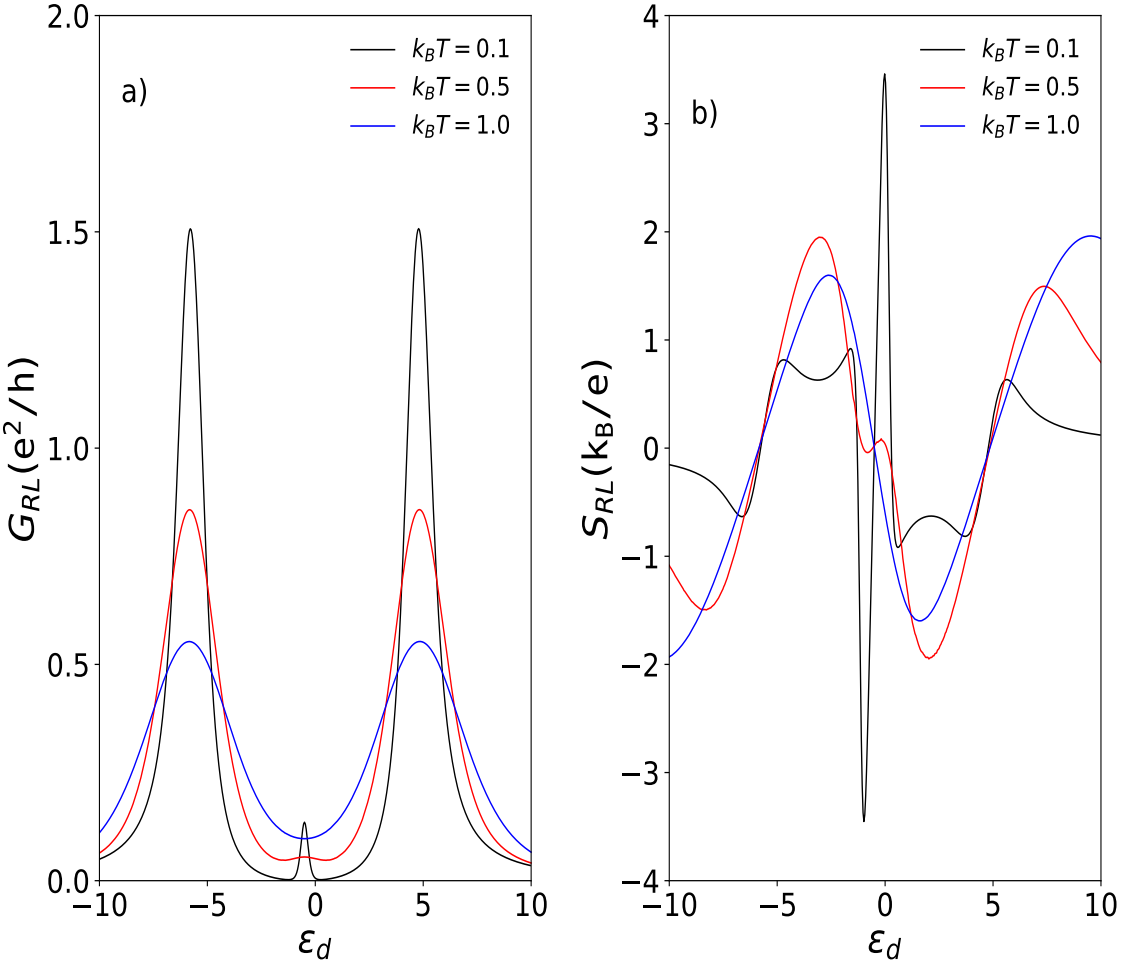


**Figure 5.** The electronic conductance $G_{RL}$ and Seebeck coefficient $S_{RL}$ in unit $k_B/e$ as function of the QD level position $\varepsilon$ for different values of the temperature $K_BT$. Other parameters are chosen as $t = 5\Gamma_L$, $U = 1\Gamma_L$, $\Delta = 1\Gamma_L$ and $\Gamma_S = \Gamma_L = \Gamma_R$.

### 3.1.3 Effect interdot tunneling

The electronic conductance $G_{RL}$ and the thermopower $S_{RL}$ as a function of $\varepsilon_d$ for different values of interdot tunneling $t$ are shown in Fig. 6. Fig. 6 (a) shows that the lateral peaks of $G_{RL}$ move away from each other as the value of $t$ increases. When $t = 0$ there are only 2 peaks of $G_{RL}$. When $t \neq 0$ a narrow peak appears, whose height decreases as $t$ increases. The reduction of the height of the central peak is due to the progressive decrease of the overlap between the fermi function and the transmission $T_{RL}^{ET}$ as $t$ increases.

On the other hand, in Fig.6(b) one can observe the increase of the maximum of $|S|$ as $t$ increases. This is mainly due to the decrease of $G_{RL}$ near the Fermi energy as $t$ increases due to the progressive reduction of the overlap between the Fermi derivative function and the two narrow central peaks of $T_{RL}^{ET}$ located within the superconductor energy gap and the increase of the quotient $L_{RL,T}^{ET}/G_{RL}$ as t increases.

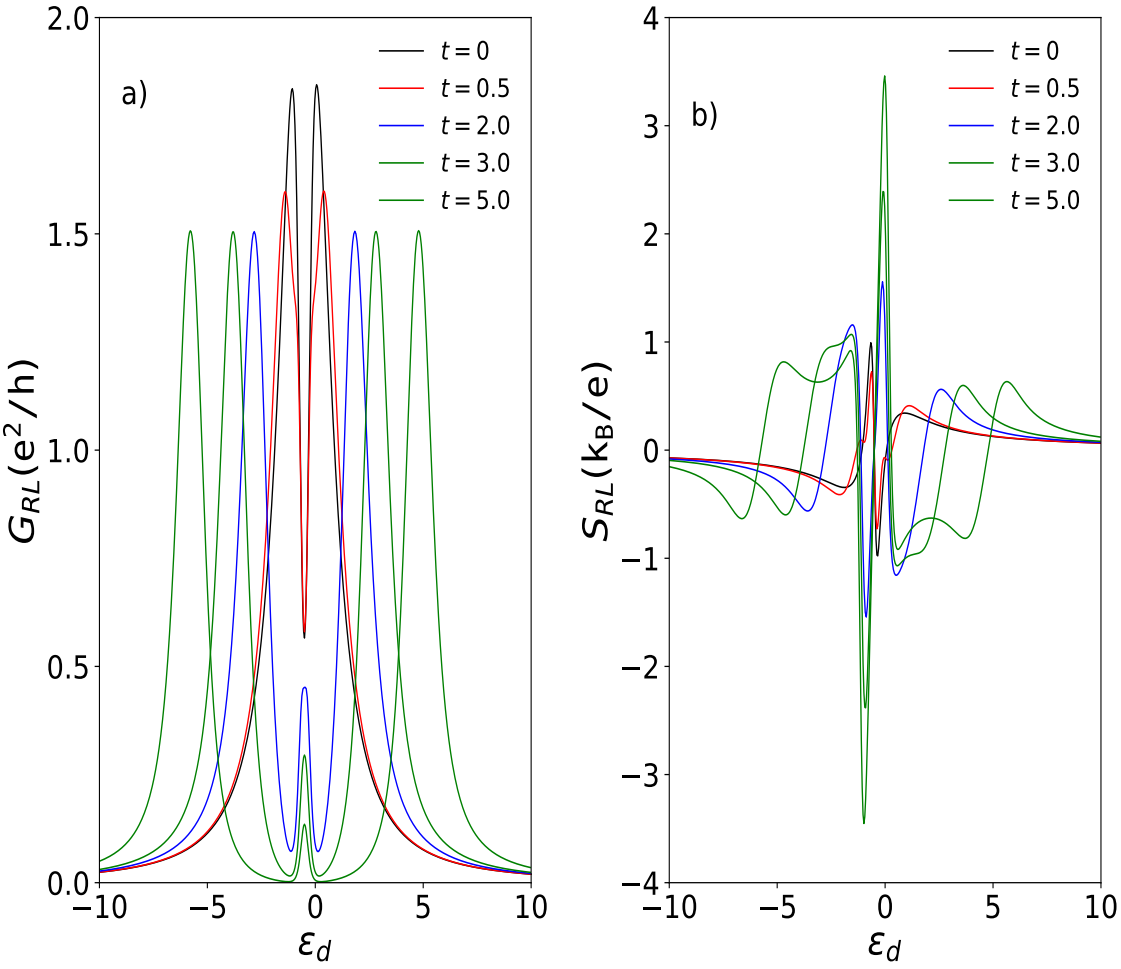


**Figure 6.** The electronic conductance $G_{RL}$ (a))and The Seebeck coefficient $S_{RL}$ (b)) in unit $k_B/e$ as function of the QD level position $\varepsilon$ for different values of the interdot tunneling. Other parameters are chosen as $\Delta = 1\Gamma_L$, $U = 1\Gamma_L$, $k_BT = 0.1\Gamma_L$ and $\Gamma_L = \Gamma_R = \Gamma_S$.

#### 3.1.4 *Effect of* $r = \Gamma_S/\Gamma_N$

Electronic conductance $G_{RL}$ and thermopower $S_{RL}$ as a function of $\varepsilon_d$ for different values of coupling rate $r = \Gamma_S/\Gamma_L$ are shown in Fig. 7. It can be seen in Fig. 7 a) that the height of the lateral peaks of $G_{RL}$ decreases as the coupling rate $\Gamma_S/\Gamma_L$ increases. On the contrary, the maximum height of $G_{RL}$ in $\varepsilon_d = -U/2$ grows slightly as $\Gamma_S/\Gamma_L$ grows. Interestingly, $G_{RL}$ rapidly decreases to zero in the neighborhood of $\varepsilon_d = -U/2$ when $\Gamma_S/\Gamma_L \leq 1$, however, when $\Gamma_S/\Gamma_L > 1$, the conductance $G_{RL}$ does not become zero at any point within the Coulomb blockade region. However, the maximum value of thermopower as a function of $\varepsilon_d$ decreases as $r$ increases (see Fig. 7b).

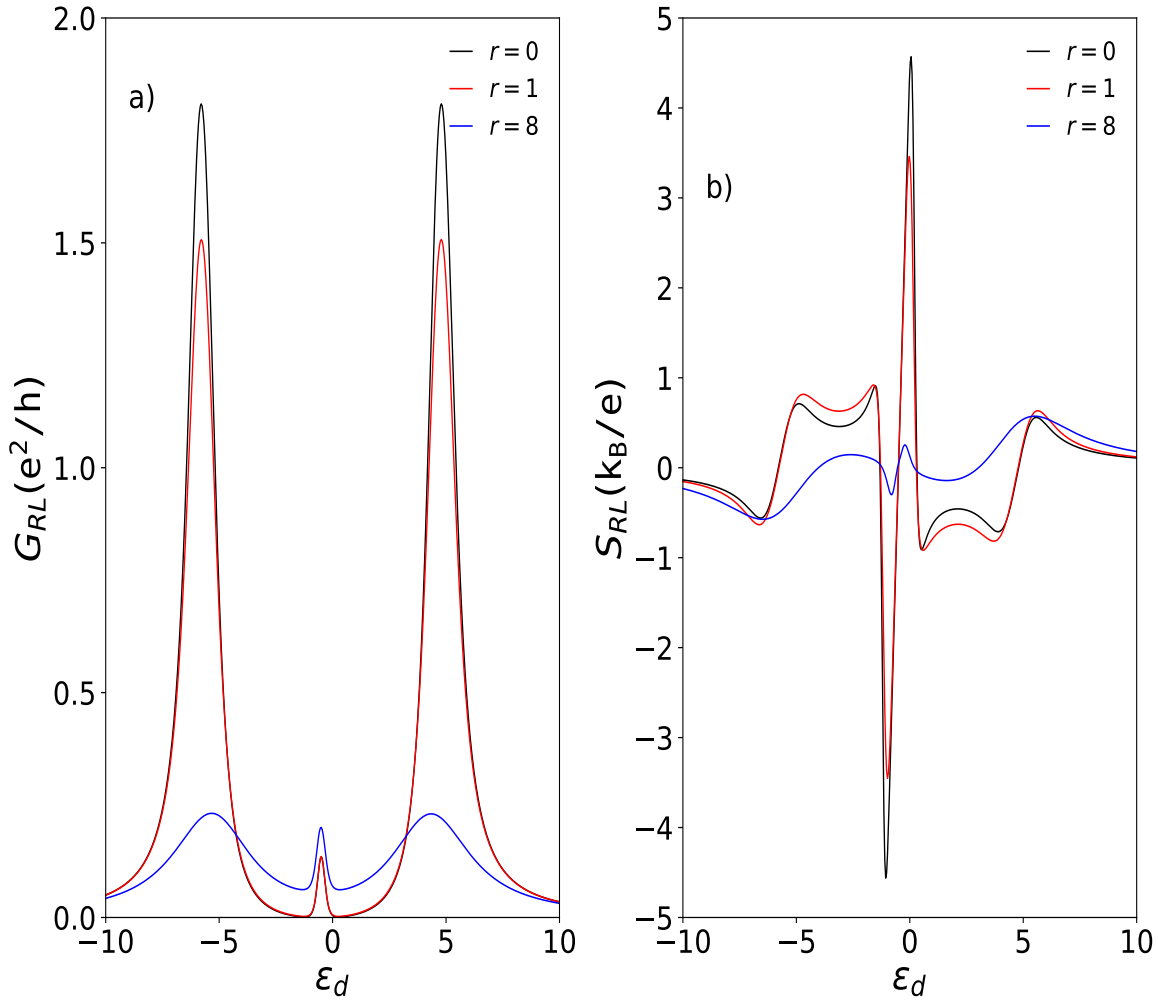


**Figure 7.** The electronic conductance $G_{RL}$ (a))and The Seebeck coefficient $S_{RL}$ (b)) in unit $k_B/e$ as function of the QD level position $\varepsilon$ for different values of the coupling ratio $\Gamma_S/\Gamma_L$ . Other parameters are chosen as $t = 5\Gamma_L$, $\Delta = 1\Gamma_L$, $U = 1\Gamma_L$, $k_BT = 0.1\Gamma_L$, and $\Gamma_L = \Gamma_R$.

# Bibliography


[1] Yannick David Baines. *Kondo physics in side coupled quantum dots.* Theses, Université Joseph-Fourier - Grenoble I, December 2010.

[2] S. Tarucha, D. G. Austing, T. Honda, R. J. van der Hage, and L. P. Kouwenhoven. Shell filling and spin effects in a few electron quantum dot. *Phys. Rev. Lett.*, 77:3613–3616, Oct 1996.

[3] Timothy Child, Martin Cross, Alexandra Tully, and Max Werner. An introduction to the kondo effect. 2018.

[4] Wilfred Wiel, De S, Toshimasa Fujisawa, J. Elzerman, Seigo Tarucha, and L. Kouwenhoven. The kondo effect in the unitary limit. *Science (New York, N.Y.)*, 289:2105–8, 10 2000.

[5] R. H. Dicke. The effect of collisions upon the doppler width of spectral lines. *Phys. Rev.*, 89:472–473, Jan 1953.

[6] A M Calle, M Pacheco, G B Martins, V M Apel, G A Lara, and P A Orellana. Fano–andreev effect in a t-shape double quantum dot in the kondo regime. *Journal of Physics: Condensed Matter*, 29(13):135301, feb 2017.

[7] W.J. de Haas, J. de Boer, and G.J. van dën Berg. The electrical resistance of gold, copper and lead at low temperatures. *Physica*, 1(7):1115–1124, 1934.

[8] M. P. Sarachik, E. Corenzwit, and L. D. Longinotti. Resistivity of mo-nb and mo-re alloys containing 1 *Phys. Rev.*, 135:A1041–A1045, Aug 1964.

[9] Jun Kondo. Resistance Minimum in Dilute Magnetic Alloys. *Progress of Theoretical Physics*, 32(1):37–49, 07 1964.

[10] Sara Cronenwett. Coherence, charging, and spin effects in quantum dots and point contacts. 08 2002.

[11] R. H. Dicke. Coherence in spontaneous radiation processes. *Phys. Rev.*, 93:99–110, Jan 1954.

[12] T. V. Shahbazyan and M. E. Raikh. Two-channel resonant tunneling. *Phys. Rev. B*, 49:17123–17129, Jun 1994.

[13] P. A. Orellana, M. L. Ladrón de Guevara, and F. Claro. Controlling fano and dicke effects via a magnetic flux in a two-site anderson model. *Phys. Rev. B*, 70:233315, Dec 2004.

[14] E. Vernek, P. A. Orellana, and S. E. Ulloa. Suppression of kondo screening by the dicke effect in multiple quantum dots. *Phys. Rev. B*, 82:165304, Oct 2010.

[15] Piotr Trocha and Józef Barnaś. Kondo-dicke resonances in electronic transport through triple quantum dots. *Phys. Rev. B*, 78:075424, Aug 2008.

[16] A. I. Buzdin. Proximity effects in superconductor-ferromagnet heterostructures. *Rev. Mod. Phys.*, 77:935–976, 2005.

[17] A F Andreev. Thermal conductivity of the intermediate state of superconductors. *Zh. Eksperim. i Teor. Fiz.*, 46, 1964.

[18] M. L. Ladrón de Guevara, F. Claro, and Pedro A. Orellana. Ghost fano resonance in a double quantum dot molecule attached to leads. *Phys. Rev. B*, 67:195335, May 2003.

[19] Haizhou Lu, Rong Lü, and Bang-fen Zhu. Tunable fano effect in parallel-coupled double quantum dot system. *Phys. Rev. B*, 71:235320, Jun 2005.

[20] J. Barański and T. Domański. Decoherence effect on fano line shapes in double quantum dots coupled between normal and superconducting leads. *Phys. Rev. B*, 85:205451, May 2012.

[21] Guo-Hui Ding, Chul Koo Kim, and Kyun Nahm. Fano resonance in electron transport through parallel double quantum dots in the kondo regime. *Phys. Rev. B*, 71:205313, May 2005.

[22] A. Calle, Monica Pacheco, and P. Orellana. Fano effect and andreev bound states in t-shape double quantum dots. *Physics Letters A*, 377, 02 2013.

[23] Jan Barański, Tomasz Zienkiewicz, Magdalena Barańska, and Konrad Kapcia. Anomalous fano resonance in double quantum dot system coupled to superconductor. *Scientific Reports*, 10:2881, 02 2020.

[24] Idali Gomez, Francisco Domínguez-Adame, and P. Orellana. Fano-like resonances in three-quantum-dot aharonov–bohm rings. *Journal of Physics: Condensed Matter*, 16:1613, 02 2004.

[25] Xiao-Jie Liu, Xue-Yang Zhao, Xiao-Fei Wang, Hui-Jie Xue, Li-Feng Feng, Di Zhang, and Hua Li. Spin polarization in a double-quantum dot interferometer with rashba spin–orbit interaction. *Physica Scripta - PHYS SCR*, 85, 05 2012.

[26] Piotr Trocha and Józef Barnaś. Quantum interference and coulomb correlation effects in spin-polarized transport through two coupled quantum dots. *Phys. Rev. B*, 76, 10 2007.

[27] D Sztenkiel and R Świrkowicz. Interference effects in a double quantum dot system with inter-dot coulomb correlations. *Journal of Physics: Condensed Matter*, 19(17):176202, mar 2007.

[28] Yushen Liu, Hao Chen, and Xi-Feng Yang. Transport properties of an aharonovcbohm ring with strong interdot coulomb interaction. *Journal of physics. Condensed matter : an Institute of Physics journal*, 19:246201, 06 2007.

[29] Tobias Brandes. Coherent and collective quantum optical effects in mesoscopic systems. *Physics Reports*, 408, 09 2004.

[30] T. V. Shahbazyan and S. E. Ulloa. Localized states in a strong magnetic field: Resonant scattering and the dicke effect. *Phys. Rev. B*, 57:6642–6653, Mar 1998.

[31] T. Vorrath and T. Brandes. Dicke effect in the tunnel current through two double quantum dots. *Phys. Rev. B*, 68:035309, Jul 2003.

[32] Bernhard Wunsch and Alexander Chudnovskiy. Quasistates and their relation to the dicke effect in a mesoscopic ring coupled to a reservoir. *Phys. Rev. B*, 68:245317, Dec 2003.

[33] P Trocha and J Barnaś. Dicke-like effect in spin-polarized transport through coupled quantum dots. *Journal of Physics: Condensed Matter*, 20(12):125220, mar 2008.

[34] Qiang Wang, Haiqing Xie, Yi-Hang Nie, and Wei Ren. Enhancement of thermoelectric efficiency in triple quantum dots by the dicke effect. *Phys. Rev. B*, 87:075102, Feb 2013.

[35] Qing-feng Sun, Jian Wang, and Tsung-han Lin. Resonant andreev reflection in a normal-metal–quantum-dot–superconductor system. *Phys. Rev. B*, 59:3831–3840, Feb 1999.

[36] SUN Qing-Feng ZHU Yu and LIN Tsung-Han. Effect of intra-dot coulomb interaction on andreev reflection in normal-metal/quantum-dot/superconductor system. *Communications in Theoretical Physics*, 36(01):101, 2001.

[37] E. C. Siqueira and G. G. Cabrera. Andreev tunneling through a double quantum-dot system coupled to a ferromagnet and a superconductor: Effects of mean-field electronic correlations. *Phys. Rev. B*, 81:094526, Mar 2010.

[38] Piotr Trocha and Józef Barnaś. Quantum interference and coulomb correlation effects in spin-polarized transport through two coupled quantum dots. *Phys. Rev. B*, 76, 10 2007.

[39] Piotr Trocha and Józef Barnaś. Spin-dependent thermoelectric phenomena in a quantum dot attached to ferromagnetic and superconducting electrodes. *Phys. Rev. B*, 95:165439, Apr 2017.

[40] guevara Bai, Rong Zhang, and Chenguevara Duan. Andreev reflection tunneling through a triangular triple quantum dot system. *Physica B: Condensed Matter*, 405:4875–4880, 12 2010.

[41] J. Bardeen, L. N. Cooper, and J. R. Schrieffer. Microscopic theory of superconductivity. *Phys. Rev.*, 106:162–164, Apr 1957.

[42] Pedro A. Orellana, Gustavo A. Lara, and Enrique V. Anda. Kondo and dicke effect in quantum dots side coupled to a quantum wire. *Phys. Rev. B*, 74:193315, Nov 2006.

[43] M. L. Ladrón de Guevara and P. A. Orellana. Electronic transport through a parallel-coupled triple quantum dot molecule: Fano resonances and bound states in the continuum. *Phys. Rev. B*, 73:205303, May 2006.

[44] Long Bai, Yang-Jin Wu, and Baigeng Wang. Andreev reflection in a triple quantum dot system coupled with a normal-metal and a superconductor. *physica status solidi (b)*, 247(2):335–341, 2010.

[45] Wei-Ping Xu, Yu-Ying Zhang, Qiang Wang, Zhi-Jian Li, and Yi-Hang Nie. Thermoelectric effects in triple quantum dots coupled to a normal and a superconducting leads. *Physics Letters A*, 380(7):958–964, 2016.

[46] S. Głodzik, K. P. Wójcik, I. Weymann, and T. Domański. Interplay between electron pairing and dicke effect in triple quantum dot structures. *Phys. Rev. B*, 95:125419, Mar 2017.

[47] J Hubbard. Electron correlations in narrow energy bands. *Proc. Roy. Soc. (London), Ser. A*.

[48] AC Hewson. The kondo problem problem to heavy fermions. *Cambridge Studies in Magnetism (Cambridge University Press, Cambridge, 2007)*, pages 235440–11, 2007.

[49] Tai Kai Ng and Patrick A. Lee. On-site coulomb repulsion and resonant tunneling. *Phys. Rev. Lett.*, 61:1768–1771, Oct 1988.

[50] L. I. Glazman and M. É. Raĭkh. Resonant Kondo transparency of a barrier with quasilocal impurity states. *Soviet Journal of Experimental and Theoretical Physics Letters*, 47:452, April 1988.

[51] Yigal Meir, Ned S. Wingreen, and Patrick A. Lee. Transport through a strongly interacting electron system: Theory of periodic conductance oscillations. *Phys. Rev. Lett.*, 66:3048–3051, Jun 1991.

[52] Rosario Fazio and Roberto Raimondi. Resonant andreev tunneling in strongly interacting quantum dots. *Phys. Rev. Lett.*, 80:2913–2916, Mar 1998.

[53] Hartmut Haug and Antti-Pekka Jauho. *Quantum kinetics in transport and optics of semiconductors; 2nd, substantially rev. ed.*, volume 123 of *Springer series in solid-state sciences*. Springer, Berlin, 2008.

[54] T. Domański and A. Donabidowicz. Interplay between particle-hole splitting and the kondo effect in quantum dots. *Phys. Rev. B*, 78:073105, Aug 2008.

[55] D N Zubarev. Double-time green functions in statistical physics. *Soviet Physics Uspekhi*, 3(3):320, mar 1960.

[56] Hong-Kang Zhao and Lina Zhao. Spin-flip mesoscopic transport through a quantum dot coupled to carbon nanotube terminals. *Physics of Condensed Matter*, 47:295–303, 09 2005.

[57] A M Calle, M Pacheco, G B Martins, V M Apel, G A Lara, and P A Orellana. Fano–andreev effect in a t-shape double quantum dot in the kondo regime. *Journal of Physics: Condensed Matter*, 29(13):135301, feb 2017.

[58] Hao Zhang, Dong E. Liu, Michael Wimmer, and Leo P. Kouwenhoven. Next steps of quantum transport in majorana nanowire devices. *Nature Communications*, 10(1), nov 2019.

[59] Leo P. Kouwenhoven, Gerd Schön, and Lydia L. Sohn. *Introduction to Mesoscopic Electron Transport*. Springer Netherlands, 1997.

[60] Xiao-Qi Wang, Shu-Feng Zhang, Yu Han, and Wei-Jiang Gong. Fano-andreev effect in a parallel double quantum dot structure. *Phys. Rev. B*, 100, 2019.

[61] J. Gramich, A. Baumgartner, and C. Schönenberger. Andreev bound states probed in three-terminal quantum dots. *Phys. Rev. B*, 96:195418, Nov 2017.

[62] Jean-Damien Pillet, Charis Quay, Pascal Morfin, Cristina Bena, Alfredo Yeyati, and Philippe Joyez. Andreev bound states in supercurrent-carrying carbon nanotubes revealed. *Nature Physics*, 6:695, 05 2010.

[63] Tanuj Chamoli and Ajay . Andreev bound states in superconductor-quantum dot josephson junction at infinite-u limit, 07 2020.

[64] Travis Dirks, Taylor Hughes, Siddhartha Lal, Bruno Uchoa, Yung-Fu Chen, Cesar Chialvo, Paul Goldbart, and Nadya Mason. Transport through andreev bound states in a graphene quantum dot. *Nature Physics*, 7, 05 2010.

[65] Rosario Fazio and Roberto Raimondi. Resonant andreev tunneling in strongly interacting quantum dots. *Phys. Rev. Lett.*, 80:2913–2916, Mar 1998.

[66] Jan Barański and T. Domański. Fano-type interference in quantum dots coupled between metallic and superconducting leads. *Phys. Rev. B*, 84:195424, Nov 2011.

[67] T. Domański, A. Donabidowicz, and K. I. Wysokiński. Influence of pair coherence on charge tunneling through a quantum dot connected to a superconducting lead. *Phys. Rev. B*, 76:104514, Sep 2007.

[68] Grzegorz Górski and Krzysztof Kucab. Transport properties of proximitized double quantum dots. *Physica E: Low-dimensional Systems and Nanostructures*, 126:114459, 02 2021.

[69] T. Domański, I. Weymann, M. Barańska, and G. Górski. Constructive influence of the induced electron pairing on the kondo state. *Scientific Reports*, 2016.

[70] U. Fano. Effects of configuration interaction on intensities and phase shifts. *Phys. Rev.*, 124:1866–1878, Dec 1961.

[71] Andrey E. Miroshnichenko, Sergej Flach, and Yuri S. Kivshar. Fano resonances in nanoscale structures. *Rev. Mod. Phys.*, 82:2257–2298, Aug 2010.

[72] Gao Wen-Zhu, Gong Wei-Jiang, Zheng Yi-Song, Liu Yu, and Lü Tian-Quan. Fano effect in t-shaped double quantum dot structure with decoherence effect. *Communications in Theoretical Physics*, 49(3):771, mar 2008.

[73] Grzegorz Michałek, Bogdan Bułka, Marcin Urbaniak, Tomasz Domanski, and K. Wysokinski. Andreev spectroscopy in three-terminal hybrid nanostructure. *Acta Physica Polonica Series a*, 127:293, 02 2015.

[74] Grzegorz Michałek, Tomasz Domanski, and K. Wysokinski. Cooper pair splitting efficiency in the hybrid three-terminal quantum dot. *Journal of Superconductivity and Novel Magnetism*, 30, 01 2017.

[75] Yu Zhu, Qing-feng Sun, and Tsung-han Lin. Andreev reflection through a quantum dot coupled with two ferromagnets and a superconductor. *Phys. Rev. B*, 65:024516, Dec 2001.

[76] Grzegorz Michałek, Tomasz Domanski, Bogdan Bułka, and K. Wysokinski. Novel non-local effects in three-terminal hybrid devices with quantum dot. *Scientific Reports*, 5, 05 2015.

[77] E. C. Siqueira and G. G. Cabrera. Andreev tunneling through a double quantum-dot system coupled to a ferromagnet and a superconductor: Effects of mean-field electronic correlations. *Phys. Rev. B*, 81:094526, Mar 2010.

[78] Ezequiel Siqueira, P. Orellana, Antonio Seridonio, R. Cestari, M. Figueira, and Guillermo Cabrera. Interference effects induced by andreev bound states in a hybrid nanostructure composed by a quantum dot coupled to ferromagnetic and superconductor leads. 09 2014.

[79] E.C. Siqueira, P.A. Orellana, R.C. Cestari, M.S. Figueira, and G.G. Cabrera. Fano effect and andreev bound states in a hybrid superconductor–ferromagnetic nanostructure. *Physics Letters A*, 379(39):2524–2529, 2015.

[80] T. Domański and A. Donabidowicz. Interplay between particle-hole splitting and the kondo effect in quantum dots. *Phys. Rev. B*, 78:073105, Aug 2008.

[81] Grzegorz Michałek, Bogdan R. Bułka, Tadeusz Domański, and Karol I. Wysokiński. Interplay between direct and crossed andreev reflections in hybrid nanostructures. *Phys. Rev. B*, 88:155425, Oct 2013.

[82] Sachin Verma and Ajay Singh. Non-equilibrium thermoelectric transport across normal metal–quantum dot–superconductor hybrid system within the coulomb blockade regime. *Journal of Physics: Condensed Matter*, 34(15):155601, feb 2022.

[83] Hartmut Haug and A. P. Jauho. Quantum kinetics in transport and optics of semiconductors. 2004.

[84] J. Rammer and H. Smith. Quantum field-theoretical methods in transport theory of metals. *Rev. Mod. Phys.*, 58:323–359, Apr 1986.

[85] J Hubbard. Electron correlations in narrow energy bands. *Proc. Roy. Soc. (London), Ser. A*.

[86] R. Franz and G. Wiedemann. Ueber die wärme-leitungsfähigkeit der metalle. *Annalen der Physik*, 165(8):497–531, 1853.

[87] Melvin Cutler and N. F. Mott. Observation of anderson localization in an electron gas. *Phys. Rev.*, 181:1336–1340, May 1969.

[88] L. D. Hicks and M. S. Dresselhaus. Thermoelectric figure of merit of a one-dimensional conductor. *Phys. Rev. B*, 47:16631–16634, Jun 1993.

[89] L. D. Hicks and M. S. Dresselhaus. Effect of quantum-well structures on the thermoelectric figure of merit. *Phys. Rev. B*, 47:12727–12731, May 1993.

[90] C. W. J. Beenakker and A. A. M. Staring. Theory of the thermopower of a quantum dot. *Phys. Rev. B*, 46:9667–9676, Oct 1992.

[91] Ya. M. Blanter, C. Bruder, Rosario Fazio, and Herbert Schoeller. Aharonov-bohm-type oscillations of thermopower in a quantum-dot ring geometry. *Phys. Rev. B*, 55:4069–4072, Feb 1997.

[92] M. Turek and K. A. Matveev. Cotunneling thermopower of single electron transistors. *Phys. Rev. B*, 65:115332, Mar 2002.

[93] Jens Koch, Felix von Oppen, Yuval Oreg, and Eran Sela. Thermopower of single-molecule devices. *Phys. Rev. B*, 70:195107, Nov 2004.

[94] Björn Kubala and Jürgen König. Quantum-fluctuation effects on the thermopower of a single-electron transistor. *Phys. Rev. B*, 73:195316, May 2006.

[95] X. Zianni. Coulomb oscillations in the electron thermal conductance of a dot in the linear regime. *Phys. Rev. B*, 75:045344, Jan 2007.

[96] Xu-Ming Zhang, Xiaoshuang Chen, and Wei Lu. Thermopower of a multilevel quantum dot coupled with leads in coulomb blockade. *Physics Letters A - PHYS LETT A*, 372:2816–2819, 04 2008.

[97] Akram Boukai, Yuri Bunimovich, Jamil Tahir-Kheli, Jen-Kan Yu, William Goddard, and James Heath. Silicon nanowires as efficient thermoelectric materials. *Nature*, 451:168–71, 02 2008.

[98] G D Mahan and J O Sofo. The best thermoelectric. *roceedings of the National Academy of Sciences of the United States of America*, 93:7436–9, 1996.

[99] Tae-Suk Kim and S. Hershfield. Thermoelectric effects of an aharonov-bohm interferometer with an embedded quantum dot in the kondo regime. *Phys. Rev. B*, 67:165313, Apr 2003.

[100] R. Franco, J. Silva–Valencia, and M. S. Figueira. Thermopower and thermal conductance through parallel coupled quantum dots. *Journal of Applied Physics*, 103(7):07B726, 02 2008.

[101] R. Świrkowicz, M. Wierzbicki, and J. Barnaś. Thermoelectric effects in transport through quantum dots attached to ferromagnetic leads with noncollinear magnetic moments. *Phys. Rev. B*, 80:195409, Nov 2009.

[102] T. A. Costi and V. Zlatić. Thermoelectric transport through strongly correlated quantum dots. *Phys. Rev. B*, 81:235127, Jun 2010.

[103] Jie Liu, Qing-feng Sun, and X. C. Xie. Enhancement of the thermoelectric figure of merit in a quantum dot due to the coulomb blockade effect. *Phys. Rev. B*, 81:245323, Jun 2010.

[104] David M.-T. Kuo and Yia-chung Chang. Thermoelectric and thermal rectification properties of quantum dot junctions. *Phys. Rev. B*, 81:205321, May 2010.

[105] Yushen Liu and X. Yang. Enhancement of thermoelectric efficiency in a double-quantum-dot molecular junction. *Journal of Applied Physics*, 108:023710 – 023710, 08 2010.

[106] M Tsaousidou and G P Triberis. Thermoelectric properties of a weakly coupled quantum dot: enhanced thermoelectric efficiency. *Journal of Physics: Condensed Matter*, 22(35):355304, aug 2010.

[107] Krzysztof P. Wójcik and Ireneusz Weymann. Proximity effect on spin-dependent conductance and thermopower of correlated quantum dots. *Phys. Rev. B*, 89:165303, Apr 2014.

[108] R. S. Deacon, Y. Tanaka, A. Oiwa, R. Sakano, K. Yoshida, K. Shibata, K. Hirakawa, and S. Tarucha. Tunneling spectroscopy of andreev energy levels in a quantum dot coupled to a superconductor. *Phys. Rev. Lett.*, 104:076805, Feb 2010.

[109] Qing-feng Sun, Jian Wang, and Tsung-han Lin. Resonant andreev reflection in a normal-metal–quantum-dot–superconductor system. *Phys. Rev. B*, 59:3831–3840, Feb 1999.

[110] Jian Wang, Yadong Wei, Hong Guo, Qing-feng Sun, and Tsung-han Lin. Nonlinear transport theory for hybrid normal-superconducting devices. *Phys. Rev. B*, 64:104508, Aug 2001.

[111] T. Domański, A. Donabidowicz, and K. I. Wysokiński. Influence of pair coherence on charge tunneling through a quantum dot connected to a superconducting lead. *Phys. Rev. B*, 76:104514, Sep 2007.

[112] T. Domański and A. Donabidowicz. Interplay between particle-hole splitting and the kondo effect in quantum dots. *Phys. Rev. B*, 78:073105, Aug 2008.

[113] Yong-Ping Zhang, Hui Yu, Ying-Fang Gao, and J. Q. Liang. Quantum transport through a double aharonov-bohm interferometer in the presence of andreev reflection. *Phys. Rev. B*, 72:205310, Nov 2005.

[114] Rosa López, Mahn-Soo Choi, and Ramón Aguado. Josephson current through a kondo molecule. *Phys. Rev. B*, 75:045132, Jan 2007.

[115] Feng Jiang, Yonghong Yan, Shikuan Wang, and Yijing Yan. The current-induced heat generation in a spin-flip quantum dot sandwiched between a ferromagnetic and a superconducting electrode. *Physics Letters A*, 381(45):3831–3842, 2017.

[116] Tie-Feng Fang, Ai-Min Guo, and Qing-Feng Sun. Nonequilibrium kondo effect by the equilibrium numerical renormalization group method: The hybrid anderson model subject to a finite spin bias. *Phys. Rev. B*, 97:235115, Jun 2018.

[117] Xiao-Qi Wang, Shu-Feng Zhang, Yu Han, and Wei-Jiang Gong. Fano-andreev effect in a parallel double quantum dot structure. *Phys. Rev. B*, 100:115405, Sep 2019.

[118] Zoltán Scherübl, András Pályi, and Szabolcs Csonka. Transport signatures of an andreev molecule in a quantum dot–superconductor–quantum dot setup. *Beilstein Journal of Nanotechnology*, 10:363–378, 02 2019.

[119] Jasper van Veen, Damaz de Jong, Lin Han, Christian Prosko, Peter Krogstrup, John D. Watson, Leo P. Kouwenhoven, and Wolfgang Pfaff. Revealing charge-tunneling processes between a quantum dot and a superconducting island through gate sensing. *Phys. Rev. B*, 100:174508, Nov 2019.

[120] R. Taranko, K. Wrześniewski, B. Baran, I. Weymann, and T. Domański. Transient effects in a double quantum dot sandwiched laterally between superconducting and metallic leads. *Phys. Rev. B*, 103:165430, Apr 2021.

[121] R. Świrkowicz, M. Wierzbicki, and J. Barnaś. Thermoelectric effects in transport through quantum dots attached to ferromagnetic leads with noncollinear magnetic moments. *Phys. Rev. B*, 80:195409, Nov 2009.

[122] Piotr Trocha and Józef Barnaś. Spin-dependent thermoelectric phenomena in a quantum dot attached to ferromagnetic and superconducting electrodes. *Phys. Rev. B*, 95:165439, Apr 2017.

[123] Niu PB. Zhang C. et al Yao, H. Thermoelectric efficiency enhanced in a quantum dot with polarization leads, spin-flip and external magnetic field. *Eur. Phys. J. B 91*, 91, 2018.

[124] Sun-Yong Hwang, Rosa López, and David Sánchez. Large thermoelectric power and figure of merit in a ferromagnetic–quantum dot–superconducting device. *Phys. Rev. B*, 94:054506, Aug 2016.

[125] Po Zhang, Hao Wu, Jun Chen, Sabbir A. Khan, Peter Krogstrup, David Pekker, and Sergey M. Frolov. Signatures of andreev blockade in a double quantum dot coupled to a superconductor. *Phys. Rev. Lett.*, 128:046801, Jan 2022.

[126] Piotr Trocha and Józef Barnaś. Spin-dependent thermoelectric phenomena in a quantum dot attached to ferromagnetic and superconducting electrodes. *Phys. Rev. B*, 95:165439, Apr 2017.

[127] Hui Yao, Chao Zhang, Peng bin Niu, Zhi-Jian Li, and Yi-Hang Nie. Enhancement of charge and spin seebeck effect in triple quantum dots coupling to ferromagnetic and superconducting electrodes. *Physics Letters A*, 382(44):3220–3229, 2018.

[128] Wei-Ping Xu, Yu-Ying Zhang, Qiang Wang, Zhi-Jian Li, and Yi-Hang Nie. Thermoelectric effects in triple quantum dots coupled to a normal and a superconducting leads. *Physics Letters A*, 380(7):958–964, 2016.

[129] Sachin Verma and Ajay Singh. Non-equilibrium thermoelectric transport across normal metal–quantum dot–superconductor hybrid system within the coulomb blockade regime. *Journal of Physics: Condensed Matter*, 34(15):155601, feb 2022.

[130] G. Michałek, M. Urbaniak, B. R. Bułka, T. Domański, and K. I. Wysokiński. Local and nonlocal thermopower in three-terminal nanostructures. *Phys. Rev. B*, 93:235440, Jun 2016.

[131] Francesco Mazza, Riccardo Bosisio, Giuliano Benenti, Vittorio Giovannetti, Rosario Fazio, and Fabio Taddei. Thermoelectric efficiency of three-terminal quantum thermal machines. *New Journal of Physics*, 16(8):085001, aug 2014.